A MEASUREMENT OF INCLUSIVE QUASI-ELASTIC ELECTRON SCATTERING CROSS SECTIONS AT HIGH MOMENTUM TRANSFER

Thesis by

David Henry Potterveld

In Partial Fulfillment of the Requirements

for the Degree of

Doctor of Philosophy

California Institute of Technology

Pasadena, California

1989

(Submitted July 6, 1988)

Acknowledgments

This work would not have been possible were it not for the support, help, and guidence of a great many people. I am particularly indebted to the students, staff, and faculty at Kellogg with whom working and playing have been such pleasures. I am grateful to Bob McKeown for providing the opportunity to pursue this research, and for many useful discussions about the data analysis. Special thanks go to Juerg Jourdan, for analyzing the Fe data from our second experimental run. Thanks also go to my friends and office mates who, through the years, have helped keep me sane.

Technical support for the experiment was provided by many groups at SLAC, all of whom were indispensable. The efforts of John Marks and the cryogenic target group deserve special note for the design, construction, and maintenance of our targets and related apparatus. I am also grateful to the American University group for lending us the solid targets and for helping with the on-line software. Here at Caltech, I must thank Pat Huber, our computer manager, for his patience while I consumed so much of his computer resources.

Lastly, I would like to thank my parents, who made it all possible. Their support and encouragement of my education have allowed me to follow my interests wherever they lay. This work is dedicated to them and to everyone else who has had a part in shaping my life.

Abstract

We have measured inclusive electron-scattering cross sections for targets of ^{4}He, C, Al, Fe, and Au, for kinematics spanning the quasi-elastic peak, with squared, four-momentum transfers (q^2) between 0.23 and 2.89 (GeV/c)^2. Additional data were measured for Fe with q^2's up to 3.69 (GeV/c)^2. These cross sections were analyzed for the y-scaling behavior expected from a simple, impulse-approximation model, and are found to approach a scaling limit at the highest q^2's. The q^2 approach to scaling is compared with a calculation for infinite nuclear matter, and relationships between the scaling function and nucleon momentum distributions are discussed. Deviations from perfect scaling are used to set limits on possible changes in the size of nucleons inside the nucleus.

Table of Contents

List of Figures

List of Tables

Chapter 1
Introduction

Inclusive quasi-elastic electron scattering offers a unique opportunity to probe the interactions of nucleons within the nucleus. This is so because the electron interacts with the nucleus only via the exchange of photons, which is a feeble, yet well understood process in contrast with the strong interaction. The fact that it is weak means that, to a good approximation, the electron interacts with only one "particle" in the nucleus, via the exchange of one virtual photon. Thus, final-state interactions (FSI) between the scattered electron and the nucleus are not a problem. The fact that the electron-photon vertex is exactly described by quantum electro-dynamics [1] is of obvious advantage. Furthermore, the quasi-elastic peak appears to be dominated by a simple reaction mechanism. The "particles" turn out to be only the A nucleons, which behave very much like free, albeit moving, nucleons. Since the elastic scattering of electrons from free nucleons is a very well-studied problem [2-4], we are thus able to probe the nuclear structure with little theoretical ambiguity.

The physics interests addressed by quasi-elastic scattering therefore fall into three categories. These are: the validation and understanding of the reaction mechanism, nucleon momentum distributions within nuclei, and the properties of nucleons in a nuclear medium.

Understanding the reaction mechanism is vital if any conclusions are to be drawn from such measurements. The simple knockout of bound nucleons is, in fact, an oversimplification. Final-state interactions of the recoiling nucleon are large, since it

is a hadron. Because neither it nor the residual $A-1$ nucleons are detected in an inclusive measurement, this effect is largely abated. Furthermore, the effect of FSI should diminish as q^2 (the square of the four momentum transfer) increases, and at sufficiently large q^2 cease to be a problem. Meson exchange currents, in which the photon couples to a meson instead of a nucleon, are known to be important in the "dip region" between the quasi-elastic peak and the delta resonance [5]. The contribution to the top and low ω (energy transfer) side of the quasi-elastic peak is expected to be small, but this is by no means a fully understood subject. Lastly, there is the problem of contributions from inelastic electron-nucleon scattering, primarily from the delta resonance. These peaks are also smeared out by the moving nucleons, and at high momentum transfers can overwhelm the quasi-elastic scattering on the high ω side of the peak, or even at the top of the peak! Luckily, these inelastic contributions die off rapidly as one moves over to the low ω side, where they become negligible. But as we shall see, these contributions are an obstacle to be overcome in the interpretation of some of our results.

The appropriateness of an impulse approximation (I.A.) description for quasi-elastic scattering, despite the above-mentioned effects, can be gauged by a kind of scaling, called y-scaling [6-9], that is predicted by such a model. Basically, at a high enough momentum transfer, the quasi-elastic cross section can be written as the product of an electron-nucleon cross section times a scaling function, $F(y)$ [9]. The scaling variable, y, is essentially the nucleon's momentum along the direction of $\vec{Q}$, the three-momentum transfer, assuming that transverse momentum components can be neglected. (More precisely, y is the smaller in magnitude of the two solutions allowed by kinematics for the nucleon's longitudinal momentum when the transverse components are exactly zero. The absolute value of y is the lowest momentum the nucleon may have, regardless of direction, for there to be a solution of the kinematics.)

$F(y)$ is closely related to the nucleon momentum distribution, and is independent of the details of electron-nucleon scattering. Thus, the particle physics and nuclear physics aspects of quasi-elastic scattering are neatly separated. (This is a general feature of convolution models. For example, the parton model of nucleons leads to the Bjorken scaling of deep inelastic scattering [10].) By dividing the measured quasi-elastic cross sections by the well-known, elementary cross section (σ_{eN}), we should therefore obtain a q^2 independent scaling function. Since none of the alternate reaction mechanisms has a q^2 dependence like σ_{eN}, their presence would cause a breakdown of this y-scaling. Thus, if the data scale properly, we have strong evidence that the I.A. description is sufficient.

Implicit in the simple I.A. model of quasi-elastic scattering is the assumption that the bound nucleons are the same as free nucleons, and in particular that they have the same elastic-scattering form factors. But in nuclei, the average internucleon separation can approach the rms radius of the nucleons, which might have an effect on the nucleons themselves. Some authors have conjectured that the nucleons might swell [11-14], or coalesce into 6 (or more) quark objects [15], as an explanation of the widely discussed EMC effect [16-19]. This would cause the form factors involved in quasi-elastic scattering to change from the free nucleon values, significantly altering the cross section. Such modifications of the nucleon's properties by the nuclear medium can also be studied through the y-scaling analysis. As we will show, a change in the form factors consistent with a change in the nucleon radius has little impact on the quality of scaling, but has a major effect on the normalization of the scaling function. Thus, the normalization of experimentally determined $F(y)$'s provides a sensitive test for any such swelling.

Finally, if the data do indeed scale, we can interpret the results to learn about the momentum distribution of the nucleons in the nucleus. Of particular interest are the high momentum components, which arise because of the short-range, repulsive part of the nucleon-nucleon interaction [20], and are closely linked to the pair correlation function [21-24]. This short-range behavior of the wave function is generally not well described by mean-field shell models, in which each nucleon interacts only with an average field produced by the other nucleons. Such models can correctly describe only the long-range behavior responsible for momenta $\leq k_f$, the Fermi momentum. For $k > k_f$, the momentum distribution is dominated by the short-range correlations, which therefore must be included in any proper microscopic description of the nucleus.

To illustrate some of these ideas, we consider previous measurements of quasi-elastic scattering from ^{3}He [25]. These data were taken at SLAC, with a scattering angle of 8 deg, for incident electron energies ranging between 2.81 and 14.7 GeV. Four of these cross sections are plotted in Figure 1.1, vs. the energy transfer, ω. The prominent peak in the lower energy spectra is the quasi-elastic peak; at higher energies, the peak disappears into the side of a rapidly rising, featureless background from deep-inelastic scattering. We have extracted $F(y)$'s from all of the cross sections (8 spectra in all); these are plotted in Figure 1.2.

Although the cross sections vary over several orders of magnitude, we can see that the derived $F(y)$'s collapse impressively onto a universal scaling curve, at least for $y \leq 0$, corresponding to the low ω side of the peak. In this region, the I.A. reaction mechanism serves very well to describe the data. For $y > 0$, we see deviations from perfect scaling that grow larger as the momentum transfer increases. This is the result of the inelastic background that dominates the cross section there. The theoretical $F(y)$, however, is symmetric about $y = 0$. Thus, the background can be ignored by

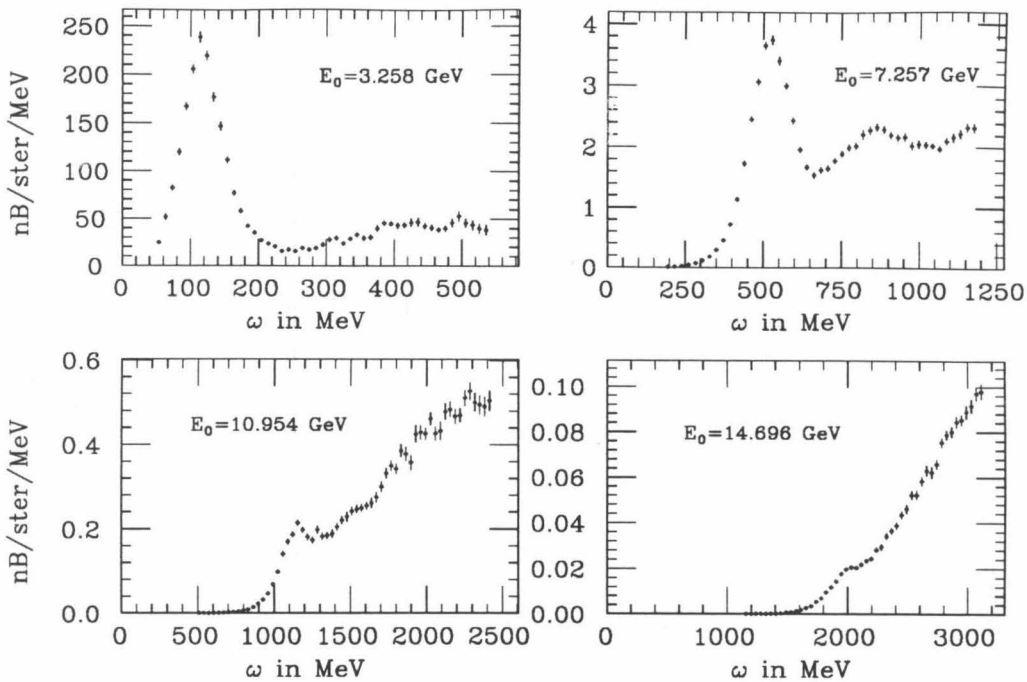

Figure 1.1 – Differential cross sections ($d\sigma/d\Omega/d\omega$) in units of nB/ster/MeV for electron scattering from ^{3}He at an angle of 8 degrees.

reflecting $F(y)$ about the y axis. The normalization of these scaling functions is close to that predicted for standard nucleons, and has been used to set stringent limits on nucleon swelling [26].

As we will show, the momentum distribution $n(k)$ is related to the scaling function through:

$$n(k) = \frac{-1}{2\pi k} \cdot \frac{dF(-k)}{dk}; \quad k \geq 0. \tag{1.1}$$

Examination of Figure 1.2 shows that we can therefore probe the momentum distribution at large momenta ($\sim$ 0.5 GeV/c). This regime is not easily accessed with hadronic probes, since multistep reactions with nucleons of lower momenta will obscure the desired single-step reaction. The Fermi momentum is $\sim$ 0.15 GeV/c (for heavier nuclei it saturates at about 0.26) [27], so that at the higher momenta we see

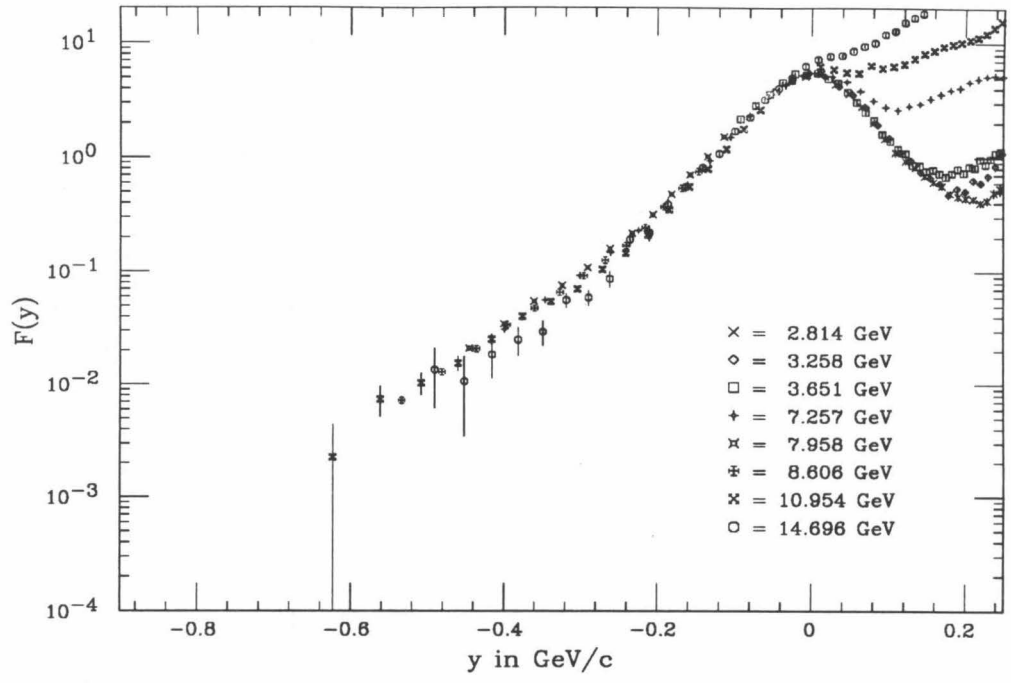

Figure 1.2 – $F(y)$ scaling functions derived from the ^{3}He cross sections. F has units of GeV^{-1}, and y has units GeV/c. (Only data with ω more than 50 MeV above the elastic peak are plotted.)

that there is significant strength that is due to the short range correlations. Thus, we see that quasi-elastic scattering at high q^2 and low ω is a useful probe of nuclear structure.

Previous experimental work has focused on light nuclei such as ^{2}H, ^{3}He, and ^{4}He [28,29] at high q^2, and on ^{40}Ca [7] for low q^2 and $|y| < 0.3$ GeV/c. We have attempted to address these physics issues for a broad range of nuclei by measuring quasi-elastic cross sections from targets of ^{4}He, C, Al, Fe, and Au, and performing a y-scaling analysis of the results. This work was performed at SLAC during the spring of 1985, under the auspices of the NPAS (Nuclear Physics At SLAC) program, with an additional data run one year later. We made use of the NPI injector, which provided beams of 2.020 and 3.6 GeV (4.0 GeV for the later run) to our targets

in end station A. Scattered electrons were detected with the 8 GeV spectrometer, at angles between 15 and 39 degrees, and energies between 1.6 GeV and the beam energy. The 1986 data run used only the Fe target, at a scattering angle of 30 deg. Our measurements therefore cover a range $0.25 < q^2 < 3.7$ GeV and extend y-scaling results to heavy nuclei.

We will show that the data do indeed scale, although the approach to scaling becomes worse with increasing A. The approach to scaling will be shown to compare qualitatively with a calculation for infinite nuclear matter, including FSI [30]. A renormalization of the calculated $F(y)$'s is needed, however, to achieve detailed agreement, which we take to be an indication that the calculation, based on the Paris potential [31], overestimates the strength of the hard-core repulsion. Implications of the shape of the scaling function will be discussed, and finally, limits on changes to the nucleon radius will be presented.

The organization of this paper is as follows. Chapter 2 discusses the details of the experimental equipment, and Chapter 3 covers the off-line data analysis performed at Caltech for the data taken in 1985. The 1986 data run, which made use of an upgraded detector package in the spectrometer, was analyzed with the same algorithm, and largely the same software as the 1985 data. Its analysis is therefore not separately discussed. Chapter 4 reviews the systematic corrections applied to the data, as well as the systematic uncertainties in the cross-section measurements. Chapter 5 develops the theoretical framework of the y-scaling formalism, and Chapter 6 presents the results for the cross sections and scaling functions, with conclusions drawn in Chapter 7. Two appendices are included. The first covers details of the unfolding of radiative effects from the cross sections; the second presents tables of all the cross sections and derived $F(y)$'s.

Chapter 2
Experimental Details

2.1 Upstream Beamline

Our electron beam was produced by the SLAC accelerator, which is an RF linac, operated in a pulsed mode. At the time of our experiment, it could provide approximately 1 GeV of energy gain per linac sector to beam pulses of up to 1.6 μs duration, at pulse rates of up to 180 Hz. The full linac is 30 sectors long, and thus is capable of delivering very high energy beams. Low-energy beams of a few GeV, however, suffer from significant losses in the linac due to the low RF power levels, and could be delivered only at very low beam currents. For this reason, a new beam injector (NPI) was built for the Nuclear Physics program at SLAC (NPAS). This injector was located six sectors from the linac exit, and thus could provide beams of up to $\sim$5 GeV in energy, at very high beam currents. Our experiment, (NE3), was the first experiment to make use of this injector. After some adjustments, the NPI was able to provide beams of 60 mA peak current at 3.6 GeV into full width pulses at 180 pulses per second (PPS), as measured in the experimental hall. Most of the data, however, were taken at 120 pps with $\sim$40 mA peak current and 1.6 μs pulse width.

The beam pulses from the linac were directed into the A-beamline, which served end-station A (ESA). The layout of the A-line is shown in Figure 2.1. The energy and profile of the beam at the target were determined by the A-bend. Eight identical dipole magnets in the A-bend (B10-17) defined the beam energy. A ninth dipole,

in series with the other eight, was used to monitor the beam energy. This magnet, not part of the beam transport, had a rotating wire coil (flip-coil) mounted in the nominal beam position. The flip-coil was used to monitor the dipoles' magnetic field, which determines the central energy of the beam. The energy spread of the beam was limited by the slits SL10 and SL11. These slits were typically set to a full width of 0.75%. The actual energy spread was ~0.5% (FWHM), verified by closing the slits until the beam current dropped. Quadrupoles Q10-14 were used to shape the beam spot at the target. These magnets were given a standard excitation for each beam energy to produce a spot ~3 mm vertical by 10 mm horizontal.

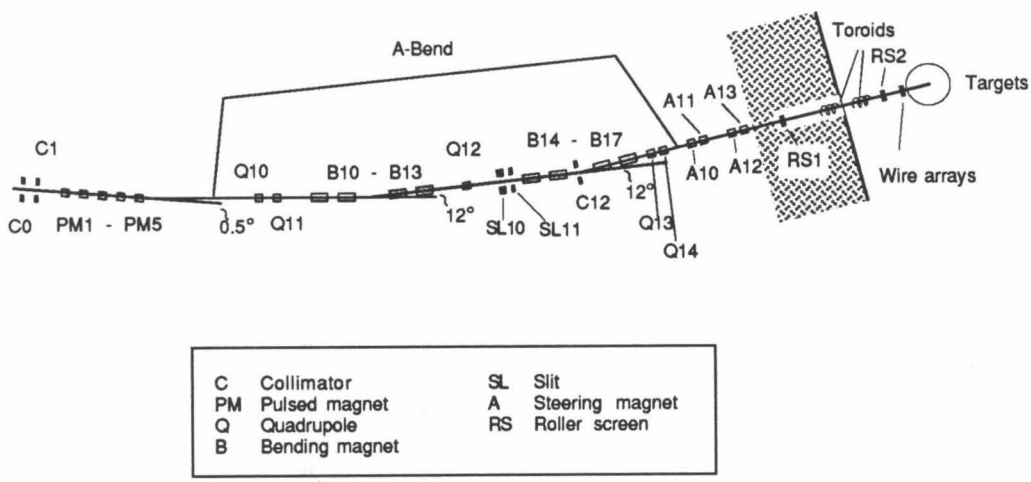

Figure 2.1 – Diagram of the beamline used to transport electrons from the linac to the end station. The locations of the magnets and slits refered to in the text are shown.

The final beam steering was under the experimenter's control, via magnets A10-13. Two ZnS-coated plastic "roller screens" (RS1-2) could be remotely inserted into the beam and viewed by TV camera to inspect the beam steering visually. In addition, two arrays of thin Al wires (0.005 inch diam., 0.0156 inch spacing) were permanently mounted in the beam's path (Figure 2.2). Secondary emission from these wires when struck by the beam produced currents in external circuits to which the wires were connected. An LSI minicomputer was used to monitor the wire array currents on a pulse by pulse basis, and to control two of the steering magnets to keep the beam spot centered on the target. The other two magnets were manually adjusted to keep the beam's trajectory straight along the beam centerline, as verified periodically with the roller screens.

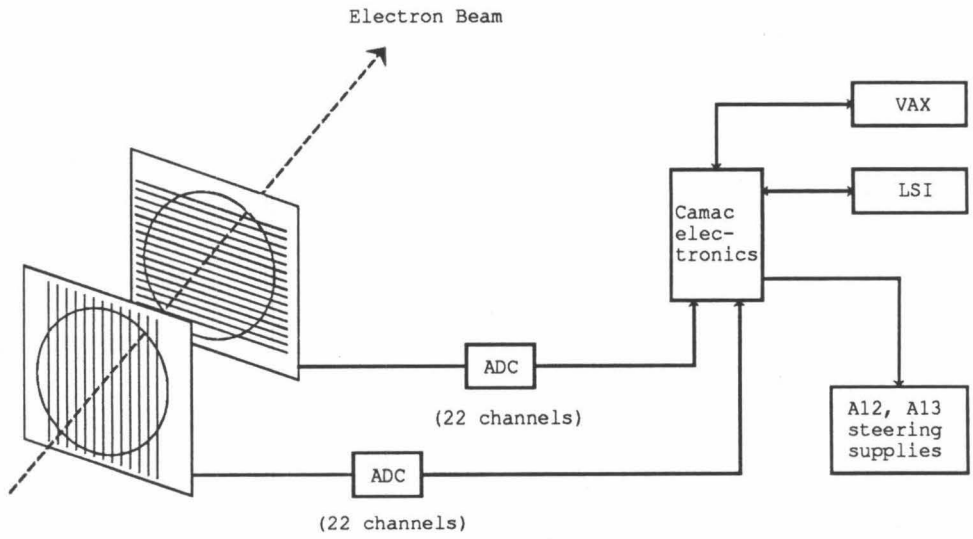

Figure 2.2 – Secondary emision wire arrays used to monitor the beam steering.

Beam current was integrated on a pulse by pulse basis as well, using two independent, non-intercepting toroidal transformers (TOR_0 and TOR_1). The electron beam itself serves as the primary winding of these transformers. The secondary windings are connected to a resistor and capacitor to form a resonant circuit. A beam pulse will excite a damped oscillation in this circuit, as shown in Figure 2.3.

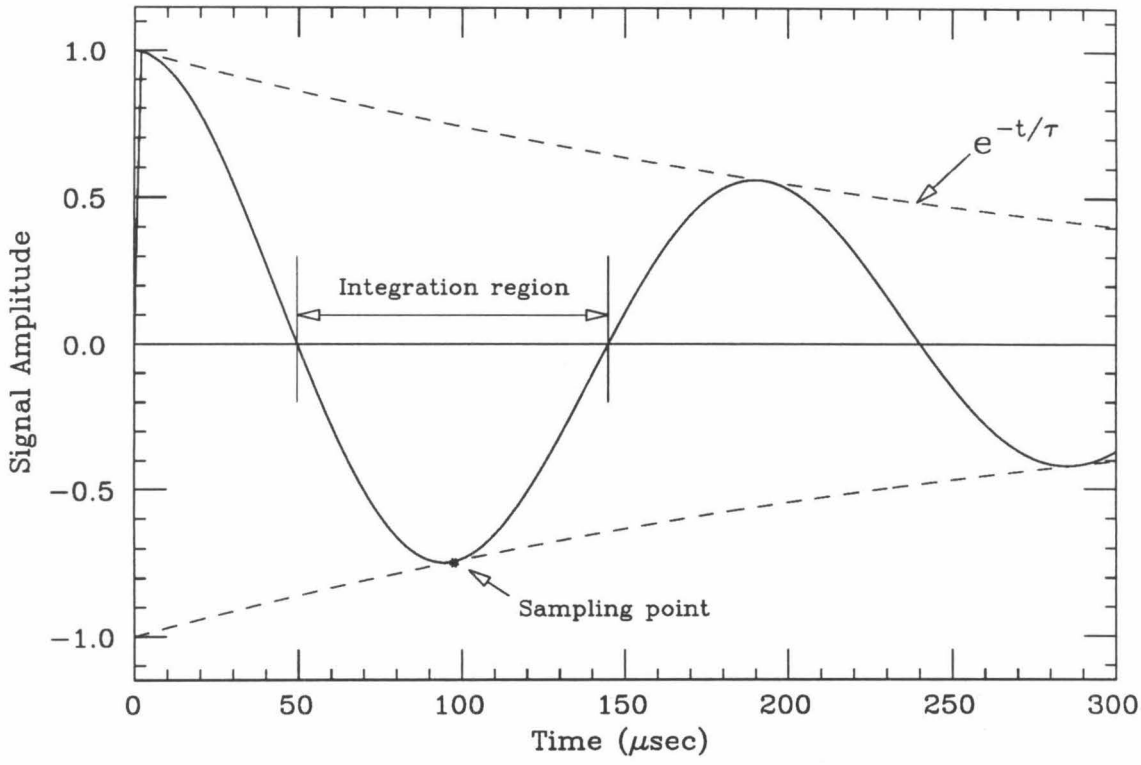

Figure 2.3 – Typical voltage waveform from toroidal charge monitors.

Two separate systems monitored this signal from each toroid. The first and original system sampled the amplified waveform at a fixed time after the start of the beam pulse. The delay time was chosen to minimize sensitivity to the pulse width. The second system integrated the toroid signal over its first negative portion. Each system was independently calibrated by passing a known pulse through a tertiary winding. Thus, we had four independent measurements of the beam current: T0 and

T2 from TOR_0, T1 and T3 from TOR_1, with T0 and T1 from the original monitoring system. Typically, these four values agreed to better than 0.5%. Figure 2.4 shows a diagram of the associated electronics for both the new and the old toroid readout systems.

Beam quality was monitored with two plastic scintillators, each coupled to a phototube. The bad-spill monitor was located in the upstream alcove, near RS1, adjacent to the beam pipe. This scintillator was used to minimize beam halo when tuning the beam. The good-spill monitor was mounted ~10 m from the target, at a scattering angle of ~ 70 degrees. This scintillator was used to observe the time structure of the beam current with each beam pulse. Anode signals from each phototube were viewed on an oscilloscope, and were provided to the main control center (MCC) as a diagnostic for beam tuning. Ideally, no signal should be observed in the bad spill, while the good spill should be a square wave. Actual beam tunes usually came very close.

2.2 Pivot Area

The three spectrometers in the end station share a common pivot, as shown in Figure 2.5. The pivot itself is a modified naval gun mount, the top of which is a flat deck ~8 ft. in diameter. Attached to this deck was the scattering chamber and target assembly. The scattering chamber itself was an aluminum cylinder 32 inches in diameter, with 1-inch thick walls. The electron beam entered the chamber through a 5-inch circular aperture, in which was mounted a 0.001 inch aluminum window. This window isolated the chamber vacuum ($\leq 10^{-7}$ torr) from the beamline vacuum (~10 micron Hg.) A manually operated vacuum valve and bleed bypass were located just upstream of the window to protect it from damaging pressures during idle periods.

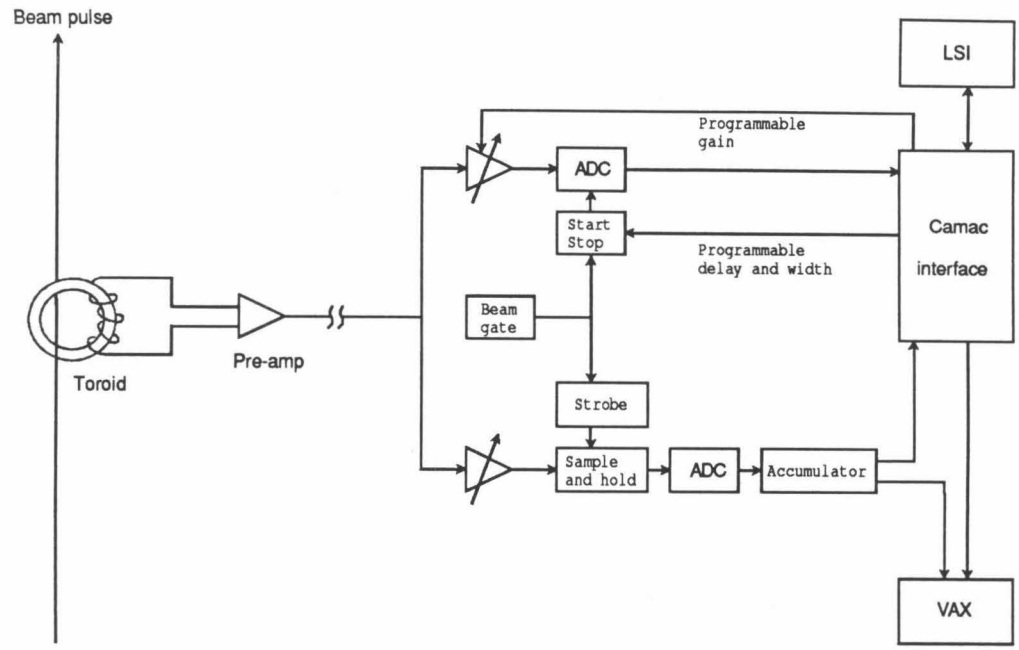

Figure 2.4 – Schematic of toroid electronics. The pulse integrating system was read by an LSI-11 microcomputer linked to the Vax. The older system was directly read by the Vax computer.

The electron beam exited the scattering chamber through a 0.008 inch Al window, and traversed ~3 ft. of room air before entering the downstream beampipe's endcap. Electrons scattered by the target would also pass through the exit window, traverse a 73-inch air gap, and enter the 8 GeV spectrometer's entrance window. The exit window covered an angle of ±90 degrees in scattering angle, and was 4 inches tall, so that it did not restrict the spectrometer's angular acceptance.

During the checkout phase of this experiment, we observed a non-zero event rate with no target in the beam. This was due to electrons scattered from the beam by the chamber's exit window, which was within the spectrometer's acceptance at forward angles. To eliminate these events, we constructed a wedge-shaped shield from a

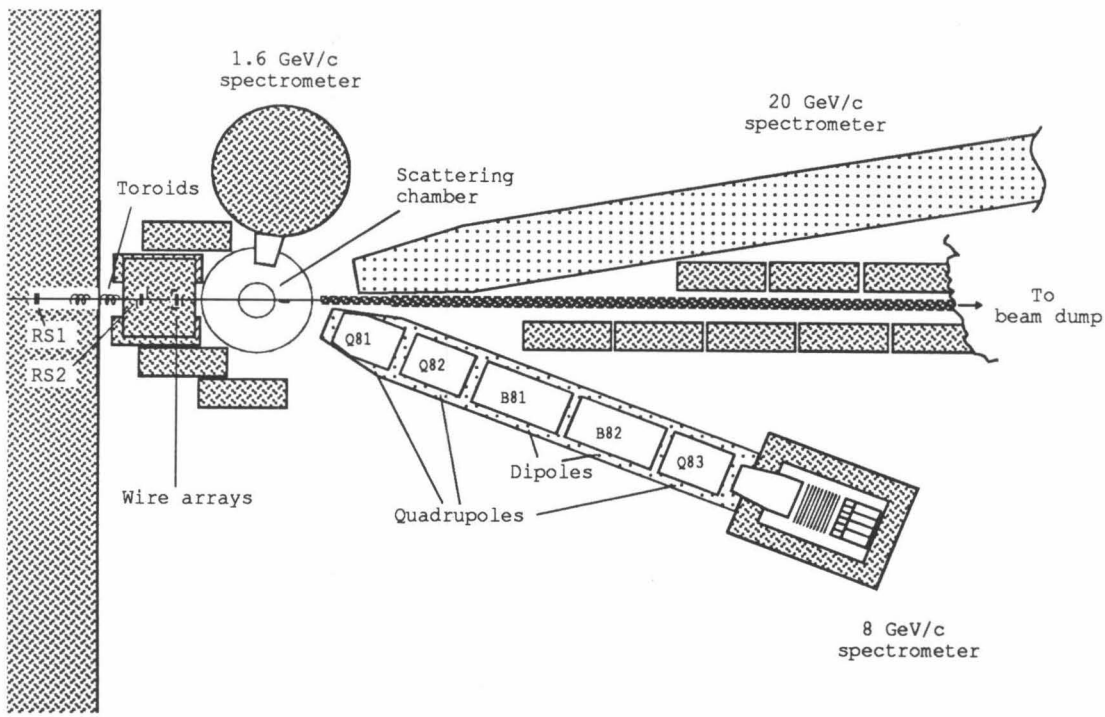

Figure 2.5 – Overhead view of the pivot area showing the three spectrometers in the end station, the scattering chamber, and the pivot area shielding. Also shown are the locations of the toroids, roller screens, and wire arrays discussed in the text.

machinable alloy of tungsten and copper. This shield was attached to an Al frame, which rested on an Al shelf bolted to the scattering chamber, as shown in Figure 2.6. In operation, the electron beam passed between the shield and its support frame. Electrons scattered by the window were intercepted by the shield, while electrons scattered by the target were unimpeded on the way to the spectrometer. Because of the change in geometry when the spectrometer angle was changed, it was necessary to move the shield to a different location for each angle. This shielding strategy proved completely effective: electrons scattering from the targets were unobstructed, yet the "no target" event rate was reduced to an undetectable level.

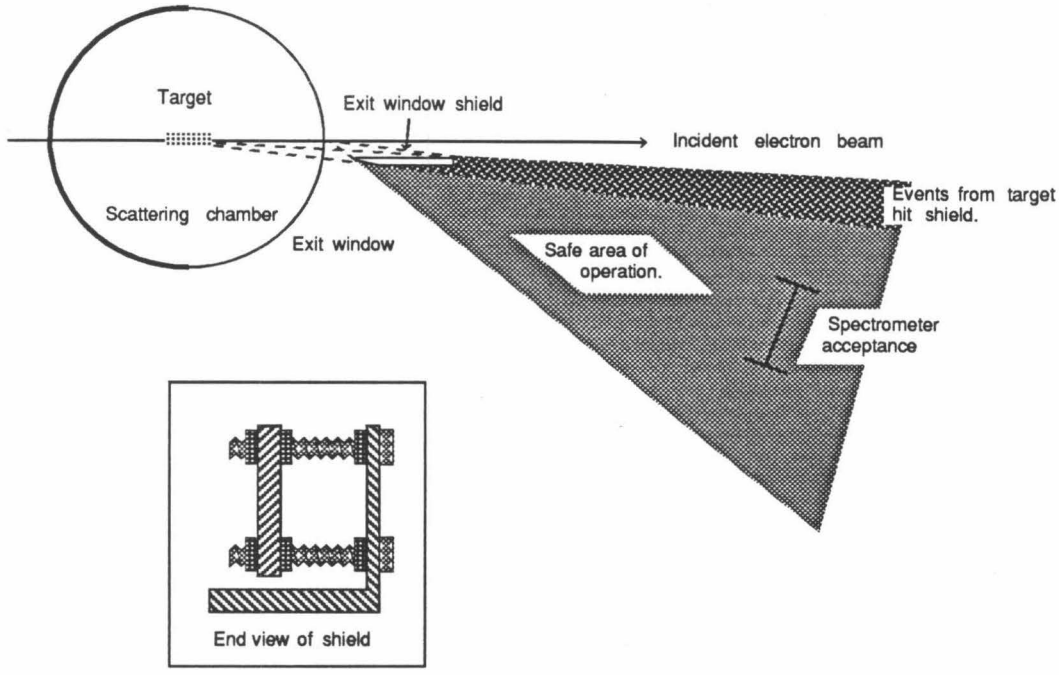

Figure 2.6 – Details of the scattering chamber exit window shield.

The targets for the spectrometer were located on a carriage suspended from the target assembly housing. This carriage could be remotely raised, lowered, and rotated about a vertical axis by compressed air motors, to bring any target into the beam. Movement of the targets was monitored by digital encoders driven by toothed belts attached to the drive mechanism. The encoder settings for the proper positioning of each target were initially determined by survey with a theodolite with the targets at room temperature and the entrance and exit windows removed. The correct target alignment was also marked on a TV picture of the targets, which were viewed through a Lucite flange on the upstream side of the scattering chamber.

The filling of the cryogenic targets and heat exchanger caused the target positions to change because of thermal contraction of the carriage. Thus, new encoder settings

that restored the target positions in the TV picture were found. Soon afterwards, the horizontal encoder settings were lost when the encoder's drive belt broke. After replacing the belt, we again used the TV camera to re-establish the encoder settings. Finally, we used a weak electron beam to check the centering of the solid targets by slowly moving the targets until the beam began to hit the target holder. This event was easily observed through a large increase in the good spill signal. These beam-survey and TV-survey results were averaged to obtain the final encoder settings. Disassembly of the targets after the experiment revealed beam burn spots in the exact centers of the solid targets, and within 5 mm of the cryogenic target centers. The change in effective target thickness caused by this misalignment was negligibly small.

2.3 Target Construction

The arrangement of the target assembly is shown in Figure 2.7. Uppermost are the four cylindrical cryogenic cells. Gaseous ^{4}He at 25 atm. (absolute pressure) was recirculated through the top cell, and liquid hydrogen at 2 atm. (absolute pressure) was recirculated through the cell next to the top. Both targets were maintained at $\sim$21 deg K by passing the return flow through a heat exchanger immersed in a reservoir of liquid hydrogen at atmospheric pressure. The 1 atmosphere overpressurization of the hydrogen target raised its boiling temperature by $\sim$2 deg K over the reservoir to prevent boiling in the target. To insure uniform flow throughout each cell, a 1.43 inch diameter cylinder of 0.001 inch thick Al foil was mounted inside, concentric with the cell walls. In operation, the target fluid would flow inside this tube from the target inlet to the end of the cell, then back to the target outlet in the space between the tube and the cell wall. The target fluid flows were effected by centrifugal, fanlike pumps that could maintain axial flows of > 1 m/s in each target.

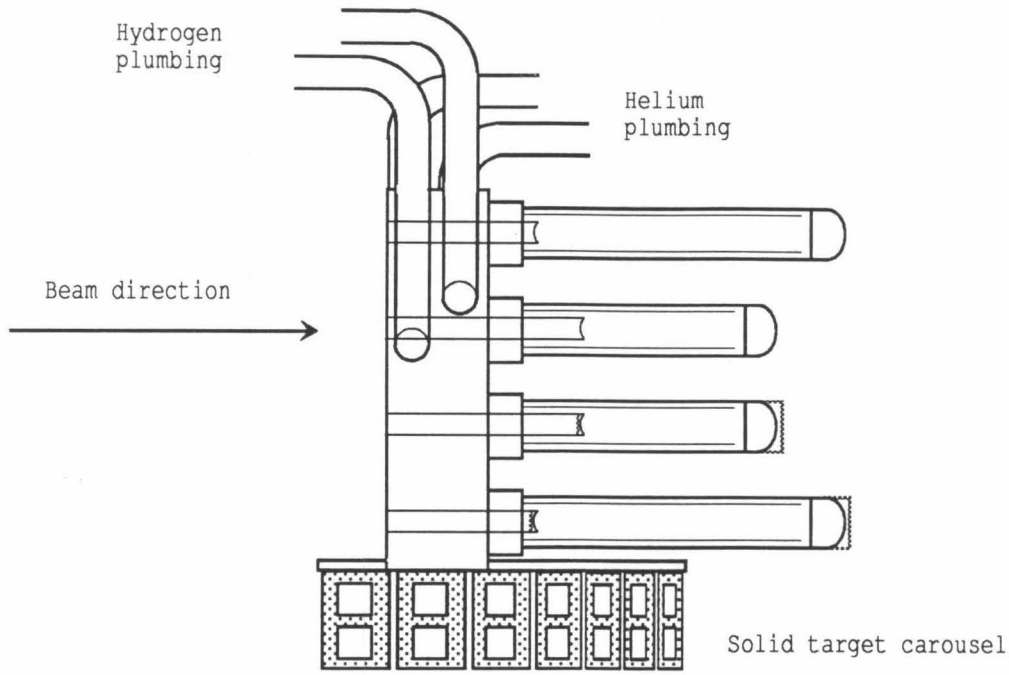

Figure 2.7 – Target assembly showing the cryogenic target cells and the solid target carousel. The two lower dummy cells were fitted with additional aluminum endcaps to achieve the same total thickness in radiation lengths as the real cells.

The temperature and pressure of each cell were carefully monitored throughout the experiment. Inlet and outlet temperatures were each measured by a hydrogen vapor pressure cell and a platinum wire resistor. The ^{4}He target also had a platinum wire resistor mounted near the end of its cell. Cell pressures (measured with a pressure transducer) and temperatures were used to compute a nominal average target density on a run-by-run basis. Testing revealed that the actual ^{4}He target density deviated from the nominal value because of heating by the beam. This deviation was linear with respect to the average beam current, and was corrected for in the data analysis, as we discuss in Chapter 4. The largest (but not typical) correction was 18 percent. No such effects were observed for the hydrogen target at any beam current.

The two lower cells, of identical construction, were always kept evacuated. These dummy targets were used to measure the contribution of the target entrance and exit windows to the scattering rates of the real targets. These dummy rates were subtracted from the real target rates during the data analysis, as we describe in Chapter 3. The radiative effects of the fluid in the real targets were simulated in the dummies by fitting additional aluminum endcaps to the front and rear of the dummy cells. These endcaps made the thickness in radiation lengths of the real and dummy cells equivalent. Table 2.1 lists all of the relevant parameters for the cryogenic cells.

Component	Hydrogen	^{4}He
Cell length (internal)	14.930 cm	24.973 cm
Cell diameter (external)	2.00 in	2.00 in
Outer wall thickness	0.0045 in	0.0167 in
Internal tube diameter	1.43 in	1.43 in
Internal tube thickness	0.001 in	0.001 in
Upstream endcap diameter	1.00 in	1.00 in
Upstream endcap thickness	0.0027 in	0.008 in
Downstream endcap thickness	0.004 in	0.016 in
Solder thickness	0.0018 in	0.0020 in
Solder width	0.4 in	0.4 in
Dummy preradiator thickness	0.0302 in	0.0296 in
Dummy postradiator thickness	0.0297 in	0.0217 in

Table 2.1 – Target cell dimensions. All materials are aluminum, except for a ring of Sn-Pb-Ag solder attaching the downstream endcap to the cell wall. Target lengths were measured under pressure at 20° K and corrected for endcap thicknesses.

Mounted directly below the cryogenic cells was the carousel of solid targets. The carousel consisted of a horizontal Cu plate to which were bolted in a circular arc seven vertical Al target holders. Clamped in each holder were two solid targets, to give us two horizontal rows of targets. Several of the targets had a small thermocouple glued

to it with heat sink grease near a corner. These thermocouples were used to monitor the target temperature rise because of beam heating. Because the solid targets were in relatively poor thermal contact with the H_2 reservoir, the temperature rise was much larger than in the cell targets. Under worst case conditions, the beam deposited $\sim$30 watts in the carbon target, which raised its temperature $\sim$50 degrees K. These temperature rises were easily withstood and had an insignificant effect on the target densities.

The solid targets had originally been obtained by the American University group at SLAC for a previous experiment [19], and were lent to us for NE3. Data were taken for five solid targets of natural isotopic composition: carbon (pyrolytic), Al, Fe (two thicknesses), and Au. Each target was rectangular in shape, with nominal transverse dimensions of 1.50 by 1.25 inches. The thicknesses were chosen to be close to either 2% of a radiation length (C, Al, Fe) or 6% r.l. (Fe, Au). The targets were weighed on an analytic balance before and after this experiment, and the thicknesses were measured with a micrometer in several spots near the center and corners. Similar measurements were undertaken by the A.U. group for their experiment [32]. All of the weights and dimensions were averaged, and a density extracted assuming a rectangular shape. Table 2.2 summarizes these averages and the standard deviations of the measurements (combined in quadrature for ρ). The true densities of the metallic targets are well known [33] and are also listed in Table 2.2. The data analysis used the calculated density for the carbon target, the known density for the others, and the average thickness in the center of the targets to calculate the scattering cross sections.

Three positions in the solid target carousel were reserved for diagnostics. In two of these spots, a piece of roller screen material was mounted so that we could

	C	Al	Fe (2% r.l.)	Fe (6% r.l.)	Au
wt.	10.885 (14)	6.348 (13)	3.5577 (87)	10.140 (13)	4.687 (12)
X	3.8092 (00)	3.8706 (58)	3.8887 (10)	3.8177 (91)	3.8166 (10)
Y	3.1772 (26)	3.221 (11)	3.2305 (31)	3.194 (27)	3.1995 (40)
Z	.41040 (63)	.18978 (58)	.03669 (43)	.10760 (64)	.02039 (38)
Z (cntr)	.41036 (54)	.18988 (69)	.03681 (50)	.10748 (73)	.02047 (45)
ρ	2.1914 (44)	2.683 (14)	7.719 (92)	7.729 (82)	18.84 (35)
ρ (book)	N/A	2.699	7.86	7.86	19.32

Table 2.2 – Summary of dimensional measurements for the solid targets. Wt is the weight, in grams; X, Y, and Z are the width, height, and thickness in cm; ρ is the derived density in gm/cc; and ρ (book) is the true density. The numbers in parentheses are the standard deviations of the measurements, applicable to the last two significant digits.

observe the beam position and profile at the target location. The third position was left empty, in order to check for scattering of any beam halo from the target frame. No such contamination was ever observed.

2.4 Downstream Beamline

After passing through the target chamber, the electron beam traversed a three foot air gap and entered an evacuated pipe, which carried the beam towards a beam dump $\sim$ 100 meters downstream. At several locations, ($>$ 25 meters downstream), this beam pipe was interrupted by air gaps of several feet, because of the installation of magnets and other hardware for a following experiment. All the air gaps and associated windows contributed significantly to the multiple scattering of the beam on its way to the beam dump, resulting in a substantial amount of radiation at the rear wall of the end station. This had no effect on the measurements with the spectrometer, which was well upstream, and heavily shielded.

2.5 Spectrometer

Electrons scattered from the targets were detected by the 8-GeV spectrometer, pictured in Figure 2.8. It is a vertical bend spectrometer, with magnets arranged in a QQDDQ pattern. Electrons entering the spectrometer beam pipe were focused by the magnets into the detector package residing inside the concrete shielding hut. The detectors consisted of a subatmospheric, nitrogen gas, threshold Cerenkov detector and a segmented lead glass, total absorption counter [34], used for triggering and particle identification, and ten planes of wire chambers [35] to determine particle trajectories.

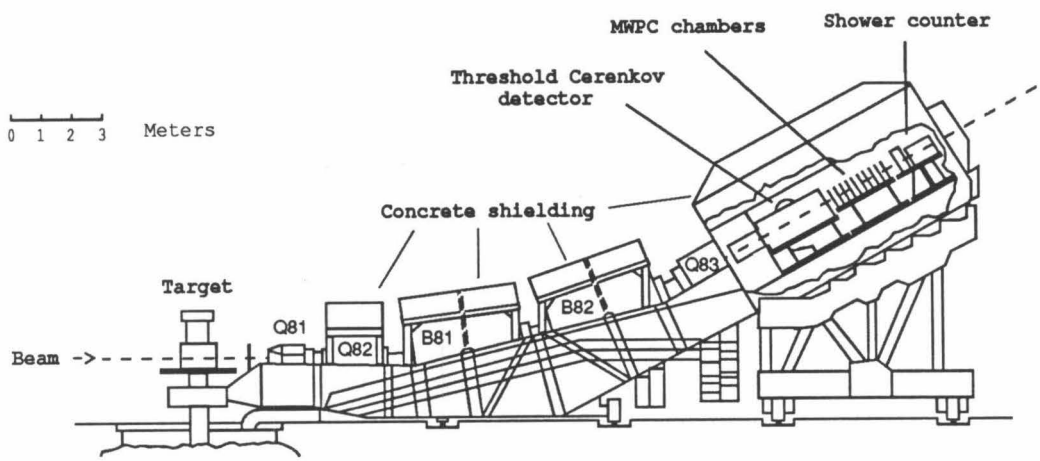

Figure 2.8 – Horizontal view of the 8 GeV/c spectrometer.

The entire spectrometer rests on steel rails set in the concrete floor, with its nose attached to the pivot. Movement of the spectrometer is effected by electric motors that drive several of the load bearing steel wheels. A toothed encoder is driven by one of these wheels and is read by computer to determine the spectrometer central angle. The precision of this encoder is 0.001 degrees, although evidence exists that the accuracy of the system is somewhat worse [36]. Calibration of the encoder was done by optical survey for the preceding experiment on this spectrometer [37], and we used this calibration ourselves. The spectrometer was operated at six different angles from 15 to 39 degrees during the course of the experiment. Because we needed to enter the end station to adjust the exit window shield with each angle change, we operated the spectrometer drive manually. Remote control from the counting house is also possible.

The optical properties of the spectrometer [38] are such that there are separate momentum and horizontal scattering angle focal planes, both contained within the wire chambers. The track position at these focal planes is only slightly disturbed by multiple scattering in the nearby Cerenkov mirror, so that the momentum and production angle can be reconstructed with good resolution (0.13% rms for P, and 0.18 mrad rms for θ). The interaction point in the target and the vertical scattering angle are most strongly correlated with the direction of the track through the wire chambers, so that multiple scattering degrades the resolution with which these quantities are reconstructed (5.8 cm rms for projected horizontal scattering origin, 1.12 mrad rms for ϕ). However, both of these are implicitly integrated over, in the calculation of our cross sections, and high resolution is not needed.

2.6 Detector Package

The Cerenkov detector was the simplest component of the detector package. It consisted of a large iron tank, inside of which was a spherical mirror that focused Cerenkov radiation from charged particles transiting the tank onto a phototube. The tank could be evacuated and filled with nitrogen at subatmospheric pressures, to provide a medium to generate the Cerenkov light. The tank was 310 cm long, with .016 inch Al entrance and exit windows, through which the scattered particles passed. The mirror was constructed from 0.25 inch thick slumped lucite, with an evaporated Al backing. For uniform efficiency, the mirror was placed in the path of the moving particles. This thick mirror is the source of most of the multiple scattering in the Cerenkov detector.

In operation, the nitrogen pressure was maintained at 550 mm Hg, for which the index of refraction is 1.00020. This corresponds to a Cerenkov threshold of 7 GeV/c for pions, which is well above our highest beam energy. The ultrarelativistic electrons are well above threshold and are efficiently ($\varepsilon = 0.999$) detected. Thus, the Cerenkov detector was used to separate electrons from pions—the only background of significance in this experiment.

Additional pion rejection was provided by a segmented lead glass shower counter at the rear of the detector package. Blocks of F-2 lead glass were arranged into two layers, designated PR (preradiator) and TA (total absorption), as shown in Figure 2.9. The PR layer was constructed from six blocks with dimensions 15.8 cm wide by 32 cm tall by 10.4 cm thick. Each PR block was individually wrapped in aluminized mylar and was viewed by a 5 inch Amperex XP2041 phototube mounted on the top. The TA layer was constructed from four blocks with dimensions 25 cm wide by 36 cm tall by 54 cm thick. Each TA block was also individually wrapped and was viewed

by a 9 inch Amperex 60DVP phototube mounted on the rear. The two layers were housed in separate boxes of cold-rolled steel bolted to an aluminum table.

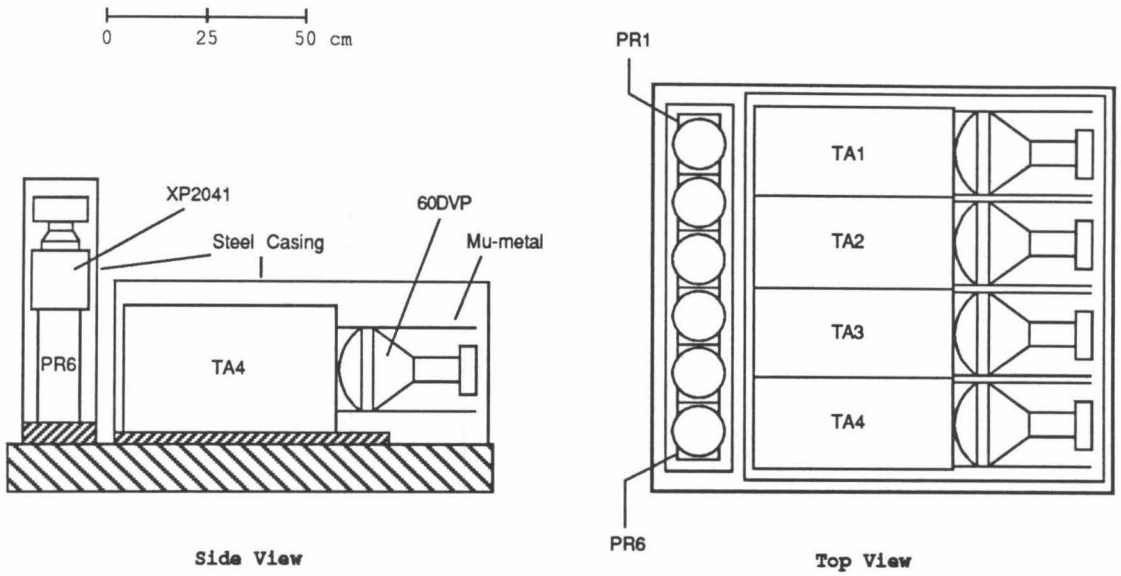

Figure 2.9 – Side and top views of the lead glass shower counter. Incident particles enter the counter from the left in both views. Details of the steel support around the lead glass has been omitted for clarity.

Expressed in radiation lengths, the PR and TA layers are 3.23 r.l. and 16.77 r.l. thick, respectively. The total thickness (20 r.l.) is sufficient to contain > 98% of a 9 GeV electromagnetic shower. Pions interact in the lead glass primarily by inducing a hadronic shower [39], for which the interaction length is ~35 cm. Thus, a significant amount of a hadronic shower's energy is not contained by the lead glass, resulting in a smaller pulse height than an electromagnetic shower of the same energy. (It should be noted that this shower counter was upgraded with a new lead glass array featuring finer segmentation during a subsequent experiment [40].)

Located between the Cerenkov and shower detectors were ten planes of proportional wire chambers with 20 cm between planes. In operation, the chambers were filled with "magic gas"—a mixture of 65.75% argon, 30.0% isobutane, 0.25% freon 13B1, and 4.0% methylal [35]. The chambers were labeled 1–10, starting with the one nearest the Cerenkov detector. Those with even numbers were P-type chambers (CH2 = P1, CH10 = P5) with 176 horizontal wires 93 cm long, spaced by 2 mm, with an insulated vertical support wire in the middle. The odd-numbered chambers were T-type (CH1 = T1, CH9 = T5), with 480 wires spaced by 2 mm, rotated by $+30°$ from the vertical for T1, T3, and T5, and $-30°$ for T2 and T4. Adjacent wires in the T chambers were electrically connected together, creating an effective wire spacing of 4 mm.

Wire chamber "hits" were recorded via a digital readout system built by Nanometrics, Inc. [41] The pulse induced in each wire or wire pair by a passing charged particle was amplified, discriminated, and fed into a dual flip-flop, delay circuit (450 ns delay/flip-flop). The delayed signal could be latched into a bit-register by a coincident "fast-load" signal ($\sim$75 ns wide) from the event trigger, and subsequently read out and cleared by a CAMAC module before the next beam pulse. The pattern of struck wires was later analyzed by software to determine the path of charged particles through the wire chambers. Each particle's momentum vector at the target was then reconstructed from its wire chamber track with a second-order optics transformation.

2.7 Fast Electronics

All of the fast electronics and data-acquisition equipment were located in a building called the counting-house, situated $\sim$ 50 feet above RS1 in Figure 2.1. Heliax coaxial cables (low loss, low dispersion, fast propagation) were used to route signals between the spectrometer and the counting house. Figure 2.10 below is a simplified

diagram of the fast electronics, showing the trigger logic, deadtime scalers, and signal ADC's.

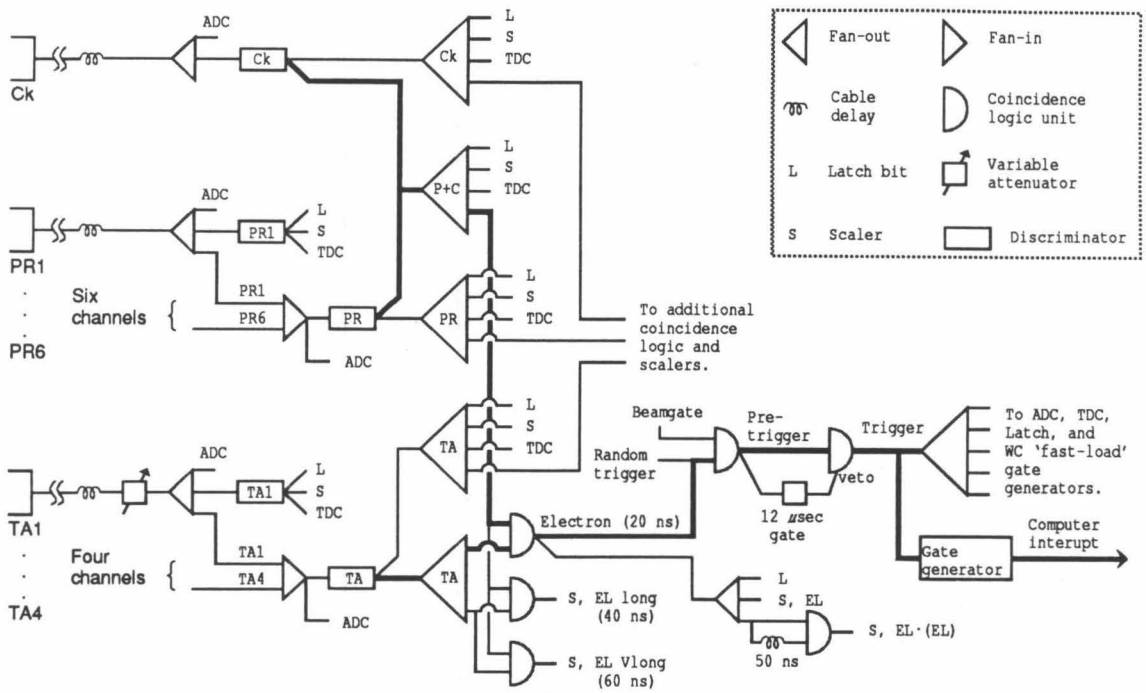

Figure 2.10 – Simplified electronics diagram. Bold lines show the digital signal paths contributing to the event trigger. Not shown are additional coincidence circuits, feeding scalers not used in the data analysis.

Each phototube anode signal was passed through a cable delay, an attenuator (TA signals only) and into a linear fan-out. The cable delays were adjusted to provide proper signal timing for the coincidence logic to follow. The TA attenuators were used to compensate for the change in signal amplitude that occurred when the spectrometer's momentum setting was changed. (No such compensation was required for the PR signals, which were insensitive to the spectrometer momentum.) The fanned-out signals were fed into ADC's, discriminators, and fan-in units that summed the signals

for the six PR and four TA phototubes. The individual ADC values were used later during the data analysis to set cuts for each event.

The discriminator outputs were used to increment scalers, stop TDC counters, set bits in latch registers, and were passed to the trigger logic. The signal timing was such that the Ck and summed PR discriminator signals were coincident, with the summed TA discriminator occurring 4 ns later. Thus, the trigger and TDC timings were determined by the TA signal. The trigger itself was composed of a coincidence between the TA and either the PR or CK (or both), with a 20 ns coincidence width. This coincidence signal fed a scaler (EL) and generated a pre-trigger signal that subsequently generated a trigger. A 12 μs veto was also generated by the pretrigger, to inhibit additional triggers during the same beam pulse.

Two other TA·(P+C) coincidences, EL-long and EL-Vlong, with coincidence widths of 40 and 60 ns, respectively, were counted in scalers to measure the electronic deadtime. Because multiple coincidences within these times were not resolved, the EL, EL-long, and EL-Vlong scaler values differed, and an extrapolation to zero coincidence width could be made. A third coincidence, between EL and a delayed copy of itself, was also used in the deadtime calculation.

In addition to the electron trigger, the pretrigger logic was presented with a random trigger. This was a random coincidence between a pulser and a discriminator attached to the good-spill phototube signal (not shown in Figure 2.10). The purpose of this trigger was to monitor ADC pedestals by initiating event readouts at random moments during good beam pulses. The pulser rate was adjusted to provide a low random-trigger rate, and random-trigger events were unambiguously identified by a latch bit that they set.

2.8 Data Acquisition System

The experimental data can be divided into three broad catagories: time critical event mode data, such as the ADC's and latches; cumulative data, such as the scalers and toroid values; and monitoring data, such as target temperatures. These data were collected by an array of CAMAC devices and were passed to a central Vax-780 computer via several readout paths. A diagram of the principal pathways is shown below in Figure 2.11.

A special problem was presented by the event mode data, since its hardware needed to be read out and reset in the time between beam pulses, which the Vax was incapable of doing. Instead, a dedicated PDP-11 computer responded to the event triggers and serviced the CAMAC hardware. With its superior real-time capabilities, the PDP-11 could easily handle the maximum event rate of 180 hz—the beam pulse frequency. These incoming data were buffered by the PDP-11 in memory shared with the Vax, which could then process the data with little overhead per event [42].

The other categories of data were collected at periodic intervals, either directly by the Vax, or indirectly by an LSI-11 computer that communicated with the Vax through a CAMAC "FIFO" serial link. The scalers and the old toroid hardware were self-cumulative, and were read out only at the end of a data run, or during a mid-run checkpoint. The LSI-11 responded in real time to each beam pulse to monitor and control the beam steering, and to read and clear the peak integrating toroid electronics. At the Vax's request, the LSI returned cumulative toroid values and beam-steering diagnostics over the serial link. Monitoring and control of hardware such as the high-voltage supplies or spectrometer magnet supplies were also handled by the Vax through CAMAC interfaces.

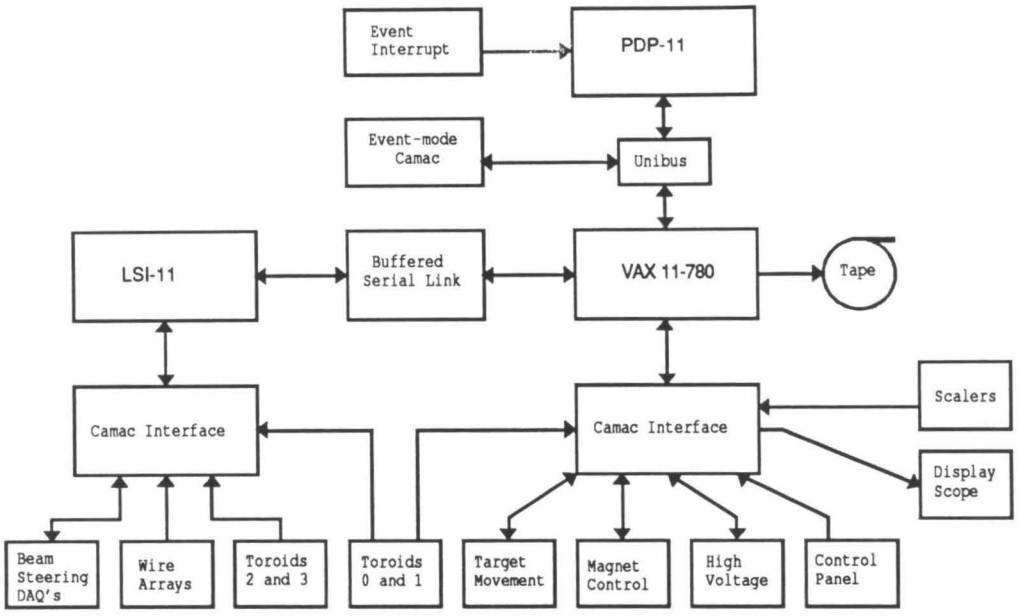

Figure 2.11 – Diagram of the data acquisition system with the principal data paths shown.

All data upon arriving in the Vax were first copied to magnetic tape in unprocessed form for later, off-line analysis. This was the highest priority task for the Vax, to insure that no data was lost. At lower priority, the Vax performed an on-line analysis of as many incoming events as it had time for. This analysis was similar in nature to what was eventually done off-line, and was used to monitor the progress of the experiment as we took data.

Software for the various computers was obtained from an extensive base developed by the various end station experimenters over the years. Unfortunately, the many existing software components were poorly organized, with a lack of flexibility, excessive interdependency, and constant revision precluding any guarantee of mutual compatibility. Consequently, a major effort was made to patch the on-line software

together and insure sufficient functionality to run the experiment. Even more effort was invested in debugging the off-line software, which ended up being largely rewritten. (This "band-aid" approach to software persists to this day because replacing the whole system is not expedient.) Although painful to use, the software proved adequate to the task of running the experiment and analyzing the data.

Chapter 3
Data Analysis

3.1 Overview

The reduction of the logtape data to experimental cross section spectra proceeded through three main steps, called Pass-1, Pass-2, and Pass-3. Each pass through the data performed a distinct set of tasks. Pass-1 performed the event-by-event analysis of the experiment's logtapes and created histograms of the events for each run. This pass also collected hardware information, such as integrated beam current and scaler values, and performed a great deal of consistency checking to insure the integrity of the data. Pass-2 analysis corrected the histograms of Pass-1 for the acceptance function of the spectrometer, and combined this with other information from Pass-1 to yield the experimental cross-section spectrum for each run. The acceptance function used in this step was obtained from a Monte-Carlo simulation of the spectrometer optics as discussed below. Finally, Pass-3 analysis combined the overlapping spectra of Pass-2 to yield the entire inelastic spectrum observed for each combination of incident energy, scattering angle, and target. These results were then corrected for radiative effects, using an iterative scheme based on the formulae of Stein, *et al.* [43], as discussed in Appendix A.

3.2 Pass-1

Pass-1 was by far the most complicated and time-consuming part of the analysis. The complexity of this step reflected the complexity of the on-line data acquisition software, which recorded the many kinds of data in a complicated order on the log-tapes. The Pass-1 software, an adaptation of the on-line system, required a very robust algorithm to properly unlog these data. Pass-1 was also very CPU-intensive, because of the event-by-event analysis. Part of the event processing was to reconstruct the trajectories of all charged particle tracks from the pattern of hits among the wire chambers. This was a highly iterative procedure and accounted for most of the computer time used by Pass-1, which was about one CPU-month on a VAX-750 computer.

For each event, six types of data were recorded on tape. These were: ADC pulse heights of the Cerenkov and shower-counter phototubes, TDC information on the phototube signal timing (relative to the event trigger), 32 bits of Latch data in which selected bits were set when corresponding discrimators in the electronics were triggered, wire chamber information, the event time within the beam gate, and the good and bad spill ADC pulse heights. Only the ADC and wire chamber data were used in the calculation of cross sections; the other information either is of a diagnostic nature or can be derived from the ADCs.

3.2.1 Cerenkov and Shower-Counter Analysis

The Cerenkov and shower-counter signals were used to separate unwanted pion from electron events, while the wire chamber data were used to reconstruct the scattering angles and energy of good electron events. A total of four cuts were applied to each event: a cut on the Cerenkov energy, on the shower energy, a track multiplicity

cut, and a fiducial cut on the track position. Only events that passed all four cuts were included in the cross-section histogram.

Figure 3.1 shows the Cerenkov pulse-height spectrum for a run taken with the ^{4}He target at kinematics for which the pion to electron ratio was highest. The sharp, low-energy peak that appears in the uncut spectrum is due to pions, which must have left some energy in the shower counter in order to have produced an event trigger. This peak is greatly reduced when a cut is placed on the shower energy, leaving the broad electron peak. The shape of the electron peak reflects the Poisson statistics of photoelectron collection. The dashed line in the figure is a Poisson distribution, fit to the data between channel 40 and 520, with a χ^2 per degree of freedom of 1.52, in which the mean number of photoelectrons is 9.18. Two photoelectrons are required to exceed the Cerenkov cut at channel 40, implying that the cut has an efficiency of 99.9%.

The shower-energy cut was more complicated because of the segmentation of the lead glass. First, each phototube ADC pulse height had its pedestal subtracted and was multiplied by a gain-matching coefficient associated with that tube. Next, each TA pulse height was corrected for the attenuator upstream from its ADC in the electronics. Lastly, these gain-matched PR and TA signals were summed together and then divided by the spectrometer central momentum to yield a normalized shower energy called SHSOFT. Figure 3.2(a) shows the SHSOFT distribution of the single track events in the previous figure; in 3.2(b) these data have been additionally cut by the Cerenkov and good fiducial cuts. The gain-matching coefficients for each phototube were chosen through an iterative fitting procedure to yield a peak at 1.0 with minimum width, for single-track events passing the Cerenkov cut. This peak position is then independent of the spectrometer momentum, because of the way in

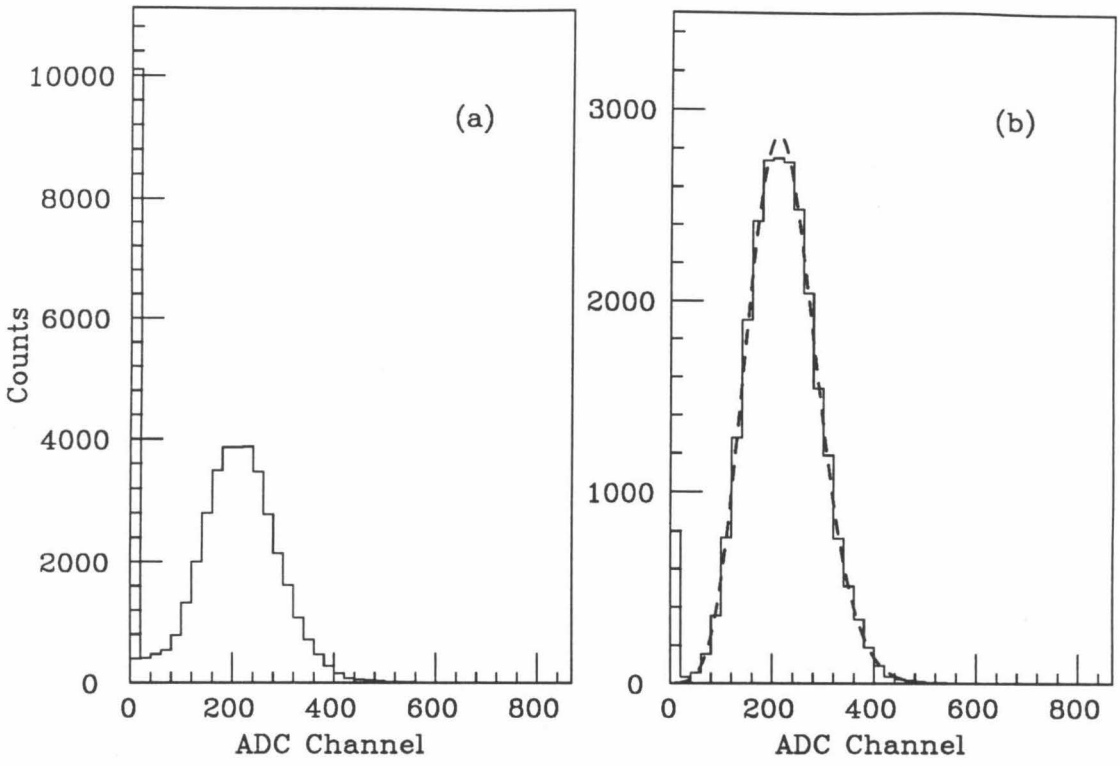

Figure 3.1 – Cerenkov pulse height spectra for the He target with $E_0 = 3.595$ GeV, $\theta = 30$ deg., $E' = 1.6$ GeV. (a) single-track events; (b) single-track events cut on good SHSOFT.

which SHSOFT is calculated. The peak width, however, shows a $1/\sqrt{E}$ variation, reflecting the statistical fluctuations of shower development. We achieved a resolution of $24\%/\sqrt{E(GeV)}$ FWHM, which compares favorably with the $\sim 30\%/\sqrt{E}$ obtained in previous experiments [44] with this detector package. At our lowest momentum of 1.6 GeV, this gives a resolution of 19.0%.

The second peak seen in Figure 3.2(a), at an SHSOFT of 0.5, is due to the hadronic shower of pions in the lead glass. As mentioned previously, this peak is at a lower energy than the electron peak because the hadronic shower wasn't fully contained in the lead glass. By placing a cut on SHSOFT between the two peaks, at an SHSOFT of 0.72, we could provide additional pion rejection, while maintaining

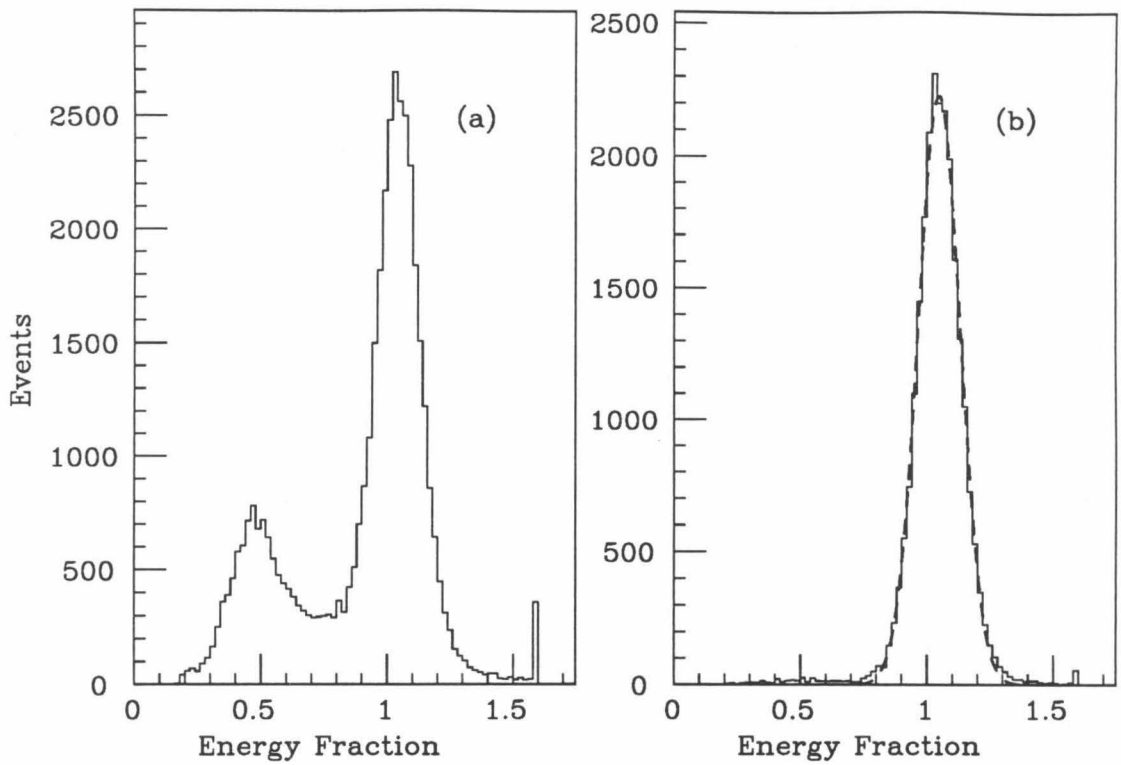

Figure 3.2 – SHSOFT distribution of the data shown in the previous figure: (a) single-track events; (b) single-track events that passed the good-fiducial and Cerenkov cuts.

good efficiency for electrons. The dashed line in Figure 3.2 is a Gaussian fit to the data between 0.80 and 1.28. Less than 0.1% of the Gaussian lies below the SHSOFT cut; hence, we assigned an efficiency of 99.9% to this cut. A high shower-energy cut was also made: events with SHSOFT greater that 1.36 were rejected. The Cerenkov spectrum of these events looks like that of the good electrons, although no good reason could be found for their excessive shower energy. Since these events were not completely understood, they were excluded from the cross-section histogram, with a correction being made if they passed the other three cuts. This correction was typically 0.2%.

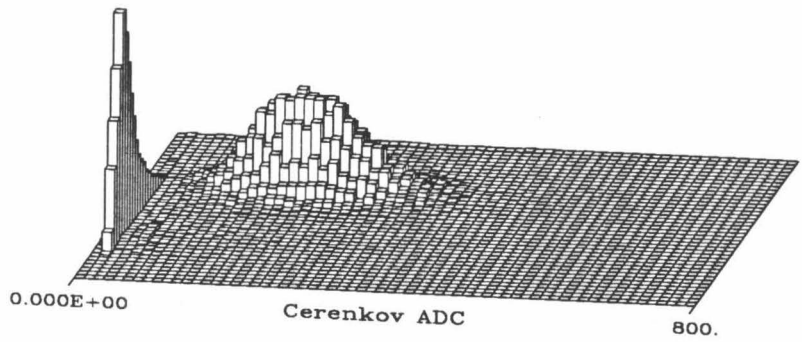

Figure 3.3 – Cerenkov ADC vs. SHSOFT histogram. SHSOFT increases from 0.0 at the lower left corner to 1.6 at the upper left corner.

In Figure 3.3 is shown the two-dimensional distribution of the Cerenkov ADC and SHSOFT energy for the data of the previous two figures. It can easily be seen that the pion and electron peaks are well separated. A slight modification was made to the Cerenkov cut for events with an SHSOFT between 0.72 and 0.80. For these events, the cut was raised to ADC channel 75. This adjustment was done to avoid contamination from a band of events near channel 60, with a pionlike SHSOFT distribution. It is important to note that there was no specific pion trigger; all pion events had to satisfy the electron trigger, which was deliberately made inefficient for them. Thus, the real pion rate and pion rejection factor were not directly measured in this experiment. Previous experiments [44], using the same detectors with a plastic-scintillator based trigger, have achieved pion rejection factors of $> 10^{-4}$. Our worst case π/e ratio was expected to be < 10, for our most inelastic runs at 3.6 GeV and 30 deg. In our region of interest between the elastic and quasi-elastic peaks, the π/e ratio should be smaller

by at least an order of magnitude. Since our pion rejection factor should be similar to that of previous experiments, the pion contamination in our final data is negligible.

3.2.2 Wire Chamber Analysis

The wire chamber data can be thought of as a very large binary number, with each bit signifying whether or not the corresponding wire was fired. (Data compression techniques were used in the logging of events to reduce the size of this sparse bit pattern.) The track reconstruction algorithm tried to find the particle trajectories that best fit the pattern of wire hits, using the known location of each wire chamber. This task was especially complicated by the fact that the wires were not arranged along orthogonal directions. Fortunately, the average number of tracks per event was always near unity, so that the misidentification of tracks was extremely unlikely. Four numbers were used to specify each track found by this procedure: the X and Y coordinates at which the track intersected a given plane Z = const., and the derivatives dX/dZ and dY/dZ of the projections of the track into the (X, Z) and (Y, Z) planes. (In this notation, the Z axis is the spectrometer central ray, and X and Y are orthogonal directions, with Y in the plane of the dipole bend.)

When more than one track was found, an attempt was made to identify one of them uniquely as an electron track. This was done using the segmentation of the shower counter. Each track was extrapolated to the lead glass to find which block it had entered. If a significant pulse height was found in the corresponding PMT's, then that track was tagged as an electron. This test was made by multiplying the corresponding PR and TA signals by a normalization coefficient and summing them. Although similar to the way SHSOFT was calculated, this sum was different in two important respects. First, only the PR and TA blocks hit by the track (and the adjacent ones when near a boundary) were used in the sum. Second, a vertical

segmentation was introduced, and the horizontal segmentation was doubled, to give an array of "shower segments" 4 rows high and 12 columns wide. This segmentation was used in an attempt to improve the shower resolution by accounting for any position dependence of the ADC signals caused by the attenuation of light in the lead glass. (Such a segmentation was not used in the SHSOFT calculation, to avoid depending on wire chamber information in the shower energy cut.) For a given track to be tagged as an electron, this restricted shower energy needed to be at least 0.72. If only one such track was found, the others in the event were ignored and analysis continued. Otherwise, the event failed the multiplicity cut, and was discarded.

If a single track or one electron track was found, it was checked against a fiducial cut. This was a cut on the intersection point of the track with the front face of the PR lead glass. The purpose of this cut was to reject tracks for which some of the shower energy might leak out of the detector sides because of the lateral spread of the shower. The cut was a rectangle centered on the lead glass, with borders inset by 4.0 cm (one-half of a shower segment) from the edges. This gave the rectangle dimensions of 87.45 cm wide by 24.15 cm high, with the center located 1.5 cm above the spectrometer central ray. If the track passed through this rectangle, it successfully passed the fiducial cut.

3.2.3 Event Histogramming

Events that passed all four cuts were histogrammed in terms of their scattering angle and energy, which were derived from the wire-chamber track information. There are five independent quantities that determine what a scattered electron's trajectory in the wire chambers will be. These are the electron's fractional excess momentum $\Delta P/P_0 \equiv (P_e - P_0)/P_0$, with P_0 the spectrometer central momentum, and four quantities that describe the track from the target: the X and Y coordinates at $Z = 0$ (the

target midplane), which are called $X_{\rm tgt}$ and $Y_{\rm tgt}$, and the angles $\Delta\theta \equiv \tan^{-1}(dX/dZ)$ and $\Delta\phi \equiv \tan^{-1}(dY/dZ)$. $\Delta\theta$ is the angle between the two vertical planes intersecting at the pivot containing the incident and scattered electron momentum-vectors, while $\Delta\phi$ is the angle between a horizontal plane and the scattered electron's momentum.

With only the four parameters of the wire-chamber track, the five parameters above could not be simultaneously determined. However, the beam was always incident on the target at $Y = 0$, and had a vertical spot size of $\sim$ 3 mm. Thus, $Y_{\rm tgt}$ was always presumed to be zero, and the other four scattering quantities were reconstructed from the wire-chamber track parameters, using a second-order transformation, with matrix elements determined from a fit to optics test data taken in 1967 [45-47]. The resolutions of the reconstructed quantities were checked with a Monte-Carlo model of the spectrometer (discussed below) for our conditions of beam spot and target dimensions. Averaged over the spectrometer acceptance, we obtained rms resolutions of 0.13% ($\Delta P/P_0$), 0.18 mr ($\Delta\theta$), 1.12 mr ($\Delta\phi$), and 5.8 cm ($X_{\rm tgt}$).

Since $X_{\rm tgt}$ and $\Delta\phi$ are not needed in the calculation of a cross section, events were binned in a two-dimensional histogram of $\Delta P/P_0$ and $\Delta\theta$. These quantities are independent of the angle and central momentum settings of the spectrometer, which facilitates correction for the acceptance function. The quantity $\Delta\phi$ is approximately the azimuthal scattering angle ϕ, while $\Delta\theta$ is approximately the difference between the scattering angle, θ, and the spectrometer central angle, θ_0. A correction for the exact transformation between these spectrometer angles and the polar scattering angles (θ, ϕ) was applied during Pass-2; this will be discussed below in Chapter 4. The event histogram binning spanned $\pm$5.0% in $\Delta P/P_0$, and $\pm$12.0 mr in $\Delta\theta$, with 64 bins in each dimension. This binning was fine enough to insure that at least three dP/P_0 bins would contribute to each 15 MeV wide energy-loss bin in which the data

would eventually be placed, thus minimizing the bin-splitting that Pass-2 would have to do.

3.3 Pass-2

The goal of the Pass-2 analysis was to compute an inelastic cross-section spectrum for each run, based on the results of Pass-1. These cross sections were to be binned in equal steps of energy loss, whereas the event histograms were binned in terms of fractional excess momentum. Consequently, it was necessary to rebin the data at some stage. This rebinning was delayed until the event histogram had been transformed into a scattering rate histogram, which encompassed most of the Pass-2 processing.

First, a multiplicative correction for the spectrometer acceptance was applied on a bin-by-bin basis to the event histogram. This correction was calculated with a Monte-Carlo model of the spectrometer, as described below. After the correction, each bin contained the number of counts that would have been seen with an ideal spectrometer. Next, each bin was divided by the total incident-beam charge and was corrected for the electronic deadtime and various inefficiencies of the hardware and the off-line analysis. (For the hydrogen or helium target, these steps were repeated for the corresponding dummy-target run, and the dummy-target histogram was subtracted from the real target.) The resulting scattering-rate histogram was then rebinned into 15 MeV bins of energy loss, summed over the $\Delta\theta$ binning, and divided by the target thickness, Monte-Carlo solid angle, and energy-loss bin width to yield the inelastic, cross-section spectrum.

This processing is summarized by:

$$\frac{d^2\sigma}{d\Omega\, d\varepsilon} = \sum_{\substack{i,j \\ \text{window}}} \left\{ h_{ij} \cdot A_{ij} \cdot \frac{C_{dt}\, C_{\text{eff}}}{Q} - \left[h^D_{ij} \cdot A_{ij} \cdot \frac{C^D_{dt}\, C^D_{\text{eff}}}{Q^D} \right] \right\} \cdot \frac{M \cdot 10^{33}\ \text{nb/cm}^2}{N_a\, \rho\, L\, \Delta\Omega\, \Delta\varepsilon}, \quad (3.1)$$

in which h_{ij} is the event histogram, A_{ij} is the acceptance-function correction, C_{dt} and $C_{\rm eff}$ are the deadtime and efficiency corrections, Q is the number of incident electrons, M is the atomic wt. of the target (g/mole), N_a is Avogadro's number, ρ and L are the target's density (g/cm^3) and length (cm), $\Delta\Omega$ is the solid angle of the summing window, and $\Delta\varepsilon$ is its energy-loss width. (Dummy target quantities are denoted by the superscript D.)

3.3.1 Acceptance Correction

The electrons that scatter from the target populate a five-dimensional phase space determined by $\Delta P/P_0$, $\Delta\theta$, $\Delta\phi$, $X_{\rm tgt}$, and $Y_{\rm tgt}$. An ideal spectrometer would accept events within a five-dimensional hypercube in this space with 100% efficiency, and would reject all events outside. However, the physical apertures of the 8-GeV spectrometer, combined with the fiducial cut, define a more complicated region of good acceptance than a hypercube. Furthermore, the boundaries of this region are not perfectly sharp—they are smeared out by multiple scattering in the spectrometer's beam-pipe windows and the Cerenkov mirror. Thus, there is an acceptance function of these five variables that represents the probability density for accepting an event with these coordinates.

In practice, three of these coordinates are of little interest. With unpolarized beams and targets, we expect no azimuthal dependence for the cross section. The X and Y coordinates are also of no use in calculating a cross section. Therefore, the scattering events were histogrammed in only a two-dimensional space. The correction for finite acceptance then becomes an average of the five-dimensional acceptance function over the three unobserved coordinates, weighted by the actual event distribution. This calculation was done via Monte-Carlo techniques, using a "transport" model of the spectrometer optics.

The Monte-Carlo program generated trial events with a phase-space distribution given by the product of six separate distributions. First, a scattering location in the target was chosen. The scattering position along the length of the target was chosen from a uniform distribution, while the horizontal and vertical positions were chosen from Gaussian distributions, truncated at $\pm 3\sigma$, to simulate the beam-spot shape. This scattering location was rotated about the pivot axis to change to spectrometer-fixed coordinates; then the scattering angles $\Delta\theta$ and $\Delta\phi$and the momentum $\Delta P/P_0$ were chosen from uniform distributions.

The resulting trajectory was then propagated through the spectrometer model, using second order coefficients from the 1967 optics data. At the Cerenkov mirror and the vacuum windows, multiple scattering was simulated by randomly adjusting the values of dX/dZ and dY/dZ. The track was checked against each aperture through which it passed: the entrance to Q81, an octagon between B81 and B82, an octagon between B82 and Q83, and the entrance to the Cerenkov detector. These apertures restrict the accepted phase space sufficiently so that no check against the internal beam-pipe needed to be made. Tracks that survived all the apertures were then smeared by Gaussians to simulate the wire-chamber resolution and were checked against the good fiducial cut we applied to real events. If this cut was passed, the event was reconstructed back to the target and histogrammed in $\Delta P/P_0$ and $\Delta\theta$, using the same analysis applied to real events.

This histogram was then used to calculate the acceptance-correction function. In Figure 3.4 are shown the projections of a typical histogram onto the $\Delta P/P_0$ and $\Delta\theta$ axes. The $\Delta P/P_0$ acceptance falls off sharply at $\pm 3\%$, because of the fiducial cut, while the shape of the central portion is governed by the apertures inside the spectrometer. The shape of the $\Delta\theta$ projection is less affected by the fiducial cut,

which is located near the aperture defined limits. For each bin in the full histogram, we expect to find $m = \rho \cdot \Delta_p \Delta_t$ counts, where Δ_p and Δ_t are the $\Delta P/P_0$ and $\Delta\theta$ bin widths, and ρ is the density of trials in the histogram space. If n counts are observed for a given bin, then the multiplicative correction function used in Pass-2 has the value m/n for that bin. To avoid large systematic uncertainties, we used only the bins within $\pm 2.97\%$ $\Delta P/P_0$ and ± 6.0 mr $\Delta\theta$ in Pass-2, for which the projected acceptance is at least 50% of the maximum.

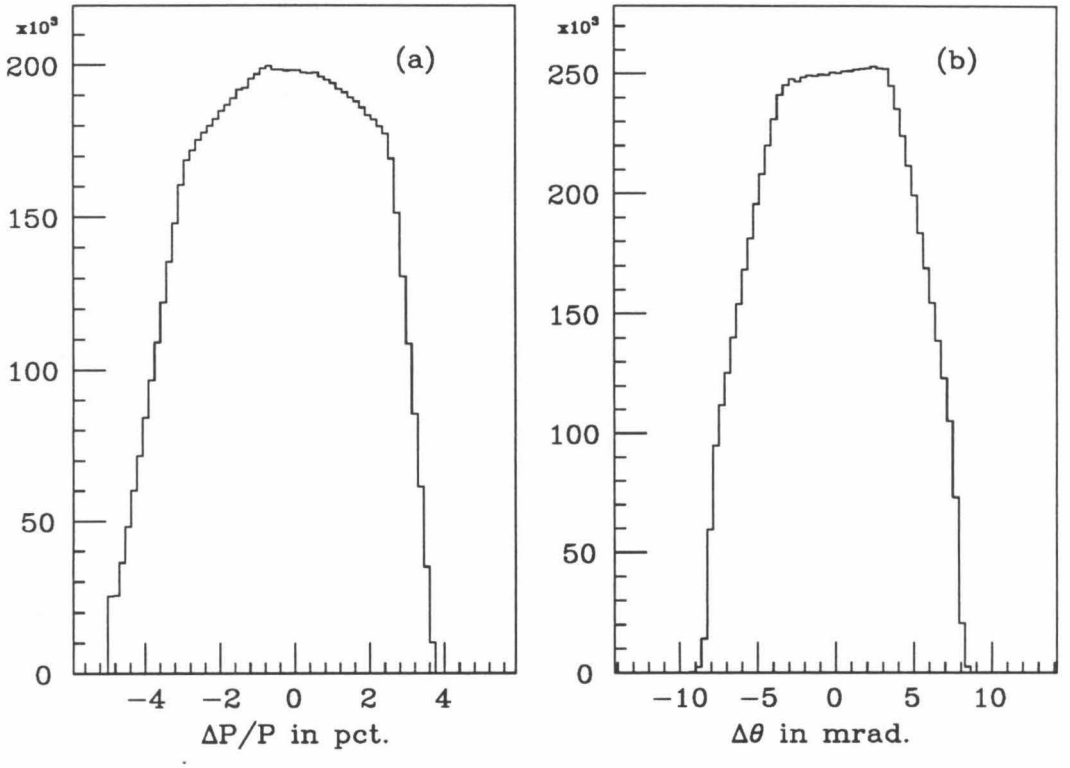

Figure 3.4 – Projections of the solid-target Monte-Carlo histogram onto the $\Delta P/P_0$ and $\Delta\theta$ axes.

This Monte-Carlo was run for a variety of target thicknesses and spectrometer angles and momenta to investigate sensitivity of the averaged acceptance function to these quantities. Comparisons were made by dividing one correction function by

another and projecting the results onto the $\Delta P/P_0$ axis. No significant variation was observed in the results for a 0.5 cm target over the NE3 angles and momenta. This was to be expected, since the target's scattering volume was much smaller than the physical acceptance of the spectrometer. Effectively, all the events emanated from a single point at the spectrometer pivot.

A different result was obtained in the tests for the 15 cm and 25 cm targets. In these cases, the target's scattering volume is essentially a line source for the spectrometer. The transverse extent of this line, as viewed by the spectrometer, becomes significant at large spectrometer angles. This causes a mild angular dependence to the correction function, so that at large angles the function deviates from that for a thin target as shown in Figure 3.5. Therefore, separate correction functions were calculated for the 15 cm target at 39 deg, and for the 25 cm target at 25 and 30 deg. All other runs were corrected with the thin (solid target) correction function, which was obtained by combining all the Monte-Carlo results to minimize the statistical fluctuations.

3.3.2 Acceptance Test Runs

Scattering data were obtained for a set of solid-target runs for the purpose of testing the acceptance function. These runs were taken with an incident energy of 3.6 GeV and a spectrometer angle of 30 degrees, and they span a range in energy loss from 1.35 to 2.04 GeV. In this kinematic region, the cross section is dominated by deep inelastic scattering, and is a featureless, smooth function of the energy loss. Any non-uniformities in the Pass-2 results that correlate with the event histogram binning would indicate a problem with the acceptance function.

To obtain the best statistics, the Pass-2 cross sections (before the energy loss rebinning) were summed over all the solid targets at each spectrometer setting to

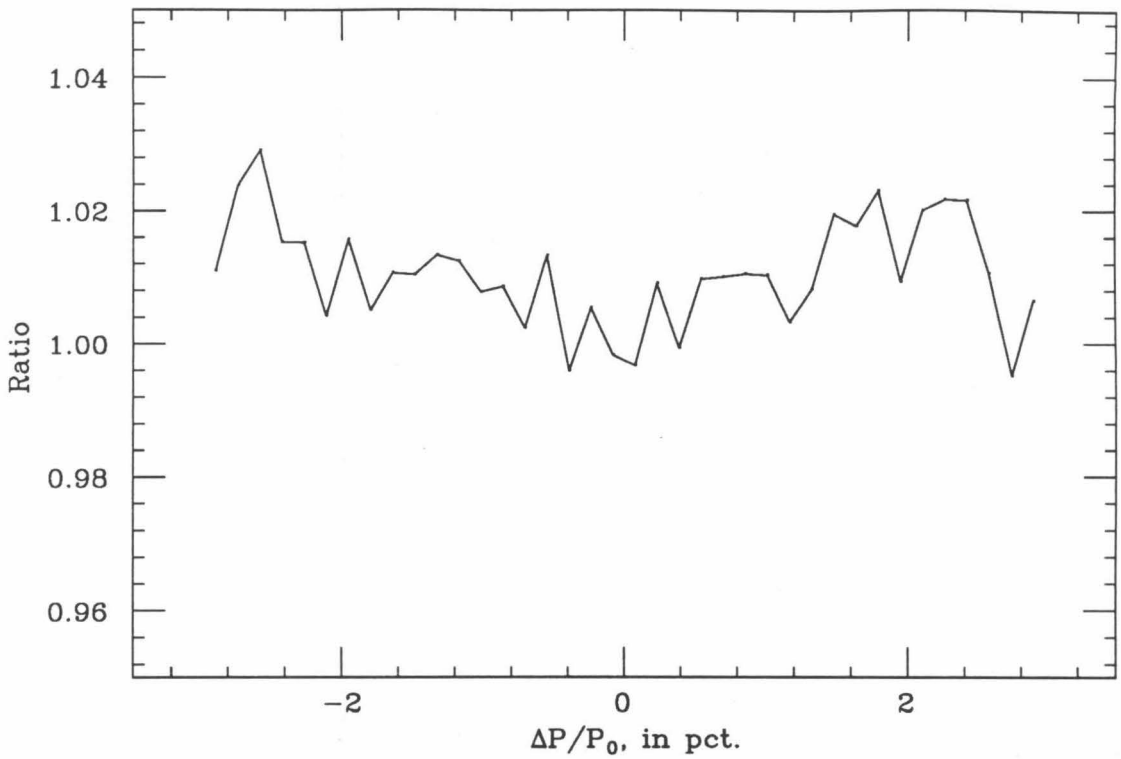

Figure 3.5 – The 25 cm target's correction function, divided by the 0.5 cm target's, and averaged over $\Delta\theta$ for each $\Delta P/P_0$ bin. The Monte-Carlo spectrometer angle is 30 degrees for the 25 cm target; the solid target's correction is independent of angle.

yield the aggregate cross section shown in Figure 3.6. The solid line through the data points is a quadratic polynomial least-squares fit to the data, with a reduced χ^2 of 1.07. The fractional deviation of the data points from this fit was then computed, and the deviations for data points that came from the same $\Delta P/P_0$ were averaged. These average deviations from the fit are plotted in Figure 3.7 versus $\Delta P/P_0$. Although some structure can be seen in this plot, the deviations are contained within a band of $\pm 2\%$, which will be taken as the systematic uncertainty of the acceptance function.

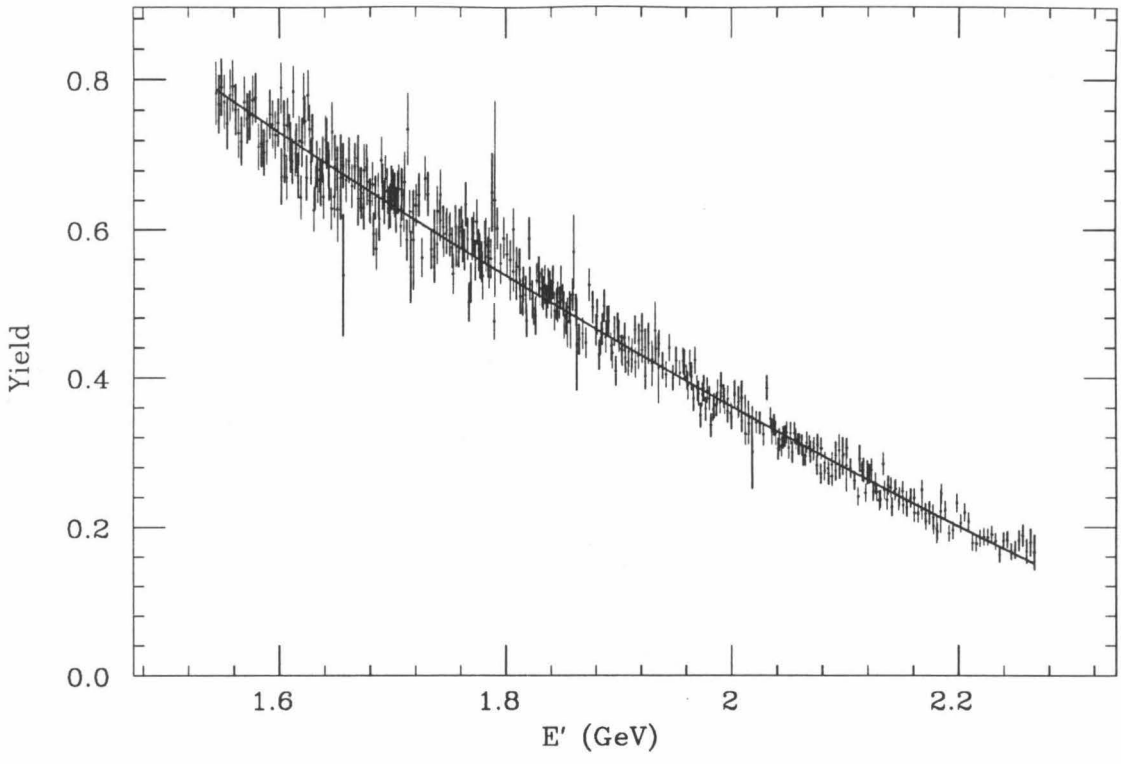

Figure 3.6 – Aggregate cross section in arbitrary units, summed over all solid-target acceptance runs, plotted versus the scattered energy, E′. The solid line is a fit to the data as discussed in the text.

3.3.3 Dead-time Corrections

The event readout trigger in this experiment consisted of the coincidence $\mathrm{El}_{20} = \Sigma\mathrm{TA} \times (\mathrm{C} + \Sigma\mathrm{PR})$ with a gate width of 20 ns. These coincidences were counted in a scaler, the value of which was called N_{20}. Because of the finite gate width, coincidences separated by less than 20 ns were not resolved and were counted as a single coincidence by the scaler. To correct for this dead-time, we used three additional scalers. Two of them, with values N_{40} and N_{60}, also scaled trigger coincidences, with gate widths of 40 and 60 ns, respectively. The third one, with value N_a, scaled the accidental coincidences between El_{20} and a copy of the same signal, delayed by 50 ns. From these scalers we extrapolated the zero dead-time, trigger coincidence rate, as follows.

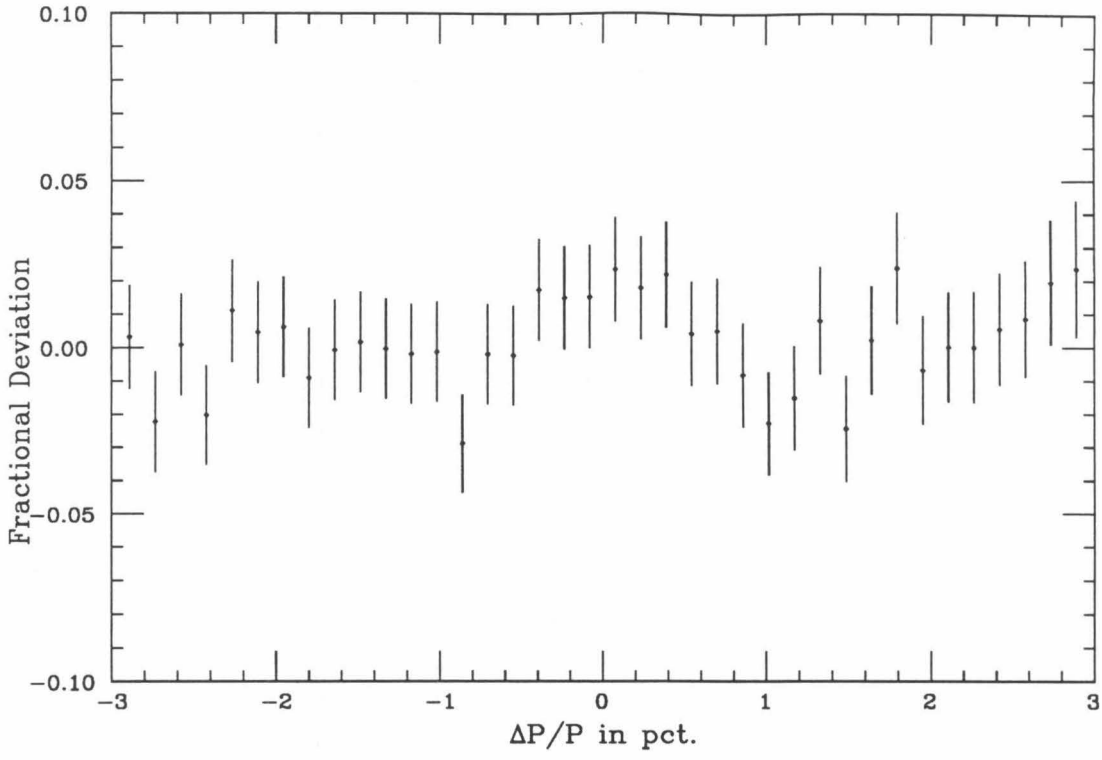

Figure 3.7 – Average fractional deviation of the data in the previous figure from the quadratic fit, plotted versus $\Delta P/P_0$, in percent. The deviations imply a 2% systematic uncertainty in the acceptance function over the range of interest between the dashed lines.

Suppose the mean time between electron events is τ. If an electron event opens a gate of width t, then the mean number of additional electron events that occur during this gate is $\overline{n} = t/\tau$. (The actual number of additional events that occur during a given gate are distributed by the Poisson distribution.) If we observe N_t gates of width t, then an estimate of the total number of events, N_0, is:

$$N_0 = N_t \cdot (1 + t/\tau). \tag{3.2}$$

We have N_t's for t =20, 40, and 60 ns, as shown in Figure 3.8. It is important to note that the statistically independent quantities are the differences between the scalers,

plus one of the scalers themselves (which we take to be N_{20}), as well as the accidental scaler, N_a. It is in terms of these statistically independent quantities that we estimate the dead-time correction, $\beta = N_0/N_{20}$.

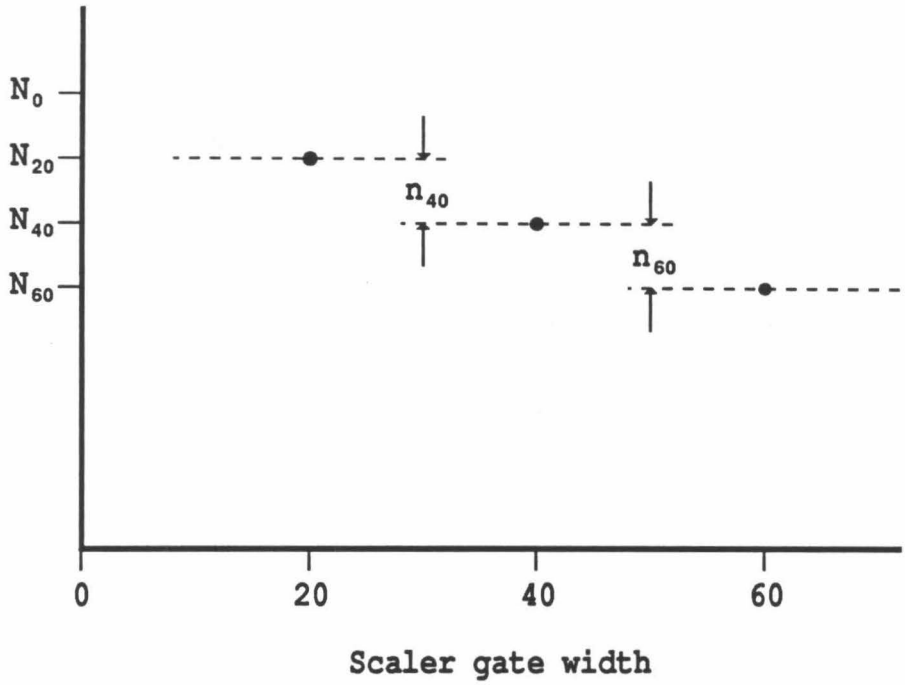

Figure 3.8 – Example of the relationship between scaler values and gate widths. N_0 is the true number of events. The values of the different scalers are plotted versus their coincidence width.

In terms of the mean event-spacing, τ, we have

$$n_{40} \equiv N_{20} - N_{40} = N_0 \cdot \frac{20/\tau}{(1+20/\tau)(1+40/\tau)} \tag{3.3}$$

and

$$\beta \equiv \frac{N_0}{N_{20}} = 1 + 20/\tau. \tag{3.4}$$

Now form

$$\alpha_{40} \equiv \frac{n_{40}}{N_{20}} = \frac{20/\tau}{1+40/\tau}, \tag{3.5}$$

so that one estimate of β is

$$\beta_{40} = \frac{1-\alpha_{40}}{1-2\alpha_{40}}. \tag{3.6}$$

Next, we form

$$\alpha_a \equiv \frac{N_a}{N_{20}} = 1 - e^{-40/\tau}. \tag{3.7}$$

This yields a second estimate of β

$$\beta_a = 1 - \tfrac{1}{2}\ln(1-\alpha_a). \tag{3.8}$$

Lastly, we defined a quantity $\alpha_{60} = n_{60}/N_{20}$ and formed a third estimate of β from it. Table 3.1 lists these estimates for all the hydrogen target runs, among which were the largest dead-times for the entire experiment. Inspection of these values shows that β_{60} is often inconsistent with the other two. It is suspected that there was some defect in the electronics feeding the N_{60} scaler, so that the corresponding dead-time estimate is too large. Thus, β_{60} was not used in computing the dead-time correction.

The standard uncertainties in the quantities N_{20}, n_{40}, and N_a were taken to be $\sqrt{N_{20}}$, $\sqrt{n_{40}\,N_{40}/N_{20}}$, and $\sqrt{N_a}$, respectively. These uncertainties were combined in quadrature to form the uncertainties $\Delta\beta_{40}$ and $\Delta\beta_a$. A weighted average of the two estimates was then used for the dead-time correction:

$$\overline{\beta} = \frac{\beta_{40}(\Delta\beta_a)^2 + \beta_a(\Delta\beta_{40})^2}{(\Delta\beta_a)^2 + (\Delta\beta_{40})^2} \quad , \quad \Delta\overline{\beta}^2 = \frac{\Delta\beta_{40}{}^2\Delta\beta_a{}^4 + \Delta\beta_a{}^2\Delta\beta_{40}{}^4}{(\Delta\beta_a{}^2 + \Delta\beta_{40}{}^2)^2}. \tag{3.9}$$

Run	β_a	β_{40}	β_{60} (not used)	$\bar{\beta}$
10602	$1.03193 \pm .00062$	$1.03260 \pm .00085$	$1.03799 \pm .00088$	$1.03217 \pm .00050$
11303	$1.03275 \pm .00078$	$1.03143 \pm .00103$	$1.03928 \pm .00110$	$1.03227 \pm .00062$
11408	$1.00460 \pm .00044$	$1.00523 \pm .00066$	$1.00396 \pm .00058$	$1.00479 \pm .00037$
11410	$1.01003 \pm .00033$	$1.00973 \pm .00046$	$1.01078 \pm .00048$	$1.00992 \pm .00027$
13702	$1.01067 \pm .00031$	$1.00995 \pm .00042$	$1.01169 \pm .00045$	$1.01041 \pm .00025$
13710	$1.00912 \pm .00027$	$1.00816 \pm .00036$	$1.01054 \pm .00040$	$1.00877 \pm .00022$
14501	$1.01475 \pm .00037$	$1.01631 \pm .00054$	$1.01538 \pm .00052$	$1.01526 \pm .00031$
16001	$1.00364 \pm .00020$	$1.00308 \pm .00026$	$1.00446 \pm .00032$	$1.00343 \pm .00016$
19285	$1.00181 \pm .00013$	$1.00145 \pm .00017$	$1.00192 \pm .00019$	$1.00167 \pm .00011$
19344	$1.00139 \pm .00026$	$1.00169 \pm .00041$	$1.00150 \pm .00038$	$1.00148 \pm .00022$
19369	$1.00016 \pm .00008$	$1.00008 \pm .00008$	$1.00025 \pm .00014$	$1.00012 \pm .00006$
19402	$1.00015 \pm .00015$	$1.00000 \pm .00029$	$1.00030 \pm .00030$	$1.00012 \pm .00013$

Table 3.1 – Electronic dead-time estimates for all hydrogen runs.

The dead-time corrections obtained in this manner for the hydrogen runs are also listed in Table 3.1.

3.3.4 Efficiency Correction

In this section we consider the corrections for the lack of perfect efficiency with which electron events were detected and analyzed. There are three basic kinds of efficiencies to consider, which combine multiplicatively to give the total efficiency. These are: the hardware efficiency of the trigger concidence, the fraction of trigger concidences that were logged to tape, and the software cut efficiencies of the data analysis. The total efficiency was corrected for by estimating it for each run, and dividing it out of the scattering-rate histogram.

First, let's consider the trigger efficiency. The trigger was a coincidence between the ΣTA and the C + ΣPR signals. Assuming that their individual efficiencies are uncorrelated, the trigger efficiency is given by:

$$\varepsilon_{\text{trig}} = \varepsilon_{\text{TA}} \cdot [1 - (1 - \varepsilon_{\text{C}}) \cdot (1 - \varepsilon_{\text{PR}})], \tag{3.10}$$

in which ε_C, ε_{PR}, and ε_{TA} are the Cerenkov, PR, and TA hardware efficiencies.

Because the PR lead-glass blocks are relatively thin, there is a non-negligible probability that an electron will pass through without showering. Examination of the latch bits shows that the PR discriminator fired in only 95-97% of the triggers, which makes it the least efficient part of the detector package. We will use $\varepsilon_{PR} = 0.95$ in calculating the trigger efficiency.

The Cerenkov hardware efficiency was measured during the checkout phase as a function of the nitrogen gas pressure and the phototube voltage. These data were taken at kinematics for which the π/e ratio was low. The CK efficiency is the fraction of events passing the SHSOFT, wire chamber, and good fiducial cuts, for which the CK latch had fired. Figure 3.9 shows the results of these tests. The operating pressure and tube voltage were chosen to yield an efficiency near unity, with low double-pulse rate (also shown in Figure 3.9), and a high pion threshold. Based on these data, we used a pressure of 550 mm Hg and a tube voltage of 2330 volts, which gave an efficiency of 0.999 ± 0.001, with a pion threshold of 7 GeV/c.

The TA efficiency is, in principle, a function of the spectrometer momentum, because the average number of photoelectrons is proportional to the showering electron's energy. In Figure 3.10 is shown a histogram of the TA ADC for single-track events that passed the Cerenkov and good-fiducial cuts, taken with a spectrometer momentum of 1.8 GeV. The bold line is a Gaussian least-squares fit to the data between channels 80 and 360, with a $\chi^2/_{DF}$ of 1.79, for 56 data points. The ΣTA discriminator threshold lies near channel 60, so that all bins below this point are zero. 99.98% of the Gaussian lies above this point, which we take to be the TA efficiency at this momentum. For higher momenta, the efficiency should be even better. At the

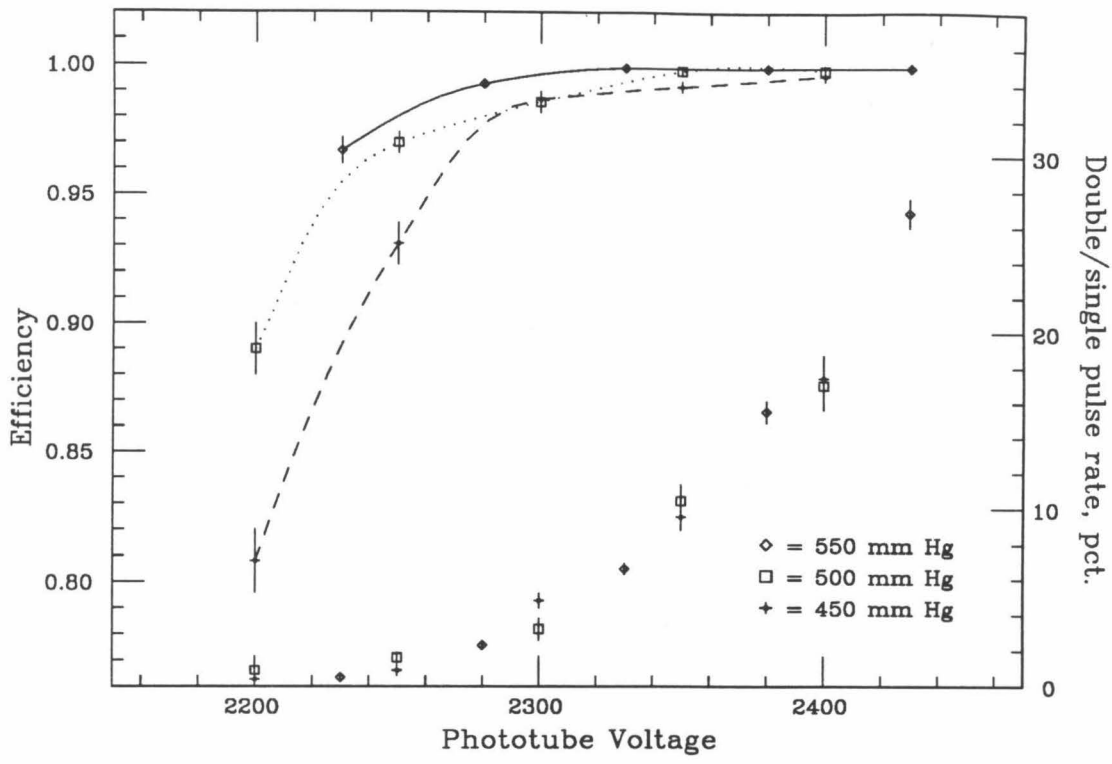

Figure 3.9 – Cerenkov efficiency and double-pulse rate as a function of nitrogen pressure and tube voltage. The data were taken with the Al target, at an incident energy of 2.02 GeV, a spectrometer momentum of 1.8 GeV, and an angle of 15 degrees.

lowest momentum (1.6 GeV), a similar analysis yields an efficiency of 99.95%. Combining this with the PR and Cerenkov efficiencies, we find that the overall trigger efficiency is at least 99.94% for all spectrometer settings.

Next, let's consider the software cut efficiencies. We have previously found the SHSOFT and CK cuts each to have an efficiency of 99.9%. The fiducial cut has no associated efficiency—it is an acceptance defining cut that is properly accounted for by the acceptance function. This leaves only the wire-chamber track multiplicity cut to be discussed.

Typically, there was an average of 9.5 of the ten chambers that fired for each track, indicating that the individual chamber efficiencies are 95%, on average. Each P

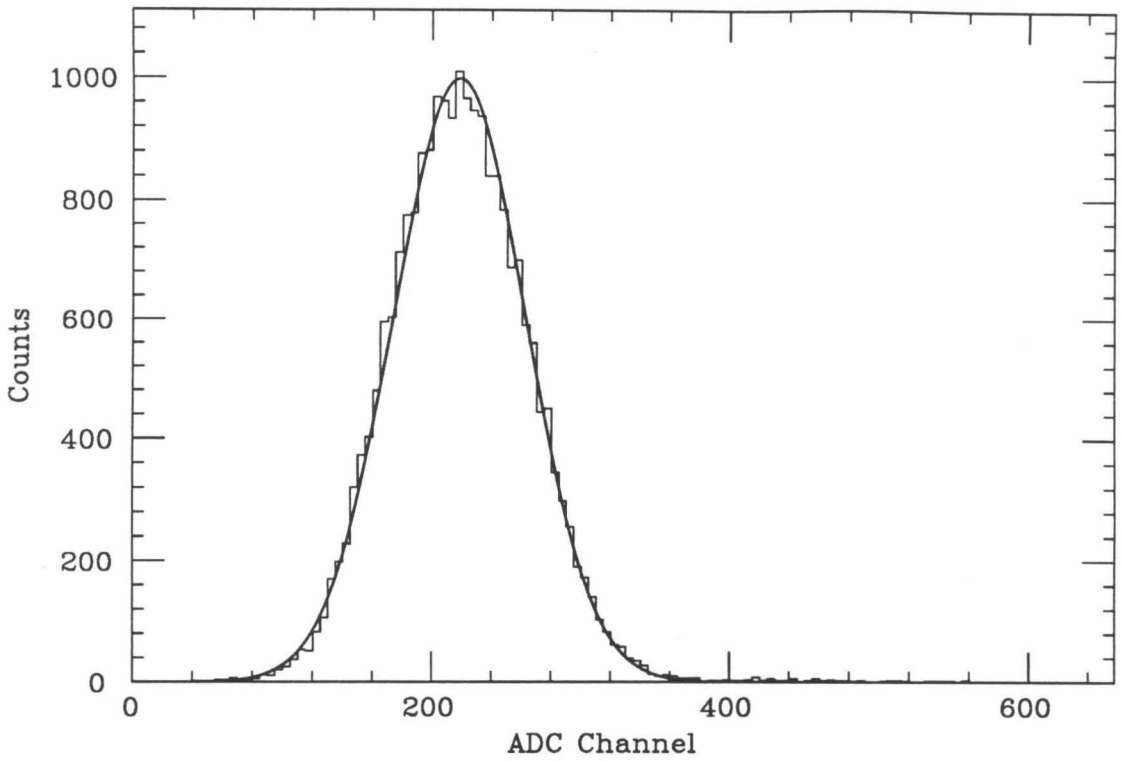

Figure 3.10 – ΣTA ADC histogram for single-track events passing the Cerenkov cut. The data were taken with the He target, at an incident energy of 2.02 GeV, a scattering angle of 20 degrees, and a spectrometer momentum of 1.8 GeV. The bold line is a fit to the data as described in the text.

chamber has a region of poor efficiency $\sim$ 1 cm wide centered on (and caused by) the support wires [35]. To assure uniform overall efficiency, the chambers were positioned so as to stagger the support wires by 2.5 cm, so that no track originating from the target could pass through all the dead zones. The track reconstruction algorithm required at least two P chambers, at least two T chambers, and at least five all told to have been hit, in order to find a track. Assuming an equal efficiency of ε for each chamber, the efficiency for all ten chambers should be

$$\varepsilon_{\rm WC} = \sum_{n=2}^{5}\sum_{m=2}^{5}\binom{5}{n}\binom{5}{m}\varepsilon^{n+m}(1-\varepsilon)^{10-n-m} \quad - \quad \left[\binom{5}{2}\varepsilon^2(1-\varepsilon)^3\right]^2, \qquad (3.11)$$

which, for $\varepsilon = 0.95$, yields $\varepsilon_{\rm WC} = 99.994\%$. However, we find typically that no track is found in 0.2% of the events (cut on Cerenkov and SHSOFT). This was assumed to be due to an inefficiency of the track reconstruction algorithm, and was corrected for.

An efficiency correction was also made for the shower-energy cut applied to multitrack events, described above. This correction assumes that the fraction of events with three or more tracks is insignificant, which is the case for this experiment. In Figure 3.11 are shown the ADC and wire-chamber gates that are opened by an electron event. If a second electron occurs in region III, then only one track will be found, and no correction is needed. If it occurs in region II, then $\sim 1/6$ of the time it enters the same PR block as the first electron, and the event fails the WC cut, but passes the CK and SHSOFT cuts. (The other 5/6 of the time, the first track is correctly retained.) The multiplicative correction for this effect is given by $(N_{\rm mlte} + N_{\rm good})/N_{\rm good}$, where $N_{\rm good}$ is the number of events that passed all the cuts, and $N_{\rm mlte}$ is the number of events that pass the CK and SHSOFT cuts, but appear to have two electron tracks. If the second electron occurs in region I, then the event will fail both the WC and SHSOFT cuts, but will pass the CK cut. This effect is corrected for by the factor $(N_{\rm good} + N_{\rm ck,\overline{sh},\overline{wc}})/N_{\rm good}$, where $N_{\rm CK,\overline{SH},\overline{WC}}$ is the number of multielectron track events passing the Cerenkov cut, but failing the SHSOFT cut.

If the second particle happened to be a pion, then the electron track is correctly retained if the pion arrived in region III. If it arrived in region I or II, then $\sim 1/6$ of the time it enters the same PR block as the electron, causing the event to fail the WC cut, while passing the CK and SHSOFT cuts. The above MLTE correction accounts for these events as well.

The last efficiency to calculate is the event-sampling efficiency. This is given by the ratio $N_{\rm tape}/N_{20}$, where $N_{\rm tape}$ is the total number of events recorded on the logtape,

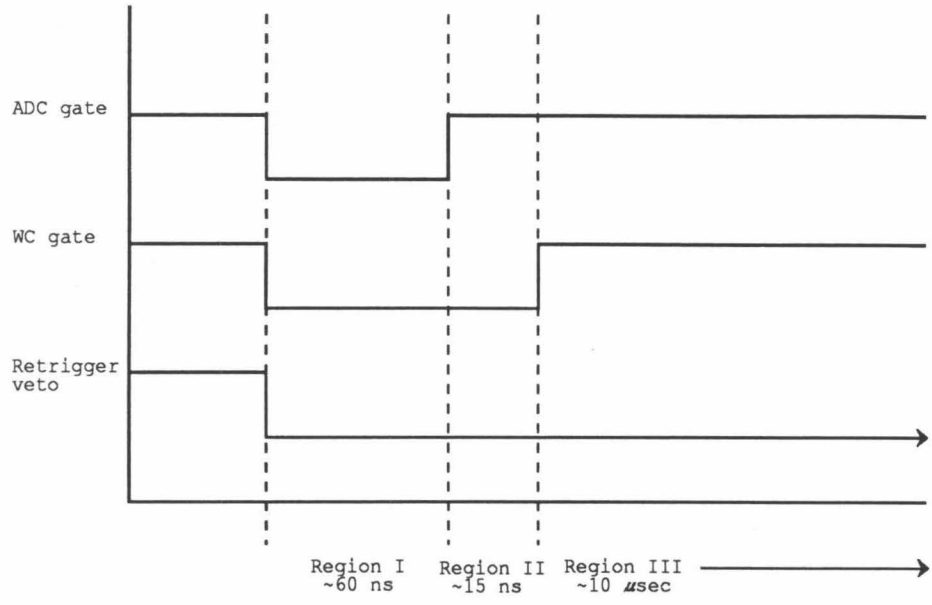

Figure 3.11 – Time structure of ADC and wire chamber gates within a beam pulse.

and N_{20} is the trigger coincidence scaler value discussed above. To summarize, the efficiency correction is obtained by dividing the observed counting rate by the total efficiency, which is given by:

$$\varepsilon_{\rm tot} = [\varepsilon_{\rm trig}\,\varepsilon_{\rm ck}\,\varepsilon_{\rm shsoft}]\cdot\alpha_{\rm hi\,shsoft}\,\varepsilon_{\rm sample}\,\alpha_{\rm 2trk}\cdot(1-f_{\rm mlte}-f_{\rm notrk}), \tag{3.12}$$

in which $\varepsilon_{\rm trig}$, $\varepsilon_{\rm ck}$, and $\varepsilon_{\rm shsoft}$ are, respectively, the trigger efficiency, Cerenkov cut efficiency, and SHSOFT cut efficiency; and

$$\alpha_{\rm hi\,shsoft} = N_{\rm good}/(N_{\rm good}+N_{\rm hi\,shsoft})$$

$$\varepsilon_{\rm sample} = N_{\rm tape}/N_{20}$$

$$\alpha_{\rm 2trk} = N_{\rm good}/(N_{\rm good}+N_{\rm ck,\overline{sh},\overline{wc}});$$

while f_{notrk} and f_{mlte} are the fraction of events passing the Cerenkov and SHSOFT cuts for which no track and multielectron tracks, respectively, were found. The quantity in brackets should be equal to 0.997, but was in practice set to 0.985 ± 0.015 in order to make the elastic-scattering cross sections agree with the world average [3], as discussed below in the chapter on systematic corrections.

3.3.5 Toroid Charge Integration

The toroidal charge monitors provided four independent measurements of the total incident charge, measured in peta-electrons (PE's), for each run. Each toroid monitor was separately adjusted periodically during the experiment to maintain a calibration accurate to better than 1%. For the majority of runs, these four numbers could simply be averaged to obtain the incident charge used in Pass-2. However, in some runs one or two of the toroids failed to work correctly, either because of experimenter error or problems with the hardware and software of the newer monitors (T2 and T3). Therefore, an algorithm was developed to deal with the problem of deviant toroid values.

The first step was to compute the average (Q) and standard deviation (ΔQ) of the four toroid values. If $\Delta Q/Q$ was less than 0.5%, then no further processing was done. Otherwise, the toroid value that deviated farthest from the average was rejected, and the average and standard deviations were recalculated. This process was repeated once more, if $\Delta Q/Q$ was still more than 0.5%. If both T0 and T1, or T2 and T3 had been rejected, or if $\Delta Q/Q$ was still greater than 0.5%, then the run was flagged for inspection by hand. Otherwise, the final average was used in the cross-section calculation, with an uncertainty given by the final standard deviation.

Twenty-nine runs were flagged for hand inspection, out of a total of $\sim$500. Several kinds of problems were uncovered by the inspection. In some cases, it was known

that the old toroid monitors (T0 and T1) had been incorrectly operated or turned off during part of the run. In these cases, the average of T2 and T3 was used. In other runs, it was discovered that the signal applied to the ADC's of T2 and T3 was close to the saturation level. The old monitors had a higher saturation level and did not suffer from this problem; hence, the average of T0 and T1 was used for these runs. The remaining runs had nearly equal values for T2 and T3 that were lower than T0 and T1 (themselves nearly equal), typically by a few pct. In one extreme case, $T2/T0 = 0.808$. The overlap between the data of this run and adjacent runs is best when the old monitors' values are used. It is conjectured that the LSI computer, which needed to read the T2 and T3 ADC's on each beam pulse, was too slow and occasionally missed pulses when it was overloaded. (It has since been replaced with a faster computer.) The old toroid monitors were designed to function at 360 Hz and would not miss pulses. Furthermore, the old monitors, part of the original equipment of SLAC, have a long history of reliable use. Therefore, the values of T2 and T3 were ignored in these cases.

3.3.6 Dummy Subtraction

The data taken with the hydrogen and helium targets contained a contribution from electrons scattering in the Al endcaps. To subtract this contribution, we took data with empty dummy-targets for identical kinematics as the real targets. These dummy runs were subjected to the same chain of analysis as for the real targets, to form a $\Delta P/P_0$ vs. $\Delta\theta$ scattering rate histogram. To simulate the effects of energy straggling in the hydrogen or helium material, additional Al endcaps, each $\approx 1/2$ the thickness in radiation lengths of the target material, were fitted to the dummy cells, which were otherwise identical to the real cells. Because the straggling effects per

unit radiation length vary only logarithmically with the Z of the material [48], they are well simulated by this arrangement [49].

The thicknesses of the hydrogen cell entrance and exit windows were 0.0027 in. and 0.0040 in., respectively, and the additional endcaps on the hydrogen dummy totaled 0.0599 in. Therefore, the hydrogen dummy target's rate histogram was multiplied by the ratio of aluminum thicknesses,

$$\frac{t_{\mathrm{H}}}{t_{\mathrm{dummy}}} = \frac{0.0067}{(0.0067 + 0.0599)} = 0.101, \tag{3.13}$$

and subtracted from the hydrogen target's histogram to remove the endcap contribution. Similarly, the Helium cell entrance and exit windows were 0.008 in. and 0.016 in. thick, respectively, and the additional endcaps on the helium dummy cell totaled 0.0513 in. The dummy subtraction weighting factor in this case was given by

$$\frac{t_{\mathrm{He}}}{t_{\mathrm{dummy}}} = \frac{0.024}{(0.024 + 0.0513)} = 0.319. \tag{3.14}$$

3.3.7 Energy Loss Rebinning

To facilitate the combination of runs into extended spectra, the Pass-2 scattering-rate histograms were rebinned in terms of energy loss (ω). The bins were chosen to be 15 MeV wide, with the center of the lowest bin at $\omega = 0$. The edges of bins from different runs will thus always line up, regardless of the actual values of P_0 or the incident energy (E_0). Binning in terms of ω also minimizes the sensitivity of the y-scaling analysis to small shifts in E_0 occurring between different runs. (This is not true for a binning defined solely in terms of E', the scattered electron's energy.)

For each run, the edges of the energy-loss bins were computed in terms of $\Delta P/P_0$. The $\Delta P/P_0$ bins between and containing the edges were summed together, weighted

by the fraction of the $\Delta P/P_0$ bin lying inside the ω bin. Thus, the bin splits were made in a linear fashion. The number of $\Delta P/P_0$ bins (of width 0.15625%) that fit into a 15 MeV bin varied from 2.7 (for $P_0 = 3.6$) to 6.0 ($P_0 = 1.6$), thus insuring that each energy-loss bin contained at least one unsplit $\Delta P/P_0$ bin. Statistical uncertainties associated with each bin were combined in quadrature, with the same weighting as the bin values.

3.3.8 Hydrogen Data

The hydrogen elastic cross sections were calculated slightly differently during the Pass-2 analysis. Instead of rebinning the $\Delta P/P_0$ vs. $\Delta\theta$ scattering-rate histogram into energy loss bins, the events within a special window were directly summed. For a given $\Delta\theta$ bin index, this window extended from 2% in $\Delta P/P_0$ below the elastic peak, up to the histogram upper limit. (The $\Delta\theta$ range covered by the window was the same ± 6.0 mr used for the other targets.) The elastic peak position varies with scattering angle, and over the acceptance of the spectrometer, it is well approximated by a linear function of $\Delta\theta$. The slope and intercept of this function were extracted from the data, as described in the next chapter, and the $\Delta P/P_0$ window limit was set accordingly. (This same 2% window was used in the calculation of radiative corrections.)

The cross section $d\sigma/d\Omega$ was calculated from this sum in the same manner as a 15 MeV energy loss bin (Eq. 3.1), except that no division by an energy bin width was needed. As a final step, multiplicative radiative corrections, computed prior to Pass-2, were applied. (The calculation of the radiative corrections is described in Appendix A.) These cross sections are well known for our momentum transfers, and were used to check the absolute normalization of the inelastic cross sections we measured.

3.4 Pass-3

The Pass-3 analysis was responsible for combining the separate cross-section results of each run into extended spectra. Because of the complete overlap of the bins, this procedure was quite simple. Overlapping bins were simply averaged, with weights equal to the integrated beam current of each run, thus treating each incident electron of the overlapping runs in an unbiased manner.

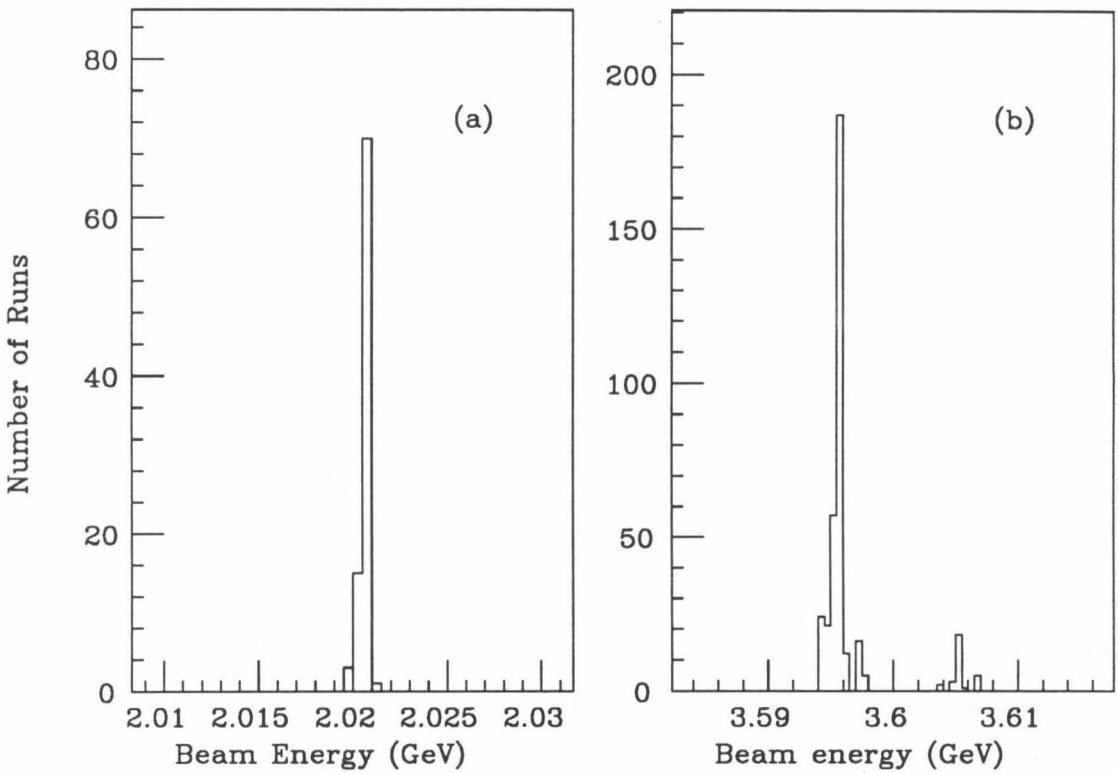

Figure 3.12 – Histogram of incident energies for (a) 2 GeV runs, (b) 3.6 GeV runs.

A slightly more complicated task for the Pass-3 software was to decide which runs to include in each spectra. In Figure 3.12 is shown a histogram of incident energies for all of the data runs. There are three peaks in the histogram, at energies of 2.020, 3.595, and 3.605 GeV, with widths of a few MeV. The 3.605 GeV energies

were due to imprecise linac tuning during the last few days of the experiment. To reduce systematic errors, it was decided not to combine these runs with the 3.595 GeV runs. Thus, the Pass-3 software separated runs into spectra of four different beam energies, six different angles, and six different targets (42 spectra in all) by requiring:

$$|E_0^{\text{run}} - E_0^{\text{spectrum}}| \leq \begin{cases} 0.014 \text{ GeV}, & \text{if } E_0^{\text{spectrum}} = 3.595 \text{ GeV}; \\ 0.003 \text{ GeV}, & \text{otherwise}, \end{cases}$$

$$\text{and} \quad |\theta^{\text{run}} - \theta^{\text{spectrum}}| \leq \quad 0.010 \text{ degrees}.$$

Chapter 4
Systematic Corrections and Uncertainties

4.1 Spectrometer Coordinates

The spectrometer angles $\theta' = \theta_0 + \Delta\theta$ and $\phi' = \Delta\phi$ are not the usual polar angles θ and ϕ in terms of which we calculate cross sections. Figure 4.1 shows the relationship between these angles and the conventional polar angles. The transformation between the two coordinate systems is given by:

$$\begin{aligned} \cos\theta &= \cos\theta' \cdot \cos\phi' \\ -\tan\phi &= \tan\phi' / \sin\theta'. \end{aligned} \tag{4.1}$$

Note that a differential element of solid angle in the spectrometer coordinates is given by:

$$d\Omega' = \cos\phi' \cdot d\phi'\, d\theta', \tag{4.2}$$

which reflects the fact that θ' and ϕ' are related to polar angles about the $\hat{y}$ (instead of the $\hat{z}$) axis.

Curves of constant θ' therefore reach a minimum θ when $\phi' = 0$. The finite ϕ' acceptance thus implies that the effective angle of the spectrometer is greater than θ_0, necessitating a correction. This and other effects arising from the finite acceptance are discussed below.

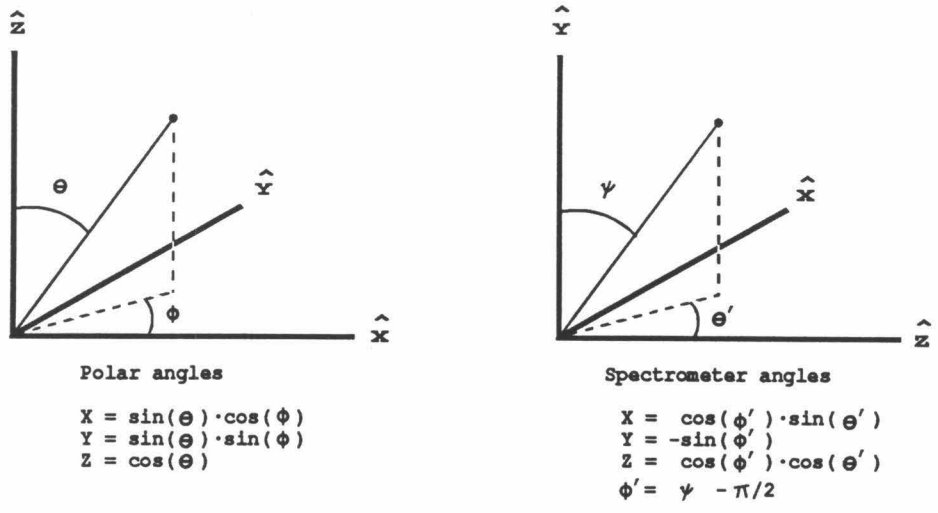

Figure 4.1 – Relationship between spectrometer angles (θ', ϕ') and conventional polar angles (θ, ϕ). The beam direction is along $\hat{z}$, and $-\hat{y}$ is the vertical direction.

4.2 Corrections for Finite Acceptances

Consider a single bin in the $\Delta P/P_0$ vs. θ' event histogram. If we were to use this single bin (with labels i, j) to measure the cross section, we would observe:

$$\sigma_{ij}^{\text{obs}} = \frac{\int \sigma_{\text{true}} \cdot \rho \, dE_0 \, dE' \, d\Omega'}{\int \rho \, dE_0 \, dE' \, d\Omega'}, \tag{4.3}$$

in which ρ is the complete acceptance function. The integration limits are given by the bin edges, the width of the incident-energy-defining slits, and by the ϕ' limits of the spectrometer. We now expand σ_{true} in a second-order Taylor series:

$$\sigma_t = \tilde{\sigma} + (A_1\, x + A_2\, y + A_3\, z) + (B_1\, x^2 + B_2\, y^2 + B_3\, z^2)/2 + (C_1\, yz + C_2\, xz + C_3\, xy), \tag{4.4}$$

in which $x = E_0 - \tilde{E}_0$, $y = E' - \tilde{E}'$, $z = \cos\theta - \cos\tilde{\theta}$, and $\tilde{E}_0$ is the central beam energy, $\tilde{E}'$ is the center of the 15 MeV energy loss bin into which the $\Delta P/P_0$ bin falls, and $\tilde{\theta}$ is an angle near θ_0, yet to be determined. This Taylor series should be an excellent approximation for our data. With E_0 integration limits of $\tilde{E}_0 \pm \alpha$, we obtain:

$$\sigma_{ij}^{\text{obs}} = \tilde{\sigma} + \frac{B_1\,\alpha^2}{6} + \frac{\int \rho \cdot [A_2\,y + A_3\,z + \frac{1}{2}(B_2\,y^2 + B_3\,z^2) + C_1\,yz]\,dE'\,d\Omega'}{\int \rho\,dE'\,d\Omega'}. \tag{4.5}$$

As confirmed by the Monte Carlo, we will now assume that ρ can be factored:

$$\rho = f(\phi') \cdot g(E', \theta'). \tag{4.6}$$

The function g doesn't vary significantly over the small range of integration and can be factored out of the integrals:

$$\sigma_{ij}^{\text{obs}} = \tilde{\sigma} + \frac{B_1\,\alpha^2}{6} + \frac{\int f(\phi') \cdot [A_2\,y + A_3\,z + \frac{1}{2}(B_2\,y^2 + B_3\,z^2) + C_1\,yz]\,dy\,d\Omega'}{\int dy \cdot \int f(\phi')\,d\Omega'}. \tag{4.7}$$

Finally, the σ_{ij}^{obs} are averaged over a range of y and θ' to form the 15 MeV energy loss bin. After some algebra, we obtain:

$$\sigma_{\text{obs}} = \tilde{\sigma} + \frac{B_1\,\alpha^2 + B_2\,\varepsilon^2}{6} + A_3\,\frac{I_1}{I_0} + \frac{B_3}{2}\,\frac{I_2}{I_0}, \tag{4.8}$$

in which $\varepsilon = 7.5$ MeV, and

$$I_n = \int_{-\pi}^{\pi} d\phi' \int_{\theta_0 - \theta'_{\text{lim}}}^{\theta_0 + \theta'_{\text{lim}}} z^n \cdot f(\phi')\,\cos\phi'\,d\theta', \tag{4.9}$$

with $\Delta\theta$ integration limits of $\pm\theta'_{\text{lim}}$.

$\theta_{\rm spec}$ (deg)	$\tilde{\theta}$ (deg)
15.000	15.023
16.000	16.021
20.000	20.017
25.000	25.013
30.000	30.011
39.000	39.008

Table 4.1 – Nominal spectrometer and effective scattering angles.

Substituting for z, we have:

$$I_n = \int_{-\pi}^{\pi} d\phi' \int_{\theta_0-\theta'_{\rm lim}}^{\theta_0+\theta'_{\rm lim}} (\cos\theta' \cos\phi' - \cos\tilde{\theta})^n \cdot f(\phi') \cos\phi' \, d\theta'. \tag{4.10}$$

Further simplification yields:

$$\frac{I_1}{I_0} = \cos\theta_0 \cdot \langle\cos\phi'\rangle \cdot \frac{\sin\theta'_{\rm lim}}{\theta'_{\rm lim}} - \cos\tilde{\theta}, \tag{4.11}$$

in which

$$\langle\cos\phi'\rangle = \frac{\int \cos\phi' \cdot f(\phi') \cos\phi' \, d\phi'}{\int f(\phi') \cos\phi' \, d\phi'}. \tag{4.12}$$

Lastly, we have a more complicated expression for I_2/I_0:

$$\frac{I_2}{I_0} = -\cos^2\tilde{\theta} + \frac{\langle\cos^2\phi'\rangle}{2}\left[1 + (2\cos^2\theta_0 - 1) \cdot \frac{\sin\theta'_{\rm lim}\cos\theta'_{\rm lim}}{\theta'_{\rm lim}}\right]. \tag{4.13}$$

In order to eliminate the A_3 term from the expression for $\sigma_{\rm obs}$, we therefore choose $\tilde{\theta}$ to make I_1/I_0 equal to zero. This is the effective central angle discussed above and is always greater than θ_0 for forward angles. With $f(\phi')$ taken from the Monte Carlo, we find:

$$\langle\cos\phi'\rangle \equiv \cos\phi'_{\rm eff}\,; \quad \phi'_{\rm eff} = 14.253 \text{ mrad}. \tag{4.14}$$

The resulting values of $\tilde{\theta}$ for each of the nominal spectrometer angles for which we took data are given in Table 4.1.

The cross section we wish to report is the value $\tilde{\sigma}$, but what we have actually measured is $\sigma_{\rm obs}$. Therefore, we applied a correction factor that was calculated from a model of the experimental cross section, which devolved from the radiative correction computations. For a given 15 MeV bin, the model was calculated at seven different combinations of incident energy, scattered energy, and scattering angle. These values were fit to extract $\tilde{\sigma}$, B_1, B_2, and B_3, from which the correction factor $\tilde{\sigma}/\sigma_{\rm obs}$ was calculated. This ratio varied between 1.00 to a minimum of 0.95 at the small energy loss end of several spectra. In some cases, this correction was not significant compared to the statistical error bars of the data. However, Figure 4.2 shows one spectrum (C tgt, 3.6 GeV, 16 deg) for which this wasn't so. Regardless of the size of the cross-section error bars, these correction factors were multiplicatively applied to all of the cross sections.

The systematic uncertainty of these corrections was estimated from their sensitivity to changes in the model's parameters. Small changes, of similar size as the statistical fluctuations in the measured cross sections, caused the correction factors to change by up to 1%. Furthermore, the correction factors for different targets at the same kinematics differed by no more than 1%. Therefore, we assigned a systematic uncertainty of 1% to these correction factors.

4.3 Spectrometer and A-bend Calibration

The positions of the hydrogen and helium (at the three lowest q^2's) elastic peaks were used to determine the energy calibration of the spectrometer and beam switchyard. The peak positions were compared with those expected from kinematics, and the deviations were minimized in a least-squares procedure to find the energy calibration factors. This procedure was also used to check for a possible offset to the spectrometer's angle encoder. No evidence for such an offset was observed.

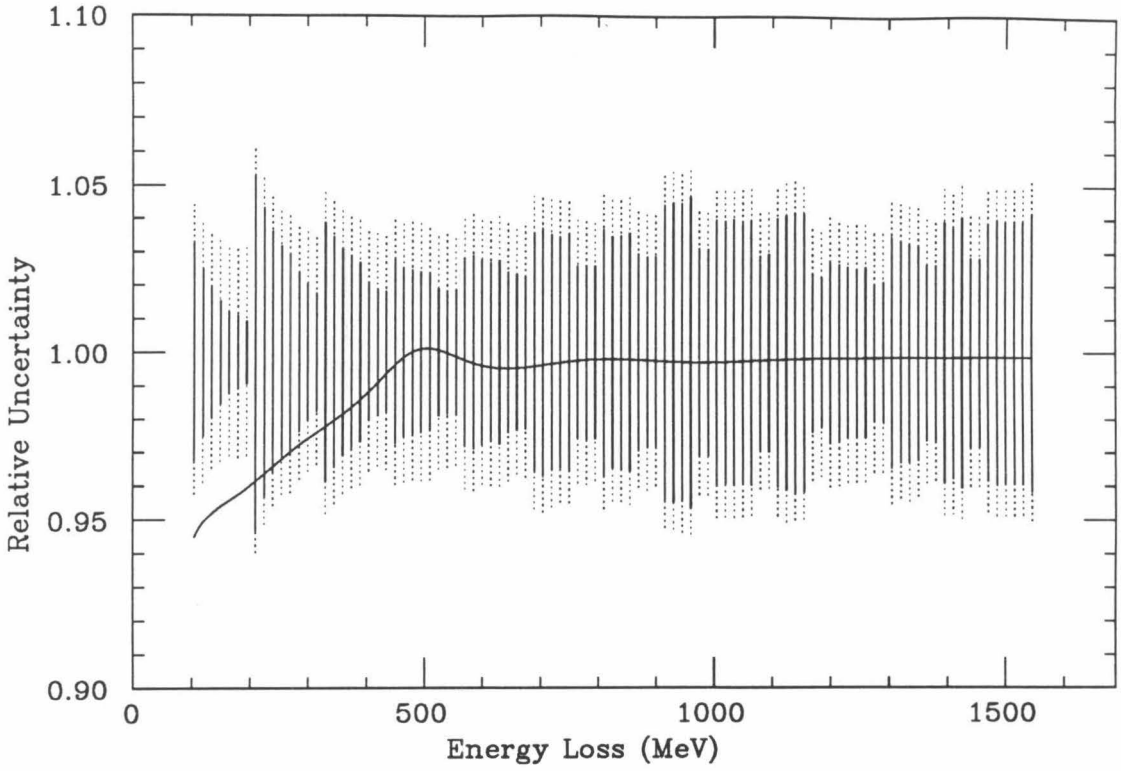

Figure 4.2 – Relative error bars for the 3.6 GeV, 16 deg. data taken with the carbon target. The solid error bars are statistical only; the dashed extensions were obtained by adding to them 3% errors in quadrature. The solid curve is the ratio $\tilde{\sigma}/\sigma_{\mathrm{obs}}$ discussed in the text.

4.3.1 Theoretical Peak Locations

The incident energy (E_1), scattered energy (E_2), and scattering angle (θ) of elastic scattering are related through the familiar equation:

$$\frac{1}{E_2} = \frac{1}{E_1} + \frac{2}{M_{\mathrm{tgt}}} \sin^2(\theta/2), \tag{4.15}$$

in which M_{tgt} is the mass of the target nucleus. Because of energy loss in the target, we have the relationship:

$$\begin{aligned} E_1 &= E_1^{\mathrm{AB}} - \epsilon_1 \\ E_2 &= E_2^{\mathrm{SP}} + \epsilon_2, \end{aligned} \tag{4.16}$$

in which $E_1^{\rm AB}$ and $E_2^{\rm SP}$ are the true A-bend and spectrometer energies respectively, and ϵ_1 and ϵ_2 are the most probable energy losses before and after the scattering. Let $E_{\rm meas}^{\rm AB}$ and $E_{\rm meas}^{\rm SP}$ be the measured A-bend and spectrometer energies. A linear relationship between the true and measured energies was assumed:

$$E_{\rm true}^{\rm AB} = C_1 \cdot E_{\rm meas}^{\rm AB} \qquad \text{and} \qquad E_{\rm true}^{\rm SP} = C_2 \cdot E_{\rm meas}^{\rm SP} + E_2^{\rm off}. \tag{4.17}$$

Thus, the expected elastic peak location ($E_2^{\rm exp}$) is given by:

$$\frac{1}{C_2 \cdot E_2^{\rm exp} + E_2^{\rm off} + \epsilon_2} = \frac{1}{C_1 \cdot E_{\rm meas}^{\rm AB} - \epsilon_1} + \frac{2}{M_{\rm tgt}} \sin^2\left(\frac{\theta + \theta_{\rm off}}{2}\right), \tag{4.18}$$

in which $\theta_{\rm off}$ is an offset to the spectrometer angle.

4.3.2 Energy Loss

The most probable energy loss ($\epsilon_{\rm mp}$) for an ultrarelativistic electron traversing x cm of material of atomic number Z, atomic weight M_A, and density ρ, is given by [50]:

$$\epsilon_{\rm mp} = \frac{2\pi\alpha^2(\hbar c)^2 A_0}{mc^2}\left(\frac{Z}{M_A}\right) \cdot \rho x \cdot \left[\ln\left(\frac{\alpha mc^2}{\hbar c}\, x\right) + 0.37\right]. \tag{4.19}$$

To compute ϵ_1 and ϵ_2 for the hydrogen and helium targets at the various scattering angles, we assumed that the elastic scatter took place in the center of the target. Thus, ϵ_1 is the same for all angles: 1.73 MeV for hydrogen, and 1.23 MeV for helium. Because the postscattering path length through the target varied with angle, ϵ_2 also varied with angle. These numbers are listed below in Table 4.2.

Run	Tgt	$E^{\mathrm{AB}}_{\mathrm{meas}}$	$\tilde{\theta}$	$E^{\mathrm{SP}}_{\mathrm{meas}}$	ε_1	ε_2
10602	H	2.0202	15.022	1.8771 ± 0.001	0.0017	0.0017
11303	H	2.0200	20.016	1.7807 ± 0.001	0.0017	0.0017
11408	H	2.0200	20.016	1.7819 ± 0.001	0.0017	0.0017
11410	H	2.0200	20.016	1.7825 ± 0.001	0.0017	0.0017
13702	H	3.5946	16.020	3.1219 ± 0.001	0.0017	0.0017
13710	H	3.5942	16.020	3.1212 ± 0.001	0.0017	0.0017
14501	H	3.5946	16.020	2.9123 ± 0.001	0.0017	0.0017
16001	H	3.5945	25.012	2.6396 ± 0.001	0.0017	0.0014
19285	H	3.5945	30.013	2.3701 ± 0.001	0.0017	0.0012
19344	H	3.6056	30.011	2.3743 ± 0.001	0.0017	0.0012
19369	H	3.6040	39.008	1.9365 ± 0.001	0.0017	0.0009
19402	H	3.5962	39.007	1.9354 ± 0.001	0.0017	0.0009
10802	He	2.0203	15.022	1.9802 ± 0.0015	0.0012	0.0010
12001	He	2.0200	20.016	1.9529 ± 0.0015	0.0012	0.0007
14101	He	3.5943	16.020	3.4560 ± 0.0025	0.0012	0.0009

Table 4.2 – Observed elastic peak postions and the most probable energy losses. All energies are in GeV, and angles in degrees.

4.3.3 Hydrogen Elastic Peak Location

The Hydrogen elastic peak locations were determined from the $\Delta P/P_0$ vs. $\Delta\theta$ scattering-rate histograms, after the dummy-target subtraction. Because both the peak position and the cross section are functions of the scattering angle, the observed peak in the projection onto the $\Delta P/P_0$ axis is shifted from the true peak at $\Delta\theta = 0$. To eliminate this effect, the peak in $\Delta P/P_0$ was located for each $\Delta\theta$ bin index, and these values were fit to a linear function of $\Delta\theta$ and extrapolated to $\Delta\theta = 0$. For each $\Delta\theta$ index, the peak was taken to be the centroid of a contiguous group of bins surrounding and including the bin with the most counts. Each bin in the group was required to have at least 70% of the counts in the biggest bin. The uncertainty in the final peak position was estimated (by eye) to be 1 MeV. Table 4.2 lists the observed peak positions and other kinematic information for both the hydrogen and helium data (discussed below).

4.3.4 ^{4}He Elastic Peak Location

The ^{4}He elastic peaks could be discerned in the dummy-subtracted, scattering-rate histograms at the three lowest q^2's when projected onto the $\Delta P/P_0$ axis. These peaks are shown in Figure 4.3. Because of the poor statistics, the unprojected histograms could not be fit for the peak positions as was done for hydrogen. Instead, the peak positions were extracted from the projected spectra, and were taken to be the centroid of the bins with at least 70% of the maximum counts, as above. Larger uncertainties were assigned to these peaks because of the poorer statistics.

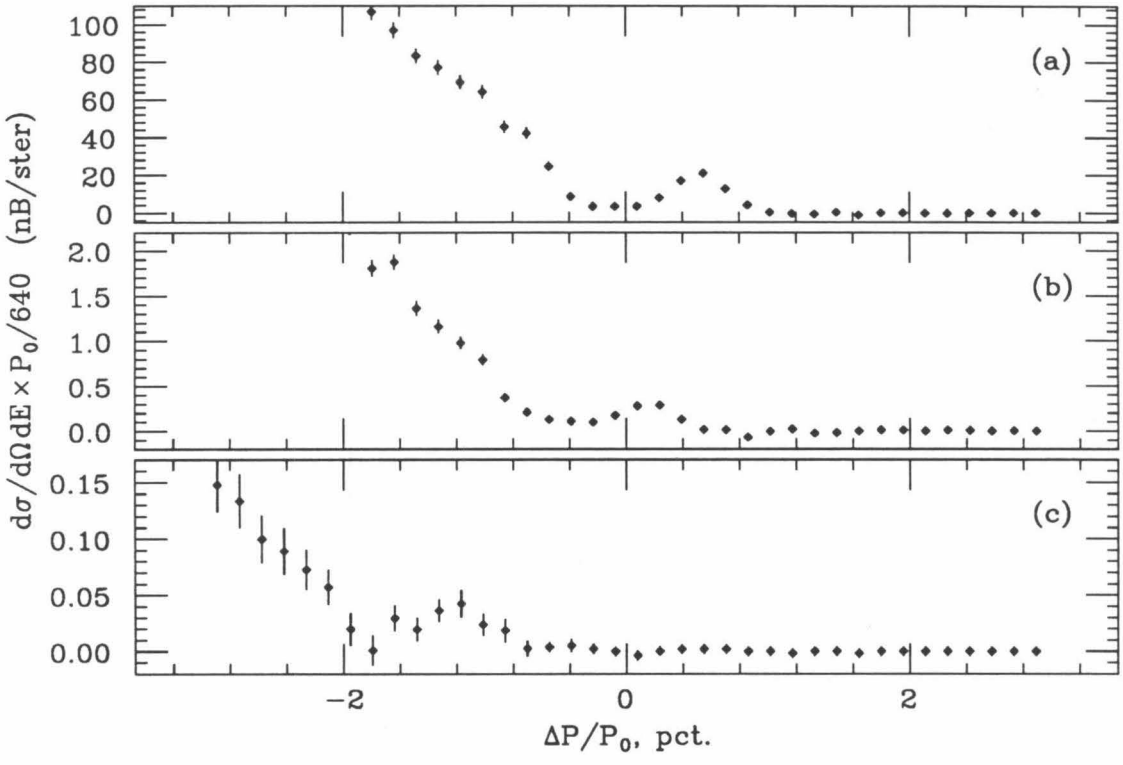

Figure 4.3 – Elastic peaks in the ^{4}He $\Delta P/P_0$ scattering rate histogram: (a) $E_0 = 2.02$ GeV, $\theta_0 = 15$ deg, $P_0 = 1.97$ GeV; (b) $E_0 = 2.02$ GeV, $\theta_0 = 20$ deg, $P_0 = 1.95$ GeV; (c) $E_0 = 3.60$ GeV, $\theta_0 = 16$ deg, $P_0 = 3.51$ GeV.

4.3.5 Fitting Procedure

A non-linear fitting procedure was used to vary the four parameters, C_1, C_2, E_2^{off}, and θ_{off} in order to minimize the χ^2 given by:

$$\chi^2 = \sum \left[\frac{E_2^{\text{peak}} - E_2^{\text{exp}}}{\delta E_2^{\text{peak}}} \right]^2 . \tag{4.20}$$

Three kinds of fits were considered: one with all parameters free, one with θ_{off} fixed at zero, and another with θ_{off} and E_2^{off} both fixed at zero. These fits were applied to three data sets: the original one described above, one in which the ΔE_2^{peak} uncertainties were scaled by $E_2^{\text{peak}}/3.4560$, and one with the same scaled uncertainties in which the data point with the worst χ^2 was thrown out. The fit results are listed in Table 4.3, and the values of C_1 vs. C_2 are plotted in Figure 4.4. Also shown in the figure is the contour for which the χ^2 of fit 1 is increased by 1 over the minimum; this gives the standard uncertainty in the fit parameters.

Fit	C_1	C_2	E_2^{off}	θ_{off}	χ^2/DF
1	1.000328	1.001571	N/A	N/A	0.615
2	1.000356	1.001690	−0.233 MeV	N/A	0.663
3	1.000487	1.001878	−0.305 MeV	−.003 deg	0.724
4	1.000665	1.001832	N/A	N/A	1.712
5	1.000668	1.001696	0.304 MeV	N/A	1.844
6	0.998961	0.999181	1.295 MeV	0.045 deg	1.911
7	1.001036	1.002049	N/A	N/A	0.964
8	1.001059	1.002384	−0.710 MeV	N/A	0.998
9	1.000634	1.001756	−0.448 MeV	0.011 deg	1.092

Table 4.3 – Energy-calibration fit parameters: fits (1-3) use original error bars, (4-6) use modified error bars, (7-9) use the same modified error bars with the worst χ^2 point thrown out. "N/A" indicates parameters not used in the fit.

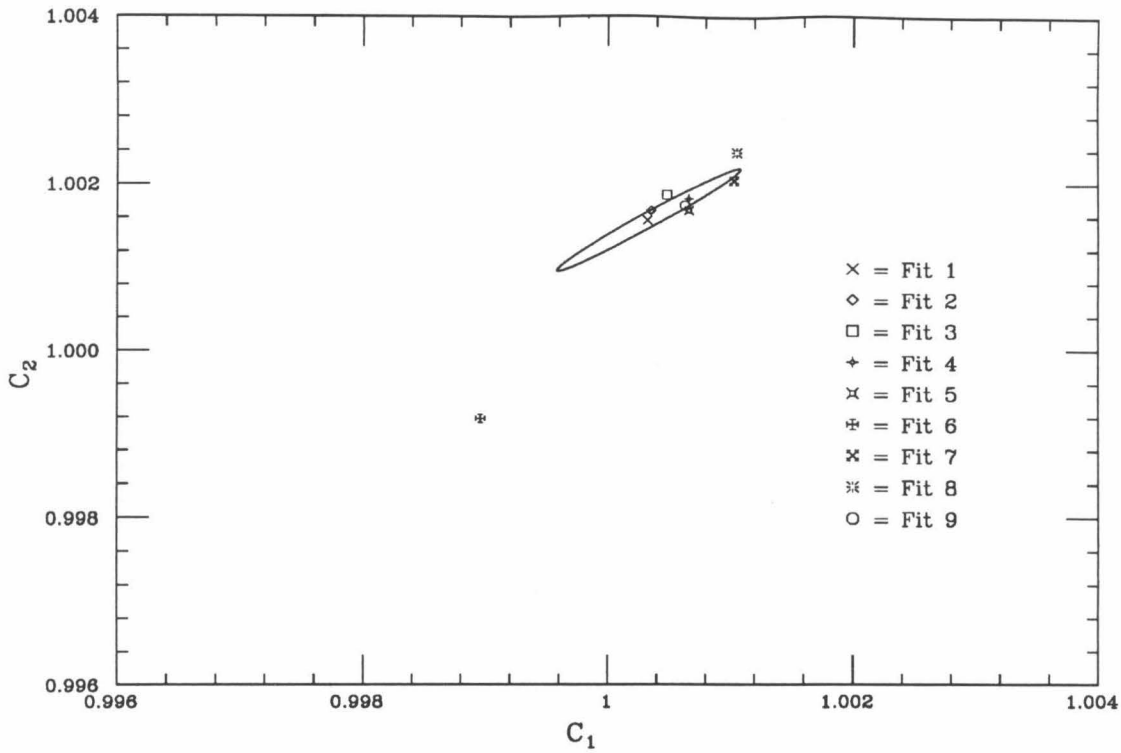

Figure 4.4 – C_1 vs. C_2 for the nine different fits. The solid line is the $\chi^2 = \chi^2_{\text{min}} + 1$ contour for fit 1.

It can easily be seen that the point $C_1 = C_2 = 1$ is excluded by all the fits. The uncertainties in C_1 and C_2 are highly correlated, but in such a way that the uncertainty in the energy loss is small. For example, if we consider a test case with $E^{\text{AB}}_{\text{meas}} = 3.595$ GeV, and $E^{\text{meas}}_2 = 3.450$ GeV, we find that the true energy loss calculated with the different fits (excluding fit 6) varies only between 141.7 MeV and 140.6 MeV. This is negligible compared with the bin width of 15 MeV. With no evidence of any significant offset in either the spectrometer angle or energy, the results of fit 1 were used to correct the incident and scattered energies in the analysis of Pass-2.

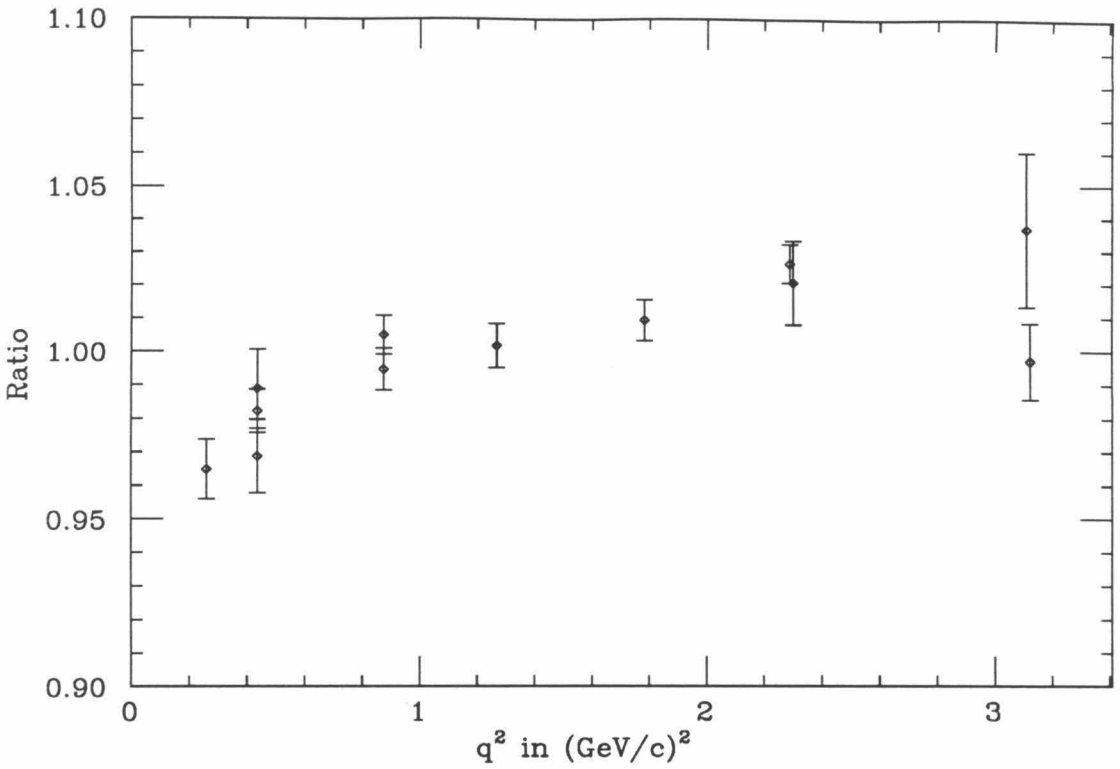

Figure 4.5 – Radiatively corrected (e,p) elastic cross sections (including the normalization correction) divided by the theoretical value, vs. q^2.

4.4 Absolute Normalization of Cross Sections

The radiatively corrected (e,p) elastic cross sections we measured with the hydrogen target were compared with a fit by Simon, *et al.* [3] to the world's data as a check on our analysis procedure. Our measured values were typically lower than the world's data, with a weighted average ratio $\sigma_{\text{meas}}/\sigma_{\text{world}}$ of 0.985. To bring our data into agreement, we applied a correction factor of 1.015 to the cross sections of every target during the Pass-2 analysis. The resulting elastic cross sections, divided by Simon's fit are shown in Figure 4.5, plotted vs. q^2. (The error bars shown are statistical only.) A mild q^2 dependence to these ratios can be seen, although it does not correlate well with either the spectrometer energy or angle. To accommodate this,

we assigned an uncertainty of 1.5% to this correction. When all sources of systematic and statistical uncertainty are included, the elastic cross sections are consistent with the world data.

4.5 ^{4}He Density Correction

As mentioned in Chapter 2, the effective density of the ^{4}He target was observed to deviate from the nominal density because of heating by the incident electron beam. We investigated this effect by taking a series of runs at the same kinematics with various beam pulse rates, from 10 Hz to 180 Hz, under stable operating conditions. For each run, we computed the deadtime-corrected electron scaler rate per peta-electron of incident beam. This rate is proportional to the effective target density, which is assumed to be equal to the nominal density in the limit of zero beam current. We observed variations in the density of as much as 18% at the highest power level, as shown in Figure 4.6.

These test runs were taken under stable conditions, whereas the beam current could and did change during ordinary running conditions. To compute a cross section, we needed to know the average density, with the average taken with equal weight for each incident electron:

$$\langle \rho \rangle = \frac{1}{Q} \int_0^T \rho(t)\, I(t)\, dt; \qquad Q = \int_0^T I(t)\, dt. \tag{4.21}$$

Presupposing the linear relationship $\rho(t) = \rho_0 \left(1 - A \cdot I(t)\right)$ between ρ and I, Eq. (4.21) becomes:

$$\begin{aligned} \langle \rho \rangle &= \rho_0 \left(1 - \frac{A}{Q} \int_0^T I^2(t)\, dt\right) \\ &= \rho_0 \left(1 - A\langle I \rangle\right), \end{aligned} \tag{4.22}$$

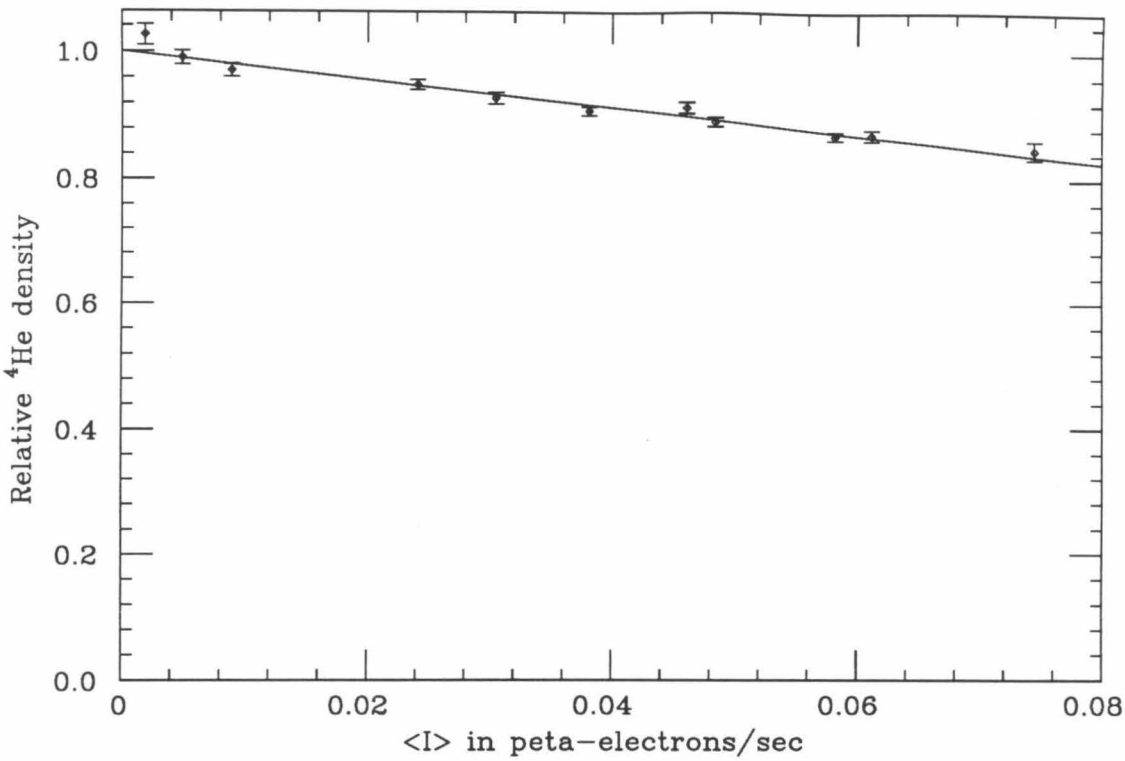

Figure 4.6 – ^{4}He density divided by the nominal density, as a function of the (beam-weighted) average beam current. The straight line is a least-squares fit to the data ($\chi^2/DF = 1.13$).

in which $\langle I \rangle$ is the beam-weighted average beam current. (This is actually what we plot as the abscissae in Figure 4.6.) To compute such beam-weighted averages, the data acquisition system logged toroid data to the logtapes at intervals of $\sim$ 15 sec. This allowed us to replace the integral in Eq. (4.22) with a discrete sum, using a very fine time step.

As can be seen from the test runs, the assumed linear relationship between $<\rho>$ and $<I>$ is substantiated. The solid straight line is a linear least-squares fit to the data, with slope $A = 2.16 \pm 0.15$ sec/PE. Therefore, we used this value, in conjunction with $\langle I \rangle$ calculated for each run, to correct the target density in all the

^{4}He runs. At the highest beam power levels, the uncertainty in the correction leads to an uncertainty of 1.3% in the density.

4.6 Systematic Uncertainties

Here we summarize the systematic uncertainties, which are mentioned elsewhere in this paper. There were six sources of uncertainty, shown below in Table 4.4: target thicknesses, the acceptance function, efficiency corrections, the toroid calibration, radiative corrections, and the finite binning correction. These were added together in quadrature to produce the total systematic uncertainty.

	^{4}He	C	Al	Fe(2% rl)	Fe(6% rl)	Au
Target thickness	1.3	0.1	0.4	1.4	0.7	2.2
Acceptance function	2.0	2.0	2.0	2.0	2.0	2.0
Efficiency	1.5	1.5	1.5	1.5	1.5	1.5
Toroid calibration	0.5	0.5	0.5	0.5	0.5	0.5
Radiative correction	2.0	2.0	2.0	2.0	2.0	2.0
Finite bin correction	1.0	1.0	1.0	1.0	1.0	1.0
Total	3.6	3.4	3.4	3.7	3.5	4.0

Table 4.4 – Systematic uncertainties for each target, in pct. The total uncertainty is the sum in quadrature of the numbers in each column.

The target thicknesses in g/cm^2 were not precisely known because of uncertainty in the target lengths (all targets), and target densities (^{4}He and C targets). The target dimensions were independently measured four times, and the standard deviations were used for the uncertainties. In the case of the C target, the density was determined from its dimensions and its measured weight, with the standard deviation of the several weighings added in quadrature to the dimensional uncertainties. For ^{4}He, the density was determined from its nominal pressure and temperature, with a correction

for the (beam-weighted) average beam current. Uncertainty in the density correction is the dominant uncertainty in target thickness for ^{4}He.

The Monte-Carlo-generated, acceptance function was checked by fitting some of the deep-inelastic cross sections to a polynomial, and looking for systematic deviations from the fit that correlated with $\Delta P/P_0$. The observed deviations were less than 2%, which we take as the systematic uncertainty in the acceptance function.

A correction was made to all cross sections in order to make the hydrogen elastic cross sections agree with the world average. This correction may reflect a normalization problem with the acceptance function, or we may have overestimated our efficiency. This correction was made by setting the product of the trigger, CK-cut, and SHSOFT-cut efficiencies numerically equal to 0.985, with an uncertainty of 1.5%, which is equal to the size of the correction.

The four toroidal charge monitors were independently calibrated at periodic intervals during the experiment, to a typical accuracy of 0.5%. The data analysis averaged the toroid values, requiring that the standard deviation be within 0.5%. Thus, we take 0.5% to be the systematic uncertainty in the beam-current integration.

Uncertainties in the radiative corrections were investigated by comparing the corrected data for iron targets of two thicknesses, and by checking the numerical sensitivity to the form of requisite model cross sections. The observed deviations were compatible with systematic errors of up to 2%. Accordingly, we assign an uncertainty of 2% to the radiative corrections.

Finite-binning corrections were calculated from the model cross sections used in the radiative corrections. The multiplicative corrections range between 0.95 (at the small energy loss limits) to 1.00, and show a sensitivity to the model parameters of up to $\sim$ 1% (for the corrections near 0.95). Although the model sensitivity varies

with the kinematics, we conservatively assign a systematic uncertainty of 1% to all the cross sections.

Chapter 5
Theoretical Considerations

5.1 Overview

In this chapter, the y-scaling formalism will be developed within the context of the plane wave impulse approximation (PWIA). Several different definitions of the scaling function, $F(y)$, exist in the literature. The approach taken here closely follows the approach of Pace and Salmè [9], yielding a scaling function simply defined in terms of the spectral function. This will be compared with an alternative approach, which exhibits better scaling, but has a less transparent interpretation.

5.2 Quasi-elastic Cross Section

The inclusive quasi-elastic cross section will be obtained by integrating the exclusive cross section over the unobserved nucleon's phase space. Under PWIA, the exclusive cross section is an incoherent sum over the individual nucleons:

$$\frac{d^5\sigma}{d\varepsilon\, d\Omega\, d^3\vec{P}'} = \sum_{\text{nucleons}} \sigma_{eN} \cdot S'_N(E, \vec{P}), \tag{5.1}$$

in which ε is the scattered electron's energy, E, $\vec{P}$ are the energy and momentum of the initial state nucleon, and E', $\vec{P}'$ are the energy and momentum of the final state nucleon. σ_{eN} is the fully relativistic, elementary cross section for elastic scattering from a moving, off-shell nucleon [51], and S'_N is the spectral function, which is the probability density for finding a nucleon with energy E and momentum $\vec{P}$.

With unpolarized beams and targets, we may take S'_N to be spherically symmetric, with normalization:

$$4\pi \int_0^\infty dE \int_0^\infty P^2 \, S'_N(E,P) \, dP = 1. \tag{5.2}$$

In addition, we will make the approximation that neutrons and protons have the same spectral function. Thus, the inclusive cross section is given by:

$$\frac{d^2\sigma}{d\Omega \, d\varepsilon} = \int (z\sigma_{ep} + n\sigma_{en}) \cdot S'(E,\vec{P}) \, d^3\vec{P}'. \tag{5.3}$$

We now define the following kinematic variables:

$$\begin{aligned}
\varepsilon_1 &= \text{incident electron energy} \\
\varepsilon_2 \equiv \varepsilon &= \text{scattered electron energy} \\
\theta &= \text{electron scattering angle} \\
q^\mu \equiv (\omega, \vec{Q}) &= \text{4-momentum transfer} \\
\psi &= \text{angle between } \vec{P} \text{ and } \vec{Q} \\
\varphi &= \text{angle between the } (\vec{P}, \vec{Q}) \text{ plane and} \\
&\quad \text{the electron scattering plane.}
\end{aligned} \tag{5.4}$$

Since $\vec{P}' = \vec{P} + \vec{Q}$, with $\vec{Q}$ fixed, then $d^3\vec{P}' = d^3\vec{P}$. Using spherical coordinates (ψ, φ), we have:

$$\begin{aligned}
\frac{d^2\sigma}{d\Omega \, d\varepsilon} &= \int (z\sigma_{ep} + n\sigma_{en}) \cdot S'(E,P) \cdot P^2 \, dP \, d\varphi \, d(\cos\psi) \\
&= 2\pi \int \tilde{\sigma}_0 \cdot S'(E,P) \cdot P^2 \, dP \, d(\cos\psi),
\end{aligned} \tag{5.5}$$

in which we have defined:

$$\tilde{\sigma}_0 = \frac{1}{2\pi} \int_0^{2\pi} (z\sigma_{ep} + n\sigma_{en}) \, d\varphi. \tag{5.6}$$

In general, for a given q^μ, $\tilde{\sigma_0}$ will be a function of P and $\cos\psi$.

For the nucleonic system, we define:

$$\begin{aligned} m_1 &= \text{invariant mass of target nucleus} \\ m_2 &= \text{invariant mass of A-1 recoil fragment} \\ m &= \text{nucleon mass} \\ E' &= \text{energy of the recoil nucleon} \\ E_s \equiv m_2 - m_1 + m &= \text{separation energy.} \end{aligned} \tag{5.7}$$

The final state particles must be on mass-shell, and we must conserve energy and momentum. These constraints yield:

$$(m_1 - E)^2 = (m_1 - m + E_s)^2 + P^2 \tag{5.8}$$

$$m_1 + \omega = (m^2 + (\vec{P} + \vec{Q})^2)^{1/2} + (m_2{}^2 + P^2)^{1/2}. \tag{5.9}$$

For fixed values of P, $\cos\psi$, and q^μ, these equations determine a unique value for E_s and E. Thus, Eq. (5.5) can be rewritten as:

$$\frac{d^2\sigma}{d\Omega\, d\varepsilon} = 2\pi \int \tilde{\sigma_0} \cdot S'(E,P) \cdot \delta(\text{Arg}) \cdot P^2\, dP\, d(\cos\psi)\, dE, \tag{5.10}$$

in which the argument of the delta function is:

$$\text{Arg} = E + \omega - (m^2 + P^2 + Q^2 + 2PQ\cos\psi)^{1/2}. \tag{5.11}$$

We now use the delta function to perform the $\cos\psi$ integration, which yields:

$$\frac{d^2\sigma}{d\Omega\, d\varepsilon} = 2\pi \int \tilde{\sigma_0} \cdot \frac{E'}{PQ} \cdot S'(E,P)\, P^2\, dP\, dE. \tag{5.12}$$

It is more convenient to work with a spectral function defined in terms of E_s; under this change of variables we have:

$$S'(E,P)\,dE = -S(E_s,P)\,dE_s, \tag{5.13}$$

in which the Jacobian has been absorbed into the definition of S. We now define $\tilde{\sigma} = \tilde{\sigma_0} \cdot (E'/Q)$ to obtain:

$$\frac{d^2\sigma}{d\Omega\, d\varepsilon} = 2\pi \int_{E_s^{\min}}^{E_s^{\max}} \int_{P_{\min}(E_s)}^{P_{\max}(E_s)} \tilde{\sigma} \cdot S(E_s,P) \cdot P\, dP\, dE_s. \tag{5.14}$$

The P integration limits are given by $P_{\min} = |y_1|$, and $P_{\max} = |y_2|$, in which y_1 and y_2 are the solutions of:

$$m_1 + \omega = (m^2 + Q^2 + y^2 + 2Qy)^{1/2} + (m_2{}^2 + y^2)^{1/2}. \tag{5.15}$$

$E_s^{\min}$ is determined by putting the A-1 fragment into its ground state, while the limit $E_s^{\max}$ (for which $P_{\min} = P_{\max}$) occurs when the final state nucleon is at rest:

$$E_s^{\max} = \left[(m_1+\omega)^2 - Q^2\right]^{1/2} - m_1. \tag{5.16}$$

As discussed below, $\tilde{\sigma}$ is an extremely slow function of P and E_s. Furthermore, $S(E_s,P)$ is expected to be sharply peaked about $E_s = E_s^0$ and $P = 0$ [52]. Thus, we can ignore the variation of $\tilde{\sigma}$ over the range of integration. Defining $\bar{\sigma} = \tilde{\sigma}(E_s^0, P_{\min})$, we have:

$$\frac{d^2\sigma}{d\Omega\, d\varepsilon} = \bar{\sigma} \cdot 2\pi \int_{E_s^{\min}}^{E_s^{\max}} \int_{P_{\min}(E_s)}^{P_{\max}(E_s)} S(E_s,P) \cdot P\, dP\, dE_s. \tag{5.17}$$

5.3 Scaling Limit

It is instructive to see how the integration limits behave as the momentum transfer is varied. Figure 5.1 shows the ^{12}C integration boundaries in the (E_s, P) plane for each of the incident energies and scattering angles that we took data. Values were chosen for ε_2, so that each curve passes through the point $y_1 = -0.25$ GeV, $E_s = 0.03$ GeV. As the momentum transfer increases, the integration region also expands. Because of the localized nature of the spectral function, the limits $E_s^{\max}$ and $P_{\max}$ effectively become ∞. $P_{\min}$ approaches a shallow, linear function of E_s.

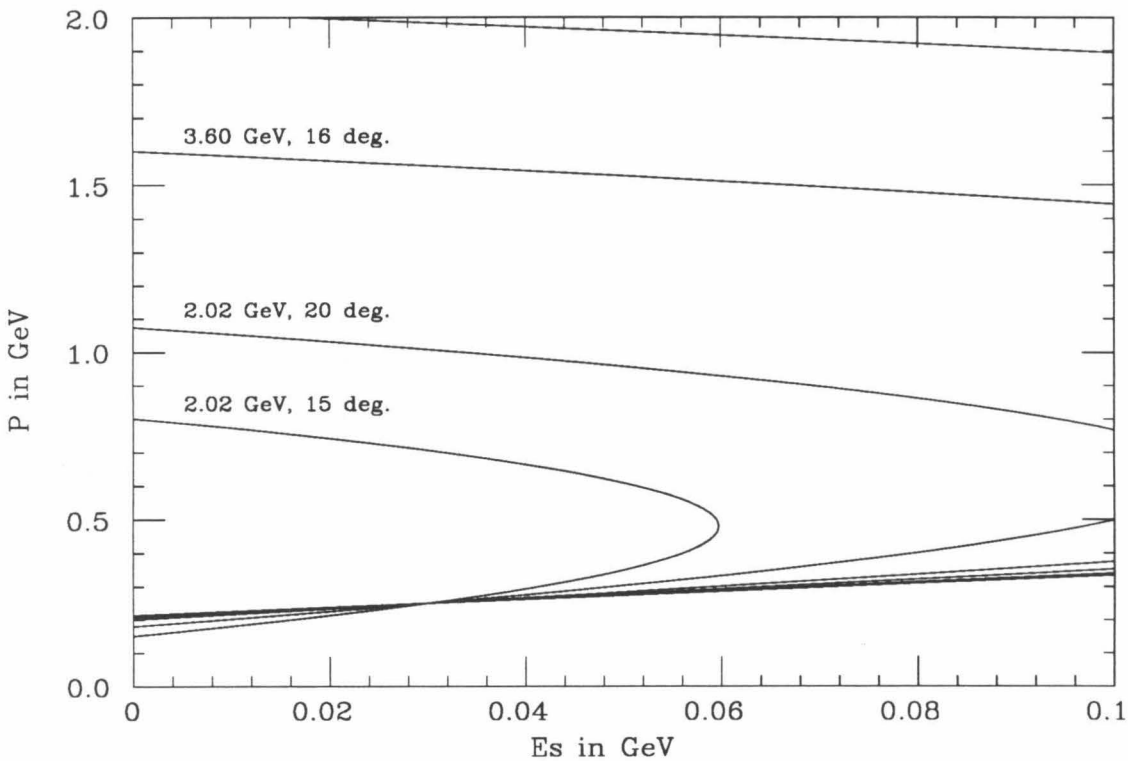

Figure 5.1 – The integration regions of Eq. (5.17) for a ^{12}C target and the incident and scattered energies and scattering angles discussed in the text.

Again, because the spectral function is sharply peaked about $E_s = E_s^0$, we will make the further approximation that $P_{\min} \approx |y_1(E_s = E_s^0)| \equiv |y|$ to yield:

$$\frac{d^2\sigma}{d\Omega\, d\varepsilon} = \bar{\sigma} \cdot F(y), \tag{5.18}$$

in which the scaling function $F(y)$ is given by:

$$F(y) \;=\; 2\pi \int_{E_s^{\min}}^{\infty} \int_{|y|}^{\infty} S(E_s, P) \cdot P\, dP\, dE_s. \tag{5.19}$$

Since the nucleon momentum distribution is given by:

$$n(P) = \int_{E_s^{\min}}^{\infty} S(E_s, P)\, dE_s, \tag{5.20}$$

we can write $F(y)$ in terms of $n(P)$:

$$F(y) = 2\pi \int_{|y|}^{\infty} n(P)\, P\, dP. \tag{5.21}$$

Differentiating with respect to y yields:

$$n(P) = \frac{-1}{2\pi P} \cdot \frac{dF(P)}{dP}. \tag{5.22}$$

The normalization of $S(E_s, P)$ implies:

$$1 = 4\pi \int_0^{\infty} n(P)\, P^2\, dP = -2 \int_0^{\infty} P \frac{d}{dP} F(P)\, dP. \tag{5.23}$$

Integrating by parts, we have:

$$1 \;\;=\;\; 2 \int_0^{\infty} F(P)\, dP \;-\; [2PF]_0^{\infty}\,, \tag{5.24}$$

in which the term in brackets vanishes for a reasonably well behaved scaling function.

5.4 Off-shell Elementary Cross Sections

Unfortunately, the relationship between the off-shell and on-shell form factors and operators is an open question, and leads to an ambiguity in calculating $\bar{\sigma}$. An excellent discussion of the problem is given by De Forest [51], and we use his formula (called σ_1^{cc}) for σ_{eN}, with form factors determined by the four-momentum transfer, $q^2 \equiv -q_\mu q^\mu = Q^2 - \omega^2$:

$$\sigma_{eN} = \frac{\sigma_m}{\bar{E}E'}\left\{\left(\frac{\bar{q}^2}{2}\tan^2\theta/2 + \frac{q^2}{4Q^2}(\bar{q}^2 - q^2)\right)(F_1 + F_2)^2 \right. \\ + \left[\left(\frac{\bar{E}+E'}{2}\frac{q^2}{Q^2} + \left(\frac{q^2}{Q^2} + \tan^2\theta/2\right)^{1/2}(\vec{P}' \times \hat{Q})\cdot\hat{n}\right)^2 \right. \\ \left.\left. + \tan^2\theta/2(\vec{P}'\cdot\hat{n})^2\right]\left({F_1}^2 + \frac{\bar{q}^2}{4m^2}{F_2}^2\right)\right\}, \quad (5.25)$$

where $\bar{E} = ((\vec{P}' - \vec{Q})^2 + m^2)^{1/2}$, $\bar{q}^2 = Q^2 - (E' - \bar{E})^2$, $\hat{n} = \vec{\varepsilon}_1 \times \vec{\varepsilon}_2/|\vec{\varepsilon}_1 \times \vec{\varepsilon}_2|$ is the normal to the electron-scattering plane, and the Mott cross section is given by:

$$\sigma_m = \frac{\alpha^2(\hbar c)^2\cos^2\theta/2}{4{\varepsilon_1}^2\sin^4\theta/2}. \quad (5.26)$$

F_1 and F_2 are related to the electric and magnetic form factors through:

$$F_1^{p(n)} = (G_e^{p(n)} + \tau G_m^{p(n)})/(1+\tau) \\ F_2^{p(n)} = (G_m^{p(n)} - G_e^{p(n)})/(1+\tau) \quad (5.27) \\ \tau = \frac{q^2}{4m^2}.$$

This leads to the expression $\tilde{\sigma} = Z\cdot\tilde{\sigma}_p + N\cdot\tilde{\sigma}_n$ with:

$$\tilde{\sigma}_{p(n)} = \frac{\sigma_m}{\bar{E}Q}\left\{\left(\frac{\bar{q}^2}{2}\tan^2\theta/2 + \frac{q^2}{4Q^2}(\bar{q}^2 - q^2)\right)(F_1 + F_2)^2 \right. \\ + \left[\left(\frac{q^2}{Q^2} + \tan^2\theta/2\right)P^2\sin^2\psi \right. \\ \left.\left. + \frac{1}{4}\frac{q^4}{Q^4}(\bar{E}+E')^2\right]\left({F_1}^2 + \frac{\bar{q}^2}{4m^2}{F_2}^2\right)\right\}. \quad (5.28)$$

Although not immediately apparent, this expression for $\tilde{\sigma}$ is only mildly dependent on P and E_s for the kinematics at which we took data. This is illustrated in Figure 5.2, in which is plotted level contours of the ratio $\tilde{\sigma}/\tilde{\sigma}_{\max}$ for an incident energy of 3.6 GeV, $\theta = 16$ degrees, and $\omega = 0.5$ GeV, with a carbon target. For a given value of E_s, the average of $\tilde{\sigma}$, weighted by a phenomenological momentum distribution, was found to deviate from the value at $P_{\min}$ by less than 3%. (The momentum distribution was obtained from a fit to the carbon data $F(y)$ by using Eq. 5.22.) Similar results were obtained at different kinematics, so that the error involved in factoring out $\bar{\sigma}$ in Eq. (5.17) is a few percent.

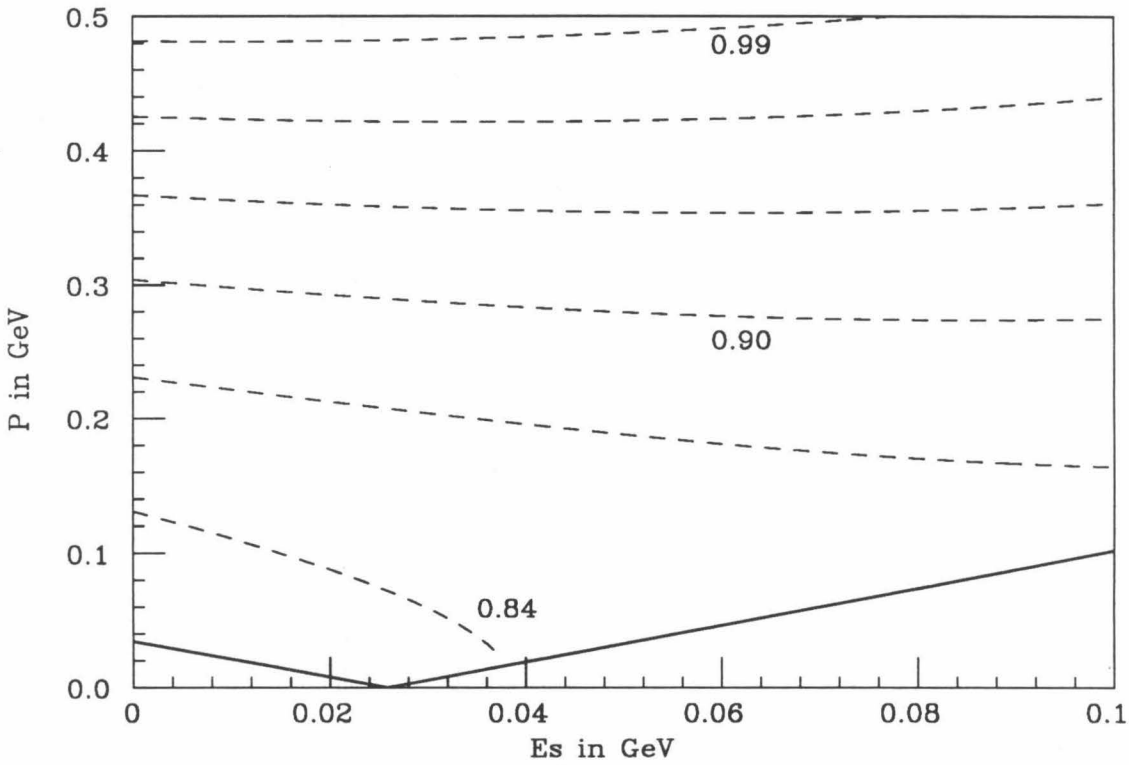

Figure 5.2 – Contours of the ratio $\tilde{\sigma}/\tilde{\sigma}_{\max}$ for the conditions discussed in the text. The contour interval is 0.03. $P_{\min}(E_s)$ is shown as a bold line.

5.5 Experimental Scaling Functions

To derive scaling functions from our measured cross sections, we have solved Eq. (5.18) for $F(y)$:

$$F(y) = \frac{d^2\sigma}{d\Omega\, d\varepsilon} \cdot \bar{\sigma}^{-1}. \tag{5.29}$$

The values of E_s^0 we used to compute y and $\bar{\sigma}$ are listed in Table 5.1 [53]. These values are basically an interpolation of those in Ref. 27, increased by $\sim$ 5 MeV to compensate for a neglect of the relativistic recoil of the nucleon, as pointed out in Ref. 55.

Nucleus	E_s^0 in MeV
^{3}He	8
^{4}He	20
C	30
Al	37
Fe	41
Au	49

Table 5.1 – Values of E_s^0 that were used to compute y and $\bar{\sigma}$ in the extraction of the experimental $F(y)$'s.

The resulting experimental scaling functions are expected to converge to the true $F(y)$ as the momentum transfer is increased. This is true even when final state interactions are considered, although the approach to convergence is considerably altered. In the simple I.A. model, the experimental scaling functions are expected to converge from below, because the integrals in Eq. (5.17) see more of the spectral function as q^2 is increased. From Figure 5.1, we might expect to have reached the scaling limit for $q^2 \sim 0.4$ GeV (the second most restrictive contour). Calculations of FSI, however, show that the approach to scaling should be from above, with convergence at

$q^2 \sim 2.0$ GeV [30]. As we shall see, the data do approach a scaling limit from above, in rough agreement with the FSI calculations.

5.6 Other Scaling Functions

An alternate y-scaling formalism was considered in the original analysis of ^{3}He data by Sick, *et al.* [8] Their method has also been applied to the NE3 data [54], resulting in scaling functions that scale better than the present analysis. In their formalism, the scaling function is defined through:

$$F_2(y') = \frac{d^2\sigma}{d\Omega\, d\varepsilon} \cdot \frac{1}{Z \cdot \sigma_{ep} + N \cdot \sigma_{en}} \frac{\partial \omega}{\partial y_2}. \tag{5.30}$$

The scaling variable, y', and the derivative $\partial\omega/\partial y'$ are obtained from the relationship:

$$\omega = (m^2 + Q^2 + 2Qy' + y'^2 + P_\perp{}^2)^{1/2} + (y'^2 + ((A-1)m)^2)^{1/2} - Am + E_s, \tag{5.31}$$

in which $P_\perp = \sqrt{0.4}$ times the Fermi momentum. For the kinematics of our data, the difference between y' and the y of Eq. (5.15) is negligible.

The significant difference between their method and the one presented here is the factor of $\partial\omega/\partial y'$. This factor is similar to the $|\partial\omega/P\partial\cos\psi|$ that occurs in our integration over the delta function in Eq. (5.10). In their analysis, the argument of the delta function is obtained from Eq. (5.31), ignoring the relationship between P, $\cos\psi$, and E correctly given by Eq. (5.11). As a result, their scaling functions are related to those of our analysis through:

$$R \equiv \frac{F_2}{F} = \frac{|\partial\omega/\partial y|}{|\partial\omega/P\partial\cos\psi|}, \tag{5.32}$$

which is a function of both q^2 and y. Thus, the two scaling functions will exhibit different approaches to the infinite q^2 scaling limit. The effect of using F_2 is to compensate somewhat for the final state interactions, although this is entirely accidental. Thus, although it scales better, the use of F_2 is somewhat misleading. In addition, the relationship between F_2 and the spectral function is not as clear as it is for our F. As shown in Ref. [9], in the infinite q^2 limit we have:

$$\lim_{q^2 \to \infty} R = 1 + y/({m_2}^2 + y^2)^{1/2}, \tag{5.33}$$

which can differ significantly from 1 for light nuclei and large $|y|$. Thus, despite its better scaling, we rejected the use of F_2 in our analysis.

Chapter 6
Results

In this chapter are presented in graphical form the cross sections and derived scaling functions, with a discussion of these results. Complete tables of cross sections and scaling funtions can be found in Appendix B.

6.1 Cross Sections and $F(y)$'s

In the figures below, all the final cross sections for a given target—unfolded for radiative effects and including all systematic corrections—have been plotted versus energy loss. The error bars shown are statistical only. The cross sections are given in nb/ster/MeV, and the energy loss is in MeV. Also plotted are the y-scaling functions obtained from the cross sections through Eq. (4.18), in units of GeV^{-1}, for the range $y < 0.25$ GeV. The results for the two Fe targets have been averaged, where applicable, with weights determined by the statistical error bars of each data point.

At the lowest q^2's, the quasi-elastic peak stands out clearly as the dominant feature of the cross section. As the momentum transfer increases, we see that the peak is broadened and shifts to a larger energy loss. It is also disappearing into a background of more inelastic processes, such as delta excitation, and deep inelastic scattering.

For a given q^2, there is also a strong A dependence to the cross sections. Aside from the rough proportionality to A, we can see that the quasi-elastic peak becomes broader with increasing A, as one would expect from the increasing Fermi momentum [55]. Thus, the inelastic background becomes even more significant for the heavy

nuclei. Fortunately, this background falls off extremely rapidly with decreasing energy loss, almost exactly at the top of the quasi-elastic peak. Thus, the low-ω side of the peak is free from background and should exhibit y-scaling, according to the impulse approximation.

This is exactly what is observed in the figures below. At large negative y, the $F(y)$'s appear to approach a scaling limit at the higher momentum transfers. The scaling is particularly impressive for the light nuclei, ^{4}He and C. Near $y = 0$, however, the $F(y)$'s diverge wildly with increasing y. (We have plotted only the $y \leq 0.25$ region.) This is because of the inelastic contributions coming into play. The fundamental electron-nucleon cross sections for these processes have different q^2 dependencies than the elastic scattering that was "factored out" to obtain the $F(y)$'s. Thus, the $F(y)$'s for inelastic cross sections will have a residual q^2 dependence, which destroys the scaling.

As mentioned previously, the quasi-elastic $F(y)$'s should be a symmetric function about $y = 0$, and it can be seen that the inelastic contribution becomes significant for $y > -0.1$ GeV/c, at worst. Furthermore, we have a good parameterization of the inelastic cross sections for the free proton and neutron [56]. If we could use these results to subtract the inelastic background from our cross sections for $y \leq 0$, we would know $F(y)$ everywhere because of its symmetry. To do this requires that we Fermi-smear the elementary cross sections, to obtain the cross sections for nuclear targets. This involves forming a convolution model of the inelastic cross sections, for which there is at present no rigorous theory. Nevertheless, we have attempted to smear and subtract these contributions, using an approximate smearing formalism suggested by Bodek and Ritchie [57]. This work, which is still in progress, is discussed below.

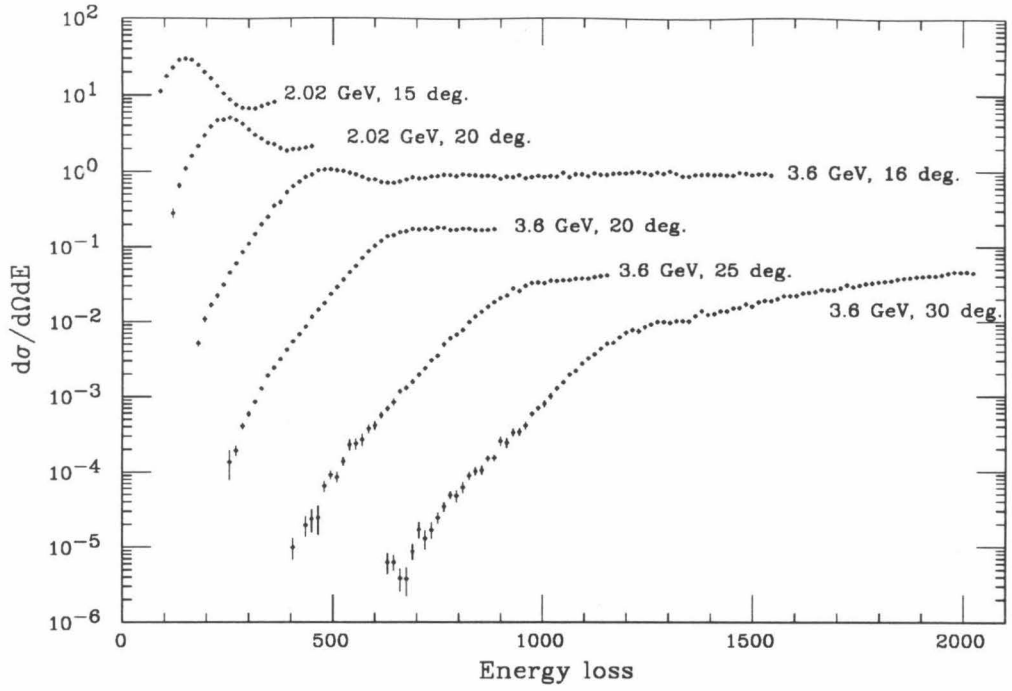

Figure 6.1 – ^{4}He cross sections.

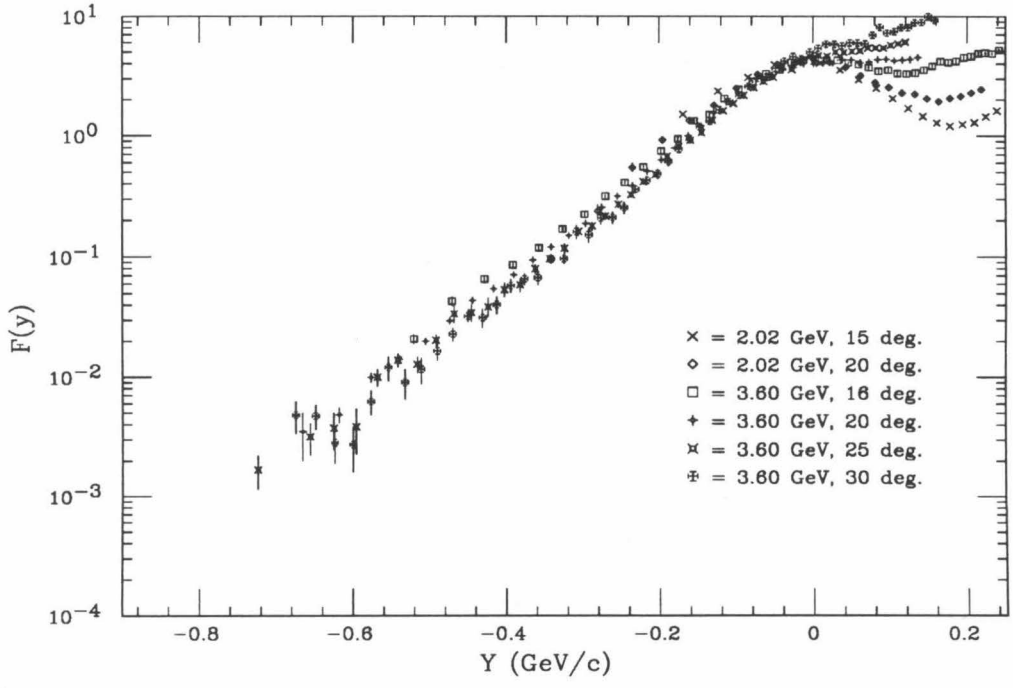

Figure 6.2 – $F(y)$ for ^{4}He.

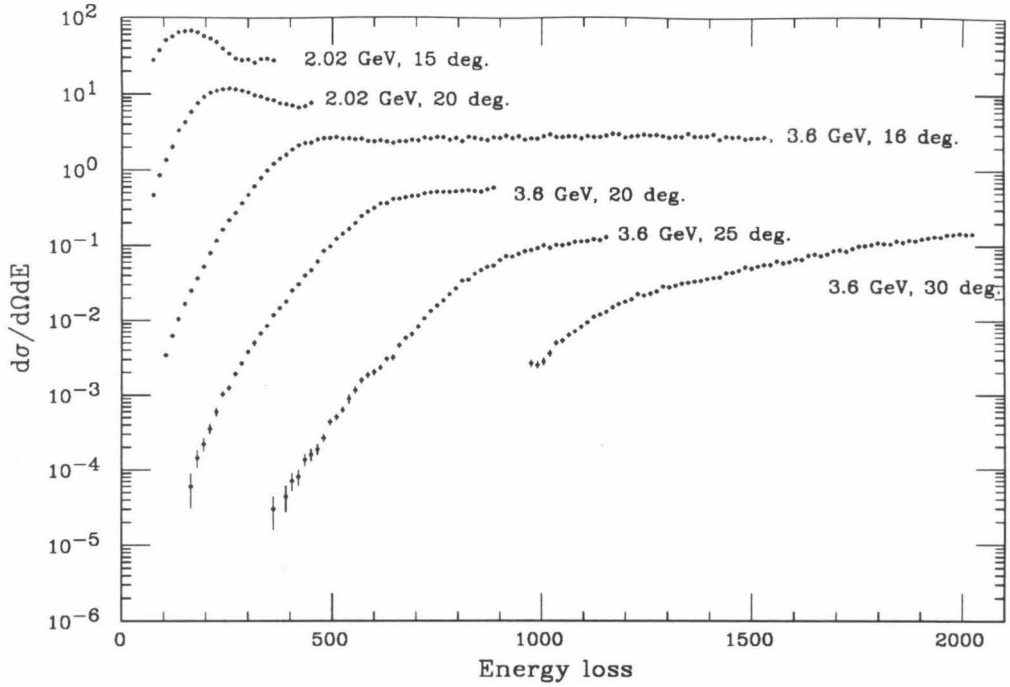

Figure 6.3 – C cross sections.

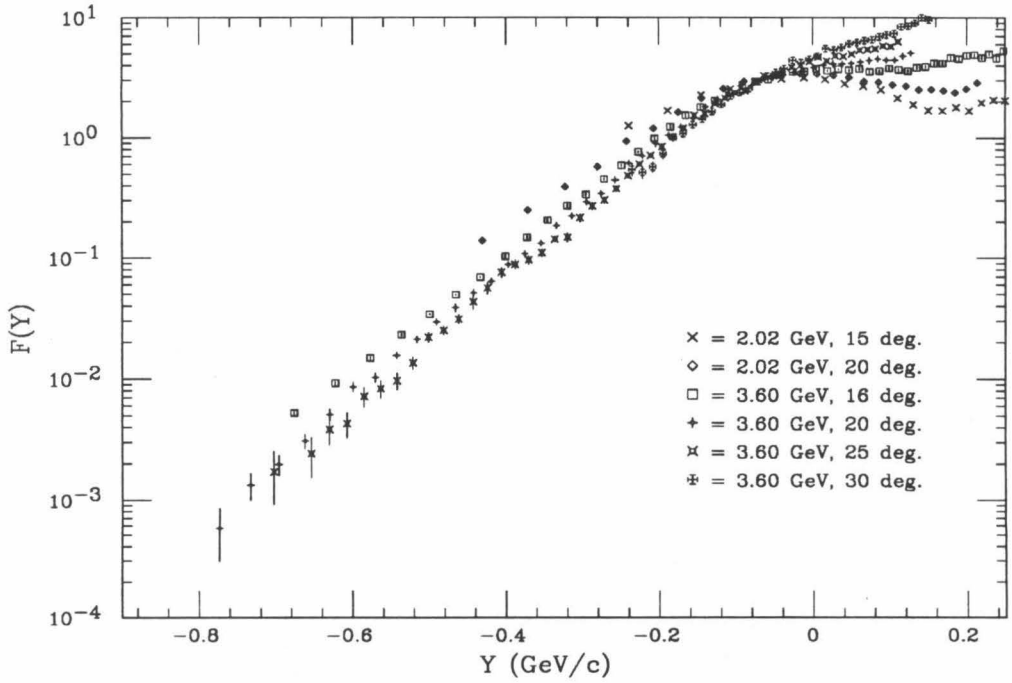

Figure 6.4 – $F(y)$ for C.

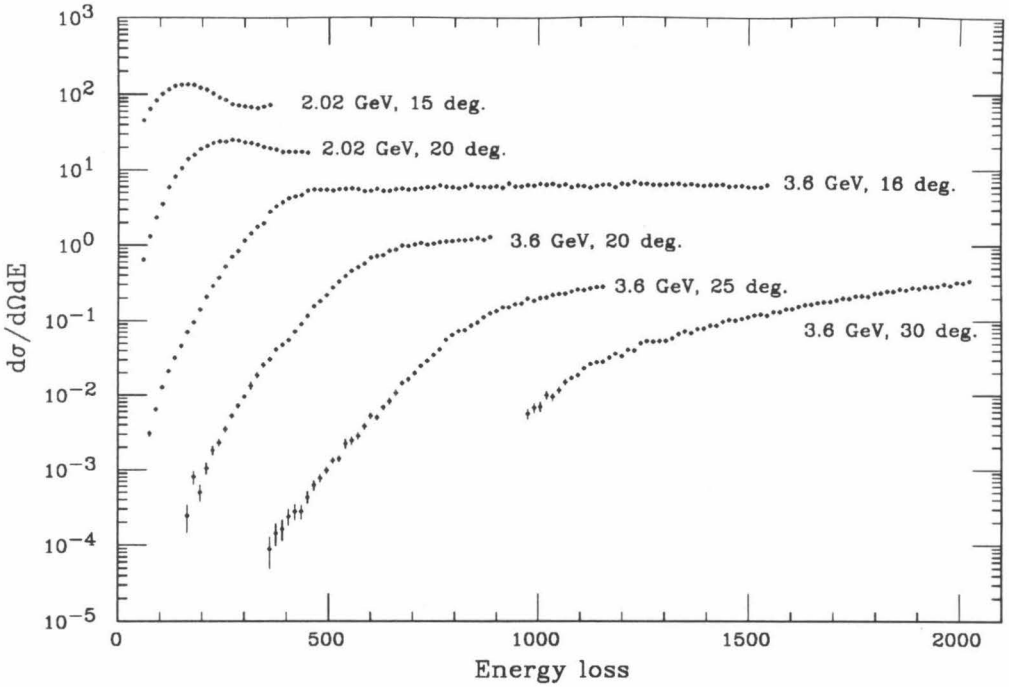

Figure 6.5 – Al cross sections.

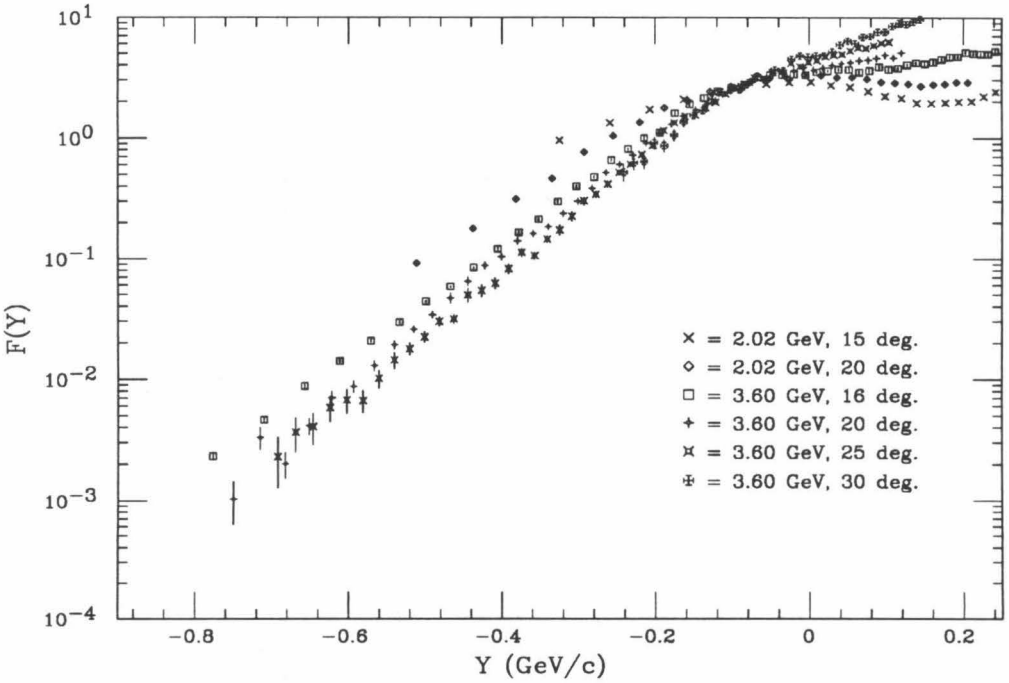

Figure 6.6 – $F(y)$ for Al.

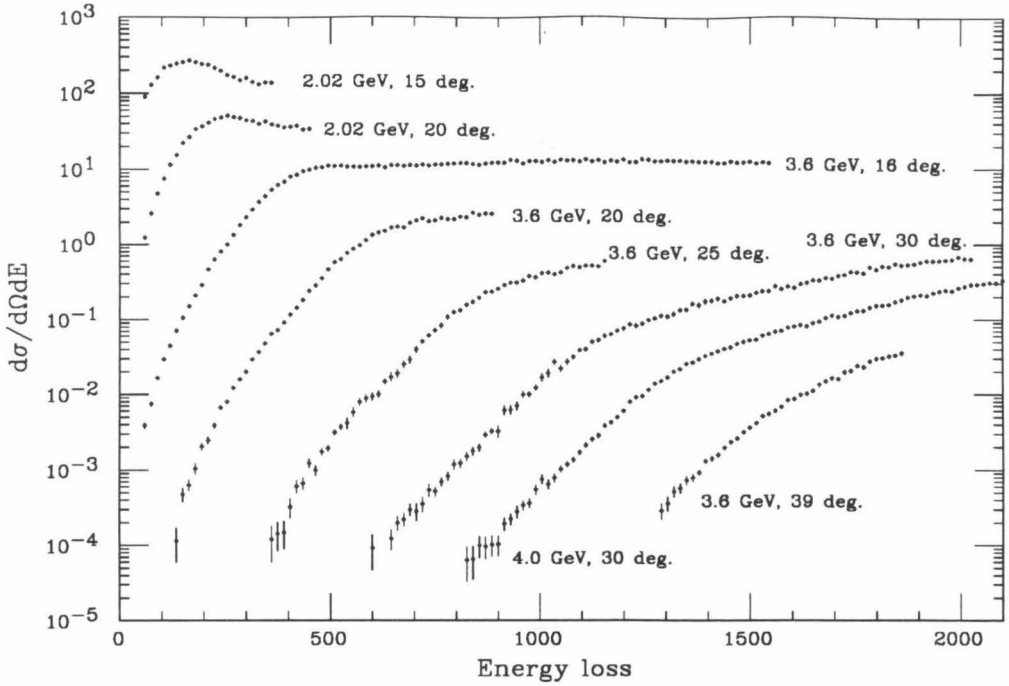

Figure 6.7 – Fe cross sections.

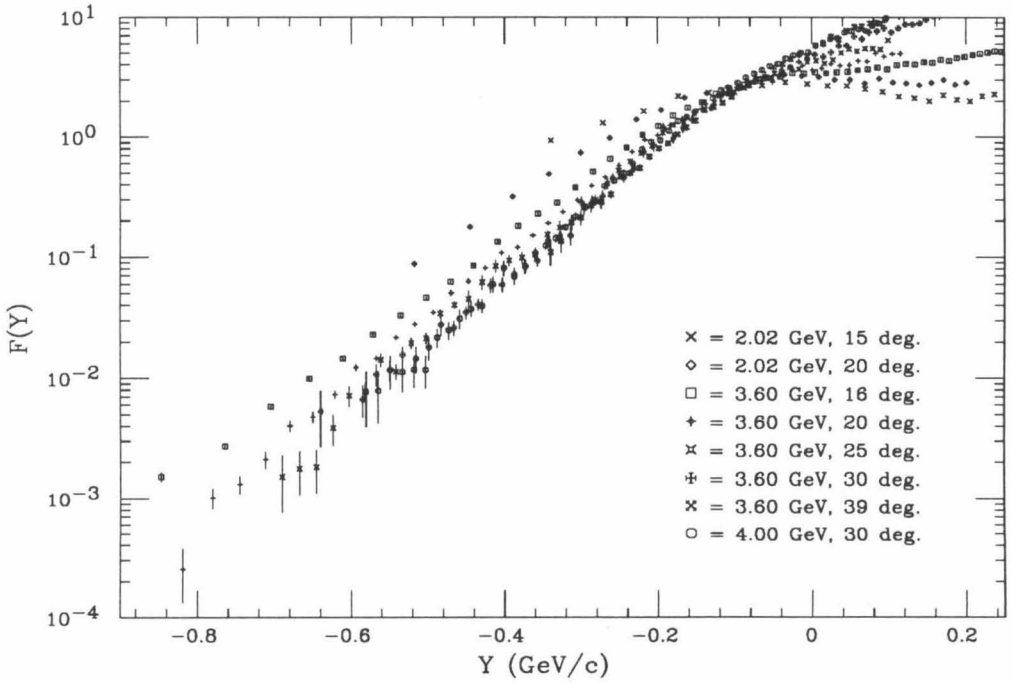

Figure 6.8 – $F(y)$ for Fe.

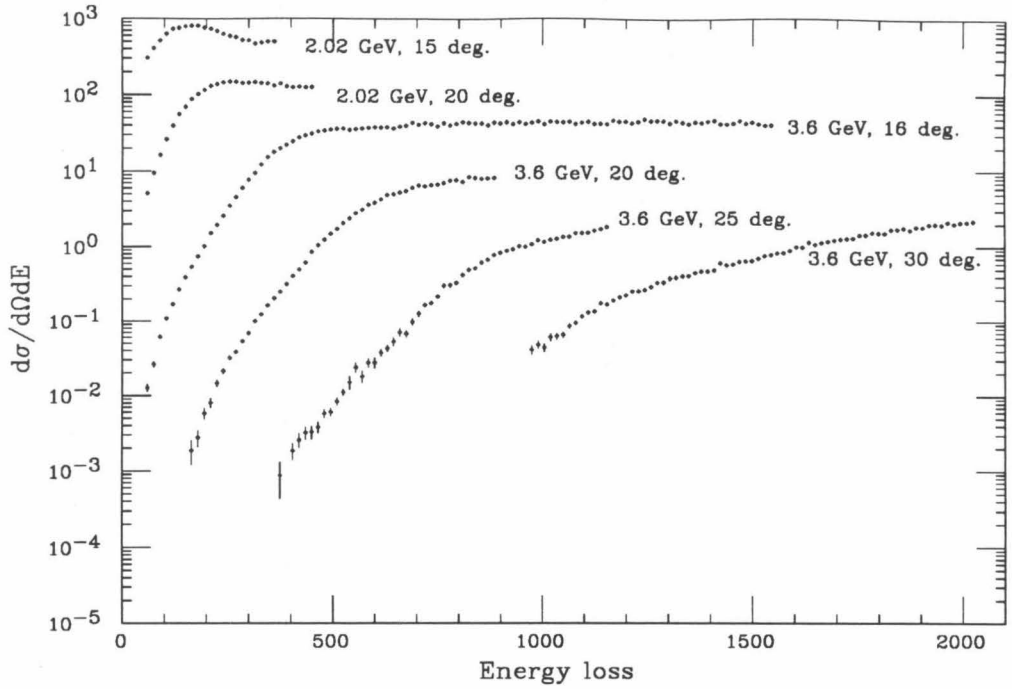

Figure 6.9 – Au cross sections.

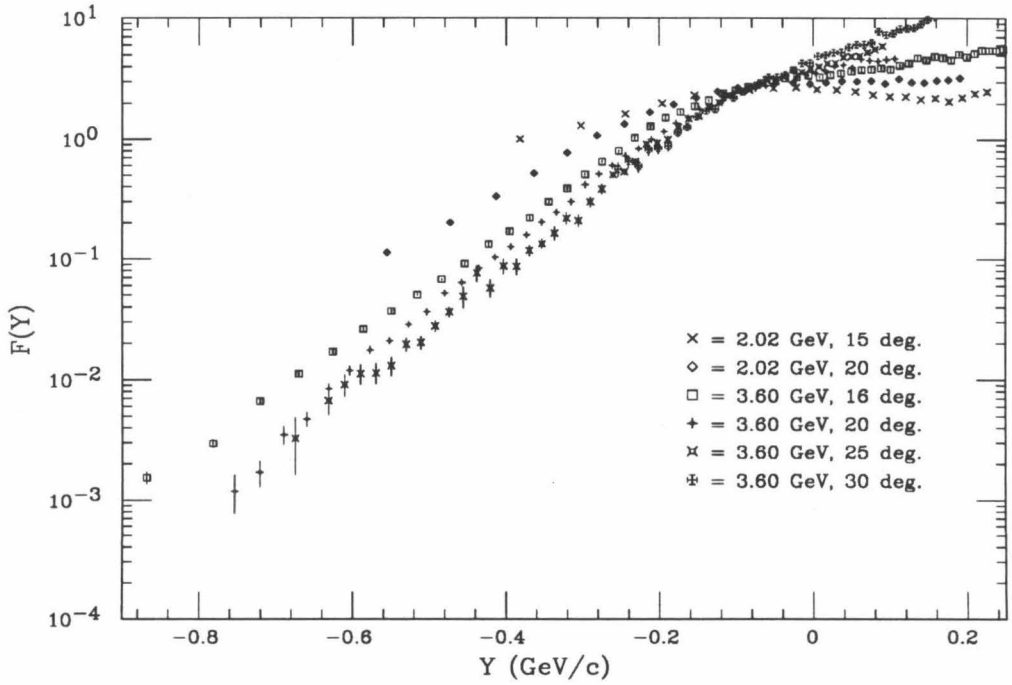

Figure 6.10 – $F(y)$ for Au.

6.2 Approach to Scaling

For a given value of y, the approach to scaling with increasing q^2 in our data is from above. This is in contrast to the prediction of the simple I.A. model, which approaches scaling from below, since its integral over the spectral function sees more of the function with increasing q^2. Clearly, there is a breakdown of the I.A. at small q^2, especially for the heavier nuclei, Fe and Au. This is believed to be due to final state interactions (FSI), which are not included in the impulse approximation.

Recent theoretical work in Kellogg Lab has focused on this problem by calculating $F(y)$'s for infinite nuclear matter, including FSI [30]. (Infinite nuclear matter, unlike finite nuclei with $A > 4$, is an exactly calculable system.) This was done by Malcolm Butler and Steve Koonin via Bruckner-Goldstone, Hartree-Fock g-matrix techniques, using the Paris potential. For $|y| > k_f$, the spectral function is dominated by two-body correlation effects, which should not differ very much between Fe or Au and infinite nuclear matter. Thus, with the intention of comparing their results with our data, the calculations were performed for a subset of our experimental kinematics. Their results are shown along with our data below.

In Figure 6.11 are plotted values of $F(y, q^2)$, at fixed values of y, as a function of q^2. (Squares are for Fe; circles for Au.) Since we binned our cross-section data in w, the corresponding values of y differ slightly between nuclei. We have interpolated our data to obtain the values plotted in Figure 6.11, and assigned error bars typical of the data in the region of interpolation. Evidently, the data do seem to be approaching some kind of a scaling limit.

The solid lines in Figure 6.11 are the result of Butler and Koonin's calculation. Although they follow the general trend of our data, the lines are consistently too high, by up to a factor of ~ 4. This may be evidence that the hard-core repulsive part

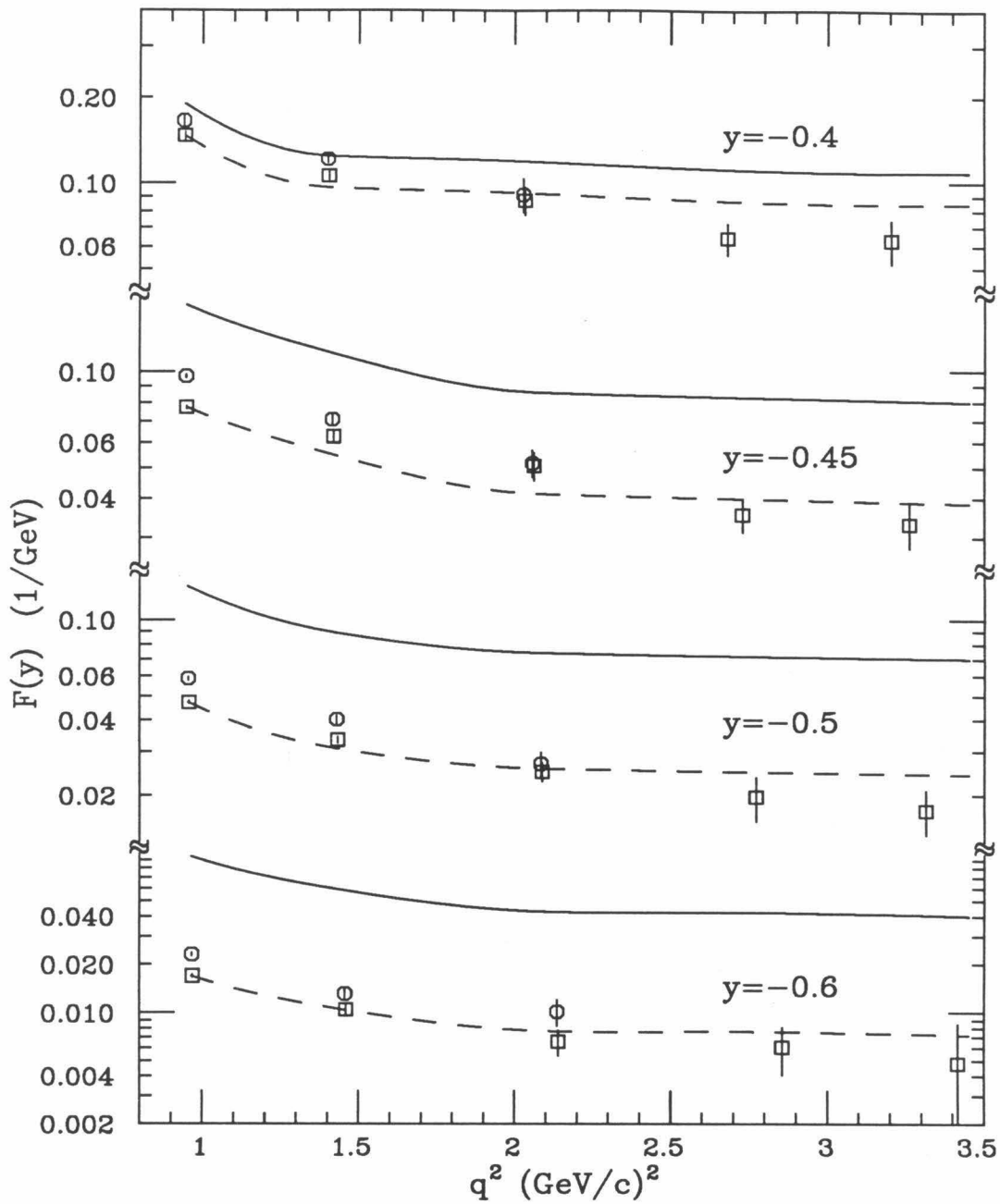

Figure 6.11 – The approach to scaling with q^2. Values of $F(y)$ at fixed y (interpolated from the data) are plotted vs. q^2 for Fe (squares) and Au (circles).

of the potential is too strong—it would be very interesting to see what would result if a softer potential, such as the Bonn potential was used [58]. By renormalizing the calculation to pass through the lowest q^2 Fe data, (dashed lines), we see that the approach to scaling is reasonable well reproduced. Thus, we conclude that final state effects, which dominate the approach to scaling, appear to be unimportant at momentum transfers above 2.5 $(\mathrm{GeV/c})^2$, where the data are approaching a scaling limit.

6.3 Subtraction of Inelastic Background

The inelastic contributions to the cross section grow rapidly with increasing y from their threshold, while the quasi-elastic cross section decreases for $y > 0$. Thus, any attempt to subtract the background faces rapidly increasing statistical and systematic uncertainties in this region. Moreover, the systematic uncertainty is difficult to estimate, since one can account only approximately for the Fermi broadening of the background one is subtracting. As a check, we expect the resulting $F(y)$'s to be symmetric about $y = 0$, and to scale for positive y. Fortunately, we need only to correct the data for $y < 0$ to obtain a complete $F(y)$. Also, the smearing is smaller and the background less important for the lighter nuclei. Thus, we obtain sensible results for ^{4}He and C.

6.3.1 Fermi-smearing Formulae

We have used corrected versions [59] of the smearing formulae of Bodek and Ritchie. The differential scattering cross section from the nucleus is given by:

$$\frac{d^2\sigma}{d\Omega\, dE'} = \sigma_{\mathrm{Mott}}(W_2^A + 2\, W_1^A \tan^2 \theta/2), \tag{6.1}$$

in which the nuclear response functions are written in terms of off-shell nucleon response functions smeared by the momentum distribution:

$$W_1^A = Z \int |\phi(\vec{P})|^2 \left(W_1^p + \frac{W_2^p}{2{m_p}^2}(\vec{P}^2 - {P_3}^2) \right) d^3\vec{P}$$
$$+ \text{similar terms for the neutrons,} \tag{6.2}$$

$$W_2^A = Z \int |\phi(\vec{P})|^2 \left[\left(1 + \frac{P_3 q^2}{m_p \omega' Q} \right)^2 \left(\frac{\omega'}{\omega} \right)^2 + \frac{P^2 - {P_3}^2}{2{m_p}^2} \left(\frac{q^2}{Q^2} \right) \right] W_2^p \, d^3\vec{P}$$
$$+ \text{similar terms for the neutrons.} \tag{6.3}$$

$\vec{P}$ is the initial state nucleon's momentum, with component P_3 along the three-momentum transfer, $\vec{Q}$. The energy transfer is ω, with $\omega' = (E_i\omega - P_3 Q)/m_p$, in which E_i is the initial state nucleon's energy, defined via the quasi-deuteron approximation:

$$E_i = M_d - (P^2 + {m_p}^2)^{1/2}. \tag{6.4}$$

For $W_1^{p(n)}$ and $W_2^{p(n)}$, we use the values from scattering off a free nucleon at the same four-momentum transfer and the same final-state invariant mass, ${M_f}^2 = (E_i + \omega)^2 - (\vec{P} + \vec{Q})^2$. The free nucleon structure function values were obtained from Bodek's fit to to SLAC hydrogen and deuterium data, which used a parameterization suggested by Atwood and Stein [60], and which included deep-inelastic scattering, the four most prominent nucleon resonances, x-scaling violations, and non-resonant behavior near the pion production threshold. The fit describes the data over the entire SLAC q^2 range from 0.1 to 20 $(\text{GeV/c})^2$.

To implement these smearing equations, we needed a momentum distribution, $\phi(P)$, which we obtained from the resulting $F(y)$'s through Equation (4.22) via an iterative, self-consistent approach. At each iteration, the background subtracted $F(y)$

for a given target with $E_0 = 3.595$ GeV, $\theta = 20$ deg. and $y < 0.1$ was fit with the function:

$$F(y) = \begin{cases} C \cdot e^{-\lambda[(y-y')/y_0]^2}, & \text{if } |y - y'| < y_0; \\ C \cdot e^{\lambda(1-2|y-y'|/y_0)}, & \text{otherwise,} \end{cases} \tag{6.5}$$

in which C, λ, y', and y_0 were free parameters. The resulting function was used to obtain a momentum distribution with which to do the smearing in the next iteration. This rapidly converged to a self-consistent momentum distribution in a few iterations, with which we smeared and subtracted the inelastic cross sections for the other kinematics.

6.3.2 Background Subtracted $F(y)$'s.

The $F(y)$'s we obtained from these subtracted cross sections are shown in the figures below, this time on a linear scale. ^{4}He stands out as being exceptionally improved for $y > 0$, with good symmetry and scaling extending out to $y \sim 0.18$. The situation degrades with increasing A, however. For Fe and Au, it is evident that too much has been subtracted from the cross sections at the higher momentum transfers, resulting in misshapen $F(y)$'s that do not scale. Clearly, this approximate smearing formalism is not valid for the heavier nuclei. However, the results for C and especially ^{4}He scale far enough into the positive y region, that for $y \leq 0$ we should be OK.

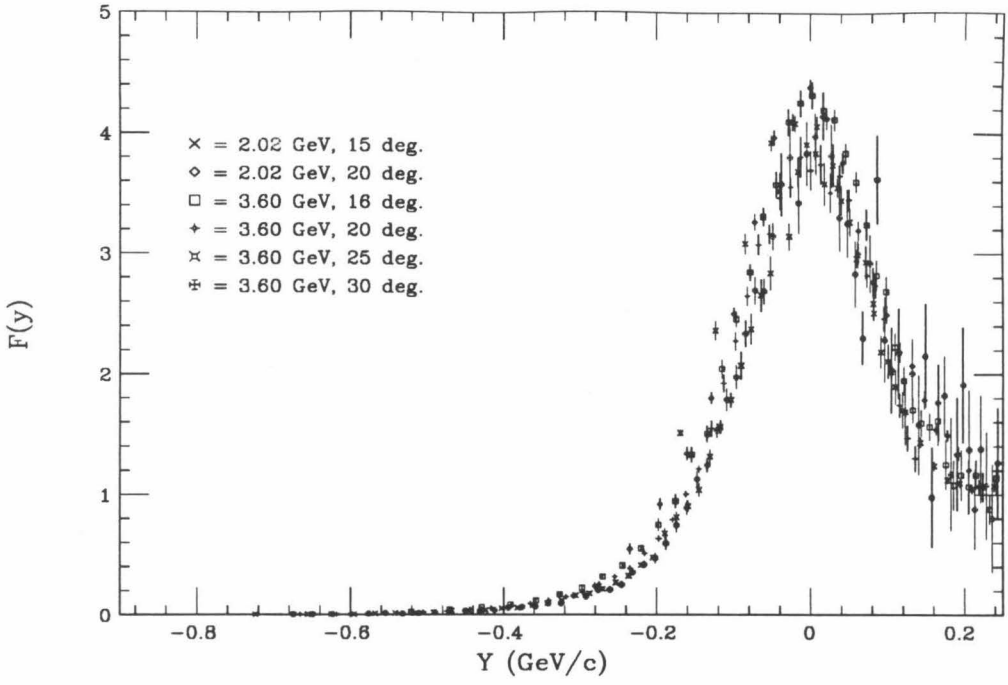

Figure 6.12 – $F(y)$ for ^{4}He (quasi-elastic only.)

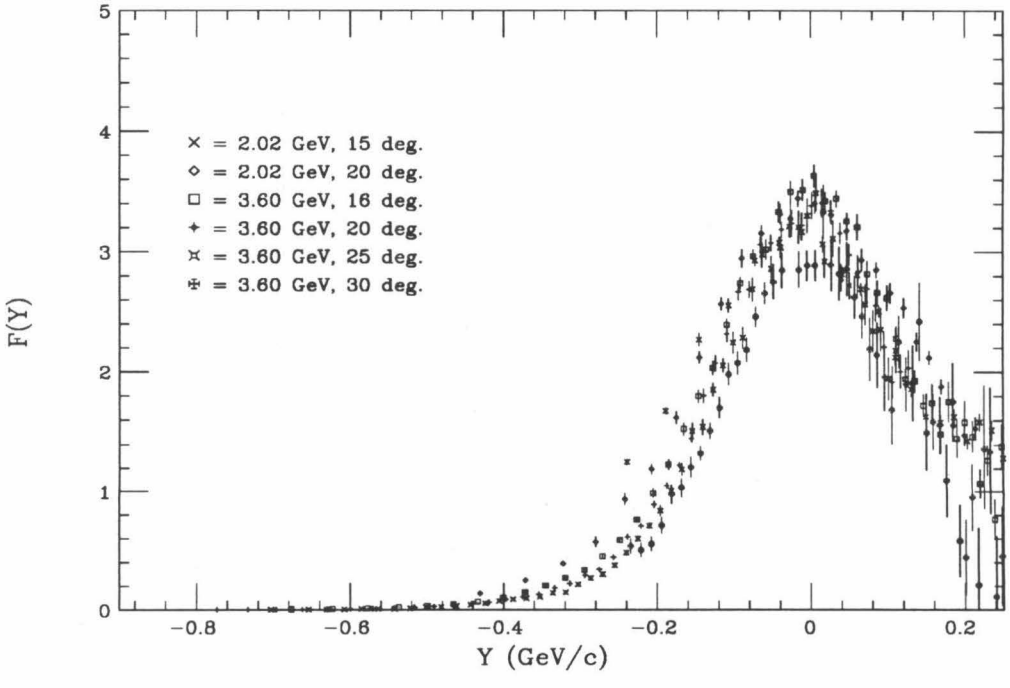

Figure 6.13 – $F(y)$ for C (quasi-elastic only.)

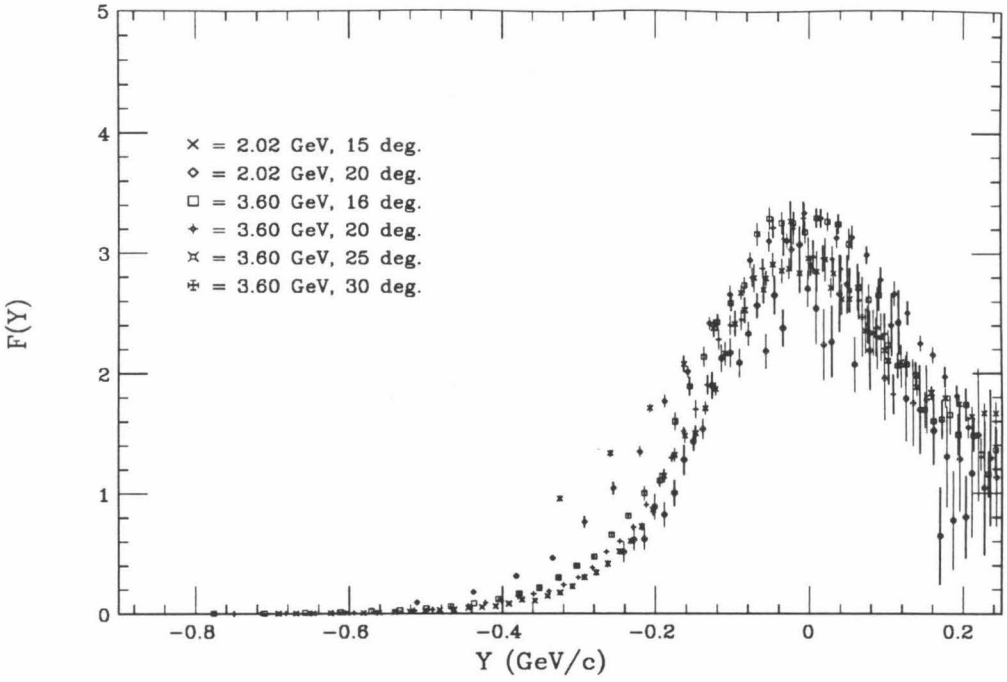

Figure 6.14 – $F(y)$ for Al (quasi-elastic only.)

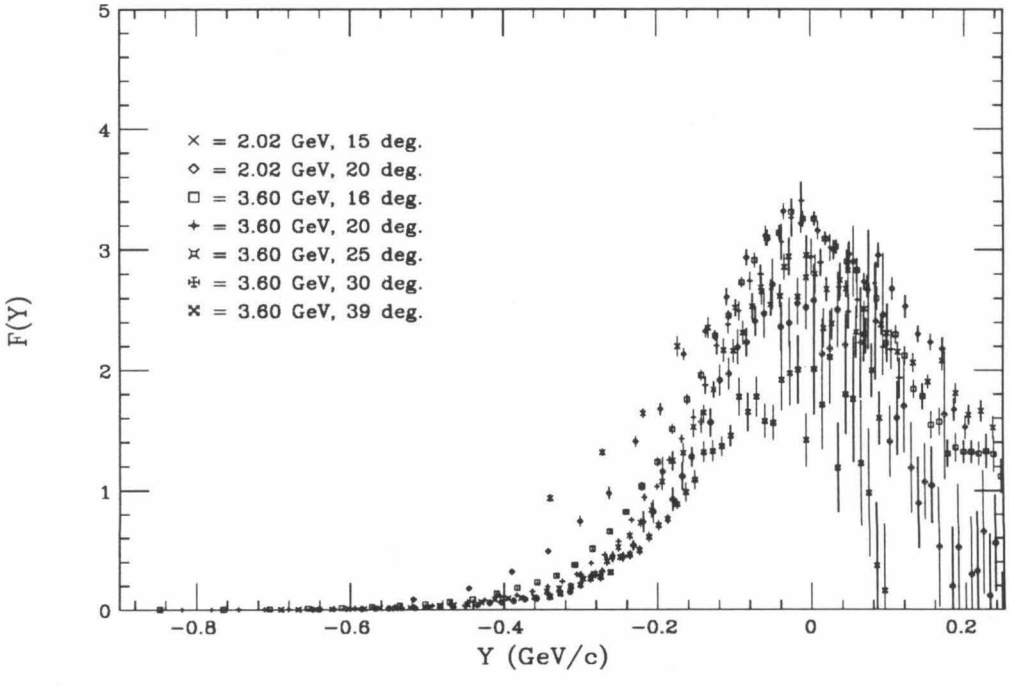

Figure 6.15 – $F(y)$ for Fe (quasi-elastic only.)

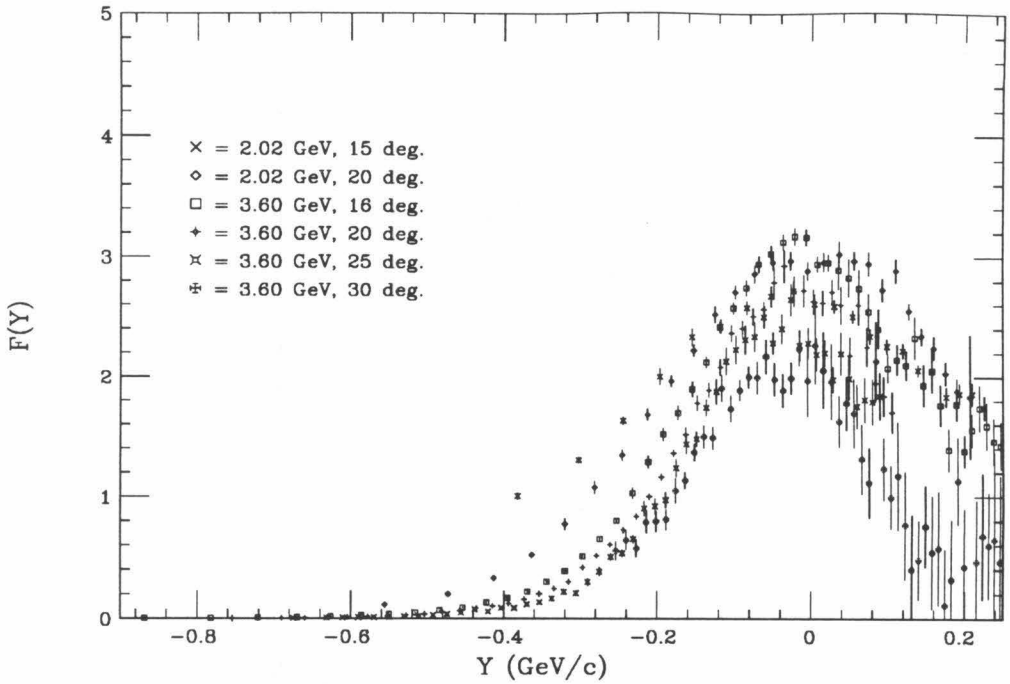

Figure 6.16 – $F(y)$ for Au (quasi-elastic only.)

6.3.3 Integrals of $F(y)$

As shown in Chapter 5, the theoretical $F(y)$'s obey the sum rule

$$2 \int_{-\infty}^{0} F(y)\, dy = 1. \tag{6.6}$$

This result is extremely sensitive to underlying assumptions of the I.A. model from which it was derived, namely, that the form factors for a nucleon in a nucleus are the same as for a free nucleon. If, for example, the rms radius of a nucleon were to increase when placed in a high density nuclear medium, the form factors at a given q^2 would be reduced, as would the measured $F(y)$. In that case, the integral of the experimental $F(y)$'s (in the scaling limit) would come out less than 1. This kind of analysis has been used in the past to set limits on the swelling of nucleons from quasi-elastic data on ^{3}He [26]. Any such swelling is expected to show an enhancement

in heavy nuclei [12,13]. We have investigated this possibility by computing similar integrals for our $F(y)$'s.

These integrals were computed from the background-subtracted $F(y)$'s, using two different methods. In the first case, integrals were derived from individual fits to each data set for $y \leq 0.05$ GeV/c, using either the parameterization of Eq. 6.5 or $A.19$ (with an extra parameter analogous to y'). Because small errors in the value we used for E_s would principally cause an offset in y, we integrated the fitted functions to their peak at y'. These peaks are typically within 0.01 GeV/c of $y = 0$, and $F(0) \approx 3$, so that the uncertainty in the integral from locating the peak is at most 6%. This method assumes that the $F(y)$ to be integrated is well fit by its parameterization.

The second method of integration was less model-dependent. In this case, an Akima cubic-spline function [61,62] (which minimizes the under and overshoots common to ordinary cubic splines) was fit to the data, and then integrated from the minimum y value up to the value of y' from the first method. This method could not be used for spectra in which the minimum value of y was too high, causing a significant portion of the integral to be left out. Where both methods were applicable, the integrated $F(y)$'s agreed to better than 2%.

The results of these integrations are shown in Figure 6.17, plotted versus the value of q^2 at $y = 0$. The solid lines are curves to guide the eye. We have not included values for Fe above $q^2 = 2.4$ (GeV/c)^2, or Au above $q^2 = 1.8$, since there are obvious problems with the background subtraction.

For ^{4}He, there is an obvious decrease in the integral with increasing q^2, saturating for $q^2 > 1.2$ at a value near 1. This decrease is to be expected from the q^2 approach to scaling induced by the final-state interactions, as discussed earlier. Above a q^2 of ~ 1.5, where we are in the scaling region, the saturation of the integral near 1.0

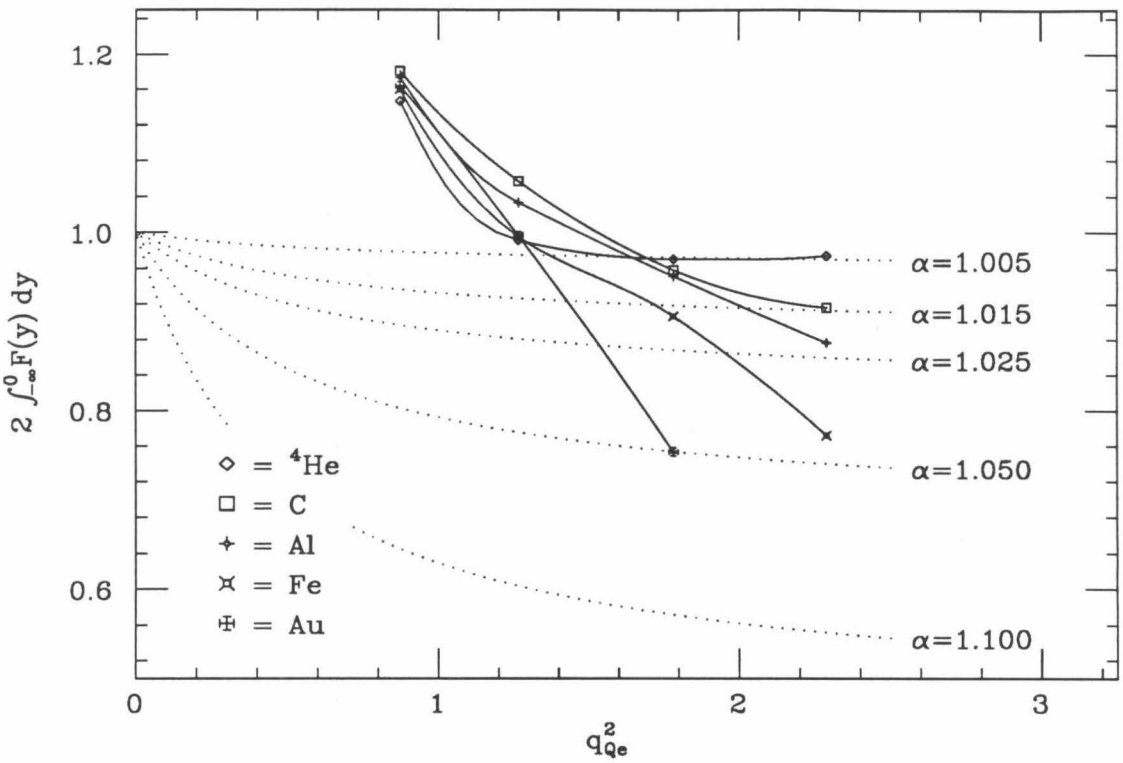

Figure 6.17 – $2\int_{-\infty}^{0} F(y)\,dy$ vs. the value of q^2 at $y = 0$.

implies that strict limits on the swelling of nucleons can be set. The case for heavier nuclei is less clear, since only C appears to be approaching any sort of limit. The observed trends certainly reflect the fact that we are overestimating the background subtraction, although it is difficult to estimate by how much.

The dotted curves in Figure 6.17 are the values we would expect to obtain with swollen nucleons of various sizes. These curves were generated by considering the effect of a radius change on the elementary form factors for elastic scattering. For a

free nucleon, these form factors closely follow the empirical dipole formula [63],

$$G(q^2) \cong G(0) \cdot (1 + q^2/{M_v}^2)^{-2}, \tag{6.7}$$

with ${M_v}^2 = (0.84 \text{ GeV})^2$. This expression is consistent with an exponential charge and magnetic moment distribution of rms radius $\sqrt{12}/M_v = 0.80$ fermi. Since the form factors are squared in the cross sections, an increase in the rms radius by a factor of α would therefore decrease the cross section by a factor of R, given by the ratio of two dipole terms, squared:

$$R = \frac{(1 + q^2/{M_v}^2)^4}{(1 + \alpha^2 q^2/{M_v}^2)^4}. \tag{6.8}$$

This is also the factor by which $F(y)$ is reduced, since $F(y)$ is proportional to the elementary cross sections. And since q^2 varies very little with y over the range where $F(y)$ is significant, the integral of $F(y)$ would be reduced by R as well. We have therefore used Eq. (6.8) to draw the dotted curves above, for α =1.005, 1.015, 1.025, 1.050, and 1.100.

For ^{4}He, we see that the results, given an uncertainty of 6%, are consistent with $\alpha = 1.0$. For an upper bound on any radius change, we take the value of α for which $R(q^2) = 0.91$, at $q^2 = 1.8$. This gives an upper bound of $\alpha \leq 1.017$. None of the other nuclei demonstrates a saturation along one of the dotted lines, so that we cannot interpret the large deviations from 1.0 as evidence for a change in the nucleon radius. However, since a correct subtraction of the background would tend to increase the integrals, we can use the results to set loose upper limits on the change in the size of

Nucleus	$2\int_{-\infty}^{0} F(y)\,dy$	α
^{4}He	$0.97 \pm .06$	< 1.017
C	> 0.90	< 1.019
Al	> 0.89	< 1.020
Fe	> 0.71	< 1.029
Au	> 0.69	< 1.065

Table 6.1 – Limits on α obtained from the integral of the background subtracted $F(y)$'s at $q^2 = 1.8$ (GeV/c)^2.

a nucleon. Since ^{4}He has saturated at $q^2 = 1.8$, we will use the $q^2 = 1.8$ values (with 6% uncertainty) to set these limits. The results so obtained are listed in Table 6.1.

As a final note, if one really believed in a change in radius by a factor of α, then the correct $F(y)$'s (in the sense of Eq. 4.19) should be extracted from the data, using modified form factors: $G_{\text{swollen}} = G_{\text{free}} \cdot \sqrt{R}$. In addition to affecting the integral of $F(y)$, this also affects the shape, since q^2 and y are not independent for fixed E_0 and θ. Thus, the q^2 approach to scaling will be altered by a change in radius (and, in fact, improved for $\alpha > 1$). The size of this effect is very small, however. For example, it takes $\alpha = 1.10$ to make the $F(y)$'s of ^{4}He independent of q^2 for $y \leq -0.05$—a subtle change, since it already scales quite well. But this increases the integral of $F(y)$ by about 70%, which is not so subtle! Thus, the dominant effect of $\alpha \neq 1$ is simply a renormalization of $F(y)$.

Chapter 7
Summary and Conclusions

We have measured inclusive electron-scattering cross sections as a function of the electron's energy transfer ω, for nuclear targets of ^{4}He, C, Al, Fe, and Au, with incident beam energies between 2.0 and 4.0 GeV, and scattering angles from 15 to 39 degrees. The cross sections extend from as low in ω as was practical, over the quasi-elastic peak, to the region of the delta resonance, and into the deep-inelastic scattering regime in some cases. The four-momentum transfer of these measurements spans the range $0.25 \leq q^2 \leq 3.7$ (GeV/c)^2. Details of the measurement and subsequent data analysis were presented in Chapters 2 through 4.

$F(y)$ scaling functions were extracted from these cross sections, using the formalism of a simple, impulse-approximation model for the reaction mechanism, as described in Chapter 5. The data were presented in Chapter 6 and were seen to approach a scaling limit for $y < 0$ at momentum transfers above 2.5 (GeV/c)^2, with ^{4}He exhibiting the least dependence on q^2. For $y \geq 0$, other inelastic processes dominate over the quasi-elastic scattering, and the scaling is destroyed. The q^2 approach to scaling at negative y is from above, in contradiction to the I.A. model, but in qualitative agreement with a calculation for infinite nuclear matter, including final-state interactions. Detailed agreement was possible only after renormalizing the calculated $F(y)$'s, implying that the repulsive part of their nucleon-nucleon potential may be too strong.

The existence of a y-scaling limit is strong evidence that the simple I.A. model is sufficient to describe quasi-elastic scattering at high q^2. We can therefore draw conclusions regarding nucleon momentum distributions and effects of the medium on the nucleons. For $|y| < 0.15$ GeV/c, the $F(y)$'s behave like Gaussians, consistent with a Gaussian momentum distribution. For large negative y, the scaling functions have an exponential behavior: $F(y) \propto e^{-ay}$. This implies that the momentum distribution for large momenta has a Yukawa-like character: $n(k) \propto e^{-ay}/y$.

To investigate possible changes in the size of the nucleons in a nucleus required that we integrate the scaling function from $y = -\infty$ to $y = 0$. At momentum transfers high enough to be in the scaling limit, there is a background from more inelastic processes that must be subtracted from $F(y)$ near $y = 0$ in order to do the integration. Lacking a correct theoretical treatment of these cross sections, we have performed an approximate calculation by Fermi-smearing a parameterization of the free nucleon, inelastic cross sections. This was partially successful, and reasonable results were obtained for ^{4}He and C. However, the calculation clearly overestimates the background for the heavier nuclei. By assuming that the properly corrected $F(y)$'s will lie above our values, we were able to set upper bounds on an increase in the size of the nucleon radius. The ^{4}He and C limits are particularly stringent: the integrals are inconsistent with an increase any larger than 1.7% for ^{4}He, or 1.9% for C.

Future work in this field is possible in both the experimental and theoretical arenas. Theoretically, we would like to see calculations of scaling functions, using different nucleon-nucleon potentials. In addition to nuclear matter, we would like to see realistic calculations for ^{4}He. Experimentally, one can consider doing exclusive measurements at high q^2 to determine the spectral function itself instead of an integral over it. Such experiments traditionally have been much harder, both because

of the small counting rates, and because one must deal with the strong final-state interactions of the detected recoiling nucleons. However, with the next generation of high-current accelerators—such as CEBAF—these experiments will likely become possible.

Appendix A
Radiative Corrections

A.1 Quasi-elastic Data

Radiative corrections for the quasi-elastic data were calculated using the formulae of Stein, *et al.* [43], which are based on the work of Mo and Tsai [64], and Tsai [48]. These expressions allow the calculation of the observed cross section in terms of a theoretical, non-radiative cross section, which one would observe in the absence of radiative effects. It is customary to unfold experimental data to remove the effects of bremsstrahlung and energy straggling in order to yield results that are independent of target thickness and are directly comparable with theoretical calculations, which always ignore radiative effects. This unfolding is non-trivial, because the equations cannot be solved directly for the non-radiative cross section.

The approach we have taken is an iterative scheme in which the parameters of a model, non-radiative cross section are adjusted until the radiated model is consistent with the observed cross sections. The measured cross sections are then multiplied by the ratio of the non-radiative over radiative models to obtain the unfolded cross sections. The sensitivity of this method to the form of the model is discussed below.

A.1.1 Radiative Correction Formulae

The radiative cross section is related to the non-radiative cross section in the angle-peaking approximation through the following equation:

$$\left(\frac{d^2\sigma}{d\Omega\, d\varepsilon_2}\right)_{\rm rad} = \left(\frac{R\,\delta}{\varepsilon_1}\right)^{b\,t'_b}\left(\frac{\delta}{\varepsilon_2}\right)^{b\,t'_a}\left[1-\frac{\xi/\delta}{1-b(t'_a+t'_b)}\right]\cdot\breve{\sigma}(\varepsilon_1,\varepsilon_2)$$
$$+\int_{\varepsilon_{1\min}}^{\varepsilon_1-R\delta}\breve{\sigma}(\varepsilon'_1,\varepsilon_2)\cdot\left(\frac{\omega_1}{R\,\varepsilon_2}\right)^{b\,t'_a}\left(\frac{\omega_1}{\varepsilon_1}\right)^{b\,t'_b}\left[\phi(\omega_1/\varepsilon_1)\cdot\frac{b\,t'_b}{\omega_1}+\frac{\xi}{2{\omega_1}^2}\right]d\varepsilon'_1$$
$$+\int_{\varepsilon_2+\delta}^{\varepsilon_{2\max}}\breve{\sigma}(\varepsilon_1,\varepsilon'_2)\cdot\left(\frac{\omega_2}{\varepsilon'_2}\right)^{b\,t'_a}\left(\frac{R\,\omega_2}{\varepsilon_1}\right)^{b\,t'_b}\left[\phi(\omega_2/\varepsilon'_2)\cdot\frac{b\,t'_a}{\omega_2}+\frac{\xi}{2{\omega_2}^2}\right]d\varepsilon'_2, \tag{A.1}$$

in which $\varepsilon_1, \varepsilon_2$ are the incident and scattered electron energies, θ is the electron-scattering angle, $\delta = 5$ MeV, m_1 is the mass of the target nucleus, m_e is the electron mass, and

$$\omega_1 = \varepsilon_1 - \varepsilon'_1 \tag{A.2}$$

$$\omega_2 = \varepsilon'_2 - \varepsilon_2 \tag{A.3}$$

$$\varepsilon_{1\min} = \frac{m_1\,\varepsilon_2}{m_1 - 2\varepsilon_2\sin^2(\theta/2)} \tag{A.4}$$

$$\varepsilon_{2\max} = \frac{m_1\,\varepsilon_1}{m_1 + 2\varepsilon_1\sin^2(\theta/2)} \tag{A.5}$$

$$R = \frac{m_1 + 2\varepsilon_1\sin^2(\theta/2)}{m_1 - 2\varepsilon_2\sin^2(\theta/2)}. \tag{A.6}$$

Let t_b and t_a be the thickness in radiation lengths of the material before and after the scatter, using the half-path-length approximation in which the scatter occurs in the center of the target. Then,

$$t'_b = t_b + t_r$$
$$t'_a = t_a + t_r \tag{A.7}$$
$$t_r = \left(\frac{\alpha}{b\pi}\right)\cdot\left[\ln({q^2}/{m_e}^2) - 1\right]. \tag{A.8}$$

The bremsstrahlung spectrum, $\phi(v)$, is:

$$\phi(v) = 1 - v + \frac{3}{4}v^2. \tag{A.9}$$

With the definitions [65]:

$$L_1 = \ln(\,1194\,Z^{-2/3}) \tag{A.10}$$

$$L_2 = \ln(\,184.15\,Z^{-1/3}) \tag{A.11}$$

$$\eta = L_1/L_2, \tag{A.12}$$

we have:

$$\xi = \Big(\frac{\pi\, m_e}{2\,\alpha}\Big) \cdot \frac{t_a + t_b}{(Z+\eta)\,L_2} \tag{A.13}$$

$$b = \frac{4}{3}\Big[1 + \frac{1}{9}\frac{(Z+1)}{(Z+\eta)\,L_2}\Big]. \tag{A.14}$$

Lastly,

$$\check{\sigma}(\varepsilon_1', \varepsilon_2') = U(q'^2) \cdot \sigma_{\rm nr}(\varepsilon_1', \varepsilon_2'), \tag{A.15}$$

with $\sigma_{\rm nr}$ the non-radiative cross section, and

$$U(q'^2) = 1 + 0.5772\,b\,(t_a + t_b) - \frac{\alpha}{2\pi}\Big[\ln(\varepsilon_1'/\varepsilon_2')\Big]^2$$
$$- \frac{2\alpha}{\pi}\Big[+\frac{14}{9} - \frac{13}{12}\ln\Big(\frac{q'^2}{{m_e}^2}\Big)\Big] + \frac{\alpha}{\pi}\Big[\frac{\pi^2}{6} - \Phi\Big(\cos^2(\theta/2)\Big)\Big], \tag{A.16}$$

in which $q'^2 = 4\varepsilon_1'\varepsilon_2'\sin^2(\theta/2)$, and $\Phi(x)$ is the Spence function:

$$\Phi(x) = \int_0^x \frac{-\ln|1-y|}{y}\,dy. \tag{A.17}$$

A.1.2 Model Cross Section

To implement Equation (A.1), we needed an accurate model cross section, $\sigma_{\rm nr}$. We have used

$$\sigma_{\rm nr} = K(w^2) \cdot (\sigma_{\rm ys} + \sigma_{\rm dis}), \tag{A.18}$$

in which σ_{ys} is a (modified) y-scaling model of the quasi-elastic peak, σ_{dis} is Bodek's model of deep inelastic scattering [56], to which we have (crudely) added Fermi-smearing, and $K(w^2)$ is an arbitrary function of w^2, the missing mass. Initially, $K(w^2) = 1$. As the correction procedure is iterated, K is adjusted as needed until a convergence test is passed.

For our model's $F(y)$, we used the functional form:

$$F(y) = \frac{C_1}{y_0} e^{-\frac{1}{2}(y/y_0)^2} + \frac{C_2}{2\cosh(C_3 y)}, \qquad (A.19)$$

in which the parameters C_1, C_2, C_3, and y_0 were determined by a fit to our data. We found that the scaling deviations observed in the data's $F(y)$'s could be reduced by adjusting m and E_s in the definition of y. The resulting scaling functions have no simple connection with the spectral function, but do provide the basis for a good empirical model of the cross section. The final parameters used for each target are listed in Table A.1.

	^{4}He	C	Al	Fe	Au
y_0	0.07727	0.1288	0.1541	0.1586	0.1587
C_1	0.1058	0.1058	0.1058	0.1058	0.1058
C_2	6.381	6.381	6.381	6.381	6.381
C_3	11.2302	11.2302	11.2302	11.2302	11.2302
λ	0.16	0.2	0.2	0.2	0.2
m^*	0.88	0.88	0.88	0.88	0.88
E^*	0.00	0.00	0.00	0.00	0.00

Table A.1 – Parameters for the model cross sections used in the radiative corrections. C_1-C_3 and λ are defined in the text. E^* and m^* are adjusted values for the separation energy and nucleon mass used in the definition of the scaling variable for these models only.

Since Equation ($A.1$) involves integrals over the model cross section, it was not feasible to do a full smearing calculation of the deep inelastic contribution. Instead, we computed:

$$\sigma_{\rm dis}(q^2, w^2) = \int_{-\infty}^{\infty} \sigma_{\rm Bodek}(q^2, w'^2) \cdot \frac{1}{\sqrt{2\pi\lambda^2}} e^{-(w^2-w'^2)^2/2\lambda^2}\, dw'^2, \qquad (A.20)$$

using a 25-point numerical method. This convolution integral is not justified on theoretical grounds; nevertheless, its results agree reasonably well with our data, and it is a definite improvement over the unsmeared model. As shown below, the radiative correction factors are insensitive to changes in the model. Thus, the use of these models for radiative corrections is proper.

A.1.3 Unfolding Procedure

Each spectrum for a given incident energy, angle, and target was unfolded independently. Only data points with an energy loss at least 50 MeV greater than that of the elastic peak and with statistical uncertainties of less than 50% were considered. In each iteration, the radiative cross section, $\sigma^i_{\rm rad}$, was computed from the model for each energy-loss bin, (superscript i), through Equation ($A.1$). From this, the ratio of the measured cross section over the radiative model, R^i_σ, was then computed. With n data points in the spectrum, and statistical uncertainty $\Delta\sigma^i$ for each measured cross section, this ratio was deemed statistically significant if:

$$|R^i_\sigma - 1| \cdot \frac{\sigma^i_{\rm rad}}{\Delta\sigma^i} > \sqrt{2}\,{\rm erf}^{-1}(1 - 1/n), \qquad (A.21)$$

in which case the adjustment factors $K^i(w^{i\,2})$ were multiplied by R^i_σ. If the convergence criteria were not met in this iteration, the K^i were smoothed and fitted with a cubic spline as a function of w^2, to yield $K(w^2)$ for use in the next iteration.

Two quantities were checked in the convergence test. The first was the χ^2 of the radiated model at each iteration:

$$\chi^2 = \sum_{i=1}^{n} (R_\sigma^i - 1)^2 \left(\frac{\sigma_{\rm rad}^i}{\Delta\sigma^i} \right)^2 . \qquad (A.22)$$

If χ^2/n had decreased by less than $1/5$ between successive iterations, then the convergence test was passed.

The second quantity involved the difference between radiative correction factors in successive iterations:

$$\Delta f = \sum_{i=1}^{n} \left(\frac{\sigma_{\rm nr}^i}{\sigma_{\rm rad}^i} - \frac{\sigma_{\rm nr}^i}{\sigma_{\rm rad}^i} \Big|_{\substack{\rm prev. \\ \rm iter.}} \right)^2 . \qquad (A.23)$$

If the χ^2 test had failed, but $\Delta f < n/10^4$, then the convergence test would still be passed. Thus, convergence was achieved if either the radiated model was consistent with the data, or if the radiative corrections were not changing very much between iterations. No run was allowed to terminate without making at least two iterations. Typically, three were sufficient for convergence, with no more than five needed for the worst case.

A.1.4 Sensitivity to Choice of Model

The second integral in Equation ($A.1$) requires knowlege of the cross section over only the same energy loss range, with fixed incident energy, for which we made measurements. If it were not for the first integral, then any model consistent with the data would yield the correct radiative corrections. As Equation ($A.1$) stands, we need to extrapolate the model cross section to kinematics for which we have no data to compare with. Thus, the possibility of model-dependent results must be considered. We have examined this problem in two different ways: by altering the model and

seeing what happened, and by comparing the unfolded cross sections of the thin and thick Fe targets taken at duplicate kinematics. We have found that the radiative corrections are quite stable, perhaps attributable to the fact that the integrands in $(A.1)$ are strongly peaked near $\varepsilon_1' = \varepsilon_1$ and $\varepsilon_2' = \varepsilon_2$.

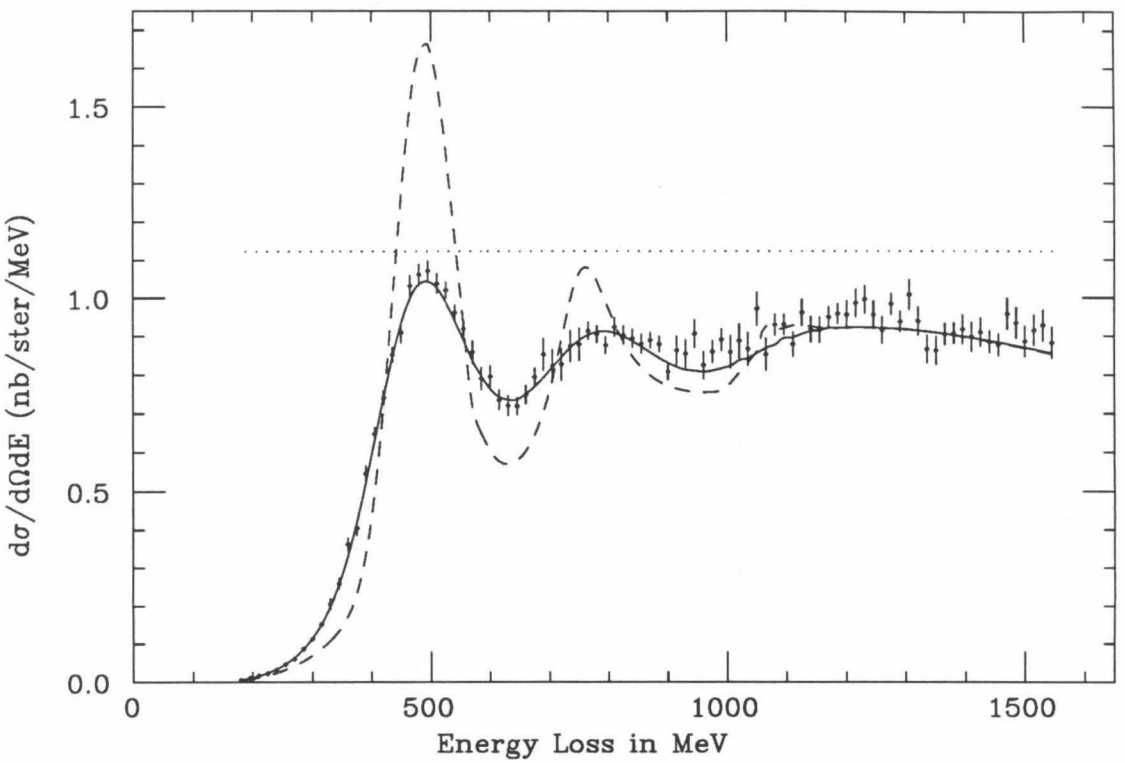

Figure A.1 – ^{4}He radiatively unfolded data at $\varepsilon_1 = 3.595$ GeV, $\theta = 16.020$ degrees, with three model cross sections described in the text.

In Figure A.1 is show the ^{4}He radiatively corrected cross section taken with $\varepsilon_1 = 3.595$ GeV, and $\theta = 16.020$ deg., along with several test model cross sections, before adjustment. The solid line is the model with which we unfolded the raw data to produce the plotted data points. The dashed line was obtained by altering the parameters of this model's $F(y)$ and suppressing the convolution integral, while the dotted line is just σ_{mott} (times a constant). After convergence is reached, each model,

when radiated, will reproduce the observed cross sections. However, the radiative correction factors could, in principle, be quite different, since the models have different ε_1 dependences.

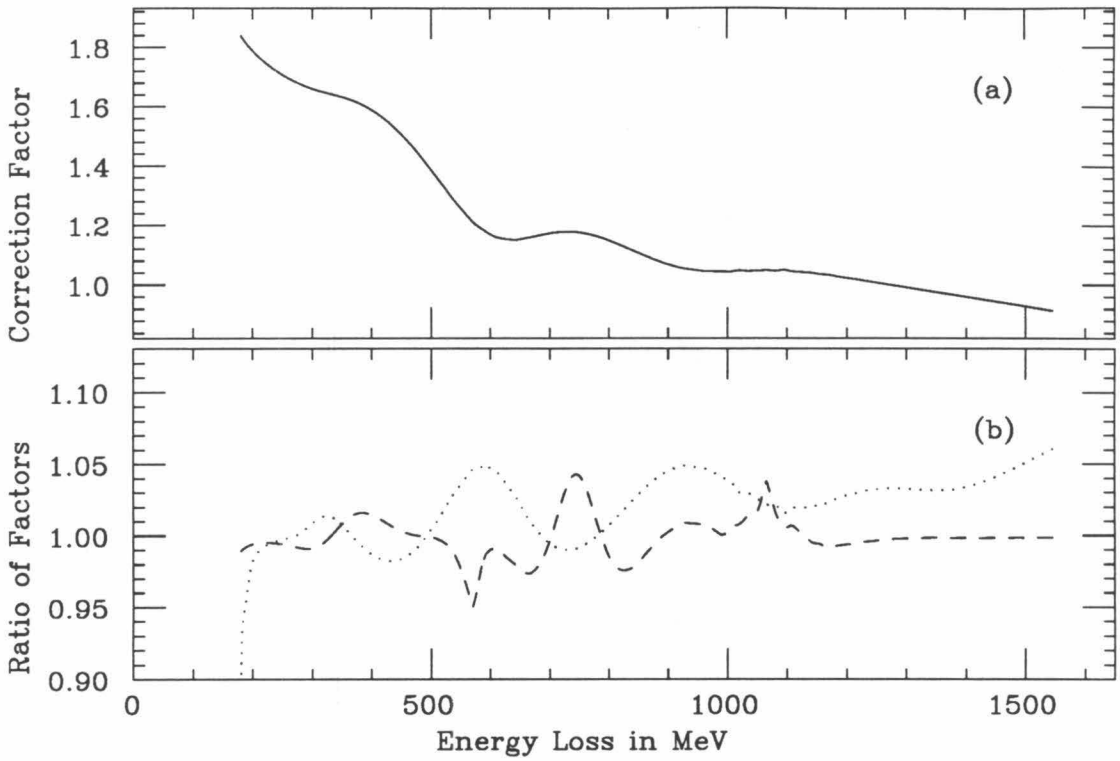

Figure A.2 – Comparison of test model radiative correction factors: (a) σ_{nr}/σ_{rad} for the data of the previous figure using the standard model; (b) radiative correction factors for the other two models divided by the curve in (a).

In Figure A.2(a) is shown the radiative correction factor σ_{nr}/σ_{rad} as a function of energy loss for the ^{4}He data of the previous figure, using the standard model. In A.2(b) are shown the correction factors obtained with the other two models, divided by the curve in A.2(a). The cusps in the dashed line are a result of kinks in the unsmeared, Bodek cross section, which are suppressed in the smeared model. At worst, the radiative corrections from this altered model deviate by 5%, in the region

of the delta resonance. On the quasi-elastic peak, the deviations are smaller. The deviations of the featureless Mott cross-section model are also in the range of 5%, except for the smallest energy loss point.

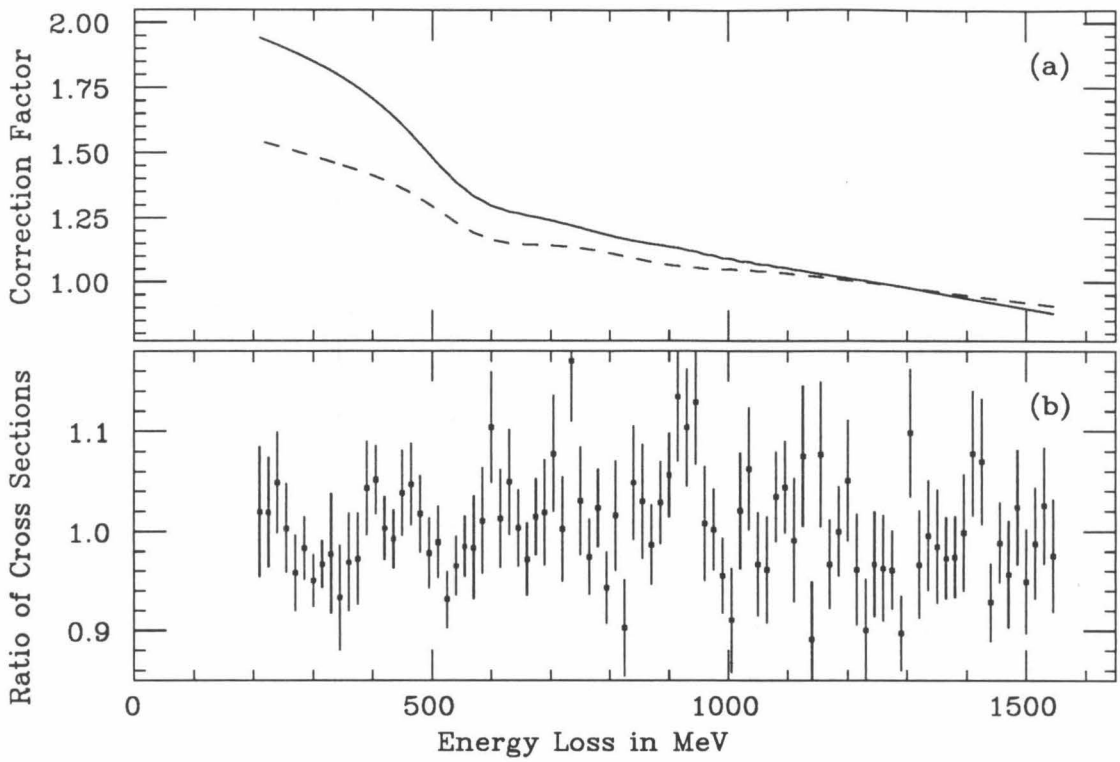

Figure A.3 – Comparison of the radiative corrections for the two Fe targets: (a) Radiative correction factors for 2% r.l. Fe (dashes) and 6% r.l. Fe (solid line) targets; (b) ratio of unfolded cross sections (6%/2% targets)

The unadjusted standard model never deviates from the unfolded cross section as badly as the curves in Figure A.1. Consequently, the adjustment factors, $K(w^2)$, are smaller, and the errors in extrapolation should be less. This is corroborated by the comparison between the thick and thin Fe data at 3.6 GeV and 16 degrees. In Figure A.3(a) are shown the radiative correction factors for the the 2% r.l. Fe target (dashes) and 6% r.l. Fe target (solid line), which are quite different. In Figure A.3(b) is

shown the ratio of the unfolded cross sections (thick/thin). The observed fluctuations are caused by fluctuations in the data, not by fluctuations in the smooth correction factors. No evidence of smoothly varying deviations from 1.0 can be seen, and the average cross-section ratio is 0.993, with $\chi^2 = 101.5$, for 90 data points. Based on these tests, we assigned a systematic uncertainty of 2% to the quasi-elastic radiative corrections.

A.2 Elastic Data

Since the non-radiative elastic cross section is a delta function of energy loss, the radiative corrections are (in principle) exactly calculable. In practice, only the corrections for one-photon diagrams are directly computed, and they take the general form [64]:

$$d\sigma/d\Omega|_{\mathrm{meas}} = (1+\delta)(d\sigma/d\Omega)|_{\mathrm{Born}}. \qquad (A.24)$$

Multiple photon emission is accounted for by replacing the $(1+\delta)$ above with e^{δ}, which is strictly valid only for the infrared divergent part of the corrections [65]. However, the error in the approximation has been estimated [64] at 0.7% at a q^2 of 20 GeV^2, and should be much smaller at our kinematics. Thus, the exponential approximation is well justified.

We computed the radiative corrections via Equations (II.6) and (II.9) of Reference [64]. These are equations for δ, including effects that are due to recoil and photon emission by the proton, and straggling by the electron before and after the primary scattering. The latter depends on the amount of material before and after the scattering. Thus, radiative corrections were computed at 2 mm intervals along the length of the target, using a model of the target's geometry [66], and averaged to

E_0	θ	F
2.020	15.023	1.388
2.020	20.017	1.389
3.595	16.021	1.410
3.595	20.017	1.410
3.595	25.013	1.408
3.595	30.011	1.406
3.595	39.008	1.402

Table A.2 – Radiative correction factors for the hydrogen elastic cross sections. E_0 is the incident energy in GeV, θ is the scattering angle, and F is the correction factor.

yield a correction to apply to our data. Table A.2 lists the multiplicative corrections for all of our kinematics.

Appendix B
Data Tables

Listed below are tables of the final, radiatively unfolded cross sections and the $F(y)$'s obtained from them. The cross-section units are nB/MeV/steradian, and are tabulated versus the energy loss (ω, in MeV) for each target. The statistical uncertainty in the two least significant digits is the number in parentheses (e.g., $1.234(56) \Longleftrightarrow 1.234 \pm 0.056$). Empty boxes in the tables indicate unmeasured data, or data that was rejected because it was within 50 MeV of the elastic peak or had uncertainty greater than 50%. The units of $F(y)$ are GeV^{-1}, and are tabulated versus y, in GeV/c.

ω	^{4}He	C	Al	Fe	Au
60			$4.58(11)E+01$	$9.04(24)E+01$	$3.058(69)E+02$
75		$2.798(48)E+01$	$6.48(13)E+01$	$1.290(29)E+02$	$4.064(78)E+02$
90	$1.131(16)E+01$	$3.759(56)E+01$	$8.38(15)E+01$	$1.619(33)E+02$	$5.145(89)E+02$
105	$1.770(55)E+01$	$5.08(12)E+01$	$1.018(32)E+02$	$2.175(82)E+02$	$6.33(21)E+02$
120	$2.296(61)E+01$	$5.69(12)E+01$	$1.159(34)E+02$	$2.320(84)E+02$	$7.34(22)E+02$
135	$2.893(47)E+01$	$6.468(99)E+01$	$1.290(27)E+02$	$2.463(65)E+02$	$7.57(17)E+02$
150	$2.971(48)E+01$	$6.70(10)E+01$	$1.331(27)E+02$	$2.593(66)E+02$	$7.95(17)E+02$
165	$2.901(62)E+01$	$6.79(15)E+01$	$1.347(39)E+02$	$2.713(98)E+02$	$8.13(26)E+02$
180	$2.482(55)E+01$	$6.43(14)E+01$	$1.333(37)E+02$	$2.580(92)E+02$	$8.12(25)E+02$
195	$2.019(47)E+01$	$5.77(13)E+01$	$1.221(35)E+02$	$2.434(86)E+02$	$7.62(23)E+02$
210	$1.668(26)E+01$	$5.376(98)E+01$	$1.150(25)E+02$	$2.377(59)E+02$	$7.38(15)E+02$
225	$1.326(23)E+01$	$4.869(93)E+01$	$1.029(24)E+02$	$2.168(57)E+02$	$6.96(14)E+02$
240	$1.064(24)E+01$	$4.01(12)E+01$	$9.11(30)E+01$	$2.000(69)E+02$	$6.34(16)E+02$
255	$8.81(21)E+00$	$3.42(11)E+01$	$8.48(29)E+01$	$1.763(63)E+02$	$5.96(15)E+02$
270	$7.52(20)E+00$	$2.95(10)E+01$	$7.47(27)E+01$	$1.653(61)E+02$	$5.73(15)E+02$
285	$6.82(14)E+00$	$2.832(74)E+01$	$7.17(19)E+01$	$1.503(41)E+02$	$5.24(12)E+02$
300	$6.76(19)E+00$	$2.90(10)E+01$	$6.96(26)E+01$	$1.619(59)E+02$	$5.17(19)E+02$
315	$6.73(19)E+00$	$2.614(98)E+01$	$6.81(26)E+01$	$1.426(54)E+02$	$4.68(18)E+02$
330	$7.21(19)E+00$	$2.92(10)E+01$	$6.59(25)E+01$	$1.330(51)E+02$	$4.82(18)E+02$
345	$7.73(21)E+00$	$2.94(11)E+01$	$6.92(27)E+01$	$1.405(55)E+02$	$4.98(19)E+02$
360	$8.17(22)E+00$	$2.79(11)E+01$	$7.27(28)E+01$	$1.392(57)E+02$	$4.98(20)E+02$

Table B.1 – $d\sigma/d\Omega/d\varepsilon$ vs. ω for $E_0 = 2.020$ GeV, $\theta = 15.023$ deg.

ω	^{4}He	C	Al	Fe	Au
60			$6.44(28)E-01$	$1.245(65)E+00$	$5.10(26)E+00$
75		$4.64(14)E-01$	$1.305(39)E+00$	$2.628(93)E+00$	$9.51(35)E+00$
90		$8.53(19)E-01$	$2.340(53)E+00$	$4.80(13)E+00$	$1.627(46)E+01$
105		$1.364(24)E+00$	$3.539(63)E+00$	$7.56(15)E+00$	$2.604(56)E+01$
120	$2.81(37)E-01$	$2.03(14)E+00$	$5.93(35)E+00$	$1.161(67)E+01$	$3.94(23)E+01$
135	$6.54(50)E-01$	$3.34(17)E+00$	$8.18(39)E+00$	$1.556(76)E+01$	$5.55(26)E+01$
150	$1.104(51)E+00$	$4.30(15)E+00$	$1.063(34)E+01$	$2.249(69)E+01$	$6.98(22)E+01$
165	$1.613(59)E+00$	$5.85(17)E+00$	$1.401(39)E+01$	$2.691(74)E+01$	$8.78(24)E+01$
180	$2.166(52)E+00$	$7.64(17)E+00$	$1.596(36)E+01$	$3.432(75)E+01$	$1.026(23)E+02$
195	$2.999(58)E+00$	$9.23(19)E+00$	$1.913(40)E+01$	$3.732(78)E+01$	$1.159(24)E+02$
210	$3.891(79)E+00$	$1.055(26)E+01$	$2.092(54)E+01$	$4.17(11)E+01$	$1.308(33)E+02$
225	$4.697(73)E+00$	$1.121(23)E+01$	$2.299(49)E+01$	$4.660(96)E+01$	$1.397(29)E+02$
240	$4.805(78)E+00$	$1.168(29)E+01$	$2.401(62)E+01$	$4.90(12)E+01$	$1.464(36)E+02$
255	$5.082(73)E+00$	$1.200(23)E+01$	$2.377(48)E+01$	$5.17(10)E+01$	$1.496(30)E+02$
270	$4.716(99)E+00$	$1.170(27)E+01$	$2.523(59)E+01$	$4.95(12)E+01$	$1.486(37)E+02$
285	$4.229(92)E+00$	$1.122(26)E+01$	$2.459(57)E+01$	$4.80(11)E+01$	$1.428(36)E+02$
300	$3.543(84)E+00$	$1.063(25)E+01$	$2.306(56)E+01$	$4.50(11)E+01$	$1.446(36)E+02$
315	$3.03(13)E+00$	$9.70(29)E+00$	$2.284(70)E+01$	$4.40(15)E+01$	$1.464(51)E+02$
330	$2.716(74)E+00$	$9.35(20)E+00$	$2.159(50)E+01$	$4.030(98)E+01$	$1.427(34)E+02$
345	$2.386(83)E+00$	$8.69(26)E+00$	$2.005(68)E+01$	$4.32(14)E+01$	$1.411(45)E+02$
360	$2.284(79)E+00$	$8.32(25)E+00$	$1.930(66)E+01$	$3.94(13)E+01$	$1.317(42)E+02$
375	$2.043(73)E+00$	$7.57(23)E+00$	$1.847(63)E+01$	$3.80(12)E+01$	$1.405(42)E+02$
390	$1.886(40)E+00$	$7.41(16)E+00$	$1.728(40)E+01$	$3.588(83)E+01$	$1.290(28)E+02$
405	$1.970(41)E+00$	$7.06(16)E+00$	$1.740(40)E+01$	$3.652(85)E+01$	$1.251(28)E+02$
420	$1.994(49)E+00$	$6.63(21)E+00$	$1.722(51)E+01$	$3.77(12)E+01$	$1.275(38)E+02$
435	$2.066(50)E+00$	$6.94(22)E+00$	$1.730(51)E+01$	$3.37(11)E+01$	$1.258(38)E+02$
450	$2.152(53)E+00$	$7.60(23)E+00$	$1.684(52)E+01$	$3.41(11)E+01$	$1.266(40)E+02$

Table B.2 – $d\sigma/d\Omega/d\varepsilon$ vs. ω for $E_0 = 2.020$ GeV, $\theta = 20.017$ deg.

ω	^{4}He	C	Al	Fe	Au
60				$3.88(32)E-03$	$1.26(14)E-02$
75			$3.08(23)E-03$	$7.45(45)E-03$	$2.60(20)E-02$
90			$6.45(32)E-03$	$1.658(65)E-02$	$6.13(30)E-02$
105		$3.42(11)E-03$	$1.279(44)E-02$	$2.949(85)E-02$	$1.077(38)E-01$
120		$6.22(16)E-03$	$2.120(58)E-02$	$4.48(11)E-02$	$1.692(49)E-01$
135		$1.031(20)E-02$	$3.203(72)E-02$	$7.18(14)E-02$	$2.686(63)E-01$
150		$1.648(25)E-02$	$4.645(84)E-02$	$1.063(16)E-01$	$3.889(73)E-01$
165		$2.488(31)E-02$	$7.07(10)E-02$	$1.509(19)E-01$	$5.376(86)E-01$
180		$3.669(40)E-02$	$9.53(13)E-02$	$2.088(24)E-01$	$7.38(11)E-01$
195		$5.206(48)E-02$	$1.401(16)E-01$	$2.867(29)E-01$	$1.010(13)E+00$

Table B.3 – $d\sigma/d\Omega/d\varepsilon$ vs. ω for $E_0 = 3.605$ GeV, $\theta = 16.021$ deg.

ω	^{4}He	C	Al	Fe	Au
180	$5.13(46)E-03$				
195	$1.083(96)E-02$				
210	$1.67(11)E-02$	$7.99(42)E-02$	$2.066(84)E-01$	$4.64(15)E-01$	$1.508(65)E+00$
225	$2.22(13)E-02$	$1.159(50)E-01$	$2.869(99)E-01$	$6.36(17)E-01$	$1.946(73)E+00$
240	$3.10(15)E-02$	$1.621(58)E-01$	$3.71(11)E-01$	$8.08(19)E-01$	$2.558(84)E+00$
255	$4.48(18)E-02$	$2.154(68)E-01$	$5.23(14)E-01$	$1.005(22)E+00$	$3.51(10)E+00$
270	$5.93(21)E-02$	$2.684(79)E-01$	$6.99(17)E-01$	$1.345(26)E+00$	$4.55(12)E+00$
285	$8.42(25)E-02$	$3.627(86)E-01$	$8.36(17)E-01$	$1.823(29)E+00$	$6.00(13)E+00$
300	$1.096(28)E-01$	$4.709(96)E-01$	$1.156(20)E+00$	$2.344(32)E+00$	$7.68(14)E+00$
315	$1.473(32)E-01$	$6.11(11)E-01$	$1.434(22)E+00$	$2.941(36)E+00$	$9.48(16)E+00$
330	$1.99(13)E-01$	$7.87(31)E-01$	$1.761(99)E+00$	$3.72(11)E+00$	$1.218(53)E+01$
345	$2.51(14)E-01$	$9.84(34)E-01$	$1.95(10)E+00$	$4.42(12)E+00$	$1.518(59)E+01$
360	$3.52(16)E-01$	$1.215(38)E+00$	$2.81(12)E+00$	$5.39(14)E+00$	$1.788(63)E+01$
375	$3.95(17)E-01$	$1.420(40)E+00$	$3.30(13)E+00$	$6.24(15)E+00$	$1.992(66)E+01$
390	$5.34(19)E-01$	$1.598(43)E+00$	$3.71(14)E+00$	$6.93(15)E+00$	$2.214(70)E+01$
405	$6.38(16)E-01$	$1.869(38)E+00$	$4.19(11)E+00$	$8.06(13)E+00$	$2.461(52)E+01$
420	$7.33(17)E-01$	$2.125(40)E+00$	$4.44(11)E+00$	$8.59(13)E+00$	$2.785(55)E+01$
435	$8.46(18)E-01$	$2.283(41)E+00$	$4.66(11)E+00$	$9.49(14)E+00$	$2.949(55)E+01$
450	$9.06(26)E-01$	$2.310(63)E+00$	$5.34(16)E+00$	$1.006(20)E+01$	$3.129(73)E+01$
465	$1.031(27)E+00$	$2.534(64)E+00$	$5.53(15)E+00$	$1.064(20)E+01$	$3.336(73)E+01$
480	$1.063(27)E+00$	$2.645(65)E+00$	$5.45(15)E+00$	$1.074(20)E+01$	$3.431(72)E+01$
495	$1.074(26)E+00$	$2.651(64)E+00$	$5.45(15)E+00$	$1.132(20)E+01$	$3.544(72)E+01$
510	$1.040(25)E+00$	$2.740(64)E+00$	$5.34(15)E+00$	$1.118(20)E+01$	$3.618(72)E+01$
525	$1.022(21)E+00$	$2.607(49)E+00$	$5.58(12)E+00$	$1.128(17)E+01$	$3.653(68)E+01$
540	$9.61(19)E-01$	$2.653(49)E+00$	$5.61(12)E+00$	$1.093(17)E+01$	$3.488(66)E+01$
555	$9.18(19)E-01$	$2.571(48)E+00$	$5.71(12)E+00$	$1.097(17)E+01$	$3.599(68)E+01$
570	$8.56(29)E-01$	$2.606(74)E+00$	$5.61(19)E+00$	$1.093(29)E+01$	$3.66(16)E+01$
585	$7.87(28)E-01$	$2.425(70)E+00$	$5.27(19)E+00$	$1.111(29)E+01$	$3.74(16)E+01$
600	$7.91(27)E-01$	$2.421(67)E+00$	$5.35(18)E+00$	$1.118(28)E+01$	$3.80(15)E+01$
615	$7.31(25)E-01$	$2.508(67)E+00$	$5.65(18)E+00$	$1.139(27)E+01$	$3.77(15)E+01$
630	$7.16(25)E-01$	$2.407(66)E+00$	$5.31(18)E+00$	$1.083(27)E+01$	$3.80(15)E+01$
645	$7.14(22)E-01$	$2.319(56)E+00$	$5.33(14)E+00$	$1.158(22)E+01$	$3.66(11)E+01$
660	$7.43(23)E-01$	$2.435(57)E+00$	$5.61(15)E+00$	$1.160(22)E+01$	$3.89(12)E+01$
675	$7.89(23)E-01$	$2.429(56)E+00$	$5.73(14)E+00$	$1.131(21)E+01$	$3.99(11)E+01$
690	$8.48(40)E-01$	$2.552(92)E+00$	$5.55(20)E+00$	$1.161(29)E+01$	$4.34(16)E+01$
705	$8.19(41)E-01$	$2.497(93)E+00$	$5.62(21)E+00$	$1.136(29)E+01$	$4.09(16)E+01$
720	$8.24(40)E-01$	$2.738(97)E+00$	$5.82(21)E+00$	$1.179(30)E+01$	$4.31(16)E+01$
735	$8.71(40)E-01$	$2.636(91)E+00$	$6.01(21)E+00$	$1.141(28)E+01$	$4.14(15)E+01$
750	$8.76(41)E-01$	$2.766(98)E+00$	$5.92(21)E+00$	$1.180(30)E+01$	$3.90(15)E+01$
765	$9.11(22)E-01$	$2.745(71)E+00$	$6.33(17)E+00$	$1.191(23)E+01$	$4.29(11)E+01$
780	$9.03(21)E-01$	$2.557(66)E+00$	$6.08(16)E+00$	$1.207(22)E+01$	$4.01(11)E+01$
795	$8.74(21)E-01$	$2.693(70)E+00$	$5.95(16)E+00$	$1.215(23)E+01$	$4.20(11)E+01$
810	$9.22(24)E-01$	$2.440(90)E+00$	$5.80(22)E+00$	$1.229(33)E+01$	$4.38(15)E+01$
825	$9.00(24)E-01$	$2.781(97)E+00$	$6.07(23)E+00$	$1.230(33)E+01$	$4.29(15)E+01$
840	$8.92(23)E-01$	$2.675(94)E+00$	$6.38(23)E+00$	$1.193(32)E+01$	$4.22(15)E+01$
855	$8.78(23)E-01$	$2.593(92)E+00$	$6.01(23)E+00$	$1.158(32)E+01$	$4.22(15)E+01$
870	$8.86(20)E-01$	$2.505(74)E+00$	$6.02(18)E+00$	$1.207(24)E+01$	$3.98(11)E+01$
885	$8.76(20)E-01$	$2.736(78)E+00$	$5.95(18)E+00$	$1.230(24)E+01$	$4.31(12)E+01$
900	$8.05(19)E-01$	$2.674(77)E+00$	$6.14(18)E+00$	$1.236(24)E+01$	$4.21(12)E+01$
915	$8.60(36)E-01$	$2.85(13)E+00$	$5.80(27)E+00$	$1.225(33)E+01$	$4.39(18)E+01$
930	$8.51(35)E-01$	$2.65(12)E+00$	$6.67(29)E+00$	$1.338(34)E+01$	$4.14(17)E+01$
945	$9.03(36)E-01$	$2.80(13)E+00$	$6.07(28)E+00$	$1.295(34)E+01$	$4.39(18)E+01$
960	$8.22(35)E-01$	$2.53(12)E+00$	$6.07(28)E+00$	$1.196(33)E+01$	$4.15(18)E+01$
975	$8.56(27)E-01$	$2.614(82)E+00$	$6.35(20)E+00$	$1.289(26)E+01$	$4.34(12)E+01$

Table B.4 – $d\sigma/d\Omega/d\varepsilon$ vs. $\omega \leq 975$ for $E_0 = 3.595$ GeV, $\theta = 16.021$ deg.

ω	^{4}He	C	Al	Fe	Au
990	$8.88(28)E-01$	$2.598(81)E+00$	$6.23(20)E+00$	$1.290(25)E+01$	$4.50(12)E+01$
1005	$8.56(41)E-01$	$2.80(11)E+00$	$6.58(28)E+00$	$1.251(36)E+01$	$4.14(16)E+01$
1020	$8.85(43)E-01$	$2.95(12)E+00$	$6.43(28)E+00$	$1.318(37)E+01$	$4.50(17)E+01$
1035	$8.64(42)E-01$	$2.74(11)E+00$	$6.59(29)E+00$	$1.254(36)E+01$	$4.45(16)E+01$
1050	$9.68(43)E-01$	$2.73(11)E+00$	$6.22(27)E+00$	$1.347(36)E+01$	$4.39(16)E+01$
1065	$8.50(41)E-01$	$2.79(11)E+00$	$6.50(28)E+00$	$1.314(37)E+01$	$4.49(16)E+01$
1080	$9.27(27)E-01$	$2.804(82)E+00$	$5.98(19)E+00$	$1.325(28)E+01$	$4.19(12)E+01$
1095	$9.28(26)E-01$	$2.629(78)E+00$	$6.31(20)E+00$	$1.277(28)E+01$	$4.41(12)E+01$
1110	$8.77(31)E-01$	$2.84(11)E+00$	$6.21(27)E+00$	$1.361(42)E+01$	$4.53(18)E+01$
1125	$9.59(33)E-01$	$2.77(11)E+00$	$5.91(26)E+00$	$1.280(41)E+01$	$4.26(17)E+01$
1140	$9.16(33)E-01$	$2.78(12)E+00$	$6.23(27)E+00$	$1.338(43)E+01$	$4.30(18)E+01$
1155	$9.14(33)E-01$	$2.89(12)E+00$	$6.47(28)E+00$	$1.244(42)E+01$	$4.25(18)E+01$
1170	$9.47(26)E-01$	$3.062(73)E+00$	$6.48(20)E+00$	$1.322(30)E+01$	$4.74(13)E+01$
1185	$9.56(25)E-01$	$3.024(68)E+00$	$5.99(18)E+00$	$1.289(29)E+01$	$4.56(12)E+01$
1200	$9.53(36)E-01$	$2.743(75)E+00$	$6.66(26)E+00$	$1.374(39)E+01$	$4.60(16)E+01$
1215	$9.84(36)E-01$	$2.836(75)E+00$	$6.52(25)E+00$	$1.268(37)E+01$	$4.35(15)E+01$
1230	$9.94(35)E-01$	$2.889(74)E+00$	$7.05(26)E+00$	$1.273(36)E+01$	$4.54(16)E+01$
1245	$9.54(35)E-01$	$2.992(76)E+00$	$6.64(25)E+00$	$1.394(38)E+01$	$4.88(16)E+01$
1260	$9.14(34)E-01$	$2.938(75)E+00$	$6.68(25)E+00$	$1.376(38)E+01$	$4.63(16)E+01$
1275	$9.82(26)E-01$	$2.965(61)E+00$	$6.43(18)E+00$	$1.305(27)E+01$	$4.64(12)E+01$
1290	$9.36(26)E-01$	$2.872(61)E+00$	$6.44(19)E+00$	$1.311(27)E+01$	$4.61(13)E+01$
1305	$1.007(39)E+00$	$2.738(95)E+00$	$6.46(26)E+00$	$1.337(39)E+01$	$4.28(18)E+01$
1320	$9.38(37)E-01$	$2.834(93)E+00$	$6.69(26)E+00$	$1.321(37)E+01$	$4.58(18)E+01$
1335	$8.65(35)E-01$	$2.811(92)E+00$	$6.62(25)E+00$	$1.332(37)E+01$	$4.38(18)E+01$
1350	$8.61(36)E-01$	$3.071(99)E+00$	$6.39(26)E+00$	$1.280(37)E+01$	$4.19(18)E+01$
1365	$9.03(27)E-01$	$2.814(74)E+00$	$6.57(18)E+00$	$1.304(27)E+01$	$4.43(14)E+01$
1380	$9.06(27)E-01$	$2.835(74)E+00$	$6.34(17)E+00$	$1.279(27)E+01$	$4.33(13)E+01$
1395	$9.16(38)E-01$	$2.86(11)E+00$	$6.24(22)E+00$	$1.272(37)E+01$	$4.50(19)E+01$
1410	$8.97(37)E-01$	$3.01(11)E+00$	$6.38(22)E+00$	$1.283(37)E+01$	$4.65(19)E+01$
1425	$9.09(37)E-01$	$2.56(10)E+00$	$6.37(22)E+00$	$1.217(35)E+01$	$4.14(18)E+01$
1440	$8.83(28)E-01$	$2.816(80)E+00$	$6.47(18)E+00$	$1.220(26)E+01$	$4.14(13)E+01$
1455	$8.76(27)E-01$	$2.754(78)E+00$	$6.04(17)E+00$	$1.283(26)E+01$	$4.25(13)E+01$
1470	$9.56(40)E-01$	$2.80(11)E+00$	$6.11(25)E+00$	$1.228(34)E+01$	$4.58(18)E+01$
1485	$9.33(39)E-01$	$2.60(10)E+00$	$6.20(25)E+00$	$1.237(34)E+01$	$4.25(17)E+01$
1500	$8.85(39)E-01$	$2.66(11)E+00$	$5.92(24)E+00$	$1.267(35)E+01$	$4.39(17)E+01$
1515	$9.13(39)E-01$	$2.67(11)E+00$	$5.88(24)E+00$	$1.193(34)E+01$	$4.18(17)E+01$
1530	$9.27(40)E-01$	$2.73(11)E+00$	$5.89(25)E+00$	$1.241(35)E+01$	$4.02(17)E+01$
1545	$8.81(39)E-01$	$2.52(10)E+00$	$6.30(26)E+00$	$1.207(35)E+01$	$4.06(17)E+01$

Table B.5 – $d\sigma/d\Omega/d\varepsilon$ vs. $\omega \geq 990$ for $E_0 = 3.595$ GeV, $\theta = 16.021$ deg.

ω	^{4}He	C	Al	Fe	Au
135				$1.14(54)E-04$	
150				$4.72(92)E-04$	
165		$6.0(28)E-05$	$2.43(96)E-04$	$6.3(11)E-04$	$1.87(65)E-03$
180		$1.44(36)E-04$	$8.0(16)E-04$	$1.04(17)E-03$	$2.75(66)E-03$
195		$2.20(40)E-04$	$5.0(12)E-04$	$2.03(22)E-03$	$5.81(95)E-03$
210		$3.53(49)E-04$	$1.05(16)E-03$	$2.47(23)E-03$	$8.1(11)E-03$
225		$5.97(66)E-04$	$1.83(22)E-03$	$3.87(29)E-03$	$1.47(15)E-02$
240		$1.027(89)E-03$	$2.31(26)E-03$	$6.65(39)E-03$	$2.12(18)E-02$
255	$1.35(57)E-04$	$1.25(10)E-03$	$3.50(33)E-03$	$8.01(44)E-03$	$3.19(23)E-02$
270	$1.93(28)E-04$	$1.92(11)E-03$	$5.27(37)E-03$	$1.216(47)E-02$	$3.84(20)E-02$
285	$4.06(33)E-04$	$2.66(13)E-03$	$7.18(42)E-03$	$1.588(53)E-02$	$5.35(23)E-02$
300	$5.89(41)E-04$	$3.77(15)E-03$	$9.58(48)E-03$	$2.001(58)E-02$	$6.91(26)E-02$
315	$8.51(48)E-04$	$5.01(38)E-03$	$1.34(13)E-02$	$2.94(14)E-02$	$9.97(49)E-02$
330	$1.278(57)E-03$	$6.71(43)E-03$	$1.86(16)E-02$	$3.71(15)E-02$	$1.235(54)E-01$
345	$1.909(65)E-03$	$8.45(49)E-03$	$2.56(18)E-02$	$4.81(17)E-02$	$1.638(61)E-01$
360	$2.412(76)E-03$	$1.174(58)E-02$	$3.06(20)E-02$	$6.49(20)E-02$	$2.043(68)E-01$
375	$3.164(86)E-03$	$1.448(65)E-02$	$4.16(24)E-02$	$7.25(21)E-02$	$2.507(76)E-01$
390	$4.213(99)E-03$	$1.780(72)E-02$	$4.84(26)E-02$	$9.16(24)E-02$	$3.170(87)E-01$
405	$5.44(11)E-03$	$2.505(80)E-02$	$5.54(23)E-02$	$1.165(26)E-01$	$4.087(95)E-01$
420	$6.81(13)E-03$	$3.035(88)E-02$	$7.15(26)E-02$	$1.443(30)E-01$	$4.96(11)E-01$
435	$8.58(14)E-03$	$3.99(10)E-02$	$9.06(30)E-02$	$1.812(34)E-01$	$6.13(12)E-01$
450	$1.163(60)E-02$	$4.70(23)E-02$	$1.163(54)E-01$	$2.41(11)E-01$	$8.50(36)E-01$
465	$1.446(64)E-02$	$6.10(26)E-02$	$1.563(61)E-01$	$2.83(12)E-01$	$1.052(39)E+00$
480	$1.762(71)E-02$	$8.44(30)E-02$	$1.830(66)E-01$	$3.54(13)E-01$	$1.239(41)E+00$
495	$2.332(79)E-02$	$9.73(32)E-02$	$2.185(71)E-01$	$4.65(15)E-01$	$1.487(45)E+00$
510	$2.889(87)E-02$	$1.221(35)E-01$	$2.746(79)E-01$	$5.84(17)E-01$	$1.715(48)E+00$
525	$3.603(90)E-02$	$1.438(33)E-01$	$3.303(80)E-01$	$6.39(16)E-01$	$2.051(47)E+00$
540	$4.56(10)E-02$	$1.677(36)E-01$	$3.921(87)E-01$	$7.73(17)E-01$	$2.384(51)E+00$
555	$5.50(11)E-02$	$1.986(40)E-01$	$4.586(95)E-01$	$8.81(19)E-01$	$2.785(56)E+00$
570	$7.00(28)E-02$	$2.455(79)E-01$	$5.14(21)E-01$	$9.89(39)E-01$	$3.10(12)E+00$
585	$8.67(31)E-02$	$2.818(84)E-01$	$5.74(23)E-01$	$1.155(43)E+00$	$3.64(12)E+00$
600	$1.025(32)E-01$	$3.143(85)E-01$	$6.88(24)E-01$	$1.356(44)E+00$	$3.87(12)E+00$
615	$1.190(34)E-01$	$3.619(89)E-01$	$7.24(24)E-01$	$1.468(45)E+00$	$4.28(13)E+00$
630	$1.379(37)E-01$	$3.656(91)E-01$	$7.40(24)E-01$	$1.542(46)E+00$	$4.88(14)E+00$
645	$1.421(34)E-01$	$4.168(83)E-01$	$8.49(22)E-01$	$1.703(44)E+00$	$5.01(12)E+00$
660	$1.559(36)E-01$	$4.218(83)E-01$	$8.80(23)E-01$	$1.754(45)E+00$	$5.28(13)E+00$
675	$1.609(35)E-01$	$4.412(82)E-01$	$9.90(23)E-01$	$1.708(43)E+00$	$5.51(13)E+00$
690	$1.733(71)E-01$	$4.55(14)E-01$	$9.80(38)E-01$	$1.973(86)E+00$	$6.09(24)E+00$
705	$1.707(69)E-01$	$4.62(14)E-01$	$1.028(39)E+00$	$2.137(89)E+00$	$6.53(25)E+00$
720	$1.759(68)E-01$	$4.95(14)E-01$	$1.080(39)E+00$	$2.276(89)E+00$	$6.34(24)E+00$
735	$1.699(67)E-01$	$5.12(14)E-01$	$1.022(38)E+00$	$2.076(86)E+00$	$6.61(25)E+00$
750	$1.807(37)E-01$	$5.21(11)E-01$	$1.059(29)E+00$	$2.132(61)E+00$	$6.72(19)E+00$
765	$1.785(35)E-01$	$5.18(11)E-01$	$1.103(29)E+00$	$2.296(61)E+00$	$7.02(19)E+00$
780	$1.674(34)E-01$	$5.18(11)E-01$	$1.131(29)E+00$	$2.214(60)E+00$	$7.53(20)E+00$
795	$1.686(39)E-01$	$5.26(15)E-01$	$1.136(41)E+00$	$2.212(78)E+00$	$7.68(28)E+00$
810	$1.746(39)E-01$	$5.34(16)E-01$	$1.170(42)E+00$	$2.382(81)E+00$	$7.27(27)E+00$
825	$1.742(39)E-01$	$5.44(15)E-01$	$1.174(41)E+00$	$2.335(80)E+00$	$8.40(29)E+00$
840	$1.671(38)E-01$	$5.30(15)E-01$	$1.203(42)E+00$	$2.687(86)E+00$	$8.13(29)E+00$
855	$1.681(38)E-01$	$5.22(15)E-01$	$1.265(44)E+00$	$2.516(84)E+00$	$7.94(29)E+00$
870	$1.687(39)E-01$	$5.59(16)E-01$	$1.187(43)E+00$	$2.615(86)E+00$	$8.09(29)E+00$
885	$1.731(40)E-01$	$5.87(17)E-01$	$1.299(46)E+00$	$2.596(87)E+00$	$8.19(30)E+00$

Table B.6 – $d\sigma/d\Omega/d\varepsilon$ vs. ω for $E_0 = 3.595$ GeV, $\theta = 20.017$ deg.

ω	^{4}He	C	Al	Fe	Au
360		$3.0(14)E-05$	$8.8(39)E-05$	$1.20(60)E-04$	
375			$1.43(45)E-04$	$1.42(56)E-04$	$8.7(43)E-04$
390		$4.4(16)E-05$	$1.62(47)E-04$	$1.49(59)E-04$	
405	$9.9(31)E-06$	$7.1(18)E-05$	$2.37(55)E-04$	$3.22(93)E-04$	$1.84(44)E-03$
420		$8.0(19)E-05$	$2.79(62)E-04$	$6.0(11)E-04$	$2.55(53)E-03$
435	$1.95(57)E-05$	$1.36(24)E-04$	$2.80(58)E-04$	$6.7(12)E-04$	$3.19(58)E-03$
450	$2.36(79)E-05$	$1.60(27)E-04$	$4.33(72)E-04$	$1.23(16)E-03$	$3.27(61)E-03$
465	$2.5(10)E-05$	$1.89(29)E-04$	$6.21(89)E-04$	$1.00(14)E-03$	$3.80(65)E-03$
480	$6.5(10)E-05$	$2.66(30)E-04$	$7.78(87)E-04$	$1.74(18)E-03$	$5.76(71)E-03$
495	$9.1(11)E-05$	$4.38(39)E-04$	$9.87(97)E-04$	$1.93(19)E-03$	$6.07(72)E-03$
510	$8.6(13)E-05$	$5.08(43)E-04$	$1.34(11)E-03$	$3.13(24)E-03$	$8.40(88)E-03$
525	$1.38(16)E-04$	$6.35(48)E-04$	$1.41(12)E-03$	$3.72(27)E-03$	$1.11(10)E-02$
540	$2.32(36)E-04$	$8.9(12)E-04$	$2.26(29)E-03$	$4.19(69)E-03$	$1.50(29)E-02$
555	$2.39(38)E-04$	$1.17(12)E-03$	$2.48(28)E-03$	$5.82(80)E-03$	$2.38(35)E-02$
570	$2.70(47)E-04$	$1.59(15)E-03$	$2.87(30)E-03$	$7.95(91)E-03$	$1.80(30)E-02$
585	$3.77(48)E-04$	$1.86(15)E-03$	$3.85(35)E-03$	$8.92(94)E-03$	$2.76(39)E-02$
600	$4.17(51)E-04$	$2.04(17)E-03$	$5.32(43)E-03$	$9.5(10)E-03$	$2.76(40)E-02$
615	$5.66(46)E-04$	$2.35(15)E-03$	$5.02(36)E-03$	$1.007(93)E-02$	$3.76(37)E-02$
630	$6.91(50)E-04$	$3.07(17)E-03$	$6.93(42)E-03$	$1.49(11)E-02$	$4.31(38)E-02$
645	$8.47(77)E-04$	$3.20(27)E-03$	$8.31(81)E-03$	$1.71(23)E-02$	$5.30(65)E-02$
660	$1.172(90)E-03$	$4.68(34)E-03$	$1.081(94)E-02$	$1.91(25)E-02$	$7.13(79)E-02$
675	$1.304(94)E-03$	$5.87(38)E-03$	$1.46(11)E-02$	$2.53(29)E-02$	$6.83(75)E-02$
690	$1.58(10)E-03$	$6.61(39)E-03$	$1.66(11)E-02$	$2.94(30)E-02$	$9.87(89)E-02$
705	$1.97(11)E-03$	$8.26(44)E-03$	$2.02(13)E-02$	$4.04(36)E-02$	$1.27(10)E-01$
720	$2.38(11)E-03$	$1.067(43)E-02$	$2.52(11)E-02$	$5.18(33)E-02$	$1.670(96)E-01$
735	$3.05(12)E-03$	$1.328(47)E-02$	$2.95(12)E-02$	$6.18(35)E-02$	$1.777(95)E-01$
750	$3.51(13)E-03$	$1.572(52)E-02$	$3.56(13)E-02$	$7.28(38)E-02$	$2.17(11)E-01$
765	$4.99(28)E-03$	$1.860(96)E-02$	$4.25(21)E-02$	$8.42(61)E-02$	$3.03(20)E-01$
780	$6.01(31)E-03$	$2.25(11)E-02$	$5.66(25)E-02$	$1.087(69)E-01$	$3.11(20)E-01$
795	$6.74(33)E-03$	$2.67(11)E-02$	$6.56(26)E-02$	$1.267(74)E-01$	$3.32(20)E-01$
810	$7.79(36)E-03$	$3.40(13)E-02$	$7.40(29)E-02$	$1.343(76)E-01$	$4.25(23)E-01$
825	$9.89(40)E-03$	$3.51(13)E-02$	$7.58(29)E-02$	$1.576(83)E-01$	$4.97(25)E-01$
840	$1.181(38)E-02$	$4.22(11)E-02$	$8.71(25)E-02$	$1.717(62)E-01$	$5.21(20)E-01$
855	$1.360(41)E-02$	$4.72(12)E-02$	$9.62(27)E-02$	$1.940(65)E-01$	$6.20(22)E-01$
870	$1.591(83)E-02$	$5.22(19)E-02$	$1.126(47)E-01$	$2.308(95)E-01$	$6.80(34)E-01$
885	$1.837(90)E-02$	$5.40(20)E-02$	$1.271(50)E-01$	$2.352(96)E-01$	$7.83(37)E-01$
900	$2.073(94)E-02$	$6.41(21)E-02$	$1.356(51)E-01$	$2.563(99)E-01$	$8.39(38)E-01$
915	$2.25(10)E-02$	$7.20(23)E-02$	$1.522(55)E-01$	$2.86(11)E-01$	$8.95(38)E-01$
930	$2.79(11)E-02$	$7.13(22)E-02$	$1.521(55)E-01$	$3.08(11)E-01$	$9.38(40)E-01$
945	$2.580(79)E-02$	$7.75(18)E-02$	$1.676(46)E-01$	$3.078(87)E-01$	$1.034(29)E+00$
960	$3.046(84)E-02$	$8.41(19)E-02$	$1.715(47)E-01$	$3.281(89)E-01$	$1.010(28)E+00$
975	$3.30(12)E-02$	$8.72(29)E-02$	$1.988(80)E-01$	$3.76(15)E-01$	$1.102(39)E+00$
990	$3.35(12)E-02$	$9.30(31)E-02$	$1.866(77)E-01$	$3.61(15)E-01$	$1.240(43)E+00$
1005	$3.30(13)E-02$	$1.012(31)E-01$	$2.019(81)E-01$	$4.13(16)E-01$	$1.182(41)E+00$
1020	$3.56(12)E-02$	$9.37(29)E-02$	$2.070(79)E-01$	$4.19(15)E-01$	$1.256(41)E+00$
1035	$3.520(83)E-02$	$1.028(32)E-01$	$2.227(84)E-01$	$3.98(15)E-01$	$1.299(43)E+00$
1050	$3.583(79)E-02$	$1.013(23)E-01$	$2.288(60)E-01$	$4.26(12)E-01$	$1.380(35)E+00$
1065	$3.602(76)E-02$	$1.055(23)E-01$	$2.310(59)E-01$	$4.85(13)E-01$	$1.387(34)E+00$
1080	$3.783(92)E-02$	$1.132(35)E-01$	$2.469(84)E-01$	$5.19(21)E-01$	$1.538(56)E+00$
1095	$3.784(92)E-02$	$1.141(35)E-01$	$2.608(87)E-01$	$4.96(20)E-01$	$1.555(56)E+00$
1110	$3.753(92)E-02$	$1.155(36)E-01$	$2.570(88)E-01$	$5.21(21)E-01$	$1.566(58)E+00$
1125	$3.947(98)E-02$	$1.220(38)E-01$	$2.694(89)E-01$	$5.19(21)E-01$	$1.670(60)E+00$
1140	$4.05(10)E-02$	$1.197(36)E-01$	$2.810(90)E-01$	$5.09(20)E-01$	$1.753(60)E+00$
1155	$4.16(10)E-02$	$1.308(38)E-01$	$2.853(92)E-01$	$6.03(23)E-01$	$1.857(62)E+00$

Table B.7 – $d\sigma/d\Omega/d\varepsilon$ vs. ω for $E_0 = 3.595$ GeV, $\theta = 25.013$ deg.

ω	^{4}He	C	Al	Fe	Au
600				$9.3(45)E-05$	
615					
630	$6.3(19)E-06$				
645	$6.3(14)E-06$			$1.23(36)E-04$	
660	$3.9(13)E-06$			$1.99(41)E-04$	
675	$3.8(15)E-06$			$2.20(41)E-04$	
690	$8.7(20)E-06$			$2.98(50)E-04$	
705	$1.71(39)E-05$			$2.83(70)E-04$	
720	$1.30(35)E-05$			$3.53(78)E-04$	
735	$1.68(41)E-05$			$5.4(10)E-04$	
750	$2.43(39)E-05$			$5.19(73)E-04$	
765	$3.41(44)E-05$			$7.01(84)E-04$	
780	$4.86(49)E-05$			$8.27(94)E-04$	
795	$4.77(83)E-05$			$1.20(17)E-03$	
810	$6.2(10)E-05$			$1.23(17)E-03$	
825	$8.9(11)E-05$			$1.51(18)E-03$	
840	$1.02(11)E-04$			$1.77(20)E-03$	
855	$1.05(13)E-04$			$1.97(21)E-03$	
870	$1.51(13)E-04$			$2.91(24)E-03$	
885	$1.53(13)E-04$			$3.25(25)E-03$	
900	$2.58(34)E-04$			$3.24(53)E-03$	
915	$2.45(34)E-04$			$6.15(77)E-03$	
930	$3.36(37)E-04$			$6.25(74)E-03$	
945	$3.42(38)E-04$			$7.05(80)E-03$	
960	$4.15(43)E-04$			$9.93(97)E-03$	
975	$5.89(39)E-04$	$2.68(30)E-03$	$5.68(89)E-03$	$1.006(82)E-02$	$4.17(55)E-02$
990	$7.04(46)E-04$	$2.55(27)E-03$	$6.86(93)E-03$	$1.227(92)E-02$	$4.88(57)E-02$
1005	$8.01(71)E-04$	$2.84(28)E-03$	$7.04(92)E-03$	$1.70(20)E-02$	$4.48(53)E-02$
1020	$1.017(83)E-03$	$3.67(33)E-03$	$1.01(12)E-02$	$1.92(22)E-02$	$6.20(65)E-02$
1035	$1.288(92)E-03$	$5.06(38)E-03$	$9.6(11)E-03$	$2.72(25)E-02$	$6.40(65)E-02$
1050	$1.552(92)E-03$	$5.44(38)E-03$	$1.18(12)E-02$	$2.24(22)E-02$	$6.69(62)E-02$
1065	$1.98(11)E-03$	$6.46(42)E-03$	$1.51(14)E-02$	$2.74(25)E-02$	$8.74(74)E-02$
1080	$2.221(88)E-03$	$7.21(29)E-03$	$1.727(87)E-02$	$3.18(18)E-02$	$9.70(49)E-02$
1095	$2.758(96)E-03$	$8.34(31)E-03$	$1.891(91)E-02$	$3.95(20)E-02$	$1.185(54)E-01$
1110	$3.25(15)E-03$	$9.55(41)E-03$	$2.36(12)E-02$	$4.06(26)E-02$	$1.332(71)E-01$
1125	$3.66(16)E-03$	$1.124(45)E-02$	$2.69(13)E-02$	$5.03(29)E-02$	$1.382(72)E-01$
1140	$4.37(17)E-03$	$1.211(48)E-02$	$2.83(13)E-02$	$5.34(31)E-02$	$1.772(84)E-01$
1155	$5.10(19)E-03$	$1.311(50)E-02$	$2.85(14)E-02$	$6.08(33)E-02$	$1.723(83)E-01$
1170	$5.24(17)E-03$	$1.508(43)E-02$	$3.25(11)E-02$	$6.44(27)E-02$	$1.941(66)E-01$
1185	$6.20(19)E-03$	$1.675(45)E-02$	$3.68(12)E-02$	$7.17(28)E-02$	$2.142(69)E-01$
1200	$7.15(44)E-03$	$1.802(73)E-02$	$3.42(16)E-02$	$7.69(46)E-02$	$2.27(10)E-01$
1215	$7.79(45)E-03$	$1.941(74)E-02$	$4.16(18)E-02$	$8.68(48)E-02$	$2.55(11)E-01$
1230	$7.46(43)E-03$	$2.267(79)E-02$	$4.09(17)E-02$	$8.34(47)E-02$	$2.57(11)E-01$
1245	$8.52(45)E-03$	$2.168(77)E-02$	$5.10(19)E-02$	$8.96(48)E-02$	$2.68(11)E-01$
1260	$9.18(33)E-03$	$2.317(63)E-02$	$5.44(17)E-02$	$9.93(40)E-02$	$2.95(10)E-01$
1275	$9.95(34)E-03$	$2.462(65)E-02$	$5.33(17)E-02$	$1.050(42)E-01$	$3.36(11)E-01$
1290	$9.91(45)E-03$	$2.85(11)E-02$	$5.49(33)E-02$	$1.134(69)E-01$	$3.38(24)E-01$
1305	$9.63(48)E-03$	$2.79(11)E-02$	$5.50(34)E-02$	$1.104(68)E-01$	$3.84(25)E-01$

Table B.8 – $d\sigma/d\Omega/d\varepsilon$ vs. $\omega \leq 1305$ for $E_0 = 3.595$ GeV, $\theta = 30.011$ deg.

ω	^{4}He	C	Al	Fe	Au
1320	$1.020(48)E-02$	$2.93(11)E-02$	$5.92(34)E-02$	$1.192(70)E-01$	$3.94(25)E-01$
1335	$1.018(46)E-02$	$3.14(11)E-02$	$6.78(36)E-02$	$1.351(73)E-01$	$4.13(25)E-01$
1350	$1.002(37)E-02$	$3.211(91)E-02$	$7.29(27)E-02$	$1.368(61)E-01$	$4.14(17)E-01$
1365	$1.184(40)E-02$	$3.331(93)E-02$	$6.96(27)E-02$	$1.621(68)E-01$	$4.56(18)E-01$
1380	$1.382(63)E-02$	$3.40(13)E-02$	$7.87(38)E-02$	$1.56(11)E-01$	$4.79(23)E-01$
1395	$1.237(59)E-02$	$3.59(14)E-02$	$8.02(38)E-02$	$1.76(12)E-01$	$4.81(23)E-01$
1410	$1.276(60)E-02$	$3.72(14)E-02$	$8.73(39)E-02$	$1.80(11)E-01$	$4.98(23)E-01$
1425	$1.382(64)E-02$	$3.81(14)E-02$	$8.75(40)E-02$	$1.91(12)E-01$	$6.13(26)E-01$
1440	$1.382(47)E-02$	$4.34(11)E-02$	$9.79(30)E-02$	$1.768(70)E-01$	$5.77(20)E-01$
1455	$1.521(50)E-02$	$4.40(11)E-02$	$1.035(31)E-01$	$1.925(72)E-01$	$5.95(21)E-01$
1470	$1.531(71)E-02$	$4.66(16)E-02$	$1.017(41)E-01$	$2.062(91)E-01$	$6.47(36)E-01$
1485	$1.715(73)E-02$	$5.18(17)E-02$	$1.070(42)E-01$	$2.058(88)E-01$	$6.53(35)E-01$
1500	$1.598(71)E-02$	$4.97(16)E-02$	$1.122(43)E-01$	$2.108(89)E-01$	$6.64(35)E-01$
1515	$1.821(55)E-02$	$5.29(12)E-02$	$1.192(33)E-01$	$2.273(74)E-01$	$7.11(25)E-01$
1530	$1.921(57)E-02$	$5.55(12)E-02$	$1.222(33)E-01$	$2.390(76)E-01$	$7.74(27)E-01$
1545	$1.900(81)E-02$	$5.59(16)E-02$	$1.182(47)E-01$	$2.39(12)E-01$	$7.99(37)E-01$
1560	$2.022(81)E-02$	$6.22(17)E-02$	$1.321(49)E-01$	$2.78(13)E-01$	$8.44(37)E-01$
1575	$2.218(83)E-02$	$5.89(16)E-02$	$1.322(47)E-01$	$2.57(12)E-01$	$8.49(36)E-01$
1590	$2.223(86)E-02$	$6.11(17)E-02$	$1.445(51)E-01$	$2.78(13)E-01$	$9.10(39)E-01$
1605	$2.238(57)E-02$	$6.66(15)E-02$	$1.452(40)E-01$	$2.666(84)E-01$	$1.019(29)E+00$
1620	$2.425(77)E-02$	$6.56(25)E-02$	$1.559(62)E-01$	$2.99(12)E-01$	$1.006(38)E+00$
1635	$2.474(77)E-02$	$7.46(27)E-02$	$1.661(64)E-01$	$3.13(12)E-01$	$1.164(41)E+00$
1650	$2.528(78)E-02$	$7.74(28)E-02$	$1.674(65)E-01$	$3.34(12)E-01$	$1.099(40)E+00$
1665	$2.709(79)E-02$	$7.39(27)E-02$	$1.769(66)E-01$	$3.34(12)E-01$	$1.161(41)E+00$
1680	$2.655(68)E-02$	$7.86(22)E-02$	$1.816(47)E-01$	$3.585(98)E-01$	$1.201(35)E+00$
1695	$2.67(12)E-02$	$8.66(36)E-02$	$1.830(65)E-01$	$3.52(14)E-01$	$1.250(59)E+00$
1710	$2.83(12)E-02$	$8.88(35)E-02$	$1.918(64)E-01$	$3.82(14)E-01$	$1.281(57)E+00$
1725	$3.13(12)E-02$	$8.53(33)E-02$	$2.019(64)E-01$	$3.94(14)E-01$	$1.310(56)E+00$
1740	$2.95(12)E-02$	$9.26(35)E-02$	$2.017(64)E-01$	$4.34(15)E-01$	$1.324(57)E+00$
1755	$3.085(86)E-02$	$9.95(26)E-02$	$2.168(53)E-01$	$4.28(13)E-01$	$1.463(43)E+00$
1770	$3.222(28)E-02$	$1.010(25)E-01$	$2.176(53)E-01$	$4.13(13)E-01$	$1.463(43)E+00$
1785	$3.286(28)E-02$	$1.041(35)E-01$	$2.142(81)E-01$	$5.00(27)E-01$	$1.567(60)E+00$
1800	$3.396(28)E-02$	$1.105(36)E-01$	$2.354(85)E-01$	$4.60(26)E-01$	$1.544(59)E+00$
1815	$3.445(28)E-02$	$1.082(35)E-01$	$2.389(85)E-01$	$5.13(27)E-01$	$1.536(58)E+00$
1830	$3.523(29)E-02$	$1.067(26)E-01$	$2.501(65)E-01$	$5.05(17)E-01$	$1.728(50)E+00$
1845	$3.700(30)E-02$	$1.171(39)E-01$	$2.492(93)E-01$	$5.51(21)E-01$	$1.742(77)E+00$
1860	$3.79(15)E-02$	$1.129(38)E-01$	$2.667(96)E-01$	$5.24(21)E-01$	$1.809(78)E+00$
1875	$3.86(15)E-02$	$1.204(39)E-01$	$2.605(94)E-01$	$5.37(21)E-01$	$1.688(75)E+00$
1890	$3.96(15)E-02$	$1.183(39)E-01$	$2.794(99)E-01$	$5.45(22)E-01$	$1.845(79)E+00$
1905	$4.00(11)E-02$	$1.256(27)E-01$	$2.728(75)E-01$	$5.76(16)E-01$	$1.837(58)E+00$
1920	$4.08(14)E-02$	$1.294(35)E-01$	$2.88(11)E-01$	$6.00(23)E-01$	$1.992(85)E+00$
1935	$4.07(14)E-02$	$1.344(34)E-01$	$2.85(11)E-01$	$6.02(22)E-01$	$2.018(84)E+00$
1950	$4.19(14)E-02$	$1.326(34)E-01$	$2.93(11)E-01$	$6.03(22)E-01$	$1.979(81)E+00$
1965	$4.452(84)E-02$	$1.421(29)E-01$	$3.117(80)E-01$	$6.14(16)E-01$	$2.142(57)E+00$
1980	$4.61(10)E-02$	$1.436(48)E-01$	$2.97(10)E-01$	$6.21(23)E-01$	$2.030(71)E+00$
1995	$4.549(98)E-02$	$1.479(49)E-01$	$3.27(11)E-01$	$6.77(24)E-01$	$2.125(72)E+00$
2010	$4.59(10)E-02$	$1.446(48)E-01$	$3.20(11)E-01$	$6.41(23)E-01$	$2.145(72)E+00$
2025	$4.48(10)E-02$	$1.451(49)E-01$	$3.40(11)E-01$	$6.36(24)E-01$	$2.203(75)E+00$

Table B.9 – $d\sigma/d\Omega/d\varepsilon$ vs. $\omega \geq 1320$ for $E_0 = 3.595$ GeV, $\theta = 30.011$ deg.

ω	Fe
1290	$2.88(65)E-04$
1305	$3.61(72)E-04$
1320	$5.19(83)E-04$
1335	$5.75(80)E-04$
1350	$7.36(93)E-04$
1365	$7.95(96)E-04$
1380	$9.26(66)E-04$
1395	$1.324(77)E-03$
1410	$1.430(99)E-03$
1425	$1.59(10)E-03$
1440	$1.98(11)E-03$
1455	$2.36(12)E-03$
1470	$2.64(11)E-03$
1485	$3.17(12)E-03$
1500	$3.65(22)E-03$
1515	$4.19(23)E-03$
1530	$5.17(26)E-03$
1545	$5.53(27)E-03$
1560	$6.07(24)E-03$
1575	$6.84(27)E-03$

ω	Fe
1590	$8.45(50)E-03$
1605	$8.74(50)E-03$
1620	$9.95(54)E-03$
1635	$1.021(45)E-02$
1650	$1.120(48)E-02$
1665	$1.355(85)E-02$
1680	$1.504(89)E-02$
1695	$1.658(96)E-02$
1710	$1.615(75)E-02$
1725	$1.99(13)E-02$
1740	$2.07(13)E-02$
1755	$2.41(14)E-02$
1770	$2.30(13)E-02$
1785	$2.75(12)E-02$
1800	$2.99(19)E-02$
1815	$3.06(19)E-02$
1830	$3.25(20)E-02$
1845	$3.33(20)E-02$
1860	$3.56(21)E-02$

Table B.10 – $d\sigma/d\Omega/d\varepsilon$ vs. ω for $E_0 = 3.595$ GeV, $\theta = 39.008$ deg.

ω	Fe
825	$6.3(30)E-05$
840	$6.6(30)E-05$
855	$9.9(31)E-05$
870	$9.6(31)E-05$
885	$1.02(30)E-04$
900	$1.03(31)E-04$
915	$1.92(33)E-04$
930	$2.23(35)E-04$
945	$2.80(51)E-04$
960	$3.39(44)E-04$
975	$3.63(47)E-04$
990	$5.50(81)E-04$
1005	$7.5(10)E-04$
1020	$6.48(91)E-04$
1035	$7.90(98)E-04$
1050	$1.03(11)E-03$
1065	$1.189(90)E-03$
1080	$1.378(98)E-03$
1095	$1.71(11)E-03$
1110	$2.12(16)E-03$
1125	$2.55(18)E-03$
1140	$2.85(19)E-03$
1155	$3.85(22)E-03$
1170	$4.26(20)E-03$

ω	Fe
1185	$4.97(21)E-03$
1200	$6.00(24)E-03$
1215	$7.96(49)E-03$
1230	$9.20(52)E-03$
1245	$9.54(53)E-03$
1260	$1.150(58)E-02$
1275	$1.395(65)E-02$
1290	$1.514(53)E-02$
1305	$1.693(56)E-02$
1320	$2.028(93)E-02$
1335	$2.190(94)E-02$
1350	$2.56(10)E-02$
1365	$2.68(10)E-02$
1380	$2.98(11)E-02$
1395	$3.295(93)E-02$
1410	$3.544(98)E-02$
1425	$3.81(16)E-02$
1440	$4.12(16)E-02$
1455	$4.32(16)E-02$
1470	$4.79(17)E-02$
1485	$5.09(18)E-02$
1500	$5.36(15)E-02$
1515	$5.43(15)E-02$
1530	$6.19(25)E-02$

ω	Fe
1545	$6.54(26)E-02$
1560	$7.03(27)E-02$
1575	$7.19(21)E-02$
1590	$7.98(22)E-02$
1605	$8.20(23)E-02$
1620	$8.57(35)E-02$
1635	$8.31(34)E-02$
1650	$9.15(36)E-02$
1665	$9.58(29)E-02$
1680	$1.067(31)E-01$
1695	$1.150(47)E-01$
1710	$1.094(44)E-01$
1725	$1.136(43)E-01$
1740	$1.241(46)E-01$
1755	$1.318(49)E-01$
1770	$1.319(39)E-01$
1785	$1.456(68)E-01$
1800	$1.533(69)E-01$
1815	$1.551(69)E-01$
1830	$1.576(70)E-01$
1845	$1.722(53)E-01$
1860	$1.808(54)E-01$
1875	$1.973(79)E-01$
1890	$2.054(79)E-01$

ω	Fe
1905	$2.109(80)E-01$
1920	$2.062(80)E-01$
1935	$2.242(62)E-01$
1950	$2.347(91)E-01$
1965	$2.432(93)E-01$
1980	$2.393(90)E-01$
1995	$2.602(70)E-01$
2010	$2.721(71)E-01$
2025	$2.900(74)E-01$
2040	$2.92(10)E-01$
2055	$2.97(10)E-01$
2070	$3.06(11)E-01$
2085	$3.058(81)E-01$
2100	$3.29(12)E-01$
2115	$3.60(13)E-01$
2130	$3.35(12)E-01$
2145	$3.64(13)E-01$
2160	$3.757(93)E-01$
2175	$3.80(13)E-01$
2190	$3.65(12)E-01$
2205	$3.82(13)E-01$
2220	$4.07(14)E-01$
2235	$4.03(14)E-01$

Table B.11 – $d\sigma/d\Omega/d\varepsilon$ vs. $\omega \leq 1530$ for $E_0 = 3.995$ GeV, $\theta = 30.011$ deg.

$E_0 = 2.020$ GeV, $\theta = 15.023$ deg.

y	$F(y)$	y	$F(y)$	y	$F(y)$	y	$F(y)$
−0.169	$1.510(22)E+00$	0.009	$4.058(86)E+00$	0.124	$1.698(39)E+00$	0.210	$1.295(36)E+00$
−0.123	$2.363(74)E+00$	0.035	$3.544(78)E+00$	0.143	$1.455(35)E+00$	0.225	$1.448(38)E+00$
−0.084	$3.082(82)E+00$	0.060	$2.953(69)E+00$	0.161	$1.287(33)E+00$	0.239	$1.622(44)E+00$
−0.050	$3.922(64)E+00$	0.082	$2.506(40)E+00$	0.178	$1.211(24)E+00$	0.252	$1.792(49)E+00$
−0.019	$4.085(65)E+00$	0.104	$2.051(35)E+00$	0.194	$1.250(34)E+00$		

$E_0 = 2.020$ GeV, $\theta = 20.017$ deg.

y	$F(y)$	y	$F(y)$	y	$F(y)$	y	$F(y)$
−0.281	$2.39(31)E-01$	−0.072	$3.262(66)E+00$	0.062	$3.197(76)E+00$	0.163	$1.930(41)E+00$
−0.235	$5.49(42)E-01$	−0.046	$3.967(61)E+00$	0.081	$2.79(12)E+00$	0.178	$2.067(43)E+00$
−0.196	$9.20(42)E-01$	−0.022	$4.098(67)E+00$	0.099	$2.544(70)E+00$	0.192	$2.147(52)E+00$
−0.161	$1.340(49)E+00$	0.000	$4.385(63)E+00$	0.116	$2.281(80)E+00$	0.206	$2.283(55)E+00$
−0.129	$1.800(43)E+00$	0.022	$4.124(86)E+00$	0.132	$2.232(78)E+00$	0.219	$2.444(60)E+00$
−0.099	$2.500(48)E+00$	0.042	$3.754(82)E+00$	0.148	$2.042(73)E+00$		

$E_0 = 3.595$ GeV, $\theta = 16.021$ deg.

y	$F(y)$	y	$F(y)$	y	$F(y)$	y	$F(y)$
−0.521	$2.09(19)E-02$	0.032	$4.280(86)E+00$	0.275	$5.37(12)E+00$	0.418	$8.62(31)E+00$
−0.471	$4.31(38)E-02$	0.046	$4.079(82)E+00$	0.282	$5.40(12)E+00$	0.423	$8.82(31)E+00$
−0.429	$6.54(44)E-02$	0.059	$3.948(82)E+00$	0.290	$5.05(12)E+00$	0.428	$8.58(32)E+00$
−0.391	$8.58(49)E-02$	0.073	$3.73(13)E+00$	0.297	$5.49(23)E+00$	0.433	$8.34(31)E+00$
−0.357	$1.185(57)E-01$	0.085	$3.48(12)E+00$	0.305	$5.53(23)E+00$	0.437	$9.08(24)E+00$
−0.326	$1.696(68)E-01$	0.098	$3.55(12)E+00$	0.312	$5.96(24)E+00$	0.442	$8.77(25)E+00$
−0.297	$2.235(81)E-01$	0.110	$3.33(11)E+00$	0.319	$5.52(23)E+00$	0.446	$9.55(37)E+00$
−0.270	$3.163(92)E-01$	0.122	$3.31(12)E+00$	0.326	$5.85(19)E+00$	0.451	$9.01(35)E+00$
−0.245	$4.11(10)E-01$	0.133	$3.36(10)E+00$	0.332	$6.17(19)E+00$	0.455	$8.41(34)E+00$
−0.221	$5.53(12)E-01$	0.144	$3.55(11)E+00$	0.339	$6.04(29)E+00$	0.459	$8.49(35)E+00$
−0.197	$7.47(48)E-01$	0.155	$3.83(11)E+00$	0.345	$6.35(31)E+00$	0.463	$9.01(27)E+00$
−0.176	$9.45(52)E-01$	0.166	$4.19(20)E+00$	0.352	$6.31(31)E+00$	0.467	$9.14(27)E+00$
−0.154	$1.331(59)E+00$	0.176	$4.11(20)E+00$	0.358	$7.18(32)E+00$	0.471	$9.34(39)E+00$
−0.134	$1.501(64)E+00$	0.186	$4.20(20)E+00$	0.364	$6.41(31)E+00$	0.475	$9.26(38)E+00$
−0.115	$2.044(74)E+00$	0.196	$4.52(21)E+00$	0.370	$7.10(20)E+00$	0.479	$9.48(38)E+00$
−0.096	$2.457(62)E+00$	0.205	$4.62(22)E+00$	0.376	$7.22(21)E+00$	0.483	$9.32(29)E+00$
−0.078	$2.845(67)E+00$	0.215	$4.89(12)E+00$	0.381	$6.93(25)E+00$	0.487	$9.34(29)E+00$
−0.061	$3.313(72)E+00$	0.224	$4.93(12)E+00$	0.387	$7.69(26)E+00$	0.490	$1.031(43)E+01$
−0.044	$3.58(10)E+00$	0.233	$4.86(12)E+00$	0.392	$7.45(27)E+00$	0.494	$1.016(43)E+01$
−0.028	$4.12(11)E+00$	0.242	$5.21(14)E+00$	0.398	$7.55(27)E+00$	0.498	$9.73(43)E+00$
−0.012	$4.29(11)E+00$	0.250	$5.18(14)E+00$	0.403	$7.95(22)E+00$	0.501	$1.015(43)E+01$
0.003	$4.39(11)E+00$	0.259	$5.22(14)E+00$	0.408	$8.14(21)E+00$	0.505	$1.039(45)E+01$
0.018	$4.30(10)E+00$	0.267	$5.23(14)E+00$	0.413	$8.23(31)E+00$	0.508	$9.98(45)E+00$

Table B.12 – $F(y)$ vs. y for ^{4}He.

$E_0 = 3.595$ GeV, $\theta = 20.017$ deg.

y	$F(y)$	y	$F(y)$	y	$F(y)$	y	$F(y)$
−0.666	$3.5(15)E-03$	−0.318	$1.502(28)E-01$	−0.113	$1.931(69)E+00$	0.038	$4.337(89)E+00$
−0.618	$4.84(70)E-03$	−0.296	$1.887(32)E-01$	−0.097	$2.293(72)E+00$	0.050	$4.323(85)E+00$
−0.577	$9.92(82)E-03$	−0.275	$2.55(13)E-01$	−0.082	$2.675(76)E+00$	0.062	$4.089(83)E+00$
−0.539	$1.409(98)E-02$	−0.255	$3.17(14)E-01$	−0.067	$3.118(83)E+00$	0.073	$4.156(95)E+00$
−0.505	$2.00(11)E-02$	−0.235	$3.86(15)E-01$	−0.053	$3.233(78)E+00$	0.084	$4.346(97)E+00$
−0.474	$2.96(13)E-02$	−0.216	$5.11(17)E-01$	−0.039	$3.571(82)E+00$	0.095	$4.377(97)E+00$
−0.444	$4.37(15)E-02$	−0.197	$6.33(19)E-01$	−0.025	$3.711(81)E+00$	0.105	$4.239(96)E+00$
−0.417	$5.47(17)E-02$	−0.179	$7.91(20)E-01$	−0.012	$4.03(16)E+00$	0.116	$4.307(98)E+00$
−0.390	$7.11(19)E-02$	−0.162	$1.003(22)E+00$	0.001	$4.00(16)E+00$	0.126	$4.37(10)E+00$
−0.365	$9.40(22)E-02$	−0.145	$1.215(25)E+00$	0.014	$4.15(16)E+00$	0.136	$4.52(10)E+00$
−0.341	$1.205(24)E-01$	−0.129	$1.552(63)E+00$	0.026	$4.04(16)E+00$		

$E_0 = 3.595$ GeV, $\theta = 25.013$ deg.

y	$F(y)$	y	$F(y)$	y	$F(y)$	y	$F(y)$
−0.724	$1.68(53)E-03$	−0.362	$7.95(65)E-02$	−0.145	$1.062(50)E+00$	0.019	$4.64(18)E+00$
−0.656	$3.17(93)E-03$	−0.343	$9.64(69)E-02$	−0.131	$1.350(54)E+00$	0.030	$5.02(17)E+00$
−0.625	$3.7(12)E-03$	−0.324	$1.18(11)E-01$	−0.117	$1.613(52)E+00$	0.040	$4.98(12)E+00$
−0.596	$3.8(16)E-03$	−0.305	$1.62(12)E-01$	−0.103	$1.861(56)E+00$	0.051	$5.09(11)E+00$
−0.568	$1.00(16)E-02$	−0.288	$1.80(13)E-01$	−0.090	$2.18(11)E+00$	0.061	$5.14(11)E+00$
−0.542	$1.39(17)E-02$	−0.270	$2.18(14)E-01$	−0.077	$2.52(12)E+00$	0.071	$5.42(13)E+00$
−0.516	$1.28(20)E-02$	−0.253	$2.70(15)E-01$	−0.064	$2.85(13)E+00$	0.081	$5.44(13)E+00$
−0.492	$2.04(23)E-02$	−0.237	$3.26(15)E-01$	−0.052	$3.10(14)E+00$	0.091	$5.42(13)E+00$
−0.468	$3.39(53)E-02$	−0.220	$4.16(17)E-01$	−0.039	$3.86(15)E+00$	0.101	$5.73(14)E+00$
−0.446	$3.47(55)E-02$	−0.205	$4.79(18)E-01$	−0.027	$3.58(11)E+00$	0.111	$5.90(15)E+00$
−0.424	$3.87(68)E-02$	−0.189	$6.80(38)E-01$	−0.016	$4.24(12)E+00$	0.120	$6.08(15)E+00$
−0.403	$5.36(68)E-02$	−0.174	$8.19(42)E-01$	−0.004	$4.60(17)E+00$		
−0.382	$5.89(72)E-02$	−0.159	$9.19(45)E-01$	0.007	$4.70(17)E+00$		

$E_0 = 3.595$ GeV, $\theta = 30.011$ deg.

y	$F(y)$	y	$F(y)$	y	$F(y)$	y	$F(y)$
−0.675	$4.8(14)E-03$	−0.216	$4.29(28)E-01$	0.068	$5.87(22)E+00$	0.264	$1.607(68)E+01$
−0.649	$4.7(10)E-03$	−0.202	$4.87(43)E-01$	0.077	$6.93(23)E+00$	0.271	$1.771(69)E+01$
−0.624	$2.85(94)E-03$	−0.188	$6.15(50)E-01$	0.087	$8.09(37)E+00$	0.278	$1.663(67)E+01$
−0.600	$2.7(11)E-03$	−0.174	$7.77(55)E-01$	0.096	$7.23(35)E+00$	0.285	$1.736(49)E+01$
−0.577	$6.3(14)E-03$	−0.161	$9.34(55)E-01$	0.105	$7.46(35)E+00$	0.291	$1.808(16)E+01$
−0.554	$1.20(28)E-02$	−0.147	$1.189(66)E+00$	0.114	$8.07(37)E+00$	0.298	$1.838(16)E+01$
−0.532	$9.0(25)E-03$	−0.134	$1.329(52)E+00$	0.123	$8.06(27)E+00$	0.304	$1.893(15)E+01$
−0.511	$1.16(28)E-02$	−0.121	$1.647(57)E+00$	0.132	$8.86(29)E+00$	0.311	$1.913(16)E+01$
−0.490	$1.66(27)E-02$	−0.109	$1.938(89)E+00$	0.141	$8.92(41)E+00$	0.317	$1.948(16)E+01$
−0.470	$2.30(29)E-02$	−0.096	$2.176(97)E+00$	0.149	$9.98(43)E+00$	0.323	$2.038(17)E+01$
−0.450	$3.24(33)E-02$	−0.084	$2.60(10)E+00$	0.158	$9.29(41)E+00$	0.329	$2.081(82)E+01$
−0.431	$3.15(55)E-02$	−0.072	$3.02(11)E+00$	0.166	$1.058(32)E+01$	0.335	$2.106(80)E+01$
−0.412	$4.04(66)E-02$	−0.060	$3.10(10)E+00$	0.174	$1.114(33)E+01$	0.341	$2.155(84)E+01$
−0.394	$5.78(70)E-02$	−0.049	$3.66(11)E+00$	0.182	$1.101(47)E+01$	0.347	$2.164(58)E+01$
−0.376	$6.59(73)E-02$	−0.037	$4.22(26)E+00$	0.190	$1.170(47)E+01$	0.353	$2.195(76)E+01$
−0.359	$6.73(84)E-02$	−0.026	$4.60(27)E+00$	0.198	$1.282(48)E+01$	0.359	$2.180(74)E+01$
−0.341	$9.61(83)E-02$	−0.015	$4.40(25)E+00$	0.206	$1.283(49)E+01$	0.364	$2.228(74)E+01$
−0.325	$9.66(82)E-02$	−0.004	$5.02(27)E+00$	0.214	$1.289(33)E+01$	0.370	$2.356(45)E+01$
−0.308	$1.62(21)E-01$	0.007	$5.40(19)E+00$	0.221	$1.395(44)E+01$	0.375	$2.426(52)E+01$
−0.292	$1.53(21)E-01$	0.017	$5.85(20)E+00$	0.229	$1.420(44)E+01$	0.381	$2.379(51)E+01$
−0.276	$2.09(23)E-01$	0.028	$5.82(26)E+00$	0.236	$1.448(44)E+01$	0.386	$2.387(52)E+01$
−0.261	$2.11(24)E-01$	0.038	$5.65(28)E+00$	0.243	$1.549(45)E+01$	0.392	$2.311(52)E+01$
−0.246	$2.55(26)E-01$	0.048	$5.98(28)E+00$	0.250	$1.515(39)E+01$		
−0.231	$3.61(24)E-01$	0.058	$5.97(27)E+00$	0.257	$1.521(68)E+01$		

Table B.13 – $F(y)$ vs. y for ^{4}He.

$E_0 = 2.020$ GeV, $\theta = 15.023$ deg.

y	$F(y)$	y	$F(y)$	y	$F(y)$	y	$F(y)$
−0.239	$1.257(22)E+00$	−0.040	$3.079(46)E+00$	0.089	$2.509(48)E+00$	0.186	$1.782(64)E+00$
−0.188	$1.679(25)E+00$	−0.011	$3.169(69)E+00$	0.110	$2.130(66)E+00$	0.203	$1.676(63)E+00$
−0.145	$2.268(52)E+00$	0.016	$3.065(65)E+00$	0.131	$1.882(63)E+00$	0.219	$1.950(69)E+00$
−0.107	$2.555(55)E+00$	0.042	$2.816(62)E+00$	0.150	$1.683(59)E+00$	0.235	$2.057(75)E+00$
−0.072	$2.931(45)E+00$	0.066	$2.692(49)E+00$	0.169	$1.676(44)E+00$	0.250	$2.039(78)E+00$

$E_0 = 2.020$ GeV, $\theta = 20.017$ deg.

y	$F(y)$	y	$F(y)$	y	$F(y)$	y	$F(y)$
−0.431	$1.396(43)E-01$	−0.144	$2.119(47)E+00$	0.027	$3.315(77)E+00$	0.154	$2.520(55)E+00$
−0.371	$2.496(56)E-01$	−0.116	$2.569(52)E+00$	0.047	$3.189(76)E+00$	0.170	$2.464(56)E+00$
−0.323	$3.912(69)E-01$	−0.089	$2.949(72)E+00$	0.067	$2.965(90)E+00$	0.185	$2.373(75)E+00$
−0.280	$5.74(39)E-01$	−0.064	$3.157(66)E+00$	0.086	$2.910(63)E+00$	0.200	$2.550(80)E+00$
−0.242	$9.36(47)E-01$	−0.040	$3.318(83)E+00$	0.104	$2.762(83)E+00$	0.214	$2.871(89)E+00$
−0.207	$1.197(42)E+00$	−0.016	$3.448(65)E+00$	0.121	$2.703(80)E+00$		
−0.175	$1.624(48)E+00$	0.006	$3.406(79)E+00$	0.138	$2.516(76)E+00$		

$E_0 = 3.605$ GeV, $\theta = 16.021$ deg.

y	$F(y)$	y	$F(y)$	y	$F(y)$	y	$F(y)$
−0.677	$5.26(17)E-03$	−0.577	$1.482(29)E-02$	−0.500	$3.417(42)E-02$	−0.434	$6.923(64)E-02$
−0.623	$9.22(23)E-03$	−0.537	$2.310(35)E-02$	−0.465	$4.951(54)E-02$		

$E_0 = 3.595$ GeV, $\theta = 16.021$ deg.

y	$F(y)$	y	$F(y)$	y	$F(y)$	y	$F(y)$
−0.401	$1.031(55)E-01$	0.047	$3.667(69)E+00$	0.291	$5.60(16)E+00$	0.442	$9.13(23)E+00$
−0.372	$1.482(64)E-01$	0.061	$3.77(11)E+00$	0.299	$6.07(27)E+00$	0.447	$9.09(23)E+00$
−0.345	$2.056(74)E-01$	0.074	$3.56(10)E+00$	0.307	$5.76(26)E+00$	0.453	$9.30(19)E+00$
−0.320	$2.717(86)E-01$	0.087	$3.61(10)E+00$	0.315	$6.18(28)E+00$	0.458	$9.14(19)E+00$
−0.295	$3.37(10)E-01$	0.099	$3.79(10)E+00$	0.322	$5.69(27)E+00$	0.463	$8.83(31)E+00$
−0.271	$4.54(11)E-01$	0.112	$3.70(10)E+00$	0.330	$5.97(19)E+00$	0.467	$9.26(31)E+00$
−0.249	$5.89(12)E-01$	0.123	$3.617(87)E+00$	0.337	$6.04(19)E+00$	0.472	$9.31(31)E+00$
−0.227	$7.64(14)E-01$	0.135	$3.859(90)E+00$	0.344	$6.63(26)E+00$	0.477	$1.030(33)E+01$
−0.205	$9.86(38)E-01$	0.147	$3.914(90)E+00$	0.351	$7.09(28)E+00$	0.482	$9.56(25)E+00$
−0.185	$1.236(43)E+00$	0.158	$4.18(15)E+00$	0.358	$6.71(27)E+00$	0.486	$9.76(26)E+00$
−0.165	$1.532(48)E+00$	0.169	$4.16(15)E+00$	0.365	$6.81(27)E+00$	0.491	$9.95(39)E+00$
−0.146	$1.798(51)E+00$	0.179	$4.64(16)E+00$	0.372	$7.06(28)E+00$	0.495	$1.060(40)E+01$
−0.127	$2.035(55)E+00$	0.190	$4.54(16)E+00$	0.378	$7.21(21)E+00$	0.499	$9.14(37)E+00$
−0.109	$2.395(49)E+00$	0.200	$4.85(17)E+00$	0.384	$6.88(20)E+00$	0.504	$1.017(29)E+01$
−0.091	$2.744(52)E+00$	0.210	$4.90(13)E+00$	0.391	$7.55(30)E+00$	0.508	$1.006(28)E+01$
−0.074	$2.974(54)E+00$	0.220	$4.64(12)E+00$	0.397	$7.47(31)E+00$	0.512	$1.034(40)E+01$
−0.058	$3.036(83)E+00$	0.229	$4.98(13)E+00$	0.403	$7.62(32)E+00$	0.516	$9.71(39)E+00$
−0.041	$3.363(85)E+00$	0.239	$4.59(17)E+00$	0.409	$8.04(34)E+00$	0.520	$1.004(40)E+01$
−0.026	$3.548(87)E+00$	0.248	$5.33(18)E+00$	0.415	$8.67(21)E+00$	0.524	$1.017(40)E+01$
−0.010	$3.596(87)E+00$	0.257	$5.22(18)E+00$	0.420	$8.69(20)E+00$	0.528	$1.052(42)E+01$
0.005	$3.760(88)E+00$	0.266	$5.15(18)E+00$	0.426	$8.01(22)E+00$	0.532	$9.79(41)E+00$
0.019	$3.622(69)E+00$	0.274	$5.06(15)E+00$	0.431	$8.40(22)E+00$		
0.033	$3.734(69)E+00$	0.283	$5.63(16)E+00$	0.437	$8.68(22)E+00$		

Table B.14 – $F(y)$ vs. y for C.

$E_0 = 3.595$ GeV, $\theta = 20.017$ deg.

y	$F(y)$	y	$F(y)$	y	$F(y)$	y	$F(y)$
-0.773	$5.7(27)E-04$	-0.397	$8.83(44)E-02$	-0.171	$1.229(26)E+00$	0.001	$3.87(11)E+00$
-0.733	$1.33(33)E-03$	-0.375	$1.082(48)E-01$	-0.155	$1.459(29)E+00$	0.014	$4.04(11)E+00$
-0.697	$1.98(36)E-03$	-0.354	$1.322(53)E-01$	-0.139	$1.809(58)E+00$	0.026	$4.141(88)E+00$
-0.662	$3.09(43)E-03$	-0.334	$1.850(59)E-01$	-0.124	$2.085(62)E+00$	0.038	$4.151(85)E+00$
-0.630	$5.11(56)E-03$	-0.314	$2.232(65)E-01$	-0.109	$2.335(63)E+00$	0.050	$4.189(87)E+00$
-0.600	$8.60(75)E-03$	-0.294	$2.926(76)E-01$	-0.094	$2.702(67)E+00$	0.062	$4.29(13)E+00$
-0.571	$1.027(83)E-02$	-0.275	$3.43(17)E-01$	-0.079	$2.744(68)E+00$	0.073	$4.40(13)E+00$
-0.543	$1.554(91)E-02$	-0.257	$4.46(19)E-01$	-0.065	$3.147(63)E+00$	0.084	$4.53(13)E+00$
-0.516	$2.11(10)E-02$	-0.239	$6.16(22)E-01$	-0.051	$3.204(63)E+00$	0.095	$4.45(13)E+00$
-0.491	$2.96(12)E-02$	-0.221	$7.09(23)E-01$	-0.038	$3.374(63)E+00$	0.106	$4.43(13)E+00$
-0.466	$3.88(30)E-02$	-0.204	$8.91(26)E-01$	-0.024	$3.51(11)E+00$	0.117	$4.79(14)E+00$
-0.442	$5.14(33)E-02$	-0.187	$1.051(24)E+00$	-0.011	$3.58(11)E+00$	0.127	$5.08(15)E+00$
-0.419	$6.41(37)E-02$						

$E_0 = 3.595$ GeV, $\theta = 25.013$ deg.

y	$F(y)$	y	$F(y)$	y	$F(y)$	y	$F(y)$
-0.703	$1.72(80)E-03$	-0.388	$8.82(73)E-02$	-0.182	$1.018(48)E+00$	-0.016	$4.03(13)E+00$
-0.654	$2.43(89)E-03$	-0.370	$9.62(79)E-02$	-0.168	$1.211(51)E+00$	-0.004	$4.31(14)E+00$
-0.631	$3.9(10)E-03$	-0.353	$1.100(71)E-01$	-0.154	$1.542(59)E+00$	0.007	$4.70(15)E+00$
-0.608	$4.3(10)E-03$	-0.336	$1.429(81)E-01$	-0.140	$1.589(59)E+00$	0.018	$4.37(14)E+00$
-0.585	$7.2(13)E-03$	-0.319	$1.48(13)E-01$	-0.127	$1.915(52)E+00$	0.029	$4.81(15)E+00$
-0.564	$8.3(14)E-03$	-0.303	$2.16(16)E-01$	-0.114	$2.143(55)E+00$	0.040	$4.76(11)E+00$
-0.542	$9.7(15)E-03$	-0.287	$2.70(17)E-01$	-0.101	$2.372(88)E+00$	0.050	$4.98(11)E+00$
-0.522	$1.35(15)E-02$	-0.271	$3.03(18)E-01$	-0.088	$2.458(89)E+00$	0.061	$5.37(17)E+00$
-0.501	$2.20(20)E-02$	-0.255	$3.77(20)E-01$	-0.075	$2.925(96)E+00$	0.071	$5.43(17)E+00$
-0.481	$2.52(21)E-02$	-0.240	$4.86(19)E-01$	-0.063	$3.29(10)E+00$	0.081	$5.52(17)E+00$
-0.462	$3.12(24)E-02$	-0.225	$6.04(21)E-01$	-0.051	$3.27(10)E+00$	0.091	$5.86(18)E+00$
-0.443	$4.34(56)E-02$	-0.210	$7.13(23)E-01$	-0.039	$3.558(84)E+00$	0.101	$5.77(18)E+00$
-0.424	$5.64(60)E-02$	-0.196	$8.43(44)E-01$	-0.027	$3.872(87)E+00$	0.111	$6.33(19)E+00$
-0.406	$7.61(69)E-02$						

$E_0 = 3.595$ GeV, $\theta = 30.011$ deg.

y	$F(y)$	y	$F(y)$	y	$F(y)$	y	$F(y)$
-0.235	$5.45(60)E-01$	-0.015	$4.22(15)E+00$	0.159	$1.017(23)E+01$	0.299	$1.944(65)E+01$
-0.221	$5.17(56)E-01$	-0.004	$4.51(12)E+00$	0.168	$1.067(23)E+01$	0.306	$2.057(66)E+01$
-0.208	$5.73(56)E-01$	0.006	$4.78(13)E+00$	0.176	$1.073(31)E+01$	0.313	$2.008(65)E+01$
-0.194	$7.39(66)E-01$	0.017	$5.53(22)E+00$	0.185	$1.192(32)E+01$	0.320	$1.975(49)E+01$
-0.181	$1.015(77)E+00$	0.027	$5.41(22)E+00$	0.193	$1.129(30)E+01$	0.327	$2.159(72)E+01$
-0.168	$1.086(77)E+00$	0.037	$5.68(22)E+00$	0.201	$1.169(32)E+01$	0.333	$2.075(70)E+01$
-0.156	$1.287(84)E+00$	0.047	$6.07(22)E+00$	0.209	$1.274(28)E+01$	0.340	$2.204(71)E+01$
-0.143	$1.432(58)E+00$	0.057	$6.22(18)E+00$	0.217	$1.253(48)E+01$	0.346	$2.156(72)E+01$
-0.131	$1.653(61)E+00$	0.067	$6.45(18)E+00$	0.225	$1.423(51)E+01$	0.353	$2.279(49)E+01$
-0.118	$1.887(82)E+00$	0.077	$6.57(26)E+00$	0.233	$1.474(53)E+01$	0.359	$2.340(63)E+01$
-0.106	$2.217(89)E+00$	0.087	$6.94(27)E+00$	0.241	$1.404(51)E+01$	0.365	$2.417(62)E+01$
-0.094	$2.382(94)E+00$	0.096	$7.19(27)E+00$	0.248	$1.492(42)E+01$	0.372	$2.374(61)E+01$
-0.083	$2.576(99)E+00$	0.105	$7.36(28)E+00$	0.256	$1.641(67)E+01$	0.378	$2.531(52)E+01$
-0.071	$2.957(83)E+00$	0.115	$8.37(22)E+00$	0.263	$1.678(66)E+01$	0.384	$2.545(85)E+01$
-0.060	$3.278(87)E+00$	0.124	$8.49(22)E+00$	0.271	$1.609(63)E+01$	0.390	$2.607(86)E+01$
-0.048	$3.52(14)E+00$	0.133	$8.98(31)E+00$	0.278	$1.743(65)E+01$	0.396	$2.534(84)E+01$
-0.037	$3.79(14)E+00$	0.142	$9.98(33)E+00$	0.285	$1.868(48)E+01$	0.402	$2.528(86)E+01$
-0.026	$4.42(15)E+00$	0.151	$9.57(32)E+00$	0.292	$1.892(48)E+01$		

Table B.15 – $F(y)$ vs. y for C.

$E_0 = 2.020$ GeV, $\theta = 15.023$ deg.

y	$F(y)$	y	$F(y)$	y	$F(y)$	y	$F(y)$
−0.325	$9.57(23)E-01$	−0.056	$2.790(56)E+00$	0.076	$2.416(56)E+00$	0.177	$1.949(74)E+00$
−0.259	$1.335(27)E+00$	−0.026	$2.870(83)E+00$	0.099	$2.205(74)E+00$	0.194	$1.985(75)E+00$
−0.207	$1.713(30)E+00$	0.002	$2.898(81)E+00$	0.120	$2.123(73)E+00$	0.211	$2.003(77)E+00$
−0.163	$2.079(65)E+00$	0.028	$2.715(77)E+00$	0.140	$1.937(70)E+00$	0.227	$2.198(85)E+00$
−0.124	$2.379(69)E+00$	0.053	$2.625(57)E+00$	0.159	$1.931(52)E+00$	0.242	$2.411(93)E+00$
−0.088	$2.671(55)E+00$						

$E_0 = 2.020$ GeV, $\theta = 20.017$ deg.

y	$F(y)$	y	$F(y)$	y	$F(y)$	y	$F(y)$
−0.512	$9.18(40)E-02$	−0.188	$1.769(49)E+00$	−0.006	$3.332(78)E+00$	0.128	$2.780(94)E+00$
−0.438	$1.789(54)E-01$	−0.157	$2.014(46)E+00$	0.016	$3.295(77)E+00$	0.145	$2.664(61)E+00$
−0.382	$3.122(70)E-01$	−0.129	$2.420(50)E+00$	0.036	$3.139(76)E+00$	0.161	$2.749(63)E+00$
−0.334	$4.627(83)E-01$	−0.102	$2.658(69)E+00$	0.056	$3.164(97)E+00$	0.176	$2.790(82)E+00$
−0.293	$7.64(44)E-01$	−0.076	$2.941(62)E+00$	0.075	$3.048(71)E+00$	0.191	$2.879(85)E+00$
−0.255	$1.043(50)E+00$	−0.052	$3.098(80)E+00$	0.094	$2.889(98)E+00$	0.206	$2.879(89)E+00$
−0.220	$1.347(44)E+00$	−0.028	$3.101(63)E+00$	0.111	$2.841(97)E+00$		

$E_0 = 3.605$ GeV, $\theta = 16.021$ deg.

y	$F(y)$	y	$F(y)$	y	$F(y)$	y	$F(y)$
−0.777	$2.32(17)E-03$	−0.612	$1.413(38)E-02$	−0.534	$2.945(53)E-02$	−0.467	$5.828(78)E-02$
−0.710	$4.62(23)E-03$	−0.571	$2.078(47)E-02$	−0.500	$4.398(65)E-02$	−0.437	$8.448(95)E-02$
−0.657	$8.80(30)E-03$						

$E_0 = 3.595$ GeV, $\theta = 16.021$ deg.

y	$F(y)$	y	$F(y)$	y	$F(y)$	y	$F(y)$
−0.406	$1.210(49)E-01$	0.038	$3.673(79)E+00$	0.286	$5.79(17)E+00$	0.435	$9.55(35)E+00$
−0.378	$1.663(57)E-01$	0.052	$3.66(13)E+00$	0.294	$5.57(26)E+00$	0.441	$9.13(34)E+00$
−0.352	$2.132(65)E-01$	0.065	$3.49(12)E+00$	0.302	$6.51(28)E+00$	0.446	$9.31(35)E+00$
−0.327	$2.988(79)E-01$	0.078	$3.59(12)E+00$	0.310	$6.04(28)E+00$	0.451	$9.10(26)E+00$
−0.303	$3.977(94)E-01$	0.091	$3.85(12)E+00$	0.318	$6.14(28)E+00$	0.456	$9.24(27)E+00$
−0.280	$4.744(99)E-01$	0.103	$3.68(12)E+00$	0.325	$6.54(21)E+00$	0.461	$9.39(38)E+00$
−0.257	$6.55(11)E-01$	0.115	$3.75(10)E+00$	0.333	$6.52(21)E+00$	0.466	$9.85(38)E+00$
−0.235	$8.12(13)E-01$	0.127	$4.01(10)E+00$	0.340	$7.01(30)E+00$	0.471	$9.89(38)E+00$
−0.214	$9.99(56)E-01$	0.139	$4.16(11)E+00$	0.347	$6.97(31)E+00$	0.476	$9.67(39)E+00$
−0.194	$1.108(57)E+00$	0.150	$4.10(15)E+00$	0.354	$7.26(31)E+00$	0.481	$1.007(27)E+01$
−0.174	$1.600(70)E+00$	0.161	$4.22(16)E+00$	0.361	$6.98(30)E+00$	0.486	$9.84(27)E+00$
−0.155	$1.892(76)E+00$	0.172	$4.45(16)E+00$	0.368	$7.41(32)E+00$	0.490	$9.81(35)E+00$
−0.137	$2.139(80)E+00$	0.183	$4.67(16)E+00$	0.375	$6.93(22)E+00$	0.495	$1.014(35)E+01$
−0.119	$2.432(63)E+00$	0.193	$4.68(17)E+00$	0.381	$7.44(23)E+00$	0.499	$1.025(35)E+01$
−0.101	$2.590(64)E+00$	0.203	$5.09(13)E+00$	0.388	$7.44(32)E+00$	0.504	$1.053(29)E+01$
−0.084	$2.740(66)E+00$	0.213	$4.98(13)E+00$	0.394	$7.19(32)E+00$	0.508	$9.96(27)E+00$
−0.067	$3.172(93)E+00$	0.223	$4.95(13)E+00$	0.400	$7.70(33)E+00$	0.512	$1.018(41)E+01$
−0.051	$3.315(92)E+00$	0.232	$4.91(19)E+00$	0.406	$8.12(35)E+00$	0.516	$1.045(42)E+01$
−0.035	$3.301(91)E+00$	0.242	$5.23(20)E+00$	0.412	$8.26(26)E+00$	0.521	$1.008(41)E+01$
−0.020	$3.337(91)E+00$	0.251	$5.60(20)E+00$	0.418	$7.76(24)E+00$	0.525	$1.012(41)E+01$
−0.005	$3.308(90)E+00$	0.260	$5.38(20)E+00$	0.424	$8.76(34)E+00$	0.529	$1.025(43)E+01$
0.010	$3.500(77)E+00$	0.269	$5.48(16)E+00$	0.430	$8.71(34)E+00$	0.533	$1.106(45)E+01$
0.024	$3.566(76)E+00$	0.277	$5.51(17)E+00$				

Table B.16 – $F(y)$ vs. y for Al.

$E_0 = 3.595$ GeV, $\theta = 20.017$ deg.

y	$F(y)$	y	$F(y)$	y	$F(y)$	y	$F(y)$
-0.750	$1.03(41)E-03$	-0.401	$1.042(68)E-01$	-0.179	$1.297(29)E+00$	-0.007	$3.80(14)E+00$
-0.715	$3.31(68)E-03$	-0.380	$1.408(80)E-01$	-0.163	$1.521(32)E+00$	0.006	$3.63(13)E+00$
-0.683	$2.01(47)E-03$	-0.359	$1.625(87)E-01$	-0.147	$1.708(71)E+00$	0.018	$3.79(10)E+00$
-0.652	$4.13(65)E-03$	-0.339	$1.852(77)E-01$	-0.132	$1.916(76)E+00$	0.030	$3.98(10)E+00$
-0.622	$7.04(84)E-03$	-0.320	$2.379(88)E-01$	-0.117	$2.306(81)E+00$	0.042	$4.12(11)E+00$
-0.594	$8.73(97)E-03$	-0.301	$3.005(99)E-01$	-0.102	$2.439(81)E+00$	0.054	$4.18(15)E+00$
-0.567	$1.30(12)E-02$	-0.282	$3.84(18)E-01$	-0.088	$2.506(82)E+00$	0.065	$4.34(15)E+00$
-0.541	$1.92(14)E-02$	-0.264	$5.16(20)E-01$	-0.074	$2.892(76)E+00$	0.076	$4.40(16)E+00$
-0.515	$2.58(15)E-02$	-0.246	$6.03(22)E-01$	-0.060	$3.013(78)E+00$	0.088	$4.55(16)E+00$
-0.491	$3.40(17)E-02$	-0.229	$7.20(23)E-01$	-0.046	$3.414(81)E+00$	0.098	$4.83(17)E+00$
-0.468	$4.69(47)E-02$	-0.212	$9.06(26)E-01$	-0.033	$3.40(13)E+00$	0.109	$4.58(16)E+00$
-0.445	$6.44(55)E-02$	-0.195	$1.091(26)E+00$	-0.020	$3.59(14)E+00$	0.120	$5.06(18)E+00$
-0.422	$8.80(63)E-02$						

$E_0 = 3.595$ GeV, $\theta = 25.013$ deg.

y	$F(y)$	y	$F(y)$	y	$F(y)$	y	$F(y)$
-0.692	$2.3(10)E-03$	-0.409	$6.20(64)E-02$	-0.189	$1.156(51)E+00$	-0.024	$4.13(17)E+00$
-0.669	$3.6(11)E-03$	-0.392	$8.25(75)E-02$	-0.175	$1.339(54)E+00$	-0.012	$3.89(16)E+00$
-0.646	$4.1(12)E-03$	-0.374	$1.133(91)E-01$	-0.161	$1.511(58)E+00$	-0.001	$4.22(17)E+00$
-0.624	$5.8(14)E-03$	-0.357	$1.063(76)E-01$	-0.148	$1.547(59)E+00$	0.010	$4.34(16)E+00$
-0.603	$6.8(15)E-03$	-0.341	$1.456(89)E-01$	-0.135	$1.778(51)E+00$	0.021	$4.69(18)E+00$
-0.582	$6.7(14)E-03$	-0.325	$1.74(17)E-01$	-0.122	$1.967(54)E+00$	0.032	$4.84(13)E+00$
-0.561	$1.02(17)E-02$	-0.308	$2.25(20)E-01$	-0.109	$2.305(96)E+00$	0.043	$4.90(13)E+00$
-0.541	$1.44(21)E-02$	-0.293	$3.03(22)E-01$	-0.096	$2.60(10)E+00$	0.053	$5.26(18)E+00$
-0.521	$1.78(20)E-02$	-0.277	$3.42(23)E-01$	-0.083	$2.78(10)E+00$	0.063	$5.58(19)E+00$
-0.501	$2.23(22)E-02$	-0.262	$4.16(26)E-01$	-0.071	$3.13(11)E+00$	0.074	$5.52(19)E+00$
-0.482	$3.00(25)E-02$	-0.247	$5.19(23)E-01$	-0.059	$3.14(11)E+00$	0.084	$5.81(19)E+00$
-0.463	$3.13(26)E-02$	-0.232	$6.06(24)E-01$	-0.047	$3.464(96)E+00$	0.094	$6.08(19)E+00$
-0.445	$4.96(64)E-02$	-0.217	$7.28(27)E-01$	-0.035	$3.555(96)E+00$	0.103	$6.21(20)E+00$
-0.427	$5.39(61)E-02$	-0.203	$8.69(43)E-01$				

$E_0 = 3.595$ GeV, $\theta = 30.011$ deg.

y	$F(y)$	y	$F(y)$	y	$F(y)$	y	$F(y)$
-0.241	$5.21(82)E-01$	-0.023	$4.46(17)E+00$	0.152	$1.028(28)E+01$	0.295	$1.796(68)E+01$
-0.228	$6.27(85)E-01$	-0.012	$4.75(15)E+00$	0.161	$1.054(28)E+01$	0.302	$1.969(71)E+01$
-0.214	$6.40(84)E-01$	-0.002	$4.66(15)E+00$	0.170	$1.018(40)E+01$	0.309	$1.991(71)E+01$
-0.201	$9.1(10)E-01$	0.009	$4.79(29)E+00$	0.178	$1.137(42)E+01$	0.316	$2.079(54)E+01$
-0.188	$8.7(10)E-01$	0.019	$4.80(29)E+00$	0.187	$1.137(41)E+01$	0.322	$2.064(77)E+01$
-0.175	$1.06(11)E+00$	0.030	$5.15(30)E+00$	0.195	$1.241(44)E+01$	0.329	$2.201(79)E+01$
-0.163	$1.36(12)E+00$	0.040	$5.90(32)E+00$	0.203	$1.246(34)E+01$	0.336	$2.142(77)E+01$
-0.150	$1.544(78)E+00$	0.050	$6.34(24)E+00$	0.211	$1.336(53)E+01$	0.343	$2.289(81)E+01$
-0.138	$1.687(81)E+00$	0.060	$6.05(23)E+00$	0.219	$1.421(55)E+01$	0.349	$2.225(61)E+01$
-0.126	$2.10(11)E+00$	0.069	$6.84(33)E+00$	0.227	$1.431(55)E+01$	0.356	$2.342(92)E+01$
-0.114	$2.39(11)E+00$	0.079	$6.96(33)E+00$	0.235	$1.510(56)E+01$	0.362	$2.305(88)E+01$
-0.102	$2.51(12)E+00$	0.089	$7.57(34)E+00$	0.243	$1.547(40)E+01$	0.368	$2.357(88)E+01$
-0.090	$2.51(12)E+00$	0.098	$7.58(35)E+00$	0.250	$1.556(55)E+01$	0.375	$2.496(64)E+01$
-0.079	$2.868(97)E+00$	0.107	$8.48(26)E+00$	0.258	$1.628(54)E+01$	0.381	$2.369(82)E+01$
-0.067	$3.24(10)E+00$	0.117	$8.96(26)E+00$	0.266	$1.710(54)E+01$	0.387	$2.591(85)E+01$
-0.056	$3.01(14)E+00$	0.126	$8.80(36)E+00$	0.273	$1.704(54)E+01$	0.393	$2.520(83)E+01$
-0.045	$3.65(16)E+00$	0.135	$9.25(36)E+00$	0.280	$1.827(45)E+01$	0.399	$2.663(88)E+01$
-0.034	$3.58(15)E+00$	0.144	$9.69(37)E+00$	0.287	$1.830(45)E+01$		

Table B.17 – $F(y)$ vs. y for Al.

$E_0 = 2.020$ GeV, $\theta = 15.023$ deg.

y	$F(y)$	y	$F(y)$	y	$F(y)$	y	$F(y)$
−0.340	$9.38(25)E-01$	−0.065	$2.687(69)E+00$	0.069	$2.513(66)E+00$	0.171	$2.234(81)E+00$
−0.271	$1.316(30)E+00$	−0.034	$2.86(10)E+00$	0.092	$2.390(82)E+00$	0.189	$2.050(78)E+00$
−0.218	$1.639(34)E+00$	−0.006	$2.770(98)E+00$	0.113	$2.178(78)E+00$	0.205	$1.993(77)E+00$
−0.173	$2.199(83)E+00$	0.021	$2.673(95)E+00$	0.133	$2.115(78)E+00$	0.222	$2.197(86)E+00$
−0.133	$2.355(85)E+00$	0.046	$2.678(67)E+00$	0.153	$1.996(55)E+00$	0.237	$2.274(93)E+00$
−0.098	$2.521(66)E+00$						

$E_0 = 2.020$ GeV, $\theta = 20.017$ deg.

y	$F(y)$	y	$F(y)$	y	$F(y)$	y	$F(y)$
−0.518	$8.77(46)E-02$	−0.195	$1.675(46)E+00$	−0.013	$3.219(76)E+00$	0.123	$2.807(90)E+00$
−0.446	$1.779(63)E-01$	−0.165	$2.134(46)E+00$	0.009	$3.162(75)E+00$	0.140	$2.717(63)E+00$
−0.390	$3.160(82)E-01$	−0.136	$2.325(48)E+00$	0.030	$3.011(74)E+00$	0.156	$2.834(66)E+00$
−0.342	$4.879(99)E-01$	−0.109	$2.608(67)E+00$	0.050	$2.994(99)E+00$	0.171	$3.003(92)E+00$
−0.301	$7.38(43)E-01$	−0.083	$2.934(61)E+00$	0.069	$2.797(68)E+00$	0.186	$2.749(90)E+00$
−0.263	$9.79(48)E-01$	−0.059	$3.113(79)E+00$	0.088	$3.060(98)E+00$	0.201	$2.864(95)E+00$
−0.228	$1.405(43)E+00$	−0.035	$3.318(65)E+00$	0.106	$2.852(92)E+00$		

$E_0 = 3.605$ GeV, $\theta = 16.021$ deg.

y	$F(y)$	y	$F(y)$	y	$F(y)$	y	$F(y)$
−0.848	$1.52(13)E-03$	−0.655	$9.95(29)E-03$	−0.536	$3.311(51)E-02$	−0.471	$6.274(73)E-02$
−0.765	$2.73(17)E-03$	−0.612	$1.465(35)E-02$	−0.502	$4.610(59)E-02$	−0.441	$8.494(85)E-02$
−0.705	$5.80(23)E-03$	−0.572	$2.289(44)E-02$				

$E_0 = 3.595$ GeV, $\theta = 16.021$ deg.

y	$F(y)$	y	$F(y)$	y	$F(y)$	y	$F(y)$
−0.410	$1.336(43)E-01$	0.033	$3.459(53)E+00$	0.282	$5.70(11)E+00$	0.433	$8.42(24)E+00$
−0.383	$1.812(48)E-01$	0.047	$3.492(92)E+00$	0.290	$5.75(16)E+00$	0.438	$9.35(25)E+00$
−0.357	$2.282(54)E-01$	0.060	$3.601(94)E+00$	0.298	$6.39(16)E+00$	0.444	$9.36(26)E+00$
−0.332	$2.822(62)E-01$	0.073	$3.676(91)E+00$	0.306	$6.29(17)E+00$	0.449	$9.00(18)E+00$
−0.308	$3.761(74)E-01$	0.086	$3.802(91)E+00$	0.314	$5.91(16)E+00$	0.454	$9.18(19)E+00$
−0.285	$5.082(81)E-01$	0.098	$3.670(91)E+00$	0.322	$6.48(13)E+00$	0.460	$9.48(27)E+00$
−0.262	$6.521(90)E-01$	0.110	$3.986(75)E+00$	0.330	$6.60(13)E+00$	0.465	$9.50(27)E+00$
−0.241	$8.18(10)E-01$	0.122	$4.056(75)E+00$	0.337	$6.51(19)E+00$	0.470	$9.71(27)E+00$
−0.220	$1.036(32)E+00$	0.134	$4.018(74)E+00$	0.344	$6.98(20)E+00$	0.475	$9.45(27)E+00$
−0.200	$1.233(34)E+00$	0.145	$4.19(10)E+00$	0.351	$6.75(19)E+00$	0.479	$9.75(20)E+00$
−0.180	$1.507(38)E+00$	0.157	$4.17(11)E+00$	0.358	$7.38(20)E+00$	0.484	$9.68(20)E+00$
−0.161	$1.754(41)E+00$	0.168	$4.40(11)E+00$	0.365	$7.31(20)E+00$	0.489	$9.76(28)E+00$
−0.142	$1.957(43)E+00$	0.178	$4.33(11)E+00$	0.372	$7.50(16)E+00$	0.493	$9.96(29)E+00$
−0.124	$2.291(37)E+00$	0.189	$4.56(12)E+00$	0.379	$7.35(16)E+00$	0.498	$9.56(28)E+00$
−0.107	$2.460(38)E+00$	0.199	$4.682(89)E+00$	0.385	$7.95(25)E+00$	0.502	$9.69(20)E+00$
−0.089	$2.738(40)E+00$	0.209	$4.830(89)E+00$	0.391	$7.61(25)E+00$	0.507	$1.031(21)E+01$
−0.073	$2.927(59)E+00$	0.219	$4.948(93)E+00$	0.398	$8.07(26)E+00$	0.511	$9.98(28)E+00$
−0.057	$3.126(60)E+00$	0.228	$5.09(14)E+00$	0.404	$7.63(26)E+00$	0.515	$1.017(28)E+01$
−0.041	$3.189(59)E+00$	0.238	$5.19(14)E+00$	0.410	$8.23(19)E+00$	0.519	$1.053(29)E+01$
−0.025	$3.397(61)E+00$	0.247	$5.12(14)E+00$	0.416	$8.15(18)E+00$	0.524	$1.002(28)E+01$
−0.010	$3.392(61)E+00$	0.256	$5.06(14)E+00$	0.422	$8.82(25)E+00$	0.528	$1.053(30)E+01$
0.005	$3.466(53)E+00$	0.265	$5.37(11)E+00$	0.427	$8.26(24)E+00$	0.532	$1.035(30)E+01$
0.019	$3.400(52)E+00$	0.274	$5.57(11)E+00$				

Table B.18 – $F(y)$ vs. y for Fe.

$E_0 = 3.595$ GeV, $\theta = 20.017$ deg.

y	$F(y)$	y	$F(y)$	y	$F(y)$	y	$F(y)$
−0.819	$2.5(12)E-04$	−0.448	$6.30(26)E-02$	−0.200	$1.034(25)E+00$	−0.012	$3.92(15)E+00$
−0.781	$1.01(20)E-03$	−0.426	$8.10(29)E-02$	−0.184	$1.252(28)E+00$	0.001	$3.61(15)E+00$
−0.745	$1.32(22)E-03$	−0.404	$1.083(33)E-01$	−0.168	$1.430(31)E+00$	0.013	$3.73(11)E+00$
−0.712	$2.11(34)E-03$	−0.383	$1.202(35)E-01$	−0.152	$1.611(64)E+00$	0.025	$4.05(11)E+00$
−0.680	$4.02(43)E-03$	−0.363	$1.509(39)E-01$	−0.137	$1.887(69)E+00$	0.037	$3.94(11)E+00$
−0.650	$4.76(45)E-03$	−0.343	$1.909(43)E-01$	−0.122	$2.226(72)E+00$	0.049	$3.97(14)E+00$
−0.622	$7.30(54)E-03$	−0.324	$2.354(48)E-01$	−0.107	$2.419(74)E+00$	0.060	$4.32(15)E+00$
−0.594	$1.232(72)E-02$	−0.305	$2.945(55)E-01$	−0.093	$2.555(77)E+00$	0.072	$4.27(15)E+00$
−0.568	$1.457(80)E-02$	−0.287	$3.90(18)E-01$	−0.079	$2.837(73)E+00$	0.083	$4.97(16)E+00$
−0.542	$2.177(84)E-02$	−0.269	$4.58(19)E-01$	−0.065	$2.939(75)E+00$	0.094	$4.70(16)E+00$
−0.517	$2.800(93)E-02$	−0.251	$5.72(21)E-01$	−0.051	$2.880(72)E+00$	0.105	$4.93(16)E+00$
−0.493	$3.48(10)E-02$	−0.234	$7.50(24)E-01$	−0.038	$3.35(15)E+00$	0.115	$4.94(17)E+00$
−0.470	$5.05(23)E-02$	−0.217	$9.43(27)E-01$	−0.025	$3.65(15)E+00$		

$E_0 = 3.595$ GeV, $\theta = 25.013$ deg.

y	$F(y)$	y	$F(y)$	y	$F(y)$	y	$F(y)$
−0.690	$1.52(76)E-03$	−0.412	$8.41(96)E-02$	−0.193	$1.086(69)E+00$	−0.028	$3.81(15)E+00$
−0.668	$1.77(70)E-03$	−0.395	$9.36(99)E-02$	−0.180	$1.265(74)E+00$	−0.017	$3.67(15)E+00$
−0.646	$1.83(72)E-03$	−0.378	$9.9(11)E-02$	−0.166	$1.341(76)E+00$	−0.005	$4.22(16)E+00$
−0.624	$3.9(11)E-03$	−0.361	$1.042(96)E-01$	−0.152	$1.573(83)E+00$	0.006	$4.30(16)E+00$
−0.603	$7.2(14)E-03$	−0.344	$1.53(12)E-01$	−0.139	$1.715(61)E+00$	0.017	$4.10(16)E+00$
−0.582	$7.8(13)E-03$	−0.328	$1.76(24)E-01$	−0.126	$1.939(65)E+00$	0.027	$4.39(13)E+00$
−0.562	$1.42(18)E-02$	−0.312	$1.95(26)E-01$	−0.113	$2.309(95)E+00$	0.038	$5.03(14)E+00$
−0.542	$1.13(16)E-02$	−0.297	$2.57(29)E-01$	−0.101	$2.357(96)E+00$	0.049	$5.40(21)E+00$
−0.522	$1.95(20)E-02$	−0.281	$2.97(31)E-01$	−0.088	$2.57(10)E+00$	0.059	$5.18(21)E+00$
−0.503	$2.14(21)E-02$	−0.266	$4.07(37)E-01$	−0.076	$2.87(11)E+00$	0.069	$5.46(22)E+00$
−0.484	$3.43(27)E-02$	−0.251	$5.21(33)E-01$	−0.064	$3.10(11)E+00$	0.079	$5.47(22)E+00$
−0.466	$4.04(29)E-02$	−0.236	$6.20(35)E-01$	−0.052	$3.109(88)E+00$	0.089	$5.38(22)E+00$
−0.447	$4.51(74)E-02$	−0.222	$7.29(38)E-01$	−0.040	$3.322(90)E+00$	0.099	$6.41(24)E+00$
−0.429	$6.21(85)E-02$	−0.207	$8.42(61)E-01$				

$E_0 = 3.595$ GeV, $\theta = 30.011$ deg.

y	$F(y)$	y	$F(y)$	y	$F(y)$	y	$F(y)$
−0.640	$5.3(26)E-03$	−0.232	$5.48(41)E-01$	0.045	$5.81(26)E+00$	0.247	$1.459(58)E+01$
−0.586	$6.7(20)E-03$	−0.218	$7.54(88)E-01$	0.055	$6.87(29)E+00$	0.255	$1.582(59)E+01$
−0.568	$1.07(22)E-02$	−0.205	$8.51(96)E-01$	0.065	$6.59(46)E+00$	0.262	$1.626(58)E+01$
−0.550	$1.17(22)E-02$	−0.192	$1.20(11)E+00$	0.075	$7.44(49)E+00$	0.270	$1.787(60)E+01$
−0.533	$1.56(26)E-02$	−0.180	$9.85(96)E-01$	0.084	$7.60(48)E+00$	0.277	$1.758(53)E+01$
−0.516	$1.46(36)E-02$	−0.167	$1.20(11)E+00$	0.094	$8.08(50)E+00$	0.284	$1.692(53)E+01$
−0.499	$1.81(40)E-02$	−0.155	$1.392(79)E+00$	0.103	$7.47(29)E+00$	0.291	$2.05(11)E+01$
−0.483	$2.76(52)E-02$	−0.142	$1.722(88)E+00$	0.112	$8.13(30)E+00$	0.298	$1.87(10)E+01$
−0.467	$2.60(37)E-02$	−0.130	$1.76(11)E+00$	0.122	$8.70(38)E+00$	0.306	$2.08(11)E+01$
−0.450	$3.48(42)E-02$	−0.118	$2.18(13)E+00$	0.131	$8.68(37)E+00$	0.313	$2.046(68)E+01$
−0.435	$4.07(46)E-02$	−0.106	$2.31(13)E+00$	0.140	$8.88(38)E+00$	0.319	$2.225(87)E+01$
−0.419	$5.82(82)E-02$	−0.095	$2.62(14)E+00$	0.148	$9.57(31)E+00$	0.326	$2.108(84)E+01$
−0.403	$5.94(80)E-02$	−0.083	$2.77(12)E+00$	0.157	$1.005(32)E+01$	0.333	$2.153(84)E+01$
−0.388	$7.24(87)E-02$	−0.072	$3.08(12)E+00$	0.166	$1.006(50)E+01$	0.340	$2.175(86)E+01$
−0.373	$8.42(93)E-02$	−0.060	$3.30(20)E+00$	0.174	$1.169(53)E+01$	0.346	$2.291(64)E+01$
−0.358	$9.31(99)E-02$	−0.049	$3.72(21)E+00$	0.183	$1.078(49)E+01$	0.353	$2.377(90)E+01$
−0.343	$1.36(11)E-01$	−0.038	$3.57(20)E+00$	0.191	$1.164(53)E+01$	0.359	$2.372(87)E+01$
−0.329	$1.51(12)E-01$	−0.027	$3.83(20)E+00$	0.199	$1.116(35)E+01$	0.366	$2.367(86)E+01$
−0.314	$1.50(25)E-01$	−0.017	$4.24(17)E+00$	0.207	$1.248(49)E+01$	0.372	$2.397(64)E+01$
−0.300	$2.82(35)E-01$	−0.006	$4.48(18)E+00$	0.216	$1.305(50)E+01$	0.378	$2.415(90)E+01$
−0.286	$2.85(34)E-01$	0.005	$4.83(29)E+00$	0.224	$1.391(52)E+01$	0.384	$2.615(93)E+01$
−0.272	$3.20(36)E-01$	0.015	$4.69(29)E+00$	0.231	$1.391(52)E+01$	0.390	$2.466(90)E+01$
−0.258	$4.48(44)E-01$	0.025	$5.07(30)E+00$	0.239	$1.489(41)E+01$	0.397	$2.432(91)E+01$
−0.245	$4.52(37)E-01$	0.035	$5.74(31)E+00$				

Table B.19 – $F(y)$ vs. y for Fe.

$E_0 = 3.595$ GeV, $\theta = 39.008$ deg.

y	$F(y)$	y	$F(y)$	y	$F(y)$	y	$F(y)$
−0.340	$1.09(25)E-01$	−0.211	$6.80(39)E-01$	−0.093	$2.64(16)E+00$	0.015	$5.94(37)E+00$
−0.327	$1.36(27)E-01$	−0.199	$8.02(42)E-01$	−0.082	$2.71(15)E+00$	0.025	$6.86(39)E+00$
−0.314	$1.93(31)E-01$	−0.186	$8.87(37)E-01$	−0.070	$3.06(17)E+00$	0.035	$6.49(37)E+00$
−0.300	$2.12(29)E-01$	−0.174	$1.056(41)E+00$	−0.059	$3.11(14)E+00$	0.046	$7.69(33)E+00$
−0.287	$2.68(34)E-01$	−0.162	$1.206(73)E+00$	−0.048	$3.38(14)E+00$	0.055	$8.28(52)E+00$
−0.274	$2.87(35)E-01$	−0.151	$1.371(75)E+00$	−0.038	$4.06(25)E+00$	0.065	$8.40(52)E+00$
−0.261	$3.30(24)E-01$	−0.139	$1.676(83)E+00$	−0.027	$4.46(27)E+00$	0.075	$8.85(53)E+00$
−0.249	$4.67(27)E-01$	−0.127	$1.777(85)E+00$	−0.016	$4.88(28)E+00$	0.085	$8.96(53)E+00$
−0.236	$5.00(35)E-01$	−0.116	$1.932(77)E+00$	−0.006	$4.71(22)E+00$	0.095	$9.50(56)E+00$
−0.223	$5.49(35)E-01$	−0.104	$2.156(86)E+00$	0.005	$5.75(38)E+00$		

$E_0 = 3.995$ GeV, $\theta = 30.011$ deg.

y	$F(y)$	y	$F(y)$	y	$F(y)$	y	$F(y)$
−0.581	$7.6(37)E-03$	−0.245	$4.97(21)E-01$	0.015	$6.11(24)E+00$	0.216	$1.877(71)E+01$
−0.565	$7.8(36)E-03$	−0.232	$5.97(24)E-01$	0.024	$6.56(25)E+00$	0.224	$1.830(71)E+01$
−0.549	$1.17(37)E-02$	−0.220	$7.88(49)E-01$	0.034	$6.69(20)E+00$	0.231	$1.984(55)E+01$
−0.534	$1.12(36)E-02$	−0.208	$9.07(51)E-01$	0.043	$7.41(21)E+00$	0.238	$2.070(80)E+01$
−0.518	$1.18(35)E-02$	−0.197	$9.37(52)E-01$	0.052	$7.60(21)E+00$	0.246	$2.138(81)E+01$
−0.503	$1.17(35)E-02$	−0.185	$1.126(57)E+00$	0.061	$7.94(32)E+00$	0.253	$2.096(79)E+01$
−0.488	$2.17(38)E-02$	−0.173	$1.360(63)E+00$	0.070	$7.68(32)E+00$	0.260	$2.272(62)E+01$
−0.473	$2.50(39)E-02$	−0.162	$1.471(51)E+00$	0.079	$8.45(34)E+00$	0.267	$2.366(62)E+01$
−0.459	$3.11(56)E-02$	−0.151	$1.640(54)E+00$	0.088	$8.83(27)E+00$	0.274	$2.512(64)E+01$
−0.444	$3.73(49)E-02$	−0.140	$1.959(90)E+00$	0.096	$9.82(28)E+00$	0.280	$2.519(88)E+01$
−0.430	$3.96(51)E-02$	−0.128	$2.109(90)E+00$	0.105	$1.056(43)E+01$	0.287	$2.553(89)E+01$
−0.416	$5.96(88)E-02$	−0.118	$2.463(98)E+00$	0.113	$1.003(40)E+01$	0.294	$2.620(91)E+01$
−0.402	$8.1(11)E-02$	−0.107	$2.57(10)E+00$	0.122	$1.039(40)E+01$	0.300	$2.606(69)E+01$
−0.388	$6.90(96)E-02$	−0.096	$2.84(10)E+00$	0.130	$1.133(42)E+01$	0.307	$2.79(10)E+01$
−0.374	$8.4(10)E-02$	−0.085	$3.140(89)E+00$	0.138	$1.201(45)E+01$	0.313	$3.04(11)E+01$
−0.360	$1.08(11)E-01$	−0.075	$3.370(93)E+00$	0.147	$1.199(36)E+01$	0.320	$2.82(10)E+01$
−0.347	$1.241(94)E-01$	−0.065	$3.61(15)E+00$	0.155	$1.322(61)E+01$	0.326	$3.04(11)E+01$
−0.334	$1.43(10)E-01$	−0.054	$3.90(15)E+00$	0.163	$1.389(62)E+01$	0.333	$3.124(77)E+01$
−0.321	$1.76(11)E-01$	−0.044	$4.08(15)E+00$	0.171	$1.402(62)E+01$	0.339	$3.15(11)E+01$
−0.308	$2.17(17)E-01$	−0.034	$4.52(16)E+00$	0.178	$1.421(63)E+01$	0.345	$3.00(10)E+01$
−0.295	$2.60(18)E-01$	−0.024	$4.79(17)E+00$	0.186	$1.549(47)E+01$	0.351	$3.12(10)E+01$
−0.282	$2.89(19)E-01$	−0.014	$5.03(14)E+00$	0.194	$1.622(48)E+01$	0.357	$3.31(11)E+01$
−0.269	$3.88(22)E-01$	−0.004	$5.09(14)E+00$	0.202	$1.766(70)E+01$	0.363	$3.25(11)E+01$
−0.257	$4.27(20)E-01$	0.005	$5.79(24)E+00$	0.209	$1.833(70)E+01$		

Table B.20 – $F(y)$ vs. y for Fe.

$E_0 = 2.020$ GeV, $\theta = 15.023$ deg.

y	$F(y)$	y	$F(y)$	y	$F(y)$	y	$F(y)$
−0.382	$1.006(23)E+00$	−0.083	$2.576(56)E+00$	0.055	$2.512(50)E+00$	0.158	$2.216(82)E+00$
−0.302	$1.306(25)E+00$	−0.052	$2.673(85)E+00$	0.078	$2.358(59)E+00$	0.176	$2.087(80)E+00$
−0.244	$1.635(28)E+00$	−0.022	$2.721(83)E+00$	0.099	$2.290(58)E+00$	0.193	$2.239(84)E+00$
−0.196	$2.005(66)E+00$	0.005	$2.611(79)E+00$	0.120	$2.280(59)E+00$	0.210	$2.412(92)E+00$
−0.154	$2.333(71)E+00$	0.031	$2.593(51)E+00$	0.140	$2.160(48)E+00$	0.226	$2.515(99)E+00$
−0.117	$2.424(55)E+00$						

$E_0 = 2.020$ GeV, $\theta = 20.017$ deg.

y	$F(y)$	y	$F(y)$	y	$F(y)$	y	$F(y)$
−0.556	$1.129(59)E-01$	−0.212	$1.685(46)E+00$	−0.026	$2.969(74)E+00$	0.111	$3.184(95)E+00$
−0.473	$2.008(75)E-01$	−0.181	$1.967(44)E+00$	−0.004	$2.891(73)E+00$	0.128	$2.990(66)E+00$
−0.413	$3.330(94)E-01$	−0.152	$2.224(46)E+00$	0.017	$2.974(75)E+00$	0.144	$2.970(66)E+00$
−0.364	$5.21(11)E-01$	−0.124	$2.519(64)E+00$	0.037	$3.06(11)E+00$	0.160	$3.103(93)E+00$
−0.320	$7.75(44)E-01$	−0.098	$2.706(56)E+00$	0.057	$3.039(73)E+00$	0.175	$3.142(96)E+00$
−0.281	$1.079(51)E+00$	−0.073	$2.861(70)E+00$	0.075	$3.065(97)E+00$	0.190	$3.25(10)E+00$
−0.245	$1.346(43)E+00$	−0.049	$2.953(60)E+00$	0.094	$2.921(92)E+00$		

$E_0 = 3.605$ GeV, $\theta = 16.021$ deg.

y	$F(y)$	y	$F(y)$	y	$F(y)$	y	$F(y)$
−0.868	$1.54(16)E-03$	−0.670	$1.118(40)E-02$	−0.550	$3.711(69)E-02$	−0.484	$6.782(98)E-02$
−0.782	$2.95(23)E-03$	−0.626	$1.700(49)E-02$	−0.516	$5.027(80)E-02$	−0.454	$9.14(11)E-02$
−0.721	$6.62(32)E-03$	−0.586	$2.625(61)E-02$				

$E_0 = 3.595$ GeV, $\theta = 16.021$ deg.

y	$F(y)$	y	$F(y)$	y	$F(y)$	y	$F(y)$
−0.423	$1.325(57)E-01$	0.022	$3.436(65)E+00$	0.273	$5.82(16)E+00$	0.425	$8.96(31)E+00$
−0.396	$1.691(63)E-01$	0.036	$3.54(15)E+00$	0.282	$6.19(25)E+00$	0.431	$9.77(32)E+00$
−0.369	$2.205(73)E-01$	0.050	$3.66(16)E+00$	0.290	$5.94(24)E+00$	0.437	$9.39(32)E+00$
−0.344	$3.007(87)E-01$	0.063	$3.78(15)E+00$	0.298	$6.40(26)E+00$	0.442	$9.55(25)E+00$
−0.320	$3.87(10)E-01$	0.076	$3.81(15)E+00$	0.306	$6.15(26)E+00$	0.447	$9.61(26)E+00$
−0.297	$5.10(11)E-01$	0.088	$3.90(16)E+00$	0.314	$6.54(19)E+00$	0.452	$9.03(39)E+00$
−0.275	$6.50(12)E-01$	0.100	$3.80(12)E+00$	0.321	$6.91(19)E+00$	0.458	$9.80(39)E+00$
−0.253	$8.02(13)E-01$	0.112	$4.11(12)E+00$	0.329	$6.46(25)E+00$	0.463	$9.49(39)E+00$
−0.232	$1.031(45)E+00$	0.124	$4.29(12)E+00$	0.336	$7.13(26)E+00$	0.468	$9.19(39)E+00$
−0.211	$1.288(50)E+00$	0.136	$4.73(17)E+00$	0.343	$7.17(26)E+00$	0.472	$9.84(30)E+00$
−0.192	$1.521(54)E+00$	0.147	$4.54(17)E+00$	0.350	$7.20(26)E+00$	0.477	$9.75(30)E+00$
−0.172	$1.700(56)E+00$	0.158	$4.86(18)E+00$	0.357	$7.48(27)E+00$	0.482	$1.025(43)E+01$
−0.154	$1.900(60)E+00$	0.169	$4.75(17)E+00$	0.364	$7.10(20)E+00$	0.487	$1.072(44)E+01$
−0.136	$2.124(45)E+00$	0.179	$4.54(18)E+00$	0.371	$7.59(21)E+00$	0.491	$9.66(41)E+00$
−0.118	$2.420(47)E+00$	0.190	$5.08(14)E+00$	0.377	$7.92(31)E+00$	0.496	$9.77(30)E+00$
−0.101	$2.582(48)E+00$	0.200	$4.84(13)E+00$	0.384	$7.57(30)E+00$	0.500	$1.014(30)E+01$
−0.084	$2.763(64)E+00$	0.210	$5.15(14)E+00$	0.390	$7.76(32)E+00$	0.504	$1.106(43)E+01$
−0.068	$2.973(65)E+00$	0.219	$5.47(19)E+00$	0.396	$7.78(33)E+00$	0.509	$1.035(42)E+01$
−0.052	$3.088(65)E+00$	0.229	$5.45(19)E+00$	0.402	$8.82(25)E+00$	0.513	$1.083(43)E+01$
−0.036	$3.224(65)E+00$	0.238	$5.45(19)E+00$	0.408	$8.60(23)E+00$	0.517	$1.041(42)E+01$
−0.021	$3.328(66)E+00$	0.247	$5.55(20)E+00$	0.414	$8.82(31)E+00$	0.521	$1.012(43)E+01$
−0.006	$3.400(63)E+00$	0.256	$5.32(15)E+00$	0.420	$8.45(30)E+00$	0.525	$1.031(44)E+01$
0.008	$3.286(62)E+00$	0.265	$5.87(16)E+00$				

Table B.21 – $F(y)$ vs. y for Au.

$E_0 = 3.595$ GeV, $\theta = 20.017$ deg.

y	$F(y)$	y	$F(y)$	y	$F(y)$	y	$F(y)$
−0.754	$1.19(41)E-03$	−0.415	$1.035(35)E-01$	−0.194	$1.167(25)E+00$	−0.022	$3.30(12)E+00$
−0.721	$1.70(41)E-03$	−0.394	$1.260(38)E-01$	−0.178	$1.367(27)E+00$	−0.009	$3.46(13)E+00$
−0.690	$3.50(57)E-03$	−0.374	$1.582(43)E-01$	−0.163	$1.527(57)E+00$	0.003	$3.55(10)E+00$
−0.660	$4.74(64)E-03$	−0.354	$2.028(47)E-01$	−0.147	$1.796(62)E+00$	0.015	$3.733(99)E+00$
−0.632	$8.42(84)E-03$	−0.334	$2.451(52)E-01$	−0.132	$1.917(61)E+00$	0.027	$4.04(11)E+00$
−0.604	$1.19(10)E-02$	−0.315	$3.015(59)E-01$	−0.117	$2.129(63)E+00$	0.039	$4.15(15)E+00$
−0.578	$1.76(13)E-02$	−0.297	$4.17(18)E-01$	−0.103	$2.438(69)E+00$	0.051	$3.97(15)E+00$
−0.552	$2.09(11)E-02$	−0.279	$5.15(19)E-01$	−0.089	$2.517(62)E+00$	0.062	$4.63(16)E+00$
−0.528	$2.87(12)E-02$	−0.261	$6.06(20)E-01$	−0.075	$2.671(64)E+00$	0.073	$4.52(16)E+00$
−0.504	$3.65(14)E-02$	−0.244	$7.26(22)E-01$	−0.061	$2.802(64)E+00$	0.084	$4.46(16)E+00$
−0.480	$5.20(26)E-02$	−0.227	$8.38(23)E-01$	−0.048	$3.12(13)E+00$	0.095	$4.59(16)E+00$
−0.458	$6.37(28)E-02$	−0.210	$1.003(23)E+00$	−0.035	$3.37(13)E+00$	0.106	$4.69(17)E+00$
−0.436	$8.37(31)E-02$						

$E_0 = 3.595$ GeV, $\theta = 25.013$ deg.

y	$F(y)$	y	$F(y)$	y	$F(y)$	y	$F(y)$
−0.675	$3.3(16)E-03$	−0.404	$8.7(12)E-02$	−0.203	$9.37(60)E-01$	−0.037	$3.36(12)E+00$
−0.632	$6.7(16)E-03$	−0.387	$8.7(13)E-02$	−0.189	$9.97(61)E-01$	−0.026	$3.79(13)E+00$
−0.611	$9.1(19)E-03$	−0.370	$1.18(12)E-01$	−0.175	$1.277(70)E+00$	−0.015	$3.62(13)E+00$
−0.590	$1.13(20)E-02$	−0.353	$1.34(12)E-01$	−0.162	$1.494(77)E+00$	−0.004	$3.87(13)E+00$
−0.570	$1.14(21)E-02$	−0.337	$1.64(20)E-01$	−0.149	$1.566(60)E+00$	0.007	$4.01(13)E+00$
−0.550	$1.30(22)E-02$	−0.321	$2.19(24)E-01$	−0.135	$1.865(66)E+00$	0.018	$4.27(11)E+00$
−0.531	$1.95(24)E-02$	−0.306	$2.09(23)E-01$	−0.123	$2.05(10)E+00$	0.029	$4.31(11)E+00$
−0.511	$2.03(24)E-02$	−0.290	$3.01(27)E-01$	−0.110	$2.36(11)E+00$	0.040	$4.80(17)E+00$
−0.493	$2.78(29)E-02$	−0.275	$3.85(31)E-01$	−0.097	$2.53(11)E+00$	0.050	$4.87(18)E+00$
−0.474	$3.65(33)E-02$	−0.260	$5.06(29)E-01$	−0.085	$2.70(12)E+00$	0.060	$4.92(18)E+00$
−0.456	$4.89(93)E-02$	−0.246	$5.37(29)E-01$	−0.073	$2.84(12)E+00$	0.070	$5.27(19)E+00$
−0.438	$7.6(11)E-02$	−0.231	$6.54(32)E-01$	−0.061	$3.136(89)E+00$	0.080	$5.56(19)E+00$
−0.421	$5.73(96)E-02$	−0.217	$9.14(59)E-01$	−0.049	$3.071(87)E+00$	0.090	$5.91(20)E+00$

$E_0 = 3.595$ GeV, $\theta = 30.011$ deg.

y	$F(y)$	y	$F(y)$	y	$F(y)$	y	$F(y)$
−0.254	$5.63(75)E-01$	−0.036	$3.43(14)E+00$	0.140	$8.94(32)E+00$	0.283	$1.910(73)E+01$
−0.240	$6.55(76)E-01$	−0.026	$3.78(13)E+00$	0.149	$9.73(33)E+00$	0.291	$1.876(72)E+01$
−0.227	$5.99(71)E-01$	−0.015	$4.29(14)E+00$	0.157	$1.003(46)E+01$	0.298	$1.860(71)E+01$
−0.214	$8.25(87)E-01$	−0.004	$4.31(30)E+00$	0.166	$1.059(46)E+01$	0.305	$2.087(60)E+01$
−0.201	$8.48(86)E-01$	0.006	$4.90(32)E+00$	0.174	$1.064(45)E+01$	0.312	$2.096(93)E+01$
−0.189	$8.83(82)E-01$	0.016	$5.01(31)E+00$	0.183	$1.138(48)E+01$	0.319	$2.169(93)E+01$
−0.176	$1.149(98)E+00$	0.027	$5.25(32)E+00$	0.191	$1.273(36)E+01$	0.325	$2.016(89)E+01$
−0.164	$1.272(65)E+00$	0.037	$5.26(21)E+00$	0.199	$1.255(48)E+01$	0.332	$2.195(94)E+01$
−0.151	$1.550(71)E+00$	0.047	$5.78(23)E+00$	0.207	$1.450(52)E+01$	0.339	$2.176(68)E+01$
−0.139	$1.737(93)E+00$	0.056	$6.08(29)E+00$	0.215	$1.367(50)E+01$	0.345	$2.35(10)E+01$
−0.127	$1.796(93)E+00$	0.066	$6.09(29)E+00$	0.223	$1.442(51)E+01$	0.352	$2.369(98)E+01$
−0.115	$2.30(11)E+00$	0.076	$6.31(29)E+00$	0.231	$1.488(43)E+01$	0.358	$2.312(95)E+01$
−0.104	$2.23(11)E+00$	0.085	$7.76(33)E+00$	0.239	$1.546(73)E+01$	0.365	$2.489(66)E+01$
−0.092	$2.506(85)E+00$	0.095	$7.29(26)E+00$	0.246	$1.581(71)E+01$	0.371	$2.347(82)E+01$
−0.081	$2.760(89)E+00$	0.104	$7.51(26)E+00$	0.254	$1.614(69)E+01$	0.377	$2.444(83)E+01$
−0.069	$2.92(13)E+00$	0.113	$8.16(45)E+00$	0.262	$1.627(70)E+01$	0.383	$2.452(83)E+01$
−0.058	$3.28(14)E+00$	0.122	$8.24(44)E+00$	0.269	$1.792(53)E+01$	0.389	$2.503(85)E+01$
−0.047	$3.29(14)E+00$	0.131	$8.36(44)E+00$	0.276	$1.788(52)E+01$		

Table B.22 – $F(y)$ vs. y for Au.

References

[1] J. D. Bjorken and S. D. Drell, *Relativistic Quantum Mechanics*, McGraw Hill Book Co., N.Y. (1964).

[2] G. Höhler, *et al.*, Nucl. Phys. **B114**, 505 (1976).

[3] G. G. Simon, *et al.*, Nucl. Phys. **A333**, 381 (1980).

[4] M. Gari and W. Krümpelmann, Phys. Lett. **141B**, 295 (1984).

[5] T. W. Donnelly, *et al.*, Phys. Lett. **76B**, 393 (1978).

[6] G. B. West, Phys. Rep. **18C**, 264 (1975).

[7] Peter D. Zimmerman, C. F. Williamson, and Yoshiyuki Kawazoe, Phys. Rev. **C19**, 279 (1979).

[8] I. Sick, D. Day, and J. S. McCarthy, Phys. Rev. Lett. **45**, 871 (1980).

[9] E. Pace and G. Salmè, Phys. Lett. **110B**, 411 (1982).

[10] J. D. Bjorken, Phys. Rev. **179**, 1547 (1969).

[11] J. V. Noble, Phys. Rev. Lett. **46**, 412 (1981).

[12] R. L. Jaffe, *et al.*, Phys. Lett. **134B**, 449 (1984), and references therein.

[13] L. S. Celenza, *et al.*, Phys. Rev. **C31**, 212; 232; 946 (1985).

[14] P. J. Mulders, Nucl. Phys. **A459**, 525 (1986).

[15] J. P. Vary, Nucl. Phys. **A418**, 195c (1984), and references therein.

[16] J. J. Aubert, *et al.*, Phys. Lett. **123B**, 123 (1983).

[17] A. Bodek, *et al.*, Phys. Rev. Lett. **50**, 1431 (1983).

[18] A. Bodek, *et al.*, Phys. Rev. Lett. **51**, 534 (1983).

[19] R. G. Arnold, *et al.*, Phys. Rev. Lett. **52**, 727 (1984).

[20] M. A. MacGregor, R. A. Arndt, and R. M. Wright, Phys. Rev. **182**, 1714 (1969).

[21] W. Czyz and K. Gottfried, Ann. Phys. **21**, 47 (1963).

[22] K. W. McVoy and L. Van Hove, Phys. Rev. **125**, 1034 (1962).

[23] J. G. Zabolitzki and W. Ey, Phys. Lett. **76B**, 527 (1978).

[24] T. deForest, Ann. Phys. **45**, 365 (1967).

[25] D. Day, *et al.*, Phys. Rev. Lett. **43**, 1143 (1979).

[26] R. D. McKeown, Phys. Rev. Lett. **56**, 1452 (1986).

[27] E. J. Moniz, *et al.*, Phys. Rev. Lett. **26**, 445 (1971).

[28] P. Bosted, *et al.*, Phys. Rev. Lett. **49**, 1380 (1982).

[29] I. Sick, *et al.*, Phys. Rev. Lett. **45**, 871 (1980).

[30] M. N. Butler, Ph.D. Thesis, Caltech, Pasadena (1987).

[31] M. Lacombe, *et al.*, Phys. Rev. **C21**, 861 (1980), and references therein.

[32] E139 hardware logbook, unpublished.

[33] *Handbook of Chemistry and Physics*, 68$^{\text{th}}$ ed., CRC Press, Boca Raton, Fl. (1987).

[34] J. Gomez, SLAC report SLAC-NPAS-84-1 (1984).

[35] P. Bosted and A. Rahbar, SLAC report SLAC-NPAS-85-1 (1985).

[36] J. M. Lambert, Survey Results for the 8 GeV/c Spectrometer (1984), unpublished.

[37] Ray Arnold, private communication.

[38] Luke Mo and C. Peck, SLAC report TN-65-29 (1965).

[39] K. Kleinknecht, *Detectors for Particle Radiation*, Univ. Press, N.Y. (1986).

[40] S. Dasu, Ph.D. thesis, Rochester Univ., Rochester (1988).

[41] Universal Wire Detector CAMAC Scanning System, Nanometric Systems, 837 North Cuyler Ave, Oak Park, Ill. 60302.

[42] M. J. Brown, *et. al.*, SLAC report SLAC-PUB-2494 (1980).

[43] Stein, *et al.*, Phys. Rev. **D12**, 1884 (1975).

[44] Alan F. Sill, Ph.D. thesis, American University, Washington, D.C. (1986).

[45] D. H. Coward, *et al.*, Phys. Rev. Lett. **20**, 292 (1968).

[46] P. N. Kirk, *et al.*, Phys. Rev. **D8**, 63 (1973).

[47] A. F. Sill, SLAC report SLAC-NPAS-TN-86-1 (1986), and references therein.

[48] Yung-su Tsai, SLAC Report SLAC-PUB-848 (1971).

[49] A. Bodek, Nucl. Instr. Methods **109**, 603 (1973).

[50] R. M. Sternheimer, *Methods of Experimental Physics*, Vol. 5A, p. 17, Academic Press, N.Y. (1961).

[51] T. De Forest, Nuc. Phys. **A392**, 232 (1983).

[52] A. E. L. Dieperink, *et al.*, Phys. Lett. **63B**, 261 (1976).

[53] R. D. McKeown, private communication.

[54] D. B. Day, *et al.*, Phys. Rev. Lett. **59**, 427 (1987).

[55] R. R. Whitney, *et al.*, Phys. Rev. **C9**, 2230 (1974).

[56] A. Bodek, *et al.*, Phys. Rev. **D20**, 1471 (1979).

[57] A. Bodek and J. L. Ritchie, Phys. Rev. **D23**, 1070 (1981).

[58] R. Machleidt, K. Holinde, and Ch. Elster, Phys. Rep. **149**, 1 (1987), and references therein.

[59] B. W. Filippone, private communication.

[60] W. B. Atwood and S. Stein, Phys. Rev. D12, 1884 (1975).

[61] H. Akima, Journal of the A. C. M. **17**, 589 (1970).

[62] Carl DeBoor, *A Practical Guide to Splines*, Springer-Verlag, N.Y. (1978).

[63] D. H. Perkins, *Introduction to High Energy Physics*, Addison Wesley Publishing Co., Reading, Mass. (1972).

[64] L. W. Mo and Y. S. Tsai, Rev. Mod. Phys. **41**, 205 (1969).

[65] These are updated values of the parameters appearing in references [43,48,64]. See, for example, Y. S. Tsai, Rev. Mod. Phys. **46**, 815 (1974).

[65] L. C. Maximon, Rev. Mod. Phys. **41**, 193 (1969), and references therein.

[66] Zen Szalata, private communication.